

THE UNIVERSITY OF HULL

**Probing Cardiac Metabolism in Uraemic
Cardiomyopathy**

being a Thesis submitted for the Degree of Doctor of Philosophy

in the University of Hull

by

Robert Atkinson, BSc

April 2017

Abstract

Cardiovascular complications are the leading cause of death in patients with chronic kidney disease (CKD). Uraemic cardiomyopathy (UCM) is characterised by structural and cellular remodelling including left ventricular hypertrophy (LVH), metabolic remodelling and mitochondrial dysfunction. Although *ex vivo* studies have highlighted evidence of enhanced glucose utilisation in the hypertrophied heart, cardiac glucose metabolism in uraemia has yet to be established *in vivo*. In addition, little is known about mitochondrial morphology or the impact of iron therapy on cardiac mitochondrial function in CKD. The aims of this study were to (I) investigate cardiac glucose metabolism *in vivo* using ^{18}F -fluorodeoxyglucose positron emission tomography (^{18}F -FDG PET) during the development of UCM and (II) characterise mitochondrial morphology and the impact of iron therapy on cardiac mitochondrial function in uraemia.

Experimental uraemia was induced surgically in male Sprague-Dawley rats via a subtotal nephrectomy. Dynamic PET/CT scans were acquired at 5, 9 and 13 weeks post-surgery using ^{18}F -FDG PET. The rate and distribution of ^{18}F -FDG uptake were determined using Patlak and polar map analysis. In a separate series of experiments the iron complex, ferumoxytol, was administered 6 weeks post-surgery and mitochondrial respiratory rates and enzyme activities determined following sacrifice 6 weeks later. Cardiac mitochondrial morphology was characterised by probing the expression of key mitochondrial fusion and fission proteins and evaluating mitochondrial size and structure in left ventricular tissue and isolated mitochondria.

Renal dysfunction was prominent in uraemic animals by 12 weeks as evidenced by elevated serum creatinine, urea and the presence of anaemia. LVH was

associated with moderately increased ^{18}F -FDG uptake in the uraemic heart at 5, 9 and 13 weeks. This was paralleled at the cellular level by altered mitochondrial morphology, characterised by a more sparsely packed cristae, and increased mitochondrial state 4 respiration, indicative of reduced efficiency. However, ferumoxytol treatment did not impact on cardiac mitochondrial function at this stage of uraemia. Collectively these data suggest there is evidence of enhanced glucose utilisation in the uraemic heart *in vivo* and these changes are associated with altered mitochondrial structure and bioenergetics.

Acknowledgements

I am sincerely grateful to my supervisor, Dr Anne-Marie Seymour, for her continued guidance, mentorship and patience throughout my PhD. In particular, I would like to thank Anne-Marie for her constant encouragement and support. I am also thankful for the support provided by my second supervisors; Professor Sunil Bhandari, Dr Chris Cawthorne and Professor Steve Archibald.

I would like to thank Mrs Kathleen Bulmer, Miss Laura Goodlass, Mrs Ann Lowry and Dr Torsten Ruest for their invaluable technical assistance over the last 4 years.

I would like to thank my family and friends for their unwavering support during my PhD, and my colleague and friend Mr Faisal Nuhu for the camaraderie we shared.

I am extremely grateful to the University of Hull for funding this PhD and giving me this opportunity.

Finally, I would like to dedicate this thesis to my wife, Sarah, who has given me endless strength, support and encouragement, without her this thesis would not have been possible.

Contents

<i>Abstract</i>		i
<i>Acknowledgments</i>		iii
<i>Contents</i>		iv
<i>List of Figures</i>		xii
<i>List of Tables</i>		xvii
<i>List of Abbreviations</i>		xix
<i>Chapter 1</i>	<i>Introduction</i>	1
1.1	Chronic Kidney Disease	2
1.2	Uraemic Cardiomyopathy	3
1.3	Anaemia	5
1.4	Left Ventricular Hypertrophy	12
1.5	Calcium Handling	14
1.6	Cardiac Energy Metabolism	17
1.6.1	Cardiac Energy Provision	17
1.6.2	Fatty Acid Metabolism	18
1.6.3	Carbohydrate Metabolism	20
1.7	Energy Deficiency in the Failing Heart	22
1.8	Cardiac Mitochondria	23
1.9	Mitochondrial Biogenesis	24
1.10	Autophagy	26
1.11	Apoptosis	28
1.12	Necrosis	32

1.13	Mitochondrial Permeability Transition Pore	33
1.14	Objectives	36
Chapter 2	<i>Materials and Methods</i>	38
2.1	Induction of Experimental Uraemia	39
2.2	Characterisation of UCM Model	41
2.2.1	Markers of Renal Function and Iron Homeostasis	41
2.2.2	Indices of Cardiac Hypertrophy	42
2.2.3	Indices of Body Mass	42
2.3	Mitochondrial Studies	43
2.3.1	Mitochondrial Isolation	43
2.3.2	Mitochondrial Respiratory Rates	45
2.3.3	Mitochondrial Enzyme Activities	47
2.3.3.1	Respiratory Complex I Assay	48
2.3.3.2	Respiratory Complex II Assay	48
2.3.3.3	Respiratory Complex II + III Assay	49
2.3.3.4	Respiratory Complex IV Assay	50
2.3.3.5	Citrate Synthase Assay	51
2.3.3.5.1	Citrate Synthase Activity in Isolated Mitochondria	51
2.3.3.5.2	Citrate Synthase Activity in Cardiac Tissue	51
2.3.4	Calcium Induced Mitochondrial Swelling Assay	52

2.3.5	Mitochondrial Morphology	52
2.3.5.1	Transmission Electron Microscopy	52
2.3.5.2	Flow Cytometry	53
2.3.5.3	Dynamic Light Scattering	54
2.4	Western Blotting	54
2.5	Statistical Analysis	57
Chapter 3	<i>Characterisation of Experimental Uraemia</i>	58
3.1	Introduction	59
3.1.1	Nephrotoxic Drugs	59
3.1.2	Surgical Intervention	60
3.1.3	Iron Therapy	62
3.1.3.1	Erythropoietin	62
3.1.3.2	Iron Supplementation	63
3.1.4	Objectives	66
3.2	Methods	68
3.2.1	Experimental Design	68
3.2.2	Ferumoxytol Treatment	68
3.2.3	Markers of Renal Function	69
3.2.4	Markers of Uraemia	69
3.2.4.1	Determination of LVH	69
3.2.4.2	Anaemia	70
3.3	Results	71
3.3.1	Markers of Renal Function	71

3.3.2	Markers of Uraemia	74
3.3.2.1	Left Ventricular Hypertrophy	74
3.3.2.2	Anaemia	76
3.4	Discussion	78
3.4.1	Markers of Renal Function	78
3.4.2	Markers of Uraemia	81
3.4.2.1	Left Ventricular Hypertrophy	81
3.4.2.2	Anaemia	83
3.4.3	Conclusions	84
Chapter 4	<i>In Vivo Cardiac Glucose Metabolism</i>	86
4.1	Introduction	87
4.1.1	Metabolic Remodelling	87
4.1.2	Metabolic Remodelling in UCM	89
4.1.3	¹⁸ F-FDG PET	89
4.1.4	Principle of PET	90
4.1.5	Objectives	92
4.2	Methods	93
4.2.1	Experimental Design	93
4.2.2	<i>In Vivo</i> Scanning Protocol	93
4.2.3	Image Reconstruction	96
4.2.4	Image Analysis	96
4.2.4.1	Standardised Uptake Values	96
4.2.4.2	Rate and Distribution of Cardiac	98

	¹⁸ F-FDG Uptake	
4.2.5	Serum Metabolites	100
4.2.6	<i>Ex Vivo</i> Heart Perfusions	101
4.2.7	Image Reconstruction and Analysis	102
4.3	Results	103
4.3.1	Standardised Uptake Values	103
4.3.2	Rate and Distribution of Cardiac	111
	¹⁸ F-FDG Uptake	
4.3.3	Serum Metabolites	115
4.3.4	Development of <i>Ex Vivo</i> Heart Perfusion	116
	System	
4.3.5	<i>Ex Vivo</i> Heart Perfusions	118
4.4	Discussion	120
4.4.1	Standardised Uptake Values	120
4.4.1.1	Left Ventricle	120
4.4.1.2	Blood Pool Analysis	121
4.4.2	Rate and Distribution of ¹⁸ F-FDG Uptake	123
	in the Left Ventricle	
4.4.3	<i>Ex Vivo</i> Heart Perfusions	129
4.4.4	Conclusions	131
Chapter 5	<i>Impact of Iron Therapy on Mitochondrial Function</i>	132
5.1	Introduction	133
5.1.1	The Electron Transport Chain	133

5.1.2	Reactive Oxygen Species	135
5.1.3	Mitochondrial Dysfunction in the Failing Heart	136
5.1.4	Mitochondria and Iron	137
5.1.5	Mitochondrial Iron Transport	138
5.1.6	Mitochondrial Iron Handling	139
5.1.7	Objectives	141
5.2	Methods	142
5.2.1	Experimental Design	142
5.2.2	Isolation of Cardiac Mitochondria	142
5.2.3	Mitochondrial Respiratory Rates	143
5.2.4	Mitochondrial Enzyme Activities	144
5.2.5	Calcium Induced Mitochondrial Swelling	144
5.3	Results	145
5.3.1	Mitochondrial Respiratory Rates	145
5.3.2	Mitochondrial Enzyme Activities	149
5.3.2.1	Citrate Synthase Activities	149
5.3.2.2	Respiratory Complex Activities	149
5.3.3	Calcium Induced Mitochondrial Swelling	150
5.4	Discussion	156
5.4.1	Mitochondrial Respiration Rates	156
5.4.1.1	State 3 Respiration	156
5.4.1.2	State 4 Respiration	158
5.4.1.3	Respiratory Control Ratio	159
5.4.2	Mitochondrial Enzyme Activities	160

5.4.2.1	Citrate Synthase	160
5.4.2.2	Mitochondrial Respiratory Complex Activities	161
5.4.3	Calcium Induced Mitochondrial Swelling	162
5.5	Conclusions	163
Chapter 6	<i>Mitochondrial Morphology</i>	164
6.1	Introduction	165
6.1.1	Mitochondrial Dynamics	165
6.1.2	Mitochondrial Fusion	166
6.1.3	Mitochondrial Fission	170
6.1.4	Mitochondrial Dynamics in Heart Failure	173
6.1.5	Objectives	176
6.2	Methods	177
6.2.1	Experimental Design	177
6.2.2	Expression of Mitochondrial Fusion and Fission Proteins	177
6.2.3	Mitochondrial Morphology	178
6.2.4	Citrate Synthase Activity	178
6.2.5	Isolated Mitochondrial Size	178
6.2.5.1	Flow Cytometry	178
6.2.5.2	Dynamic Light Scattering	179
6.3	Results	180
6.3.1	Expression of Mitochondrial Fusion and Fission Proteins	180

6.3.2	Citrate Synthase Activity	184
6.3.3	Mitochondrial Morphology	184
6.3.4	Isolated Mitochondrial Size	188
6.4	Discussion	190
6.4.1	Myocardial Protein Expression	190
6.4.2	Mitochondrial Morphology	193
6.4.3	Isolated Mitochondrial Size	195
6.4.4	Conclusions	197
Chapter 7	<i>Discussion and Future Work</i>	198
7.1	Discussion	199
7.2	Conclusion	205
Chapter 8	<i>Appendix</i>	206
8.1	Development of Cannulation method	207
8.2	Optimisation of Western Blotting conditions	209
8.3	Validation of Mitochondrial Size Using Flow Cytometry	210
Publications		212
References		213

List of Figures

Chapter 1	Introduction	
1.1	Compound Effect of Anaemia and Volume Overload in CKD	8
1.2	Patterns of Left Ventricular Remodelling	13
1.3	Cardiomyocyte Calcium Handling	16
1.4	Transcriptional Regulation of Metabolic Enzymes	20
1.5	Schematic Representation of Autophagy	27
1.6	Schematic Representation of Apoptosis	30
1.7	The Mitochondrial Permeability Transition Pore	35
Chapter 2	Materials and Methods	
2.1	Surgical Induction of Uraemia	40
2.2	Full Experimental Design	41
2.3	Flowchart for the Isolation of Cardiac Mitochondria	44
2.4	Standard Curve for Determining Protein Concentration	45
2.5	Experimental Setup for Mitochondrial Respiratory Measurements	46
2.6	Recording of Mitochondrial Respiratory Rates	47
Chapter 3	Characterisation of Experimental Uraemia	
3.1	Creatinine Clearance at 12 Weeks	72
3.2	Comparison of Control and Remnant Kidneys	73

3.3	Heart Weight-to-Tibia Length Ratio at 12 Weeks	75
3.4	Packed Cell Volume as an Indicator of Haematocrit	77
Chapter 4	<i>In Vivo Cardiac Glucose Metabolism</i>	
4.1	The Principle of PET	91
4.2	<i>In Vivo</i> Imaging Bed Setup	94
4.3	Example of Continuous Recording of ECG	95
4.4	CT Scout View for Locating Heart for PET Scan	95
4.5	Co-Registered PET/CT Images Highlighting Analysed Regions of Interest	97
4.6	Localisation of Heart Using Summed FlowQuant Image	99
4.7	Polar Map Template	100
4.8	Perfusion Setup	102
4.9	Time Activity Curves for the Left Ventricle	104
4.10	Standardised Uptake Values for the Left Ventricle	105
4.11	Time Activity Curves for the Left Ventricular Blood Pool	106
4.12	Time Activity Curves for the Vena Cava Blood Pool	107
4.13	Time Activity Curves for the Aortic Blood Pool	108
4.14	Standardised Uptake Values for the Left Ventricular Blood Pool	109
4.15	Standardised Uptake Values for the Vena Cava Blood Pool	110
4.16	Standardised Uptake Values for the Aortic Blood Pool	110
4.17	Myocardial ¹⁸ F-FDG Uptake Rates	111
4.18	Polar Map Analysis at 5 Weeks	112

4.19	Polar Map Analysis at 9 Weeks	113
4.20	Polar Map Analysis at 13 Weeks	114
4.21	Original Schematic of Perfusion Set Up	116
4.22	Modified Imaging Bed for Perfusions	117
4.23	Representative PET/CT Image of Isolated Heart	118
4.24	Representative Time Activity Curve Showing ¹⁸ F-FDG Uptake in the Perfused Heart	119
4.25	Uptake Rates of ¹⁸ F-FDG in the Perfused Heart	119
Chapter 5	<i>Impact of Iron Therapy on Mitochondrial Functional</i>	
5.1	The Mitochondrial Electron Transport Chain	134
5.2	The Fenton Reaction	140
5.3	Mitochondrial State 3 Respiratory Rates	146
5.4	Mitochondrial State 4 Respiratory Rates	147
5.5	Mitochondrial Respiratory Control Ratio	148
5.6	Representative Time Course of Mitochondrial Swelling	151
5.7	Representative Time Course of Mitochondrial Swelling	151
5.8	Mitochondrial Swelling in the Absence of Calcium	152
5.9	Mitochondrial Swelling in the Presence of 40μM Calcium	153
5.10	Mitochondrial Swelling in the Presence of 60μM Calcium	154
5.11	Mitochondrial Swelling in the Presence of 80μM Calcium	155
Chapter 6	<i>Mitochondrial Morphology</i>	
6.1	The Balance of Mitochondrial Dynamics	166

6.2	Schematic Representation of Mitochondrial Fusion and Fission Proteins	167
6.3	The Mechanics of Mitochondrial Fusion	168
6.4	The Process of Mitochondrial Fission	172
6.5	Expression of MFN1 in Cardiac Tissue	180
6.6	Expression of MFN2 in Cardiac Tissue	181
6.7	Expression of OPA1 in Cardiac Tissue	181
6.8	Expression of DRP1 in Cardiac Tissue	182
6.9	Expression of MFN1 in Isolated Cardiac Mitochondria	182
6.10	Expression of MFN2 in Isolated Cardiac Mitochondria	183
6.11	Expression of OPA1 in Isolated Cardiac Mitochondria	183
6.12	Citrate Synthase Activity	184
6.13	Mitochondrial Aspect Ratios	185
6.14	TEM Image of Gross Cardiac Mitochondrial Structure	186
6.15	Enlarged TEM Image of Gross Cardiac Mitochondrial Structure	187
6.16	Representative Histogram of Isolated Mitochondrial Size	188
6.17	Flow Cytometric Analysis of Isolated Mitochondrial Size	189
6.18	Hydrodynamic Diameter of Isolated Mitochondria	189

Chapter 8 *Appendix*

8.1	Initial Cannulation System Used for PET Studies	207
8.2	Modified Cannulation System	208
8.3	Western Blot Analysis for Positive Control	209

8.4	Western Blot Analysis of Protein Gradients	210
8.5	Validation of Flow Cytometry Method for Assessing Isolated Mitochondrial Size	211

List of Tables

Chapter 1	Introduction	
1.1	Classification of Cardio-Renal Syndrome	4
1.2	Cardiovascular Risk Factors in UCM	4
1.3	Factors Associated with Anaemia in Heart Failure	9
Chapter 2	Materials and Methods	
2.1	Antibody Dilutions	56
Chapter 3	Characterisation of Experimental Uraemia	
3.1	Markers of Renal Function	72
3.2	Kidney Weights	74
3.3	Indices of Cardiac Hypertrophy	75
3.4	Indices of Body Mass	76
3.5	Markers of Iron Homeostasis	77
Chapter 4	In Vivo Cardiac Glucose Metabolism	
4.1	SUV Data	103
4.2	Serum Metabolites	115
Chapter 5	Impact of Iron Therapy on Mitochondrial Functional	
5.1	Protein Concentration and Citrate Synthase Activity of Mitochondrial Pellets	149
5.2	Mitochondrial Enzyme Activities	150

Chapter 6 ***Mitochondrial Morphology***

6.1 Mitochondrial Dimensions

185

List of Abbreviations

2DG	2-deoxy-D-glucose
3D OSEM	3D ordered-subsets expectation maximization
ACD	Anaemia of chronic disease
ADP	Adenosine diphosphate
AKI	Acute kidney injury
AMP	Adenosine monophosphate
ANT	Adenine nucleotide translocase
Apaf-1	Apoptotic protein activating factor-1
ATP	Adenosine triphosphate
CKD	Chronic kidney disease
CRS	Cardio-renal syndrome
CyP-D	Cyclophilin D
CsA	Cyclosporine A
CT	Computed tomography
DCPIP	Dichlorophenolindophenol
DLS	Dynamic light scattering
DMT1	Divalent metal transporter 1
DRP1	Dynamin related protein-1
ECL	Enhanced chemiluminescence
ECG	Electrocardiogram
ELISA	Enzyme-linked immunosorbent assay
ERR	Estrogen related receptor- α
ESRD	End stage renal disease

¹⁸ F-FDG	¹⁸ F-fluorodeoxyglucose
FADH ₂	Flavin adenine dinucleotide
FADD	Fas-Associated protein with Death Domain
Fis1	Fission protein 1
Fzo1p	Fuzzy onions protein
GED	GTPase effector domain
GFR	Glomerular filtration rate
GLUT1/4	Glucose transporter
GTP	Guanosine triphosphate
H ₂ O ₂	Hydrogen peroxide
HW:BW	Heart weight-to-bodyweight ratio
HW:TL	Heart weight-to-tibia length ratio
IDA	Iron deficiency anaemia
IMM	Inner mitochondrial membrane
I/P	Intraperitoneal
IRI	Ischemia reperfusion injury
IV	Intravenous
LC3-I	Microtubule-associated proteins 1A/1B light chain 3B LC3
LC3-II	LC3-phosphatidylethanolamine conjugate
LDL	Low density lipoprotein
LVH	Left ventricular hypertrophy
MCAD	Medium-chain acyl-CoA dehydrogenase
MCF	Mitochondrial carrier family

MCU	Mitochondrial calcium uniporter
Mdivi-1	Mitochondrial division inhibitor 1
MFF	Mitochondrial fission factor
MFN1/2	Mitofusin
mfrn	Mitoferrin-1
mPTP	Mitochondrial permeability transition pore
MER	Modified estrogen receptor
MtFt	Mitochondrial ferritin
MRI	Magnetic resonance imaging
NADH	Nicotinamide adenine dinucleotide
NCX	Sodium-calcium exchanger
NMR	Nuclear magnetic resonance
NRF1/2	Nuclear respiratory factor
NTBI	Non-transferrin bound iron
O ₂ ⁻	Superoxide anion
OH [·]	Hydroxyl radical
OMM	Outer mitochondrial membrane
OPA1	Optic atrophy-1
PMCA	Plasma membrane Ca-ATPase
PCV	Packed cell volume
PDH	Pyruvate dehydrogenase
PDK	PDH kinase
PET	Positron emission tomography
PGC-1 α	PPAR γ coactivator-1 α

PiC	Mitochondrial phosphate carrier
PLB	Phospholamban
PPAR	Peroxisome proliferator activated receptor
PPRE	PPAR promote response elements
PSC	Polyglucose-sorbitol-carboxymethylether
RAAS	Renin-angiotensin-aldosterone system
RCR	Respiratory control ratio
ROI	Region of interest
Respiratory complex I	NADH dehydrogenase
Respiratory complex II	Succinate dehydrogenase
Respiratory complex III	Coenzyme Q cytochrome c reductase
Respiratory complex IV	Cytochrome c oxidase
ROS	Reactive oxygen species
RXR	Retinoid x receptor
S/C	Subcutaneous
SGLT	Sodium-coupled glucose transporter
SDS-PAGE	Sodium dodecyl sulphate polyacrylamide gel electrophoresis
SEM	Standard error of the mean
SERCA	Sarcoendoplasmic reticulum calcium ATPase
SPECT	Single photon emission computed tomography
SR	Sarcoplasmic reticulum
STIM1	Stromal interaction molecule 1
SUV	Standardised uptake value

TAC	Time activity curve
TEM	Transmission electron microscopy
Tfam	Mitochondrial transcription factor A
TfR1	Transferrin receptor 1
TIBC	Total iron binding capacity
TNF α	Tumour necrosis factor- α
TUNEL assay	Terminal deoxynucleotidyl transferase dUPT nick end labelling assay
UCM	Uraemic cardiomyopathy
UCP	Uncoupling Protein
VDAC	Voltage dependent anion channel

1. Introduction

1.1 Chronic Kidney Disease

Chronic kidney disease (CKD) is a major public health concern that is estimated to affect 11-13% of the global population (Hill et al., 2016). There are approximately 2.6 million CKD patients in the UK making the condition a massive burden on the NHS (Public Health England, 2014). Furthermore, with an ever aging population the prevalence of CKD is increasing significantly (Coresh et al., 2007). Indeed, it has been estimated that the number of CKD patients in the UK will increase to 4.2 million by 2036 (Public Health England, 2014).

CKD is defined as abnormalities of kidney structure and/or function for >3 months (KDIGO, 2013). This allows the differentiation between CKD and acute kidney injury (AKI) which may stem from different aetiologies and thus require different treatments (Popat, 2011). CKD may be initially difficult to identify in clinical practice as patients tend to be asymptomatic during the early stages of kidney disease. However, as kidney function worsens, uraemic toxins start to accumulate and patients often begin presenting with clinical features such as fatigue, nausea, anorexia, haematuria and skin irritations (Popat, 2011). Further investigation using relatively simple laboratory based tests then enable the detection of CKD.

There exists a reciprocal relationship between the heart and kidney whereby primary dysfunction in one organ can cause secondary dysfunction in the other. Indeed, cardiovascular complications are the leading cause of mortality in patients with CKD (Go et al., 2004). Cardiac risk is increased 10-20 times in these patients and adverse

cardiovascular events account for approximately 50% of deaths (Foley et al., 1998). Furthermore, 30-50% of heart failure patients develop renal dysfunction (Shlipak, 2003).

1.2 Uraemic Cardiomyopathy

The co-existence of both heart disease and CKD create a unique phenotype known as cardio-renal syndrome (CRS) which carries a very poor prognosis (McAlister et al., 2004). CRS can be classified into five subtypes based on the aetiology and duration of the condition (Ronco et al., 2008) (Table 1.1). Type IV CRS includes impaired cardiac function as a consequence of CKD, termed uraemic cardiomyopathy (UCM). Although the pathogenesis of UCM is complex and incompletely understood, the association of renal dysfunction with developing cardiac risk factors, such as left ventricular hypertrophy (LVH), hypertension and anaemia, amplifies disease progression in both organs (Rigatto & Parfrey, 2001) (Table 1.2).

Table 1.1

Classification of cardio-renal syndrome

Classification	Description
Type I	Abrupt worsening of cardiac function causing acute kidney injury.
Type II	Chronic abnormalities in cardiac function leading to progressive and permanent CKD.
Type III	Abrupt worsening of renal function causing acute cardiac dysfunction.
Type IV	CKD contributing to impaired cardiac function, cardiac hypertrophy and/or increased risk of adverse cardiovascular events.
Type V	Systemic condition causing both cardiac and renal dysfunction.

Adapted from (Ronco et al., 2008). CKD = chronic kidney disease.

Table 1.2

Cardiovascular risk factors in UCM	
<ul style="list-style-type: none">• LVH• Anaemia	<ul style="list-style-type: none">• Secondary and tertiary hyperthyroidism• Oxidative stress
<ul style="list-style-type: none">• Hypertension• Volume overload	<ul style="list-style-type: none">• Chronic inflammation• Hypoalbuminaemia
<ul style="list-style-type: none">• Diabetes	<ul style="list-style-type: none">• Hyperhomocysteinaemia

Adapted from (Rigatto & Parfrey, 2001). LVH = left ventricular hypertrophy.

The uraemic heart is characterised by structural and cellular remodelling, including a wide number of factors, such as anaemia, LVH, mitochondrial dysfunction and altered calcium handling (Smith et al., 2010 & Taylor et al., 2015). These collectively contribute to impaired cardiac function, ultimately resulting in failure and potentially accounting for the high incidence of death resulting from cardiovascular causes in CKD patients (Rigatto & Parfrey, 2001).

1.3 Anaemia

Iron metabolism is complex and involves tight regulation at both the systemic and cellular level. An average man has approximately 4g of iron in the body, of which 2.5g is within red blood cells, 1g is stored in the reticuloendothelial system, and the rest is distributed in various proteins (Siah et al., 2006). Approximately 1–2 mg of iron is lost through skin, sloughed intestinal mucosal cells and minor blood loss every day. However, the body has no effective means of regulating iron loss and thus the absorption of dietary iron from the gut plays a critical role in maintaining iron homeostasis (Siah et al., 2006). Iron absorption occurs at the apical surface of duodenal enterocytes and is facilitated by the transporter protein divalent metal transporter 1 (DMT1) (McKie et al., 2001). Once iron is internalised into the cell it is either stored as ferritin or transported out of the enterocyte via ferroportin 1 (Hentze et al., 2004). Following transport across the basal membrane, the iron is oxidised to its ferric form and bound to plasma transferrin (Vulpe

et al., 1999). The uptake of transferrin bound iron into cells is facilitated by transferrin receptor (TfR)1 or 2 (Siah et al., 2006).

As only small amounts of iron are lost and gained through normal physiological functions, the majority of iron in the body is recycled via the destruction of aged red blood cells in the reticuloendothelial system (Kong et al., 2008). Phagocytic cells such as macrophages are prominent in organs with a rich blood supply such as the liver and spleen. These cells break down aged erythrocytes, yielding free iron which can be used for new red blood cell synthesis in the bone marrow (Kong et al., 2008). Disruption to iron metabolism and/or erythropoiesis can lead to anaemia.

The aetiology of anaemia in association with CKD is multifactorial and includes inflammation and iron deficiency, though the principal cause is considered to be reduced erythropoietin production in the kidney (Gill & Ferreira, 2013). Haemodilution caused by an increase in blood volume without a concomitant rise in red blood cells is also a factor, further compounding the anaemia (London & Parfey, 1997) (Figure 1.1). Both blood volume and blood pressure are regulated by the renin-angiotensin-aldosterone system (RAAS) (Siamopoulos & Kalaitzidis, 2008). A reduction in circulating erythrocytes can lower oxygen tension and lead to vasodilation and reduced peripheral vascular resistance (London & Parfey, 1997). The decrease in blood pressure, in turn, can result in renal hypoperfusion and subsequent RAAS and sympathetic activation, increasing cardiac output and enhancing sodium and water retention (Efstratiadis et al., 2008). However, the increase in blood volume adds to the haemodynamic load on the heart,

indeed, anaemia alone may be sufficient to trigger cardiac hypertrophy (Naito et al., 2009).

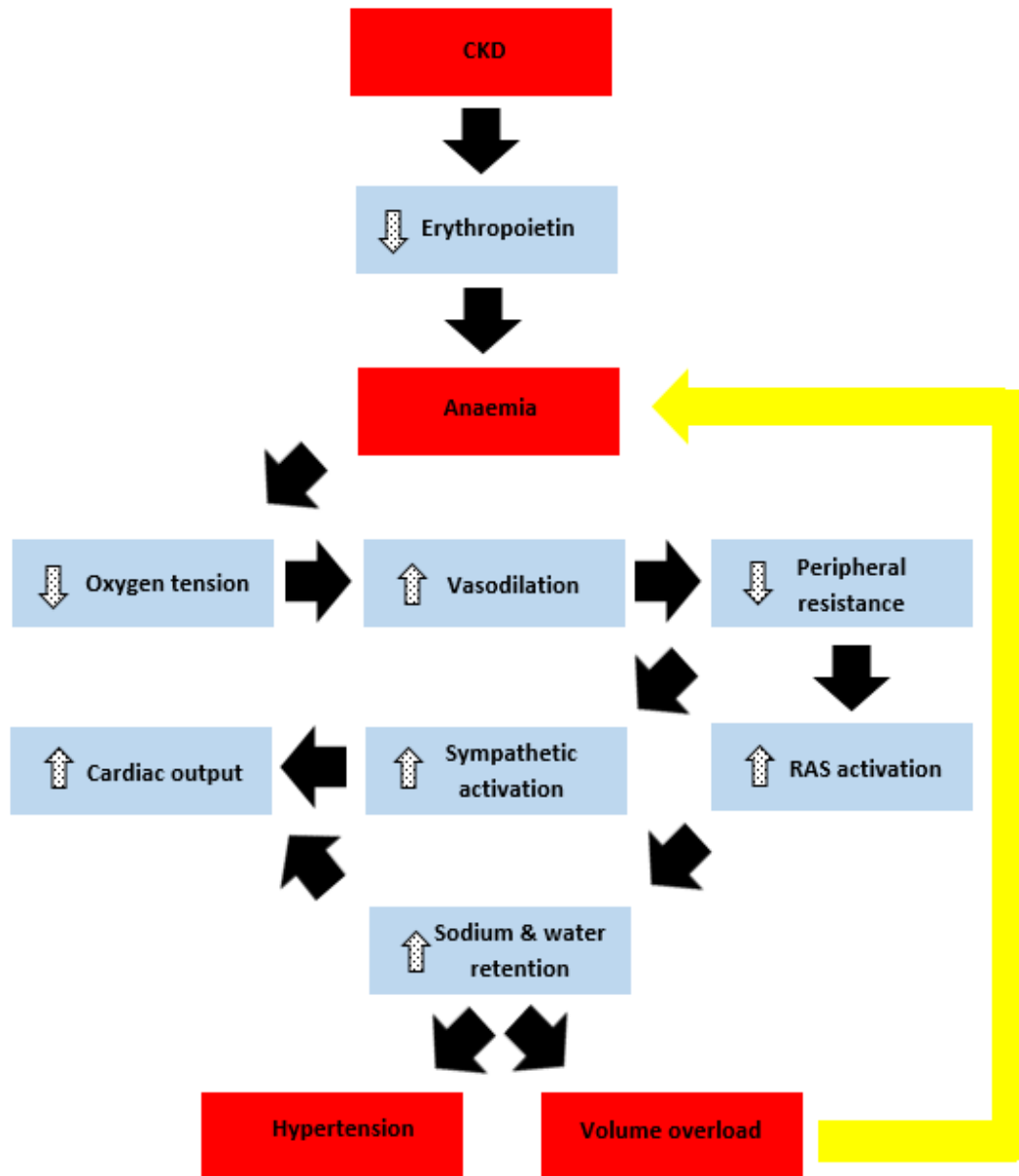


Figure 1.1. Compound effect of anaemia and volume overload in CKD. Anaemia, resulting from impaired erythropoietin production in CKD, leads to reduced oxygen tension and a consequent drop in blood pressure. This in turn triggers renin-angiotensin-aldosterone system (RAAS) and sympathetic activation resulting in increased sodium and water retention and cardiac output respectively. Enhanced sodium and water retention leads to hypertension and an increase in blood volume without a concomitant rise in erythrocytes, compounding the anaemia.

Iron deficiency anaemia (IDA) is also common in CKD and is the most prevalent form of anaemia in heart failure (Gill & Ferreira, 2013) (Table 1.3). IDA can be classified as functional, due to impaired iron metabolism, or absolute, due to depletion of iron stores (Arora & Ghali, 2013). Functional IDA has largely been attributed to increased expression of hepcidin, the principal regulator of iron homeostasis, which is frequently observed in CKD and the early stages of heart failure (Arora & Ghali, 2013). Hepcidin binds and inhibits ferroportin, the primary exporter of intracellular iron (Jankowska et al., 2013).

Table 1.3

Factors associated with anaemia in heart failure	
• Iron deficiency	• Medication
• Bleeding	• Renal failure
• Inflammation	• Nutritional deficiency
• Intestinal malabsorption	• Hypothyroidism

Adapted from (Arora & Ghali, 2013)

Anaemia can be treated with erythropoietin and/or iron supplementation, principally to stimulate erythropoiesis (Arora & Ghali, 2013). French physician Pierre Blandin was the first to market oral iron pills for the treatment of anaemia in the mid 1800's (Haden, 1938). Although many advances in medicine have been made over the

past two centuries, oral iron supplementation is still one of the first choices of treatment for anaemia due to its effectiveness and relatively low cost. However, in some cases of anaemia, oral iron therapy is not an effective treatment due to poor absorption, adverse events in the gastrointestinal tract and the duration of therapy needed to sufficiently replenish iron stores (Cancado & Munoz, 2011). Therefore alternative iron preparations have been investigated over the last 30 years leading to the development of iron compounds intended for intravenous (IV) use.

The first IV iron compound used to treat anaemia was high-molecular-weight iron dextran, which was first introduced in 1954 (Fishbane & Kowalski, 2000). Though initially a successful treatment for anaemia, several subsequent studies have identified that dextran containing iron compounds are associated with an elevated risk of anaphylactic reactions. This led to the development of two new preparations, ferric gluconate and iron sucrose, which were released as safer alternatives to iron dextran in 1999 and 2001 respectively (Cancado & Munoz, 2011). A further three preparations have since been developed, all of which have better safety profiles compared with previous compounds. Furthermore, due to increased safety, these compounds can be administered faster and at a higher dose. Indeed, it has been suggested that body iron stores can be completely replenished within 15-60 minutes (Cancado & Munoz, 2011). The three preparations developed were ferric carboxymaltose, iron isomaltoside and ferumoxytol.

Ferumoxytol is a colloidal solution of polyglucose-sorbitol-carboxymethylether (PSC)-coated superparamagnetic iron oxide particles with a molecular weight of about

750kDa (European Medicines Agency, 2012). The PSC shell consists of α -1,6 glycosidic linkages between glucose molecules and isolates the iron oxide core from plasma until the whole iron-PSC complex is taken up by the reticuloendothelial system (European Medicines Agency, 2012). Phagocytic leukocytes break down the complex into distinct iron oxide and PSC molecules. The PSC component is then degraded and the newly liberated iron is either stored within the reticuloendothelial system or released into the plasma as part of transferrin (Pai & Garba, 2012).

In the clinical setting, ferumoxytol is administered as either a single 510mg single dose or 2 x 510mg doses approximately a week apart (Pai & Garba, 2012). The principal aim of the drug is to replenish body iron stores in patients with anaemia resulting from reduced kidney function. Standard approaches for assessing the pharmacokinetics of ferumoxytol have proved unsuccessful due to the ubiquity of iron in the body and the complexities of iron metabolism. Therefore, the only accurate means of determining the pharmacokinetic properties of ferumoxytol is using nuclear magnetic resonance (NMR) due to the superparamagnetic properties of the compound (European Medicines Agency, 2012). Ferumoxytol exhibits zero-order pharmacokinetics and thus handling of the drug by the reticuloendothelial system is saturable. The compound will therefore remain in plasma until such time that the concentration is below the saturation concentration and the reticuloendothelial system can resume handling the drug linearly (European Medicines Agency, 2012). Elimination of the drug from plasma is dose dependent; clearance decreases with increasing dose, indicating a capacity-limited elimination. The terminal half-life of ferumoxytol is approximately 16 hours (Pai & Garba,

2012). Excretion, metabolism and pharmacokinetics of metabolites have not yet been studied in clinical trials (European Medicines Agency, 2012).

Although ferumoxytol is a drug designed specifically for the treatment of anaemia in patients with impaired kidney function, the majority of pre-clinical studies to date have investigated the potential of ferumoxytol as an MRI contrast agent due to the superparamagnetic properties of the compound (Gharagouzloo et al., 2017). Indeed, only one study has investigated the use of ferumoxytol in treating anaemic rodents. Furthermore, as the study was part of an application for marketing authorisation of the drug, little data were reported other than ferumoxytol was effective in ameliorating anaemia in IDA rats (European Medicines Agency, 2012).

1.4 Left Ventricular Hypertrophy

LVH, a major risk factor for heart failure, is a common cardiac adaption in CKD patients and stems from pressure- or volume-overload as a consequence of chronic RAAS activation (Figure 1.1) (Taddei et al., 2011). Although initially beneficial, LVH is a maladaptive response and can lead to a progressive decline in cardiac function, ultimately resulting in failure (Drazner, 2011).

Cardiomyocytes are terminally differentiated at birth and when faced with physiological and pathological stress, undergo hypertrophy as an adaptive response (Meerson, 1971). Initially hypertrophy of myocytes helps to maintain systolic function

by normalising wall tension (Grossman, 1980). Two distinct forms of LVH have been identified, termed concentric and eccentric hypertrophy (Figure 1.2). Concentric hypertrophy, associated with an increased wall thickness of the ventricular chamber, is predominantly the result of chronic pressure overload such as hypertension (Lip et al., 1994). At the cellular level, this hypertrophic phenotype occurs as a result of the addition of sarcomeres in parallel, leading to increased myocyte width and a relatively greater increase in the width-to-length ratio (Frey et al., 2004). Eccentric hypertrophy on the other hand is characterised by chamber dilation, caused by volume overload in conditions such as anaemia. This hypertrophic response arises from the addition of sarcomeres/myofibrils in series and longitudinal cardiomyocyte growth resulting in an increased length-to-width ratio (Carabello, 2002).

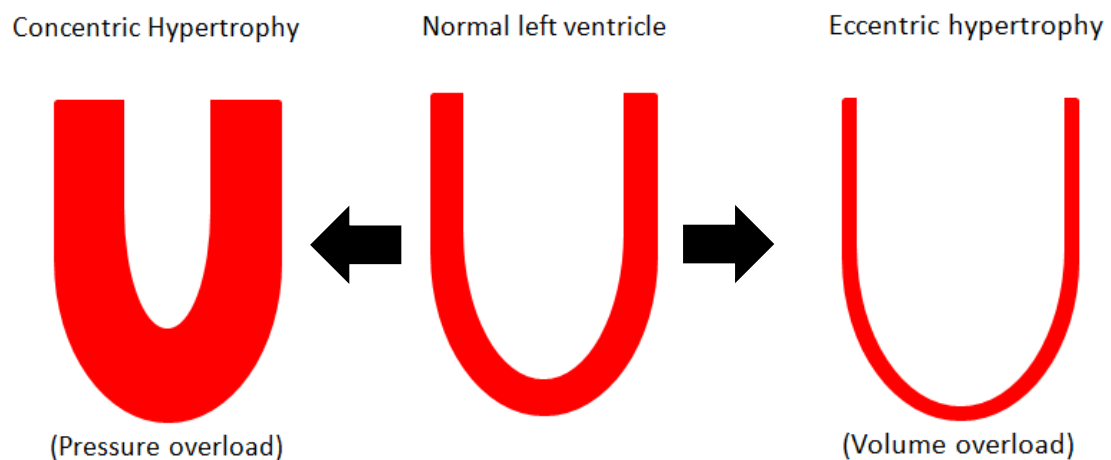


Figure 1.2. Patterns of left ventricular remodelling.

The pattern of hypertrophic remodelling in CKD is mixed due to the complex aetiology of CRS. Indeed, a study by Foley et al. (1995) reported that of the 74% of kidney dialysis patients presenting with LVH, 44% exhibited concentric hypertrophy and 30% eccentric hypertrophy. These findings are similar to those of Parfrey et al. (1996) who identified that concentric and eccentric hypertrophy were present in 40% and 28% of dialysis patients respectively.

1.5 Calcium Handling

In the healthy heart, calcium stimulates muscle contraction in a process termed excitation-contraction coupling (Figure 1.3). During the plateau phase of the cardiac action potential, membrane depolarisation stimulates calcium entry into the myocyte via T-tubules and L-type calcium channels (Bers, 2002). The influx of calcium, in turn, triggers the further release of calcium stored in the sarcoplasmic reticulum via the ryanodine receptor in a process known as calcium-induced calcium release (Fabiato & Fabiato, 1979). Calcium released into the cytosol binds to troponin C stimulating a conformational change in troponin I on the thin filaments. This exposes the actin binding site to myosin and thus facilitates the interaction between actin and myosin and subsequent cross bridge formation and contraction (Bers, 2002). During relaxation, cytosolic calcium can be removed by the sarcoendoplasmic reticulum calcium ATPase (SERCA), the sodium-calcium exchanger, the plasma membrane Ca-ATPase (PMCA) and mitochondrial calcium uptake (Eisner et al., 2017). Mitochondrial calcium uptake is

largely controlled by the mitochondrial calcium uniporter (MCU), a large transmembrane protein which facilitates the passage of calcium ions from the cytosol into the mitochondrial matrix (Eisner et al., 2017). In Addition, the sarcoplasmic reticulum protein stromal interaction molecule 1 (STIM1) is thought to regulate basal calcium release in unstimulated cells via interaction with the myocyte membrane channel Orai, though the mechanism is poorly understood (Eisner et al., 2017). Phospholamban (PLB) is a key regulator of calcium homeostasis and acts by inhibiting SERCA in its dephosphorylated state, while phosphorylation of the protein relieves its inhibitory effects (Bers, 2002).

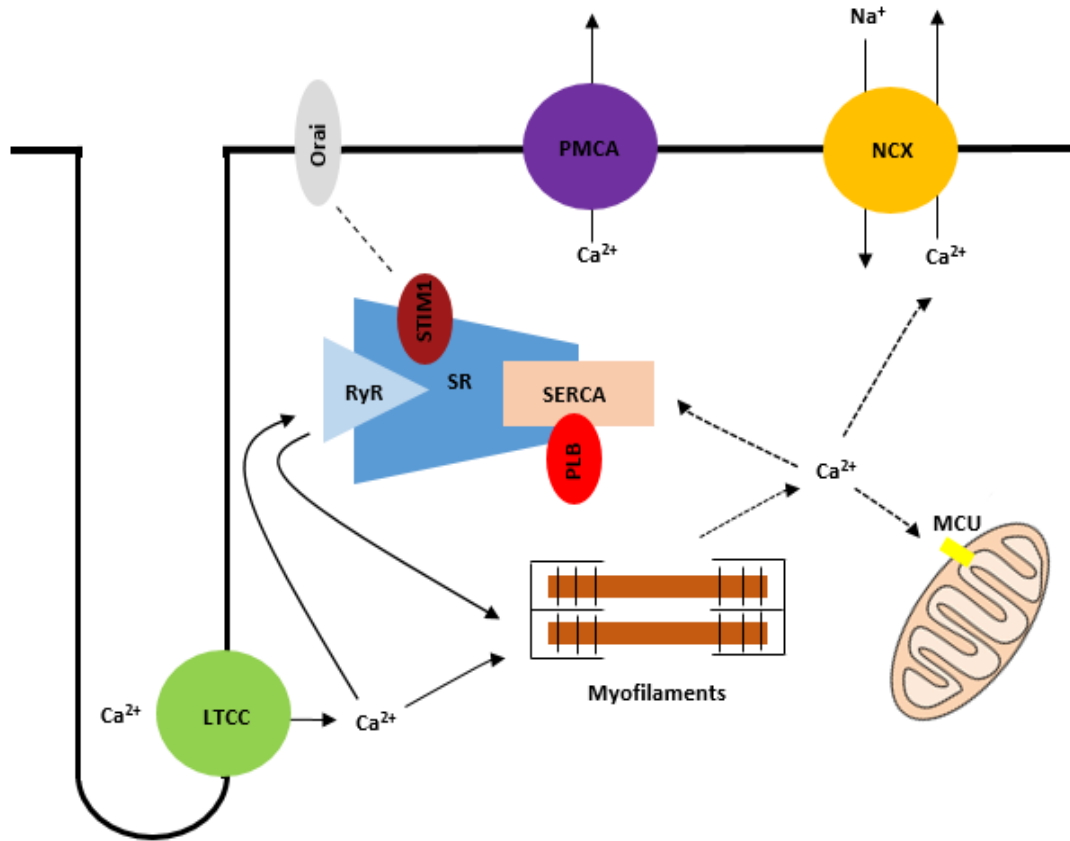


Figure 1.3. Cardiomyocyte calcium handling. Adapted from Eisner et al. (2017). Extracellular calcium enters the myocyte via T-tubules and L-type calcium channels (LTCC). The influx of calcium amplifies the release of further calcium stored in the sarcoplasmic reticulum (SR) via the ryanodine receptor (RyR). Cytosolic calcium stimulates systolic contraction and is subsequently removed by the sarcoendoplasmic reticulum calcium ATPase (SERCA), plasma membrane Ca-ATPase (PMCA), the mitochondria (via the mitochondrial calcium uniporter (MCU)) and the sodium-calcium exchanger (NCX), causing diastolic relaxation. Interaction between stromal interaction molecule 1 (STIM1) and Orai regulates the release of calcium from the SR in unstimulated cells. Phospholamban (PLB) regulates calcium homeostasis via direct interaction with SERCA.

A number of studies have shown that intracellular calcium handling is altered in the failing heart (Gorski et al., 2015). Indeed, Feldman et al. (1993) and Hasenfuss (1998) have demonstrated reduced SERCA expression in experimental and clinical studies of heart failure respectively, leading to delays in diastolic relaxation. Similar findings have

been reported in 5/6 nephrectomised rats by Kennedy et al. (2003) who identified that reduced SERCA activity was a feature of the uraemic heart. In addition, McMahon et al. (2002) reported significant delays in intracellular calcium removal in uraemic cardiomyocytes, though the mechanisms are unclear. Impaired removal of calcium could also result from changes in PLB expression. Indeed, mutations in PLB alone have been shown to result in dilated cardiomyopathy (Schmitt et al., 2003). Furthermore, mutations in protein phosphatase 1, the protein which dephosphorylates PLB, have also been reported in cardiomyopathic hamsters (Yomanda et al., 2006).

1.6 Cardiac energy metabolism

1.6.1 Cardiac energy provision

The heart has an extraordinary energy demand and requires a continuous supply of energy. ATP transfer and regeneration in the myocardium is facilitated by the phosphocreatine shuttle system, a process which involves phosphocreatine and the enzyme creatine kinase. Creatine is produced by the liver and kidneys and is transported to the heart against a large concentration gradient (Guimbal & Kilimann, 1993). Approximately two thirds of the creatine pool is phosphorylated to phosphocreatine, serving a critical role as an energy buffer when energy demand exceeds supply (Ingwall, 2009). Mitochondrial creatine kinase facilitates the transfer of the high-energy phosphate bond in ATP to creatine, forming ADP and phosphocreatine respectively

(Neubauer, 2007). Phosphocreatine can readily diffuse to the myofibrils where it is transformed back to ATP and creatine by myofibrillar creatine kinase (Neubauer, 2007).

1.6.2 Fatty Acid Metabolism

The healthy adult heart cycles approximately 6kg of ATP a day with the majority coming from fatty acid metabolism and the remainder coming from carbohydrate and lactate oxidation (Stanley et al., 2005). The relationship between fatty acids and glucose metabolism is reciprocal as evidenced by the Randle cycle (Randle et al., 1963). Elevated fatty acid oxidation can decrease the rate of glucose oxidation (Beadle & Frenneaux, 2010). Citrate derived from elevated acetyl-CoA concentrations can limit glucose uptake by inhibiting glycolytic enzymes such as phosphofructokinase-1, which catalyses the first irreversible step in glycolysis (Stanley et al., 2005). On the other hand, increased glucose oxidation can suppress fatty acid oxidation (Jaswal et al., 2011). Elevated levels of malonyl-CoA, formed from the carboxylation of acetyl-CoA by acetyl-CoA carboxylase, limits fatty acid uptake into the mitochondria by inhibiting carnitine palmitoyltransferase, a key component of the mitochondrial fatty acid transport system.

Fatty acid uptake in the myocardium is in part dependent on the concentration of free fatty acids in the plasma (Lopaschuk et al., 1992). Fatty acids are primarily transported in the plasma bound to albumin and within LDL and enter the cardiomyocyte by transporter proteins on the sarcolemma and, to a lesser extent, by passive diffusion (Van der Vusse et al., 2000). The fatty acid translocase protein, CD36, is predominantly

expressed on the plasma myocyte membrane and in part facilitates myocardial fatty acid uptake (Kintaka et al., 2002). Upon entering the cardiomyocyte approximately 70-90% of fatty acids are rapidly oxidised to CO₂ and the remainder converted to triglycerides and long-chain fatty acids by enzymes such as glycerolphosphate acyl-transferase (Stanley et al., 2005).

Fatty acid β -oxidation occurs predominantly within the mitochondrial matrix and to a lesser extent peroxisomes (Wanders et al., 2010). As the inner mitochondrial membrane (IMM) is impermeable, intracellular transport of the moieties is facilitated by a carnitine-dependent transport system (Stanley et al., 2005). Firstly carnitine palmitoyltransferase I catalyses the formation of long-chain acylcarnitine in the intermembrane space. Carnitine acyltranslocase then transports the long-chain moieties across the IMM in exchange for free carnitine and carnitine palmitoyltransferase II regenerates the long-chain fatty acid in the mitochondrial matrix, a process largely regulated by free carnitine availability (Stanley et al., 2005).

Fatty acid oxidation enzyme expression is largely governed at the transcriptional level by the peroxisome proliferator activated receptor (PPAR) family of transcription factors (Finck & Kelly, 2002) (Figure 1.4). Three PPAR isoforms have been identified, PPAR α , PPAR β and PPAR γ , though PPAR α is considered the primary form in the heart (Huss & Kelly, 2004). PPAR α regulates cardiac gene expression via heterodimeric formation with another nuclear activator, retinoid x receptor (RXR) (Finck & Kelly, 2002). Upon activation by their respective lipid ligands, the PPAR α -RXR complex binds to PPAR

promote response elements (PPRE) in the promoter region of the PPAR α target genes. Activating signals then trigger the recruitment of co-activators such as PPAR γ coactivator-1 α (PGC-1 α) which bind the complex and initiate gene transcription via interaction with PPAR α and RXR (Finck & Kelly, 2006).

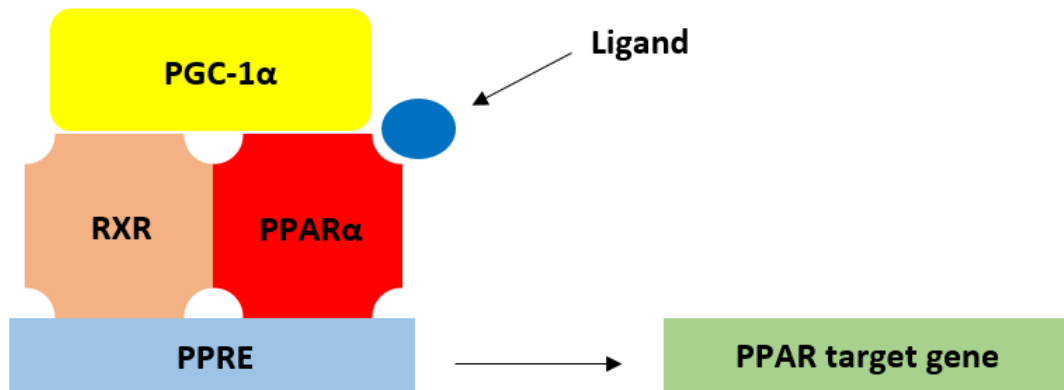


Figure 1.4. Transcriptional regulation of metabolic enzymes. Peroxisome proliferator activated receptor (PPAR α) regulates gene transcription as part of a complex also including retinoid x receptor (RXR) and PPAR γ coactivator-1 α (PGC-1 α). The RXR and PPAR α complex binds to PPRE promote response elements (PPRE) in response to binding of fatty acid ligands. Activating signals then trigger the recruitment of PGC-1 α which binds the complex and initiates gene transcription of metabolic enzymes.

1.6.3 Carbohydrate Metabolism

Glucose transport into the cardiomyocyte is facilitated by the glucose transporters GLUT1 and GLUT4 together with a transmembrane glucose gradient (Stanley et al., 2005). GLUT1 is the principal isoform expressed during foetal growth and is largely localised to the sarcolemma under basal conditions (Santalucia et al., 1992). On the other hand GLUT4 is the predominant isoform expressed in fully differentiated

cardiomyocytes and is mainly present in intracellular membrane compartments. GLUT4 is recruited to the plasma membrane to facilitate enhanced glucose uptake in response to factors such as insulin, increased workload or ischemia (Montessuit & Lerch, 2013).

Immediately after entering the cardiomyocyte, glucose is rapidly phosphorylated by hexokinase into glucose-6-phosphate, which can be further metabolised via glycolysis, forming pyruvate. Pyruvate decarboxylation to acetyl CoA by pyruvate dehydrogenase (PDH) is the key irreversible step in glucose oxidation (Randle, 1986). PDH is a multi-enzyme complex localised to the IMM and is regulated in a number of different ways. It can be activated by PDH phosphatase and calcium and inactivated by PDH kinase (PDK) (Randle, 1986). Four isoforms of PDK have been identified, though PDK4 is the predominant isoform expressed in the heart (Bowker-Kinley, 1998). PDK4 expression can be regulated by the PPAR α -RXR-PGC-1 transcriptional complex (Wu et al., 2001).

Acetyl-CoA produced from myocardial fatty acid and glucose metabolism enters the TCA cycle, generating the reduced intermediates NADH/FADH₂ (Kuzmicic et al., 2011). These reducing equivalents are then transferred through the electron transport chain, a series of four enzyme complexes (I-IV) located on the IMM, which convey electrons to molecular oxygen. The energy released from electron transfer is coupled to the translocation of protons from the matrix to the intermembrane space in a process termed oxidative phosphorylation. This creates an electrochemical gradient

(protonmotive force) which provides the energy to drive ATP synthase (Kuzmicic et al., 2011).

1.7 Energy Deficiency in the Failing Heart

The hypertrophied myocardium undergoes substantial remodelling of metabolism, characterised by a shift in cardiac substrate preference from fatty acid to glucose oxidation (Fragasso, 2016). Although this response may be initially considered beneficial as glucose oxidation is more oxygen efficient than fatty acids, ultimately carbohydrate metabolism is insufficient to meet the metabolic needs of the heart and energy depletion ensues (Ingwall, 2009). The switch in substrate profile in hypertrophied hearts results from the downregulation of genes encoding fatty acid oxidation enzymes such as PPAR α (Lehman & Kelly, 2002). At the cellular level this results in decreased expression of enzymes such as medium-chain acyl-CoA dehydrogenase (MCAD) and the fatty acid transporter CD36 (Barger et al., 2000 & Razeghi et al., 2001). Experimental studies have demonstrated that a shift in substrate preference is also a feature of the uraemic heart (Aksentijevic, 2008 & Smith et al., 2010). Furthermore, the metabolic remodelling in these studies was associated with hyperinsulinaemia, hypertension and myocardial fibrosis, features common to conditions of heart failure (Despres et al., 1996; Drazner, 2011 & Sequra et al., 2014).

The transition from compensated hypertrophy to failure leads to a decline in cardiac energy flux (Beer et al., 2002). Mitochondrial and myofibrillar creatine kinase

activities have been reported to be reduced by as much as 80% and 50% respectively in the failing heart (Neubauer, 2007 & Field et al., 1994). In addition, total creatine and phosphocreatine are significantly reduced in heart failure culminating in impaired ATP transfer and utilisation. Indeed, in the final stages of failure myocardial ATP content is decreased by approximately 40%, ultimately leading to contractile dysfunction (Neubauer, 2007). Changes in high-energy phosphate metabolism have also been reported in experimental uraemia. Raine et al. (1993) demonstrated reductions of 32% in phosphocreatine and the ATP to phosphocreatine ratio in the isolated perfused uraemic rat heart. In addition, these changes were associated with contractile dysfunction as evidenced by a decline in cardiac output. Collectively these observations highlight that cardiac metabolism undergoes substantial remodelling in both the failing and uraemic heart.

1.8 Cardiac Mitochondria

Mitochondria generate over 90% of cellular ATP via oxidative phosphorylation and occupy approximately 30% of cardiomyocyte volume. In addition, mitochondria also play a key role in calcium signalling and regulate apoptotic cell death, thus determining the survival and death of the cell (Kasahara & Scorrano, 2014). As a close relationship exists between energy generation and demand, mitochondria lie at the centre of altered myocardial energetics (Rimbaud et al., 2009). Mitochondria are also highly dynamic organelles and maintain a large interconnected network by undergoing events of fusion

and fission (Chen & Chan, 2010). Fusion allows mitochondria to exchange genetic material and proteins while fission is involved in cellular processes such as autophagy and apoptosis (Marin-Garcia & Akhmedov, 2013). However, impaired fusion or fission may impact on both the number and efficient functioning of mitochondria and hence disturbance of these processes may play a role in the onset of heart failure in UCM.

1.9 Mitochondrial Biogenesis

Mitochondrial biogenesis is a complex process dependent on the coordination of both nuclear and mitochondrial genomes. Mitochondria contain 37 genes which encode 13 subunits of electron transport chain enzymes, 22 tRNAs and 2 rRNAs (Rimbaud et al., 2009). Nuclear encoded mRNAs are translated in the cytosol to precursor proteins and transported into the mitochondria via the translocase of the outer membrane and the translocase of the inner membrane (Hood & Joseph, 2004).

Mitochondrial and nuclear gene expression are controlled by several transcription factors working in concert; PGC-1 α , nuclear respiratory factor 1 and 2 (NRF1/2) and oestrogen related receptor- α (ERR) (Rimbaud et al., 2009). NRF1/2 and ERR regulate the transcription of several nuclear encoded proteins including many subunits of the electron transport chain and MCAD (Kelly & Scarpulla, 2004). One specific target of NRF1 is mitochondrial transcription factor A (Tfam), a key protein which binds to mitochondrial promoter DNA regions to aid transcription of mitochondrial genes (Kelly & Scarpulla, 2004). Although PGC-1 α itself lacks DNA binding ability, it co-ordinates

the activities of other transcription factors including NRF1/2 and ERR, synchronising the activities of mitochondrial and nuclear genomes (Rimbaud et al., 2009). Indeed, PGC-1 α expression strongly associates with mitochondrial mass, protein content and oxidative capacity suggesting PGC-1 α is the master regulator of mitochondrial biogenesis (Lehmann et al., 2008).

Given the key role PGC-1 α plays in regulating mitochondrial biogenesis, it is unsurprising that changes in expression of the protein have been linked to altered cardiac energetics. Indeed, evidence from PGC1 α deficient animals has highlighted cardiac abnormalities such as abnormal heart rate, diminished oxidative capacity and increased body mass, alongside alterations in substrate metabolism (Leone et al., 2005). Furthermore, other PGC1 α knockout studies have reported similar findings including the downregulation of genes regulating oxidative phosphorylation and reduced mitochondrial enzyme activities and myocardial ATP content (Arany et al., 2005). Though mitochondrial biogenesis has not been investigated in the uraemic heart, citrate synthase activity, a marker of mitochondrial density, has been reported as unchanged in experimental uraemia at 12 weeks (Smith, 2009 & Taylor 2015). This may suggest that the overall number of mitochondrial is conserved at this stage of uraemia, however this does not exclude abnormal mitochondrial function or efficiency.

1.10 Autophagy

Autophagy plays a key role in maintaining normal cardiomyocyte function by recycling Intracellular components such as aging proteins and organelles (Terman & Brunk, 2005). There are three known mechanisms of autophagy; macroautophagy, microautophagy and chaperone-mediated autophagy, though macroautophagy can be considered the most prevalent form in the heart (Nishida et al., 2009). Macroautophagy involves the isolation of cytoplasmic components into a double membraned envelope known as the autophagosome (Figure 1.5). Following complete encapsulation, the autophagosome subsequently fuses with a lysosome resulting in the formation of an autolysosome. The fusion of both components results in the intralysosomal degradation of the encapsulated cellular constituents (Eskelinen & Saftig, 2009). Microphagy is the direct engulfment of intracellular components by lysosomes and chaperone-mediated autophagy is a highly selective form of autophagy specifically targeted to cytoplasmic elements containing the Hsc70 complex (Nishida et al., 2009).

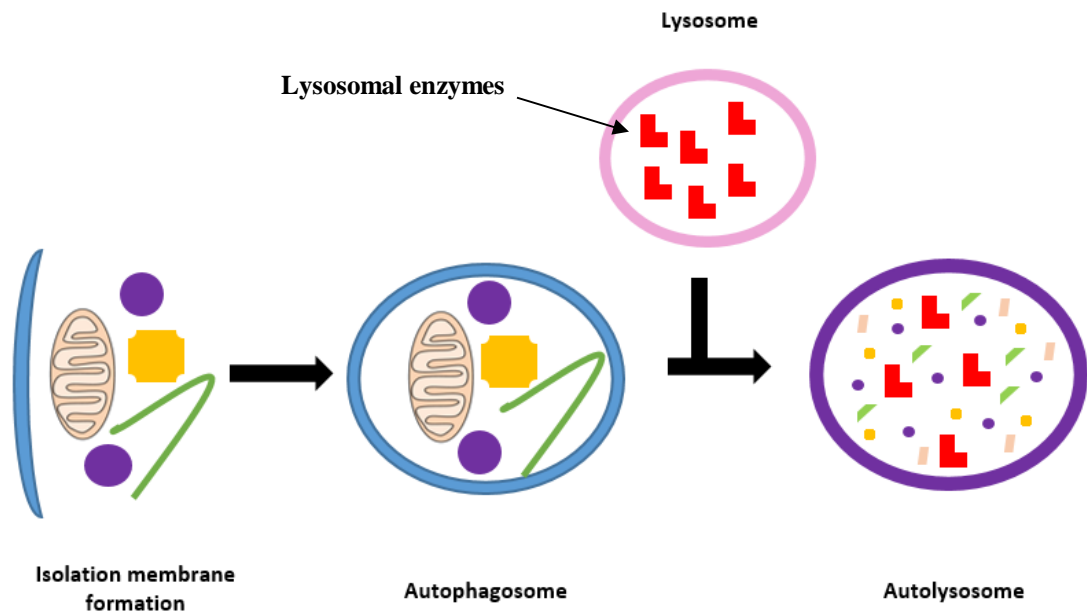


Figure 1.5. Schematic representation of autophagy. A double membraned envelope known as the autophagosome forms around the targeted cellular constituents. Subsequent fusion with a lysosome results in the formation of the autolysosome and the consequent intralysosomal degradation of the intracellular components.

In recent years the term mitophagy has been coined to describe mitochondrial specific autophagy (Iglewski et al., 2010). Mitochondria are the primary site of reactive oxygen species (ROS) production and also trigger apoptotic cell death via the release of cytochrome c. Therefore mitophagy can act as a form of quality control and contributes to cardiomyocyte survival by limiting the number of damaged/dysfunctional mitochondria in the cell (Twig et al., 2008). The selection of mitochondria to undergo mitophagy is largely dependent on their resting membrane potential. Mitochondria with an intact membrane potential are likely to fuse within the mitochondrial network

whereas de-energised mitochondria are more likely to be segregated and selected for degradation via mitophagy (Twig et al., 2008).

Changes in the rate of autophagy have been reported in several studies of cardiac hypertrophy and heart failure. Nakai et al. (2007) showed that rates of autophagy were significantly reduced 1 week following traverse aortic constriction. They hypothesised that the decreased rate of autophagic turnover facilitated the early hypertrophic response of increased protein and myofilament synthesis. Conversely, enhanced autophagy has been reported in dilated cardiomyopathy and ischemic heart disease. Shimomura et al. (2001) used transmission electron microscopy (TEM) to visualise left ventricular tissue from patients with dilated cardiomyopathy and observed prominent myocardial scarring associated with numerous intracellular vacuoles (autophagosomes) containing cellular constituents such as mitochondria. Yan et al. (2005), again using TEM to investigate autophagy in a swine model of ischemic-induced heart failure, observed similar findings. Interestingly the relationship between apoptosis and autophagy was reciprocal in this study as markers of apoptotic activity were markedly reduced despite increased autophagy. Collectively these studies suggest that there is a role for autophagy in the failing heart.

1.11 Apoptosis

Apoptosis is an essential process in early cardiac development, aiding the development of cardiac valves and coronary vasculature (Sanchis et al., 2008). In

addition, apoptosis also occurs at a low basal rate in the healthy adult heart, though the complete physiological relevance is still unclear (Fisher et al., 2000). Apoptosis is complex and involves both pro- and anti-apoptotic proteins and converging pathways (Figure 1.6). The extrinsic pathway is stimulated by the binding of extracellular death ligands, such as Fas and tumour necrosis factor- α (TNF α), to membrane bound receptors (van Empel et al., 2005). This triggers the recruitment of the adaptor protein Fas-Associated protein with Death Domain (FADD), which bridges cell surface death receptors to caspase 8 (Kim & Kang, 2010). The caspase family of proteins are cysteine proteases localised to the cytosol (Chiong et al., 2011). Cleavage of specific aspartate residues within the pro-domains results in a cascade of caspase activation, ultimately leading to the initiation of caspase 3 which degrades intracellular proteins, resulting in characteristic apoptotic bodies (Chiong et al., 2011).

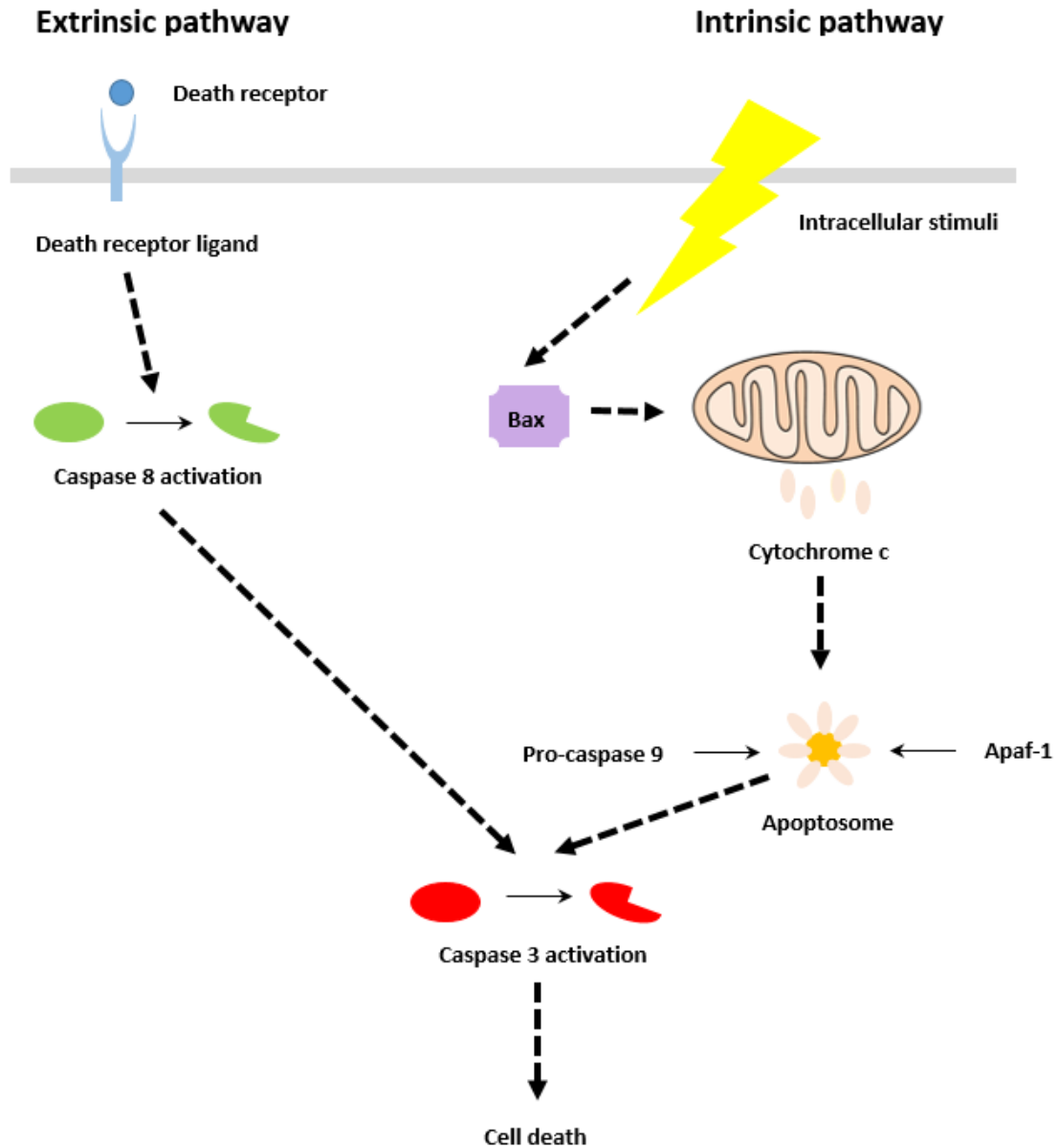


Figure 1.6. Schematic representation of apoptosis. The extrinsic pathway is stimulated via binding of a death receptor to its respective ligand. This triggers caspase 8 activation which in turn activates caspase 3 leading to cell death. The intrinsic pathway is triggered by intracellular stimuli, such as ROS, which causes the translocation of Bax to the mitochondrial membrane. Interaction of Bax with the mitochondria results in the release in of cytochrome c into the cytosol where it binds pro-caspase 9 and apoptotic protein activating factor-1 (Apaf-1), forming the apoptosome. Apoptosome formation can then trigger caspase 3 activation and subsequent cell death.

The intrinsic pathway is triggered by stimuli such as oxidative stress, ischemia, hypoxia and DNA damage and regulated by the Bcl-2 family of proteins which contain both pro- and anti-apoptotic proteins (Crow et al., 2004). Activation of pro-apoptotic Bcl-2 proteins leads to the release of cytochrome c which is normally sequestered in the mitochondrial intermembrane space (Whelan et al., 2010). Cytosolic cytochrome c then binds to apoptotic protein activating factor-1 (Apaf-1) and pro-caspase 9 forming the apoptosome complex, which in turn activates caspase 3 in a similar manner to the extrinsic pathway (Kim & Kang, 2010).

Although apoptosis has been identified in the healthy heart at a low level, enhanced rates of cardiomyocyte apoptosis have been implicated in heart failure. Gottlieb et al. (1994) identified increased apoptosis during reperfusion in the isolated perfused rabbit heart following ischaemia. Interestingly, the group found that necrosis was exclusive to ischemia and apoptosis to the reperfusion phase of ischemia reperfusion, though the underpinning mechanisms were unclear. Olivetti et al. (1997) reported a substantial increase in apoptosis rates in cardiac tissue taken from heart failure patients undergoing transplantation. Clinical studies on the infarcted human heart have shown that apoptosis rates are approximately 12% in cardiomyocytes bordering the infarction zone whereas rates are less than 1% in areas non-adjacent to the infarct (Olivetti et al., 1996). Furthermore, Takemura et al. (1998) highlighted apoptosis rates were still elevated 1 month after infarction suggesting apoptosis may play an important role in myocardial remodelling and the progression to failure following the initial infarct. Although there are little data on the impact of cardiomyocyte

apoptosis in CKD, Harwood et al. (2003) identified enhanced caspase 3 activation in nephrectomised rats highlighting a potential role for apoptosis in the uraemic myocardium.

1.12 Necrosis

Necrotic cell death is a largely unregulated process characterised by ATP depletion and cellular swelling, leading to myocyte rupture and the release of cellular constituents promoting inflammation and scar formation (Whelan et al., 2010). Necrosis can occur both as a primary mode of cell death or as a consequence of delayed clearance of apoptotic bodies (Zitvogel et al., 2010). Triggers for necrotic cell death include calcium overload, trauma and energy depletion culminating from the collapse of the mitochondrial membrane potential (Konstantinidis et al., 2012).

Myocyte necrosis is a relatively well characterised event in acute ischemic injury such as myocardial infarction. During ischemia mitochondria are starved of oxygen and unable to carry out oxidative phosphorylation, leading to a decline of ATP and a concomitant rise in ADP, AMP and Pi (Halestrap & Pasdois, 2009). This can trigger an increase in glycolysis via activation of phosphofruktokinase, however the accumulation of lactic acid causes a decrease in intracellular pH. These changes in ionic homeostasis can inhibit or reverse the calcium-sodium exchanger leading to calcium overload in the myocyte (Halestrap & Pasdois, 2009). Furthermore, elevated AMP can be converted into xanthine via a purine degradation pathway which, in turn, can be converted to ROS by

xanthine oxidase (Nishino, 1994). The rupturing of the cardiomyocyte and release of intracellular components mediates an inflammatory response involving enhanced cytokine production and the recruitment of neutrophils and leukocytes (Marchant et al., 2012).

Changes in cardiac ultra-structure have been reported to occur as early as 40 minutes post-injury (Ertl & Frantz, 2005). Collagenases and proteases start to degrade connective tissue in the infarcted area while white blood cells clear necrotic tissue. Myofibroblasts then infiltrate and begin to synthesise collagen to preserve myocardial structure and function (Ertl & Frantz, 2005). However, the repetitive fibrosis involved in scar formation contributes to increased stiffness and reduced contractility in the heart, impairing the myocardium's ability to meet the haemodynamic needs of the body and promoting the development of heart failure (Segura et al., 2014). Previous studies have revealed marked cardiac fibrosis in uraemia suggesting necrosis may occur in the uraemic myocardium and contribute to the overall decline in function and high incidence of cardiac death in patients with CKD (Smith, 2009).

1.13 Mitochondrial Permeability Transition Pore

A key process in necrotic cell death and a potential element involved in the intrinsic pathway of apoptosis is opening of the mitochondrial permeability transition pore (mPTP), a non-selective multi-protein complex located on the IMM (Figure 1.7). Although the exact composition of the mPTP remains uncertain, recent studies have

highlighted that three proteins are key to its regulation; cyclophilin D (CyP-D), adenine nucleotide translocase (ANT) and the mitochondrial phosphate carrier (PiC). CyP-D is a nuclear encoded protein of 18kDa which is localised to the mitochondrial matrix (Halestrap & Pasdois, 2009). Crompton et al. (1988) revealed that treatment of CyP-D with cyclosporine A (CsA) resulted in the formation of CyP-D-CsA complexes, which decreased the sensitivity of mPTP opening to calcium. Furthermore, Basso et al. (2005) demonstrated that CyP-D knockout mice were highly resistant to calcium-induced mPTP formation. ANT is the most abundant protein in the IMM and functions to export ATP from the matrix and ADP to the matrix in an energy dependent manner (Kaukonen et al., 2000). PiC transports phosphate to the mitochondrial matrix either by proton co-transport or individually in exchange for hydroxyl ions (Kwong et al., 2014). Knockout of PiC in HeLa cells results in a significantly reduced sensitivity to pore opening by apoptosis stimulating agents such as staurosporine (Alcala et al., 2008). On the other hand, PiC over-expression and phosphate alone can induce apoptosis (Alcala et al., 2008).

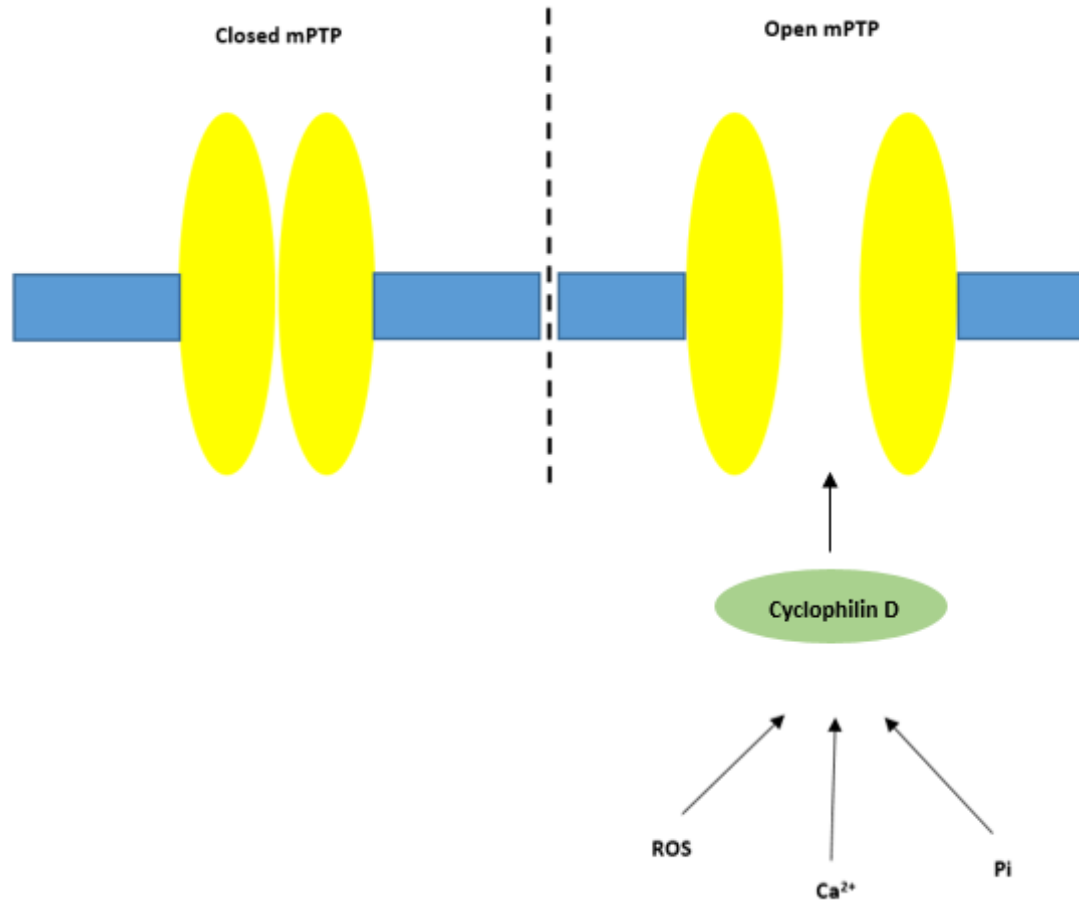


Figure 1.7. The mitochondrial permeability transition pore (mPTP). In normal physiological conditions the mPTP is closed, however states of stress such as enhanced ROS, calcium or phosphate trigger pore opening via the regulatory action of Cyclophilin D.

Pathological stress, such as calcium overload or ROS, can trigger pore opening via the regulatory action of CyP-D, resulting in the entry of solutes up to 1.5kDa into the mitochondrial matrix (Crompton et al., 1987). The influx of molecules increases osmotic pressure in the IMM, causing it to swell. As the matrix expands, it exerts pressure on the outer mitochondrial membrane (OMM) which eventually ruptures, releasing pro-apoptotic proteins such as cytochrome c into the cytosol and triggering apoptotic cell

death (Halestrap & Pasdois, 2009). In addition, the enhanced permeability of the IMM causes a leak of protons, dissipating the mitochondrial membrane potential. In the absence of the membrane potential, ATP synthase is unable to generate ATP and begins to work in reverse, breaking down ATP for energy (Halestrap et al., 2004). When a significant number of mitochondria have undergone the transition to mPTP opening, the cardiomyocyte cannot maintain its metabolic activity and undergoes necrotic cell death.

Studies on the uraemic heart have identified an impaired functional response following ischemic insult, potentially due to enhanced mPTP opening. Indeed, evidence from nephrectomised rats has demonstrated enlarged infarct areas following ligation of the left coronary artery, consistent with increased mPTP opening and subsequent necrosis (Dikow et al., 2004). Furthermore, functional recovery has been shown to be delayed in the perfused uraemic heart following ischemia reperfusion (Semple et al., 2012). Collectively these studies indicate that the uraemic heart is increasingly susceptible to cell injury and death.

1.14 Objectives

Previous studies have demonstrated significant cellular and metabolic remodelling in the uraemic heart. However the majority of these studies have been carried out under *in vitro* conditions. Therefore the aims of this study were two-fold; (I) to investigate the extent of metabolic remodelling in the uraemic heart *in vivo* using the non-invasive imaging technique positron emission tomography (PET). The hypothesis

here being that enhanced glucose uptake and metabolism may occur *in vivo* during the compensated phase of hypertrophy to maintain cardiac function. (II) To probe the cellular basis of mitochondrial dysfunction, which has been recognised as a central contributor to the pathogenesis of heart disease as a result of damaged or inefficient mitochondria. The hypothesis being that altered fusion or fission may underpin mitochondrial inefficiency and that iron therapy may counteract the inefficiency by enhancing mitochondrial function. Collectively, the central hypothesis under investigation was that impaired cardiac bioenergetics may underpin the enhanced susceptibility to cell injury and death identified in previous studies and contribute to the increased mortality from adverse cardiovascular events observed in CKD patients.

The specific aims of this study were:

- To investigate cardiac glucose metabolism *in vivo* using ^{18}F -fluorodeoxyglucose PET (^{18}F -FDG PET) during the development of UCM
- To determine the impact of iron therapy on cardiac mitochondrial function
- To characterise mitochondrial morphology in uraemic hearts by probing the expression of key mitochondrial fusion and fission proteins and assessing gross mitochondrial structure

2. Materials and Methods

2.1 Induction of Experimental Uraemia

All experiments conformed to the Home Office Guidance on the Operation of Animals Scientific Procedures Act 1986 (as amended) (Home Office, 2014). Uraemia was induced surgically via a one-stage 5/6th nephrectomy as previously described (Taylor et al., 2015). Male Sprague-Dawley rats (230-280g) (Charles River, Kent, UK) were anaesthetised with 3.5% isoflurane in 3l/min oxygen and anaesthesia maintained using 2.5% isoflurane in 1l/min oxygen. The pedal withdrawal reflex was used to indicate depth of anaesthesia. Prior to surgery, a subcutaneous (S/C) injection of Rimadyl (4mg/kg BW) (Pfizer Ltd, Kent, UK) was administered for post-operative pain relief. The procedure consisted of a laparotomy exposing the abdominal cavity. The left kidney was then decapsulated and 2/3 renal mass removed, using Surgicell haemostatic material (Johnson & Johnson, Switzerland) to stem excessive bleeding (Figure 2.1). The right kidney was subsequently decapsulated, the renal vessels ligated using silk suture material (Mersilk 0 suture, Ethicon, Sumerville, USA) and the entire kidney removed.

Sham operated animals underwent the same procedure with only kidney decapsulation, leaving both kidneys intact. Sterile isotonic saline (Animal Care Ltd, York, UK) was administered directly into the abdominal cavity to compensate for fluid loss during surgery. The abdominal musculature was closed with absorbable suture (Ethicon 3-0, Vicryl braided, Johnson & Johnson, Belgium) and the dermal layer with non-absorbable suture (Ethicon 3-0, blue monofilament, Johnson & Johnson, Belgium). Post-surgery, animals received a S/C injection of the antibiotic, Duphacillin (42mg/kg BW) (Pfizer Ltd, Kent, UK), and were allowed to recover. 24 hours later

animals were housed individually with 12:12 hour light:dark cycles and both groups pair fed a diet of standard rat chow with water *ad libitum*. Animals were sacrificed 12 to 14 weeks post-surgery.

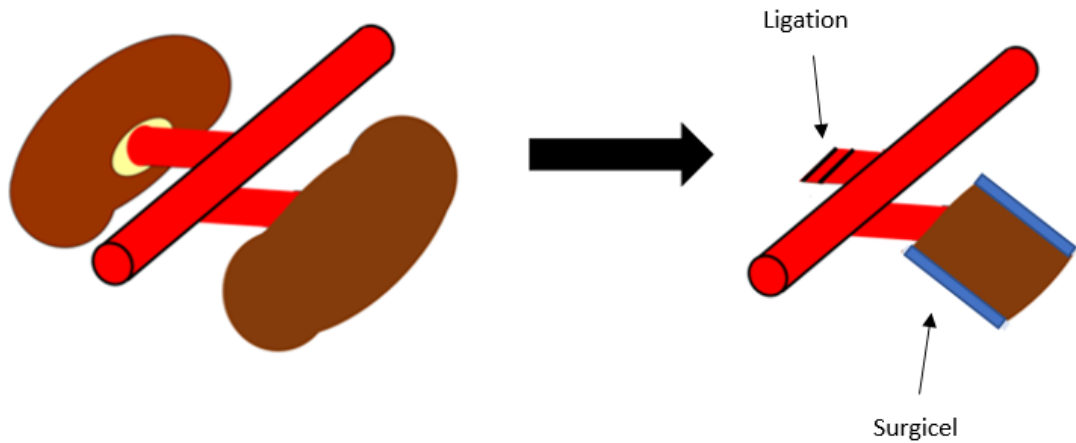


Figure 2.1. Surgical induction of uraemia. The right renal vasculature was ligated and the whole kidney removed while 2/3 of renal mass was removed from the left kidney, using Surgicel to stem blood loss.

In total 110 animals underwent surgery, the full experimental design is shown in Figure 2.2.

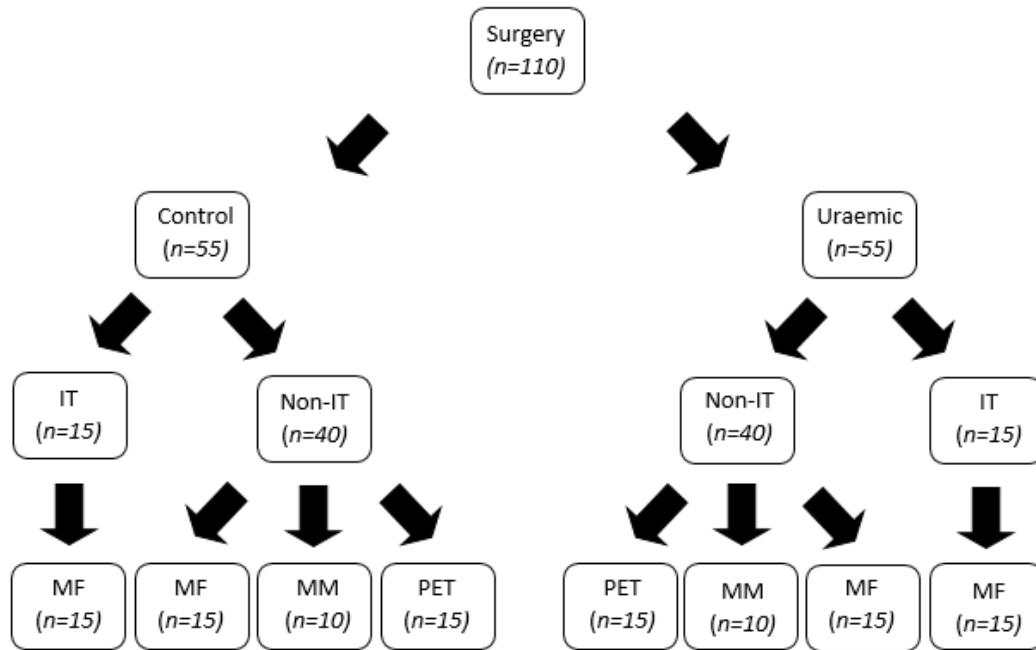


Figure 2.2. Full experimental design. IT = iron therapy, MF = mitochondrial function, MM = mitochondrial morphology and PET = positron emission tomography.

2.2 Characterisation of UCM Model

2.2.1 Markers of Renal Function and Iron Homeostasis

Serum and urine analysis was performed on an RX Monza clinical chemistry analyser (Randox Laboratories, County Antrim, UK). Blood was collected from the thoracic cavity at the time of sacrifice and centrifuged at 3000g for 10 minutes at 4°C. The packed cell volume (PCV) was measured and the serum removed and stored at -20°C until further analysis. Serum samples were assayed for creatinine (kit: CR510), urea (kit: UR220), total protein (kit: TP245), iron (kit: SI257), transferrin (kit: TF3831) and total iron binding capacity (kit: TI1010). Serum ferritin was determined using a Rat Ferritin ELISA Kit (kit: ab157732, following the manufacturer's instructions, Abcam, Cambridge, UK). Urine was collected over 24 hours from animals housed in

metabolic cages and subsequently analysed for creatinine and total protein.

Creatinine clearance was calculated according to Equation 1.

$$\text{Creatinine clearance} \frac{\text{ml/min/kg bodyweight}}{\text{ml/min/kg bodyweight}} = \frac{\left[\frac{\text{Creatinine}_{\text{urine}}}{\text{Creatinine}_{\text{serum}}} \times \frac{\text{Volume}_{\text{urine}}}{\text{Time (hours)} \times 60} \right]}{\text{Body weight (kg)}}$$

Equation 1. Calculation of creatinine clearance (Velasquez et al., 1989)

2.2.2 Indices of Cardiac Hypertrophy

Cardiac hypertrophy was quantified using the heart weight-to-tibia length ratio (HW:TL) as previously described (Yin et al., 1982). Lung weights were determined immediately after sacrifice and following 24 hours drying at room temperature to assess fluid retention.

2.2.3 Indices of Body Mass

Hind limb (gastrocnemius and soleus) muscle was excised at the time of sacrifice to determine the presence of muscle wasting. Excised muscle was normalised to body weight and tibial length to account for differences in animal size.

2.3 Mitochondrial Studies

2.3.1 Mitochondrial Isolation

Cardiac mitochondria were isolated as described previously (Taylor et al., 2015) (Figure 2.3). Animals were anaesthetised with an intraperitoneal (I/P) injection of sodium thiopentone (0.5ml/100g BW) and hearts rapidly excised and immersed in 5ml of ice cold isolation buffer A (0.3M sucrose, 10mM HEPES and 2mM EGTA (pH 7.2)). Hearts were trimmed of any extraneous tissue and minced thoroughly with scissors. Subsequently, the suspension was transferred to a 30cm³, 19mm OD glass Teflon homogeniser (Scientific Laboratory Supplies, UK) and digested with 1ml of trypsin solution (1.25mg/ml trypsin, 0.3M sucrose, 10mM HEPES and 2mM EGTA (pH 7.2)) for 15 minutes. Simultaneously, the suspension was homogenised using a loose fitting Teflon pestle (15.5mm bore) (Scientific Laboratory Supplies, UK) in 3 x 1 minute periods. Thereafter, 10ml of trypsin inhibitor solution (1mg/ml BSA, 0.3M sucrose, 10mM HEPES, 1mg/ml trypsin inhibitor and 2mM EGTA (pH 7.2)) was added and the suspension homogenised again with loose and tight fitting Teflon pestles (16mm bore, Scientific Laboratory Supplies, UK) for 5 minutes until homogenous.

The resultant suspension was centrifuged for 10 minutes (600 x g, 4°C) and the supernatant centrifuged again for a further 15 minutes (8000 x g, 4°C). The pellet was re-suspended in 5ml of isolation buffer B (0.3M sucrose, 1mg/ml BSA, 10mM HEPES and 2mM EGTA (pH 7.4)) and subjected to a final centrifugation for 15 minutes (8000 x g, 4°C). Finally, the mitochondrial pellet was re-suspended in 600µl of isolation buffer A. One aliquot of suspension was stored at -80°C for enzyme analysis and the remainder used immediately for respiratory measurements. Mitochondrial

protein content was determined using the Bio-Rad protein assay (following the manufacturer's instructions, Bio-Rad Laboratories, Munich, Germany) (Figure 2.4).

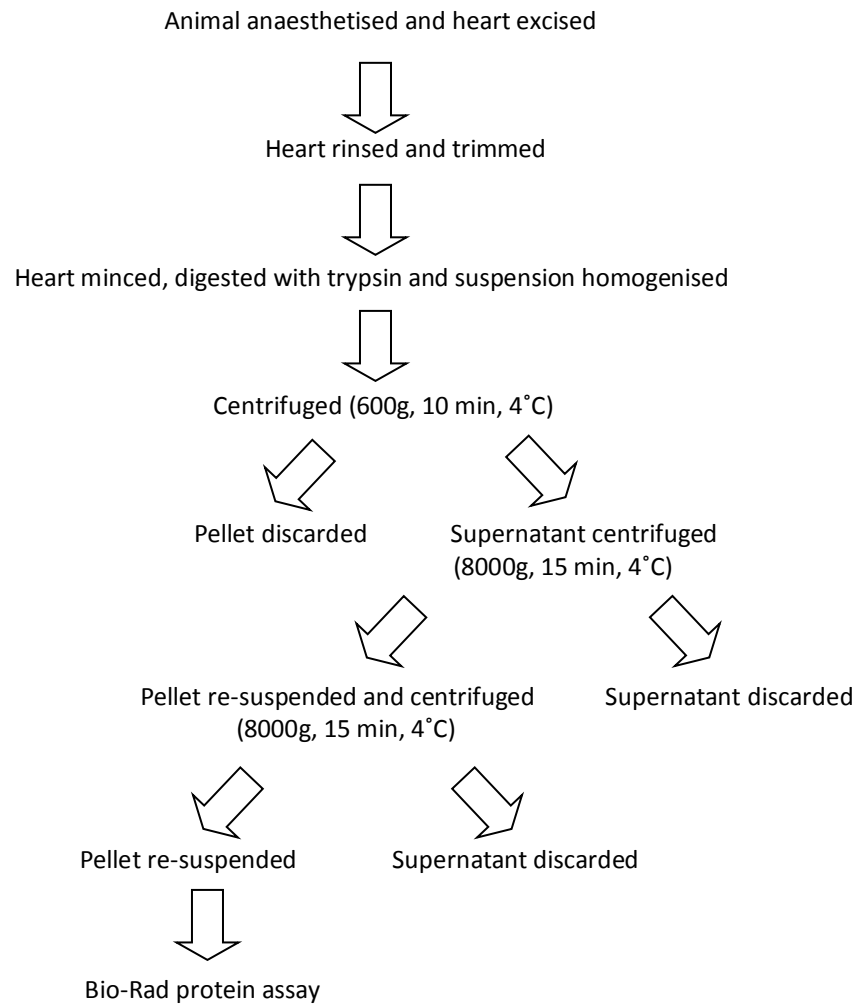


Figure 2.3. Flowchart for the isolation of cardiac mitochondria. All steps performed on ice.

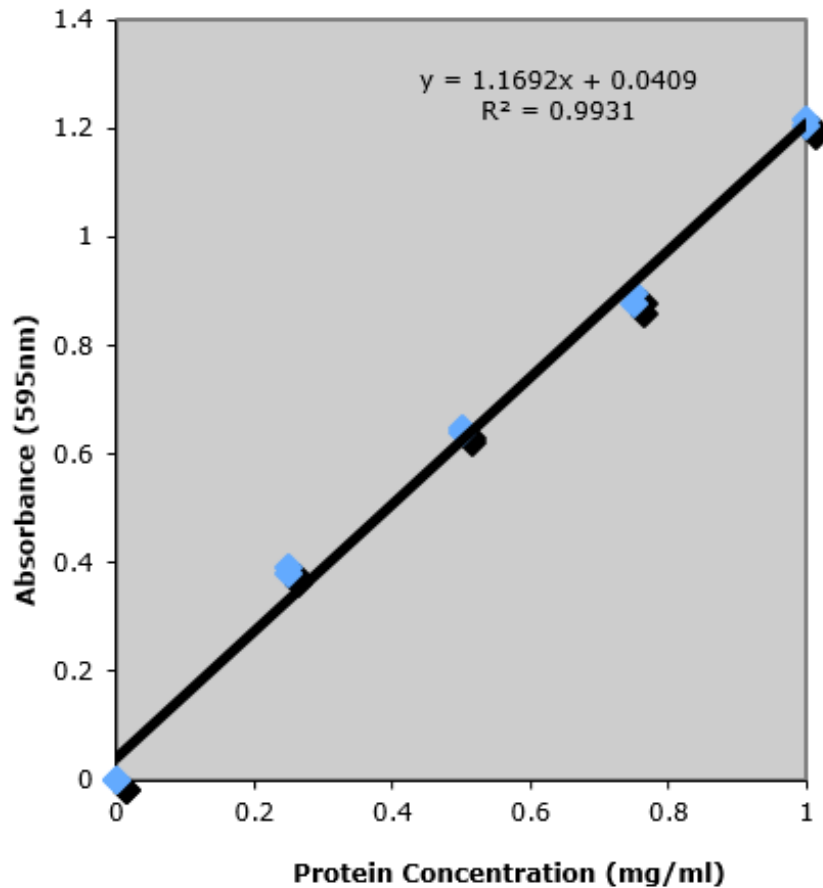


Figure 2.4. Standard curve for determining protein concentration using the Bio-Rad assay. Each point represents known protein concentrations (0, 0.25, 0.5, 0.75 & 1mg/ml) which were assayed in duplicate to generate the standard curve to determine tissue protein concentrations.

2.3.2 Mitochondrial Respiratory Rates

Mitochondrial respiratory rates were determined as described previously (Taylor et al., 2015), with a Clark-type oxygen electrode (Rank Brothers LTD, Cambridge, UK) (Figure 2.5). Respiratory buffer (125mM KCl, 20mM MOPS, 10mM Tris, 0.5mM EGTA, 2.5mM KH_2PO_4 and 2.5mM MgCl_2 (pH 7.2)) was added to the electrode chamber and equilibrated at 30°C. Subsequently, isolated mitochondria (final concentration 0.5mg/ml mitochondrial protein) were added and baseline respiration determined. 40µl of respiratory substrate containing either 5mM

glutamate & 1mM malate, 5mM succinate & 1 μ M rotenone or 40 μ M palmitoyl carnitine & 5mM malate was added. To determine state 3 (ADP stimulated) respiration 20 μ l of 0.5mM ADP was added, resulting in a rapid increase in oxygen consumption. State 4 (uncoupled) respiration was initiated by the addition of 2 μ l of 1mg/ml oligomycin. Measurements were recorded using a PowerLab system and chart5 software (Figure 2.6) (AD Instruments, Hastings, UK).



Figure 2.5. Experimental setup for mitochondrial respiratory measurements. (A) Isolated mitochondria were added to the electrode chamber and (B) maintained using a 30°C water bath. (C) Oxygen consumption was measured using a Clark-type oxygen electrode and (D) respiration rates recorded using a PowerLab system and chart5 software.

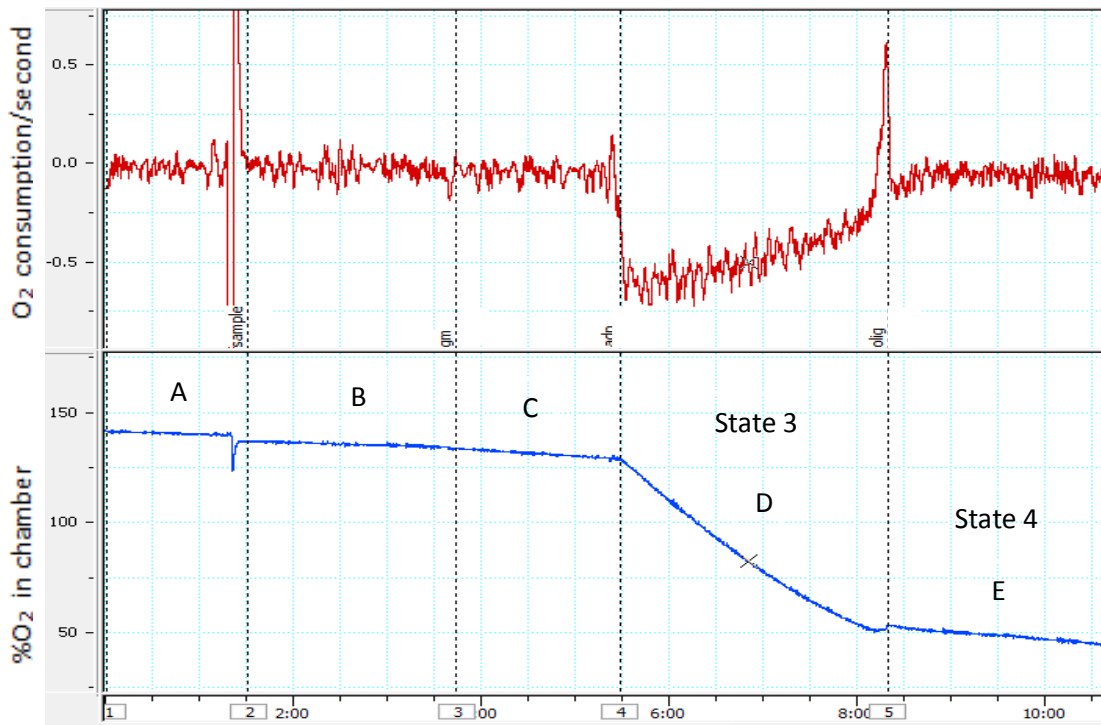


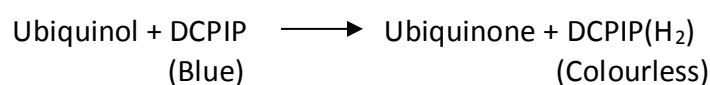
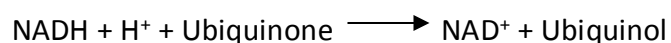
Figure 2.6. Recording of mitochondrial respiratory rates using 5mM glutamate & 1mM malate as substrates. The red trace indicates the rate of oxygen consumption and the blue trace the oxygen concentration within the chamber. (A) Respiration buffer was added to the chamber and equilibrated. (B) 0.5mg/ml mitochondrial protein was added followed by (C) the relevant respiratory substrates. (D) State 3 respiration was initiated by the addition of 0.5mM ADP and (E) state 4 respiration was determined by adding 1mg/ml oligomycin.

2.3.3 Mitochondrial Enzyme Activities

Mitochondria were isolated as described in section 2.3.1 and subjected to 3 cycles of freeze-thawing prior to analysis (Pon & Schon, 2007). Enzyme activities were determined spectrophotometrically using a Phillips Scanning Spectrophotometer (Spectronic, Leeds, UK).

2.3.3.1 Respiratory Complex I Assay

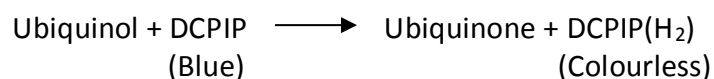
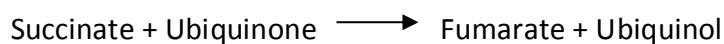
NADH dehydrogenase (complex I) catalyses electron transfer from NADH to ubiquinone forming NAD⁺ and ubiquinol which is coupled to the reduction of the artificial electron acceptor, DCPIP, in the following reaction:



Complex I activities were measured as described previously by Long et al. (2009). 950µl reaction buffer (25mM KH₂PO₄, 5mM MgCl₂, 2mM KCN, 3mg/ml BSA, 60µM decylubiquinone (dissolved in ethanol), 130 µM NADH, 2µg/ml antimycin A (dissolved in ethanol) and 264 µM DCPIP (pH 7.4)) was equilibrated for 10 minutes at 30°C. The reaction was initiated by the addition of 50µl mitochondrial suspension (containing 2.5µg mitochondrial protein) and the decrease in absorbance at 600nm followed over 3 minutes.

2.3.3.2 Respiratory Complex II Assay

Succinate dehydrogenase (complex II) catalyses electron transfer from succinate to ubiquinone, forming fumarate and ubiquinol respectively. As with the complex I assay, ubiquinol production is coupled to the reduction of DCPIP in the following reaction:



Complex II activities were measured as described previously by Pon & Schon (2007). 935µl of reaction buffer (25mM KH₂PO₄, 5mM MgCl₂, 2mM KCN, 2.2µg/ml rotenone (dissolved in ethanol), 22mM succinic acid, 2µg/ml antimycin A (dissolved in ethanol) and 176 µM DCPIP (pH 7.4)) was equilibrated for 5 minutes at 30°C. Thereafter, 50µl mitochondrial suspension (containing 15µg mitochondrial protein) was added and incubated for a further 5 minutes. The reaction was initiated by the addition of 15µl 60µM decylubiquinone (dissolved in ethanol) and the decrease in absorbance measured at 600nm over 2 minutes.

2.3.3.3 Respiratory Complex II + III Assay

Complex II catalyses electron transfer from succinate to ubiquinone forming fumarate and ubiquinol whilst coenzyme Q cytochrome c reductase (complex III) subsequently passes electrons from ubiquinol to cytochrome c. The reduction of cytochrome c results in a colour change from orange to pink in the following reaction:



Complex II + III activities were measured as described previously by Pon & Schon (2007). 940µl of reaction buffer (25mM KH₂PO₄, 5mM MgCl₂, 2mM KCN, 2µg/mL rotenone (dissolved in ethanol) and 22mM succinic acid (pH 7.4)) was equilibrated for 5 minutes at 30°C. Subsequently, 50µl mitochondrial suspension (containing 5µg mitochondrial protein) was added and incubated for a further 10 minutes. The reaction was initiated by the addition of 10µl 2mM cytochrome c (oxidised) and the increase in absorbance measured at 550nm over 3 minutes.

2.3.3.4 Respiratory Complex IV Assay

Cytochrome IV oxidase (complex IV) catalyses the transfer of electrons from cytochrome c to oxygen. The oxidation of cytochrome c results in a colour change from pink to orange in the following reaction:



Complex IV activities were measured as described previously by Pon & Schon (2007). 910µl of reaction buffer (20mM KH₂PO₄ and 0.45mM n-dodecyl-beta-D-maltoside (pH 7.0)) was equilibrated for 5 minutes at 30°C. Thereafter, 80µl mitochondrial suspension (containing 2.5µg mitochondrial protein) was added and incubated for a further 5 minutes. The reaction was initiated by the addition of 10µl 2mM cytochrome c (reduced) and the decrease in absorbance measured at 550nm over 2 minutes.

2.3.3.5 Citrate Synthase Assay

Citrate synthase activities were determined in isolated mitochondria or cardiac tissue by measuring the product of released CoA.SH with DNTB in the following reaction:



2.3.3.5.1 Citrate Synthase Activity in Isolated Mitochondria

1.85ml of reaction buffer (100mM Tris-HCl, 100 μ M DTNB, 50 μ M acetyl CoA and 0.1% w/v Triton X-100 (pH 8.0)) was equilibrated for 5 minutes at 25°C. Subsequently, 100 μ l mitochondrial suspension (containing 40 μ g mitochondrial protein) was added and incubated for a further minute. The reaction was initiated by the addition of 50 μ l 10mM oxaloacetate and the increase in absorbance at 412nm followed over 1 minute (Pon & Schon, 2007).

2.3.3.5.2 Citrate Synthase Activity in Cardiac Tissue

Powdered cardiac tissue was homogenised using an Ultra Turrax T25 homogeniser (IKA, Germany) at maximum speed for 20 seconds in ice-cold extraction buffer (100mM imidazole, 10mM MgCl₂ and 1mM EGTA (pH7.2)). 10 μ l 0.1% w/v Triton X-100 was added to the tissue homogenate, incubated for 1 hour on ice and

centrifuged (800g, 4°C). The resultant supernatant was assayed by following the same reaction described above.

1.98ml of reaction buffer (50mM Tris-HCl, 200µM DTNB, 100µM acetyl CoA, 0.5mM oxaloacetate and 0.05% w/v Triton X-100 (pH 8.0)) was equilibrated for 5 minutes at 30°C. The reaction was initiated by the addition of 20µl supernatant and the increase in absorbance at 412nm followed over 2 minutes (Morgan-Hughes et al., 1977).

2.3.4 Calcium Induced Mitochondrial Swelling Assay

Calcium-induced mitochondrial swelling was determined in isolated cardiac mitochondria (section 2.3.1) using a modification of the method of Izem-Meziane et al. (2012). 50µg mitochondrial protein was added to swelling buffer (120mM KCl, 5mM KH₂PO₄, 20mM MOPS, and 10mM Tris-HCl (pH 7.4)) and incubated for 5 minutes at 37°C in the presence or absence of 1µM cyclosporine A. Mitochondrial swelling was initiated by the addition of 0, 40, 60 or 80µM calcium and the decrease in absorption at 560nm recorded at 20 second intervals over 15 minutes.

2.3.5 Mitochondrial Morphology

2.3.5.1 Transmission Electron Microscopy

Hearts were removed as described in section 2.3.1 and approximately 50mg left ventricular tissue immediately fixed in glutaraldehyde, 0.1M cacodylate and 30mM glucose (pH 7.3) for 2 hours at room temperature. The tissue was given 3 x 5

minute washes in cacodylate buffer (0.1M cacodylate and 30mM glucose (pH 7.3)), post-fixed in osmium tetroxide solution for 1 hour (1% osmium tetroxide, 0.1M cacodylate and 30mM glucose (pH 7.3)) and given a further 3 x 5 minute washes in cacodylate buffer. The tissue was then counter-stained with 1% uranyl acetate for 1 hour and dehydrated via a series of ascending ethanol concentrations (30%, 50%, 70%, 90% and 100%, 15 minutes each). Residual ethanol was removed by 1 x 15 minute and 1 x 30 minute washes in propylene oxide. The tissue was embedded in epon/araldite resin and baked for 48 hours at 60°C. 50nm sections were cut from the resin block using a diatome diamond knife in a Leica UC6 Gatan Ultrascan 4000 digital camera attached to a Joel 2010 transmission electron microscope running at 120kV (Robards & Wilson, 1993).

Mitochondrial morphology was assessed by random selection of 6 images per tissue section containing mitochondria in a longitudinal arrangement along the sarcomere. Individual mitochondria were scored for length, width and aspect ratios (length/width). Mitochondria undergoing fusion/fission or only partially in the field of view were not scored (Song et al., 2015).

2.3.5.2 Flow Cytometry

Cardiac mitochondrial size was assessed by autofluorescence with a FACScalibur flow cytometer (BD Bioscience, California, USA) using a modification of Disatnik et al. (2013). Briefly, mitochondria were isolated as described in section 2.3.1 and diluted 1:200 in PBS immediately prior to analysis. 300µl mitochondrial

suspension was then loaded into the flow cytometer, cell count set to 25000 and forward scatter measured to confirm mitochondrial size.

2.3.5.3 *Dynamic Light Scattering*

Cardiac mitochondrial size was determined by dynamic light scattering (DLS) with a Malvern Zetasizer Nano ZS (Malvern, UK) using a modification of Mar (1981). Mitochondria were isolated as described previously in section 2.3.1, fixed in 4% formaldehyde for 15 minutes in warmed 5% sucrose, and diluted 1:40 in ddH₂O. 1ml suspension was transferred to a cuvette and the mitochondrial hydrodynamic diameter measured. The hydrodynamic diameter can be measured by DLS as scattered light intensity is proportional to mass.

2.4 *Western Blotting*

200mg frozen powdered cardiac tissue was homogenised in 1ml extraction buffer (50mM Tris, protease inhibitor cocktail (Roche Diagnostics, Penzberg, Germany) and 1% w/v SDS (pH7.4)) using an Ultra Turrax T25 homogeniser (IKA, Germany) at maximum speed in 3 x 5 second bursts. Samples were centrifuged for 10 minutes (13000 x g, 4°C), the supernatant collected and protein concentration determined using the BioRad assay (following the manufacturer's instructions, BioRad Laboratories, Munich, Germany) (Figure 2.4). Sodium dodecyl sulphate polyacrylamide gel electrophoresis (SDS-PAGE) buffer (10% glycerol, 1% SDS, 45mM Tris (pH7.4), 2.5% 2-Mercaptoethanol and 0.01% Bromophenol Blue) was added to

the samples to achieve a final protein concentration of 5µg/µl. Samples were then boiled for 3 minutes, allowed to cool and stored at -80°C until required.

Protein separation was achieved using SDS-PAGE. Briefly, proteins were separated using a 3% stacking gel and 10% running gel (running buffer; 25mM Tris, 190mM glycine and 10% SDS) (150mV, 4°C, 90 minutes) and transferred to a nitrocellulose membrane at 4°C for 2 hours using a mini-transblot (BioRad laboratories, UK) (transfer buffer; 20mM Tris, 150mM glycine and 200ml methanol) (Akki & Seymour, 2009). Membranes were blocked using blocking buffer (0.25% TBS-Tween and 5% milk powder) to reduce any non-specific protein binding, washed in 0.25% TBS-Tween and exposed to the primary antibody (Table 2.1) overnight at 4°C. Thereafter, membranes were again washed in 0.25% TBS-Tween and incubated with a secondary antibody (Table 2.1) for 1 hour at room temperature.

Visualisation of proteins was achieved using enhanced chemiluminescence (ECL) reagents (Amersham, Uppsala, Sweden) and a ChemiDoc system (BioRad, Germany). Quantification of protein bands was determined using Image Lab software (BioRad, Germany) (Palermo et al., 2016).

Table 2.1*Antibody dilutions*

Target	Antibody	Species	Dilution	Dilutant	Reference
MFN1	Primary	Mouse monoclonal	1:1000	0.25% TBS-Tween & 1% milk powder	Modification of Magnoni et al. (2013)
	Secondary	Rabbit anti-mouse (HRP)	1:2000	As above	Paiva et al. (2010)
MFN2	Primary	Mouse monoclonal	1:1000	As above	Mancini et al. (2013)
	Secondary	Rabbit anti-mouse (HRP)	1:2000	As above	Paiva et al. (2010)
OPA1	Primary	Mouse monoclonal	1:1000	As above	Modification of Gao et al. (2014)
	Secondary	Rabbit anti-mouse (HRP)	1:2000	As above	Paiva et al. (2010)
DRP1	Primary	Mouse monoclonal	1:1000	As above	Modification of Cagalinec et al. (2013)
	Secondary	Rabbit anti-mouse (HRP)	1:2000	As above	Paiva et al. (2010)
Actin	Primary	Rabbit monoclonal	1:1000	As above	Modification of Nociari et al. (2007)
	Secondary	Rabbit anti-mouse (HRP)	1:2000	As above	Paiva et al. (2010)
VDAC	Primary	Mouse monoclonal	1:1000	As above	Modification of Wang et al. (2015)
	Secondary	Rabbit anti-mouse (HRP)	1:2000	As above	Paiva et al. (2010)

All antibodies were purchased from Abcam (Cambridge, UK). MFN1 = Mitofusin 1, MFN2 = Mitofusin 2, OPA1 = optic atrophy 1, DRP1 = dynamin related protein 1, VDAC = voltage dependent anion channel and HRP = horse radish peroxidase conjugated

2.5 Statistical Analysis

Data are presented as mean \pm standard error of the mean (SEM). Means were compared by an independent two-tailed *t*-test or two-way ANOVA where appropriate using Microsoft Excel's Data Analysis ToolPak (2010 edition). Significance was accepted at the $p < 0.05$ level.

3. Characterisation of Experimental Uraemia

3.1 Introduction

Chronic kidney disease is a syndrome of persistent renal dysfunction with systemic consequences including hypertension, diabetes and cardiac dysfunction (Thomas et al., 2008). Indeed, cardiac complications are the leading cause of mortality in CKD patients (Raine et al., 1992). However, the increased susceptibility to adverse cardiac events in uraemic patients is poorly understood and requires further study. Therefore there is a need for a reliable and robust experimental model to investigate the mechanisms underpinning cardiac dysfunction in CKD.

3.1.1 Nephrotoxic Drugs

A number of different experimental models have investigated the complex relationship between the heart and kidneys in the milieu of CKD. These primarily involve either the use of nephrotoxic drugs or surgical intervention. The chemotherapy drug, cisplatin, has nephrotoxic side effects leading to cell injury and death of renal tubules which has led to its use in animal models of CKD (Yang et al., 2010). Clinically, cisplatin nephrotoxicity typically manifests as a lower glomerular filtration rate (GFR) coupled with a reduced serum electrolyte concentration and a chronic inflammatory response, features common to CKD (Arany & Safirstein, 2003).

Other agents including doxorubicin and streptozotocin have also been used extensively in modelling animal models of CKD with similar outcomes (Lee & Harris, 2011 & Wu & Yan, 2015). However, drugs such as cisplatin and doxorubicin are also highly cardiotoxic and it is difficult to differentiate between the direct toxic effects of

the drug and secondary effects caused by renal dysfunction (Okuda et al., 1986 & Heidemann et al., 1990). Furthermore, the kidneys can functionally adapt to injury by undergoing compensatory hypertrophy (Ben-Haim et al., 2000). Therefore any experimental model needs to be sufficiently severe to induce chronic renal dysfunction. Thus the majority of CKD models employ surgical procedures, primarily comprising of either ligation of renal vasculature or excision of tissue to induce sufficient renal injury.

3.1.2 *Surgical Intervention*

Unilateral ureteral obstruction gives rise to interstitial fibrosis and chronic inflammation, resulting in CKD. The ureter is either completely or partially occluded resulting in a rapid decline in kidney function, characterised by uraemia and a decreased GFR within 24 hours, ultimately leading to end stage renal failure within approximately 2 weeks (Chevalier, 2006). However, serum creatinine concentrations remain within normal limits and a lack of urine output increases the difficulty in monitoring disease progression (Yang et al., 2010).

Another approach is selective clamping of renal arteries which causes ischemia, the most common cause of acute kidney injury in humans. This was first described by Goldblatt et al. (1934) who developed the two-kidney, one-clip model of hypertension-induced CKD in dogs. A clip is used to partially occlude the left renal artery causing a substantial increase in blood pressure. The hypertension is the result of a continuous cycle of renin secretion from the ischemic kidney and fluid loss from

the unclipped kidney. Ligation of renal arteries has also been used to achieve the same effect (Yang et al., 2010). Used chronically in the rodent model, both methods can be advantageous as they do not result in the large haemorrhage associated with removal of renal tissue (Leenen & de Jong, 1971). The rate of renal failure is proportional to the extent of ischemia and common manifestations include hypertension and LVH, features common to patients with UCM (Ma et al., 2005). However, due to poor reproducibility and intra-strain variability the ischemic approach is less favourable than nephrectomy models (Novalija et al., 2003).

The sub-total, or 5/6 nephrectomy, is a well characterised and robust method for mimicking progressive renal failure in humans (Raine et al., 1993). The procedure can be accomplished in either one or two stages and involves complete ligation/removal of one kidney and 2/3 of the remaining kidney (Chow et al., 2003). As mammalian kidneys are unable to generate new nephrons, compensatory hypertrophy of the remnant kidney can occur resulting in an increased workload for the remaining nephrons and ultimately leading to a progressive decline in renal function (Hostetter et al., 1981). Disease progression can be monitored by measuring serum biochemistry and urine markers of uraemia such as proteinuria and creatinine excretion (Taylor et al., 2015). Previous studies have successfully used this procedure over the past decade in order to investigate cardiac adaptations in CKD (Smith et al., 2010; Semple et al., 2012 & Aksentijevic et al., 2009).

3.1.3 Iron Therapy

Anaemia is an early occurrence in CKD and is strongly associated with a decrease in GFR (de Silva et al., 2006). The aetiology of anaemia in association with CKD is multifactorial involving inflammation and iron deficiency, though the principal cause is reduced erythropoietin production in the kidney (Gill & Ferreira, 2013). To ameliorate the anaemia, there are two primary forms of treatment; erythropoietin and iron supplementation (Arora & Ghali, 2013).

3.1.3.1 Erythropoietin

Iron is taken up by erythroblasts and reticulocytes for haemoglobin synthesis and thus plays a key role in erythropoiesis, a process regulated by erythropoietin (Icardi et al., 2013). Erythropoietin is primarily produced by renal interstitial fibroblasts in response to hypoxia and acts on the bone marrow promoting proliferation, differentiation and survival of erythroblasts (Fisher, 2003). Although both human recombinant erythropoietin and the erythropoietin analogue darbepoetin alfa have been used to treat anaemia in association with heart failure and CKD, results from clinical trials as a whole have been conflicting (Gill & Ferreira, 2013). Mancini et al. (2003) reported that erythropoietin treatment significantly improved exercise capacity in patients with chronic heart failure. Similar results were reported by Ponikowski et al. (2007) with darbepoetin alfa. However, other studies have reported no significant differences in hospitalisation and mortality in patients treated with darbepoetin alfa or placebo (Swedberg et al., 2013). Furthermore,

treatment with darbepoetin alfa has been linked to an increased incidence of stroke and/or other thrombotic episodes (Pfeffer et al., 2009).

3.1.3.2 Iron Supplementation

An alternative approach is iron therapy via either oral supplementation or IV infusion. Oral iron is usually in the form of ferrous salts or ferric complexes and is absorbed in the gut in a similar way to food (Geisser & Burckhardt, 2011). While a typical diet provides approximately 10-20mg iron/day, only around 5mg is absorbed. Therefore a therapeutic dose of oral iron (typically ~100mg) vastly exceeds the amount that can be absorbed via normal physiological mechanisms. However, due to the physico-chemical properties of these preparations, iron absorption can occur via the paracellular route, significantly increasing uptake (Heinrich et al., 1969). Indeed, pharmacokinetic studies have shown that a large portion of the supplemented iron is absorbed directly into the blood (Geisser & Burckhardt, 2011).

Under normal physiological conditions, plasma transferrin is approximately one-third saturated (Crichton et al., 2008). However, following oral iron therapy and paracellular absorption in the gut, transferrin can become rapidly saturated. This can lead to significant increases in the amount of non-transferrin bound iron (NTBI) in circulation (Geisser & Burckhardt, 2011). NTBI is taken up via unregulated mechanisms and can lead to oxidative stress. This may be clinically relevant in patients taking 2–3 tablets a day for several months as they are exposed to oxidative stress on a daily basis for a prolonged time (Geisser & Burckhardt, 2011). A number of other adverse events are also associated with oral iron therapy, largely due to

increased expression of hepcidin, often seen in CKD and the early stages of heart failure (Jankowska et al., 2013). Hepcidin regulates iron absorption in the duodenum through inhibition of ferroportin, limiting iron transport to the bone marrow as seen in anaemia of chronic disease (ACD) (Jankowska et al., 2013). Oral iron treatment is linked to a number of gastrointestinal side effects including constipation, heartburn and unwanted drug interactions (Handelman & Levin, 2008). Indeed, the number of gastrointestinal side effects were significantly higher in patients given oral iron than those receiving IV iron (Gill & Ferreira, 2013).

IV Iron is administered in the form of iron-carbohydrate complexes consisting of a mineral core surrounded by a carbohydrate shell (Danielson, 2004). The main function of the carbohydrate component is to stabilize the complex and reduce potential toxicity in plasma. Examples of IV iron compounds include iron sucrose, ferric carboxymaltose, iron dextran and ferumoxytol. Iron-carbohydrate complexes of this type are classed as prodrugs, as the iron has to be released from the carbohydrate component (Danielson, 2004). These compounds all work in a similar way and are taken up by the reticuloendothelial system and broken down by phagocytic cells. The liberated iron is then either stored as ferritin or released into blood as part of plasma transferrin (see Section 1.3).

The effectiveness of all iron preparations is determined by the drugs bioavailability (based on serum concentrations of the administered product), safety (number of adverse events) and metabolism (ability of metabolised iron to become incorporated in to haemoglobin), and has been investigated in numerous pharmacokinetic-based clinical trials (Geisser & Burckhardt, 2011). However, as the

overall aim of iron therapy is to correct anaemia, measuring haematocrit is usually sufficient to determine a drug's effectiveness in clinical practice.

Unlike oral iron therapy, IV iron treatment has proved consistently beneficial in numerous studies. Bolger et al. (2006) reported both an increase in exercise tolerance and haemoglobin levels in anaemic heart failure patients treated with IV iron therapy. In addition, clinical trials by Okonko et al. (2008), Anker et al. (2009) and Toblli et al. (2007) all reported similar outcomes. However, the benefits observed with iron therapy seem to be more than simply correcting the associated anaemia. Indeed, not all patients from the Okonko et al. (2008) trial were anaemic, or suffered from only mild anaemia. Furthermore, the Anker et al. (2009) study reported significant improvement in cardiac function without any significant changes in haemoglobin levels in a non-anaemic subgroup. The findings from these studies suggest mechanisms other than increased haemoglobin synthesis and peripheral oxygen delivery are involved in the functional improvements seen in non-anaemic heart failure patients, a mechanism potentially involving enhanced mitochondrial function. Indeed, Melenovsky et al. (2016) demonstrated a direct relationship between mitochondrial iron content and cardiac function.

3.1.4 Objectives

The sub-total nephrectomy model is a well characterised and robust method for mimicking progressive renal failure in humans (Raine et al., 1993). When used over a 12 week timeframe, this model has consistently demonstrated substantial renal dysfunction, including uraemia, anaemia and proteinuria, and significant cardiac hypertrophy (Taylor et al., 2015; Smith et al., 2010; Semple et al., 2012). Though this model is unlikely to lead to overt heart failure over this duration, previous studies have highlighted the presence of cardiac dysfunction including arrhythmias and an impaired functional recovery following ischemia (Semple et al., 2012 & Dikow et al., 2009). This degree of renal insufficiency therefore allows the study of cardiac alterations in uraemia prior to the onset of heart failure, mirrored in the clinical setting as patients with UCM who have cardiac hypertrophy and are at an increased risk of adverse cardiac events.

In order to study the effects of uraemia and iron therapy on cardiac mitochondrial function, the experimental model required characterisation in terms of systemic impact. The hypothesis here being that sub-total nephrectomy would result in substantial kidney dysfunction and cardiac hypertrophy, consistent with previous studies using this model over the same timeframe. In addition, it was hypothesised that the anaemia associated with renal dysfunction would be ameliorated by ferumoxytol treatment.

Therefore the aims of this chapter were to:

- Assess the extent of renal dysfunction through measurement of serum and urine markers following surgical induction of uraemia
- Determine the impact of uraemia 12 weeks post-surgery on cardiac hypertrophy, anaemia, skeletal muscle wasting and fluid content of the lungs
- Investigate the impact of IV iron therapy on markers of renal function and uraemia

3.2 Methods

3.2.1 *Experimental design*

Sham surgery or sub-total nephrectomy was induced in 80 male Sprague-Dawley rats as described in section 2.1. This gave rise to the following experimental groups:

- Control (n=25)
- Uraemic (n=25)
- Control + ferumoxytol treatment (n=15)
- Uraemic + ferumoxytol treatment (n=15)

Six weeks post surgery, the iron complex, ferumoxytol (Rienso, Takeda, Japan), was administered as a single IV bolus injection (10mg/kg), via the tail vein. Saline was administered as a control. Animals were sacrificed 6 weeks later, at 12 weeks post-surgery. Immediately following sacrifice, blood samples were collected and morphological characteristics measured as described below.

3.2.2 *Ferumoxytol Treatment*

The 10mg/kg dose was chosen in this study as this has been shown to be effective in ameliorating anaemia and replenishing body iron stores in patients with CKD (European Medicines Agency, 2012). While no preclinical studies have reported the effective dose of ferumoxytol in treating anaemia in rats, mammalian iron metabolism is highly conserved, indeed, serum iron concentrations and body iron

stores are similar in humans and rats (Ganz & Nemeth, 2012), as are the major proteins involved in iron homeostasis (Latunde-Dada, 2009). Therefore this dose was deemed suitable for these initial experiments. The 6 week time point for ferumoxytol administration was chosen as previous studies on the uraemic model have demonstrated the development of anaemia between 3-6 weeks post surgery (Smith, 2009).

3.2.3 Markers of Renal Function

Serum creatinine, urea and protein levels were determined as described in section 2.2.1 12 weeks post-surgery. Urinary creatinine and protein concentrations were assessed in 24 hour timed urine samples collected from animals housed in metabolic cages as described in section 2.2.1. Creatinine clearance, as an indicator of GFR, was calculated according to equation 1 in section 2.2.1.

3.2.4 Markers of Uraemia

3.2.4.1 Determination of LVH

The extent of LVH was assessed using heart weight and the HW:TL as described in section 2.2.2. Fluid content of the lungs, as a marker of pulmonary congestion, was determined as described in 2.2.2. Evidence of changes in body mass and skeletal muscle wasting were investigated as described in 2.2.3.

3.2.4.2 Anaemia

Haematocrit was determined using the PCV as described in section 2.2.1.

Serum iron, TIBC, ferritin and transferrin were investigated as described in 2.2.1.

3.3 Results

3.3.1 Markers of Renal Function

Serum creatinine and urea concentrations were significantly increased in uraemic animals at 12 weeks post-surgery highlighting impaired kidney function (Table 3.1). Serum protein was also reduced at this timepoint in the experimental group indicating profound proteinuria. Urinary creatinine excretion was reduced by 12 weeks, while urinary protein and urine volume output were significantly increased. Creatinine clearance, an indicator of GFR, was reduced by 60% in uraemic animals (Figure 3.1).

Ferumoxytol treatment had little impact on any of the serum markers in control or uraemic animals suggesting iron therapy had no effect on renal dysfunction (Table 3.1 & Figure 3.1). In addition, ferumxytol did not alter urinary protein excretion or urine volume output over 24 hours. However, ferumoxytol administration significantly increased serum protein levels in both groups.

Table 3.1*Markers of renal function*

	Untreated		Ferumoxytol	
	Control	Uraemic	Control	Uraemic
Serum creatinine (μ M)	43 \pm 3.3 (n=18)	73.7 \pm 3.3* (n=15)	47.3 \pm 3.5 (n=13)	80 \pm 4.2* (n=10)
Serum urea (mM)	6.6 \pm 0.4 (n=18)	12.5 \pm 1* (n=15)	7.2 \pm 0.9 (n=13)	14 \pm 1.2* (n=10)
Serum total protein (g/l)	6 \pm 0.1 (n=10)	5.2 \pm 0.1* (n=9)	6.7 \pm 0.3¥ (n=5)	5.8 \pm 0.2*¥ (n=5)
Urine creatinine (mM)	17.2 \pm 2.1 (n=9)	8.7 \pm 1.1* (n=8)	18.4 \pm 2.3 (n=5)	8.7 \pm 0.7* (n=5)
Urine protein (g/dl)	1.43 \pm 0.18 (n=9)	2.89 \pm 0.33* (n=8)	1.37 \pm 0.11 (n=5)	3 \pm 0.33* (n=5)
Urine volume (ml)	16.3 \pm 2.1 (n=9)	23.2 \pm 3* (n=8)	16.4 \pm 2.4 (n=5)	21.6 \pm 3.2* (n=5)

Data are presented as mean \pm SEM. Urine samples collected over 24-hours. * = p < 0.05 vs control, ¥ = p < 0.05 vs untreated group, *¥ = p < 0.05 vs control and untreated group

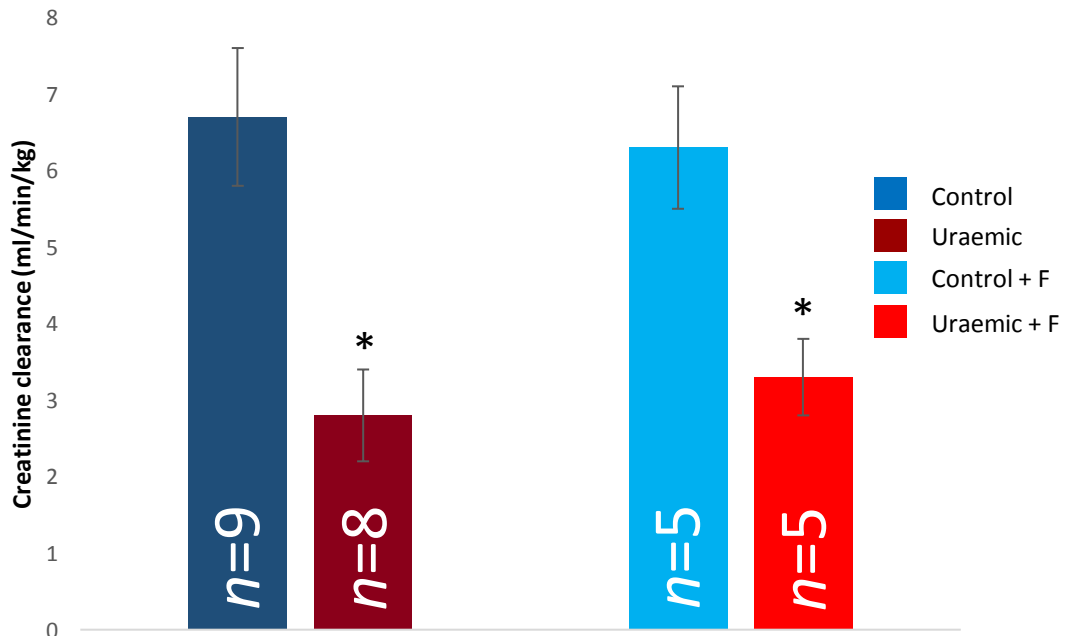


Figure 3.1. Creatinine clearance at 12 weeks. Urine samples collected over 24-hours. Data are presented as mean \pm SEM. * = p < 0.05 vs control. F = ferumoxytol

During the surgical procedure approximately 2/3 of left kidney mass was removed. However, by 12 weeks post-surgery remnant kidneys weights in uraemic animals were significantly greater than controls (Figure 3.2 & Table 3.2). Although the increase in mass may primarily be due to renal hypertrophy, haemostatic material was used during nephrectomy to stem excessive bleeding. This material was not removed post-surgery and might contribute to the increase in weight observed. Ferumoxytol did not affect kidney weights in either group (Table 3.2).

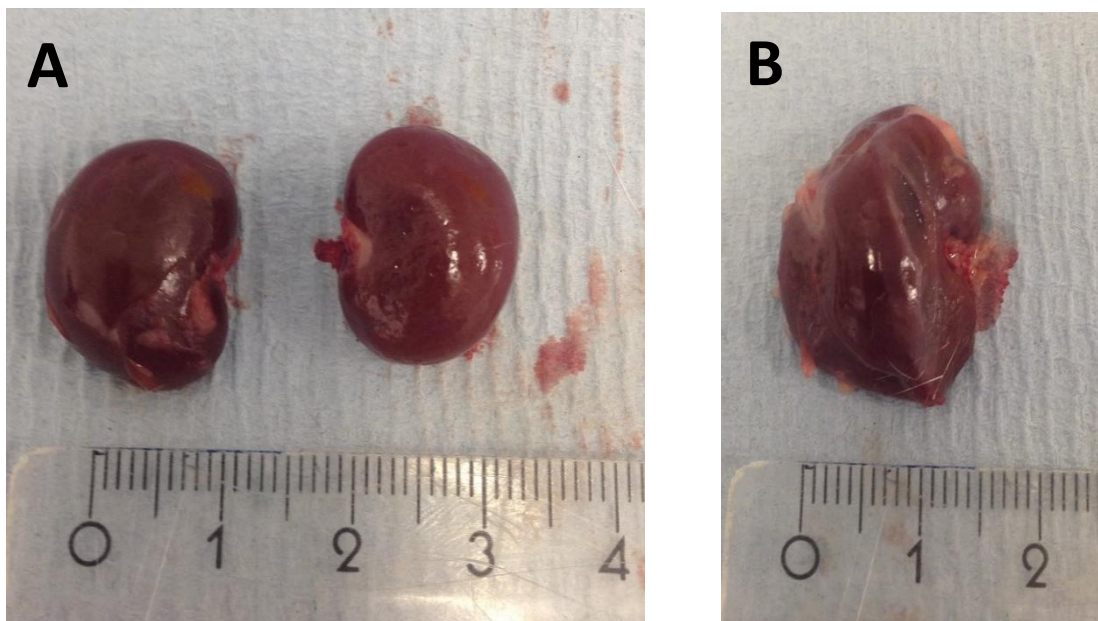


Figure 3.2. Comparison of control and remnant kidneys. (A) Kidneys taken from a control animal and (B) a left remnant kidney taken from a uraemic animal

Table 3.2*Kidney weights*

	Untreated		Ferumoxytol	
	Control	Uraemic	Control	Uraemic
Right kidney (g)	1.56 ± 0.03 (n=22)	–	1.53 ± 0.04 (n=11)	–
Left kidney (g)	1.6 ± 0.04 (n=22)	2.03 ± 0.06*	1.54 ± 0.04 (n=11)	1.97 ± 0.1*

Data are presented as mean ± SEM. * = p<0.05 vs control

3.3.2 Markers of Uraemia**3.3.2.1 Left Ventricular Hypertrophy**

Heart weight and the heart weight-to-tibia length ratio were increased by 12% and 11% respectively in uraemic animals indicating cardiac hypertrophy (Table 3.3 & Figure 3.3). Lung tissue water content did not differ between groups giving no evidence of pulmonary congestion in uraemic animals. In addition, no differences in bodyweight or skeletal muscle mass were observed despite induction of uraemia (Table 3.4). Collectively these data gave no indication of heart failure, suggesting the cardiac hypertrophy was compensatory in nature. Ferumoxytol treatment had no effect on the development of cardiac hypertrophy in uraemia (Table 3.3 & Figure 3.3).

Table 3.3*Indices of cardiac hypertrophy*

	Untreated		Ferumoxytol	
	Control	Uraemic	Control	Uraemic
Heart weight (g)	1.50 ± 0.06 (n=22)	1.69 ± 0.03*	1.45 ± 0.03 (n=13)	1.65 ± 0.05*
Tibia length (mm)	44.9 ± 0.33 (n=22)	45.7 ± 0.27 (n=19)	44.3 ± 0.32 (n=13)	44.9 ± 0.38 (n=10)
Lung water content (%)	65.0 ± 6.4 (n=9)	66.0 ± 6.2 (n=8)	67 ± 6.2 (n=5)	65.4 ± 4.3 (n=5)

Data are presented as mean ± SEM. *= p<0.05 vs control

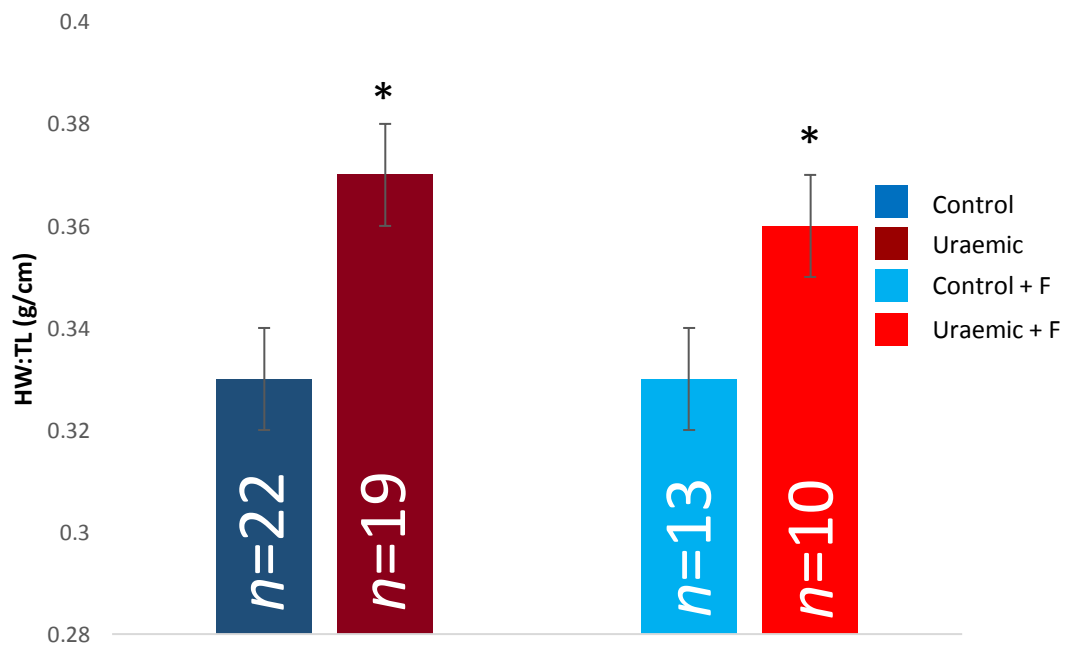


Figure 3.3. Heart weight-to-tibia length ratio (HW:TL) at 12 weeks. Data are presented as mean ± SEM. * = p < 0.05. F = ferumoxytol

Table 3.4*Indices of body mass*

	Untreated		Ferumoxytol	
	Control	Uraemic	Control	Uraemic
Bodyweight (g)	552.1 ± 8.5 (n=22)	572.8 ± 8.8 (n=19)	538.3 ± 15.2 (n=13)	559.3 ± 14.4 (n=10)
Triceps surae (g)	3.1 ± 0.08 (n=9)	3.26 ± 0.12 (n=8)	3.06 ± 0.10 (n=5)	3.17 ± 0.17 (n=5)
Triceps surae: body weight (x10 ⁻²) (g/g)	0.57 ± 0.01 (n=9)	0.56 ± 0.01 (n=8)	0.58 ± 0.01 (n=5)	0.57 ± 0.02 (n=5)
Triceps surae: tibia length (g/cm)	0.69 ± 0.01 (n=9)	0.72 ± 0.02 (n=8)	0.7 ± 0.02 (n=5)	0.71 ± 0.02 (n=5)

Data are presented as mean ± SEM.

3.3.2.2 Anaemia

Induction of uraemia resulted in a significant reduction in PCV, an indicator of haematocrit, 12 weeks post-surgery highlighting the development of anaemia in contrast to controls (Figure 3.4). This was paralleled by a decrease in serum iron, transferrin and total iron binding capacity, whilst ferritin concentrations remained unaltered (Table 3.5).

Ferumoxytol treatment did not significantly modify PCV in uraemic animals (Figure 3.4), but surprisingly caused a marked reduction in serum iron concentrations in both groups (Table 3.5). Ferumoxytol treatment also caused a significant increase in total iron binding capacity and transferrin, consistent with the decrease in serum iron. Ferritin levels remained unchanged in both groups irrespective of ferumoxytol therapy.

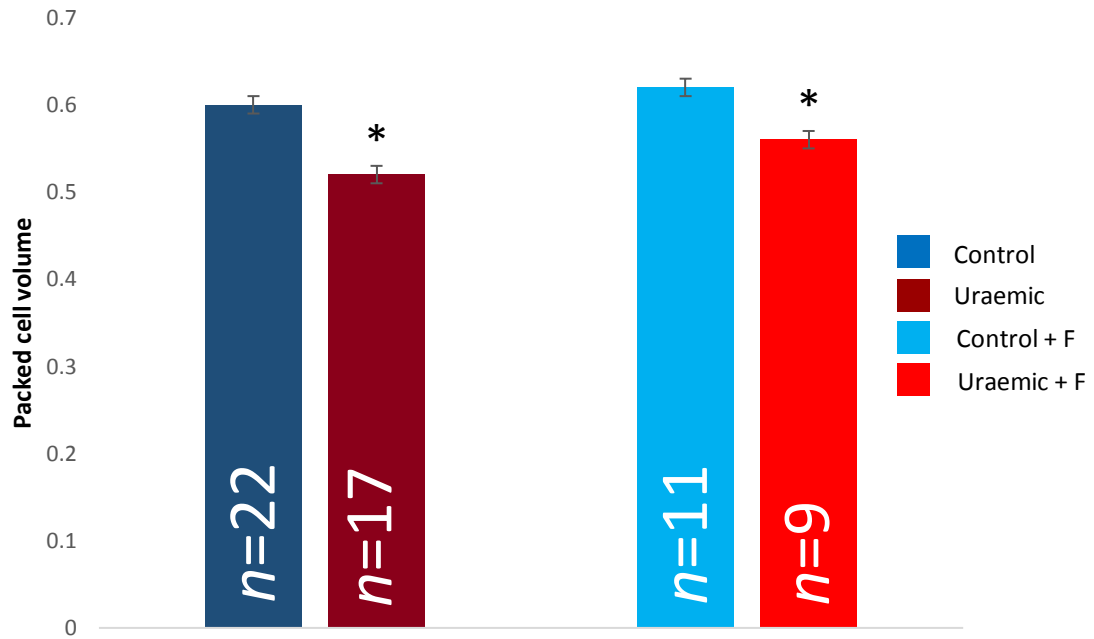


Figure 3.4. Packed cell volume as an indicator of haematocrit. Data are presented as mean \pm SEM. * = $p < 0.05$ vs control. F = ferumoxytol

Table 3.5

Markers of iron homeostasis

	Untreated		Ferumoxytol	
	Control	Uraemic	Control	Uraemic
Serum iron (μ M)	46.4 \pm 1.4 (n=11)	32.8 \pm 1* (n=11)	31.1 \pm 1.8¥ (n=9)	28.9 \pm 1.7¥ (n=9)
Ferritin (ng/ml)	58.7 \pm 8.2 (n=8)	62.7 \pm 6.8 (n=8)	58.2 \pm 3.4 (n=8)	50.8 \pm 8.3 (n=8)
Transferrin (μ M)	1.41 \pm 0.02 (n=24)	1.3 \pm 0.01* (n=22)	1.4 \pm 0.03 (n=10)	1.41 \pm 0.01¥ (n=10)
TIBC (μ M)	29.5 \pm 0.8 (n=24)	26.4 \pm 0.7* (n=22)	33.6 \pm 1.2¥ (n=10)	29.1 \pm 0.8*¥ (n=10)

Data are presented as mean \pm SEM. * = $p < 0.05$ vs control, ¥ = $p < 0.05$ vs untreated group, *¥ = $p < 0.05$ vs control and untreated group

3.4 Discussion

Subtotal nephrectomy resulted in substantial impairment of renal function as evidenced by elevated serum creatinine and urea, a decreased creatinine clearance and proteinuria. There was also significant cardiac hypertrophy and anaemia in uraemic animals by 12 weeks post-surgery, but no evidence of pulmonary oedema or muscle wasting suggesting cardiac hypertrophy was compensatory in nature. Ferumoxytol treatment did not affect the progression of renal dysfunction or ameliorate the associated anaemia.

3.4.1 *Markers of Renal Function*

Surgical induction of uraemia resulted in profound kidney dysfunction by 12 weeks (Table 3.1 & Figure 3.1). The elevated serum creatinine and urea levels were consistent with previous studies (Askentijevic et al., 2009; Smith et al., 2010 & Dikow et al., 2004). Serum creatinine is also influenced by lean body and muscle mass (Swaminathan et al., 2000), however, morphological characteristics indicated both control and uraemic animals had similar body weights and skeletal muscle mass. Thus, the change in serum creatinine here can be attributed to renal dysfunction. Urine analysis revealed creatinine excretion in uraemic animals was approximately 50% that of controls. This has been reported in other models of nephrectomy (Braunlich et al., 1997 & Dubrelle et al., 1992) and would be anticipated given that uraemia stems from a progressive decline in renal function which includes impaired clearance of uraemic toxins and metabolites (Braunlich et al., 1997).

Urine volume output was increased by 42% in uraemic animals by week 12 (Table 3.1). The formation and excretion of urine depends on several factors including GFR and tubular reabsorption. The increase here may reflect osmotic diuresis due to elevated creatinine and urea concentrations in the blood coupled with a reduced number of functioning nephrons (Feinfeld & Danavitch, 1987). Furthermore, impaired kidney function limits the reabsorption of fluid from the urine. This leads to a reduced ability to concentrate urine, potentially leading to an increase in urine volume output as observed here (Buerkert et al., 1979).

Creatinine clearance, an indicator of GFR, was diminished by approximately 60% in the uraemic group (Figure 3.1), comparable to findings of Dubrulle et al. (1992) who used a similar subtotal nephrectomy model and observed a 56% decrease in creatinine clearance. Chamberlain & Shirley (2007) investigated the impact of uninephrectomy and 5/6 nephrectomy on GFR in rats over a 32 day period immediately following surgery. Two days post-nephrectomy, GFR in uninephrectomised rats was reduced by 43%, consistent with the loss of one kidney. However, by day 8 GFR in these animals was reduced by only 23% highlighting a compensatory response. Similar findings were observed in the 5/6 nephrectomised rats where GFR was reduced by 77% 2 days post-surgery and 64% after 2 weeks. However, this compensatory response from the remaining nephrons was insufficient to restore normal renal function (Chamberlain & Shirley, 2007).

Serum protein was significantly reduced in uraemic animals (Table 3.1), linked to a substantial increase in urinary protein. Proteinuria is a frequent finding in the present model and losses can reach 200-600mg/24h as early as two weeks post-

surgery in nephrectomised rats (Yang et al., 2010). Reduced serum protein levels can also be a consequence of muscle wasting associated with CKD. However, as both groups had similar body mass and skeletal muscle mass, it is unlikely significant muscle wasting was present at this stage.

Despite a 2/3 reduction in left kidney mass, remnant kidney weights were significantly greater than controls indicating substantial hypertrophy (Figure 3.2 & Table 3.2). Previous studies have highlighted that renal hypertrophy was an early event, occurring 0-4 weeks following nephrectomy (Smith, 2009 & Ma et al., 2005). Compensatory hypertrophy of the remnant kidney is a frequent finding in rodent models of CKD (Reddy et al., 2007). However, studies employing a 50% reduction in renal mass have demonstrated that uninephrectomy results in only mild or no kidney dysfunction (Chamberlain & Shirley, 2007 & Santos et al., 2006). Therefore the elevated levels of creatinine and urea in the serum observed here indicate the remnant kidney is substantially dysfunctional.

Serum creatinine, urea and creatinine clearance values were similar in ferumoxytol treated and untreated uraemic animals suggesting iron therapy had little effect on the progression of renal failure (Table 3.1 & Figure 3.1). This is consistent with previous experimental studies using erythropoietin (Smith, 2009) and also clinical observations (Lim et al., 1990). However, iron therapy caused a significant increase in serum protein in both groups. Previous studies have highlighted IV iron therapy may stimulate an inflammatory response including increased circulating cytokines, immunoglobulins and other serum proteins (Agarwal,

2006 & Cancado & Munoz, 2011). However, it is difficult to draw conclusions from the present data as analysis of individual serum proteins were not performed.

3.4.2 Markers of Uraemia

3.4.2.1 Left Ventricular Hypertrophy

Induction of uraemia resulted in cardiac hypertrophy as evidenced by significant increases in heart weight and the HW:TL (Table 3.3 & Figure 3.3). Ferumoxytol did not affect the extent of cardiac hypertrophy in uraemic animals (Table 3.3 & Figure 3.3). Other models of LVH have used the heart weight-to-bodyweight ratio (HW:BW) as an indication of the extent of hypertrophy (Gao et al., 2009). However, as changes in body mass and lean muscle mass can occur secondary to uraemia, the HW:BW may be an unreliable marker of LVH in CKD. Thus the HW:TL provided a better indication of the extent of hypertrophy.

The findings presented here are similar to those previously reported using the 5/6 nephrectomy model (Reddy et al., 2007 & Smith et al., 2010). However, Hsueh et al. (2014) observed a more profound 40% increase in left ventricular mass in an autosomal dominant model of polycystic kidney disease. These animals spontaneously developed characteristics of CKD including a reduced GFR, hypertension, and cardiac hypertrophy by 10 weeks, ultimately experiencing terminal uraemia by 40 weeks. Interestingly, this study also highlighted altered electrophysiology including an increased susceptibility to arrhythmias. This is similar to previous work *in vitro* on the uraemic heart which demonstrated significantly

impaired cardiac function following ischemia reperfusion injury (IRI) and may contribute to the increased incidence of adverse cardiac events in CKD (Semple et al., 2012 & Dikow et al., 2009).

The development of LVH during CKD is multifactorial and incompletely understood. However, haemodynamic, metabolic and endocrine factors are all thought to be involved (Siedlecki et al., 2009; Semple et al., 2012 & Levin, 2002). Furthermore, due to the complex aetiology of CRS, the pattern of hypertrophic remodelling includes both concentric and eccentric hypertrophy (Foley et al., 1995). This is paralleled at the cellular level where increases in cell length (6.7%) and width (14.3%) of individual cardiomyocytes in uraemia have been observed as early as 3 weeks post-surgery (Reddy et al., 2007). Dimensions are further increased at 12 weeks (10.5% length vs. 18.5% width) reflecting a progressive increase in myocyte hypertrophy over study duration (Taylor et al., 2015).

There was no evidence of fluid on the lungs in uraemic animals highlighting the absence of pulmonary oedema. Alveoli are highly impermeable and any trapped fluid or protein is quickly removed via reabsorption into the interstitium by the alveolar epithelial cells (Hanley & Welsh, 2004). However, acute lung injury or an increase in left atrial filling pressure can cause an increase in pulmonary capillary pressure. This in turn forces fluid into the lung interstitium and alveoli, manifesting as pulmonary oedema (Headley & Wall, 2007). An increase in fluid accumulation on the lungs is characteristic of the failing heart and not a heart in the compensatory phase of hypertrophy. Therefore it is unsurprising that pulmonary oedema was absent in this model.

No changes in body weight or lean muscle mass were observed in uraemic animals compared to their respective controls by week 12 (Table 3.4). Furthermore, administration of ferumoxytol did not affect body mass in either group (Table 3.4). Weight loss and cachexia have been reported late in the progression of CKD and are considered important indicators of mortality and morbidity (Bergstrom & Lindholm, 1998). In the present study the triceps surae (gastrocnemius and soleus) muscle was weighed as an indicator of lean muscle mass. However, no differences were observed between control and uraemic animals at this stage highlighting the absence of heart failure and cachexia.

3.4.2.2 Anaemia

Uraemia caused a significant reduction in PCV by 12 weeks (Figure 3.4). This was accompanied with a decrease in serum iron, transferrin and total iron binding capacity, while levels of ferritin remained unchanged compared to controls (Table 3.5). This combination of serum markers of iron homeostasis is indicative of anaemia of chronic disease (ACD) which is initially triggered by a lack of erythropoietin production, due to the substantial reduction in renal mass in the present model (Peng & Uprichard, 2016). However, as CKD progresses ACD is driven by a profound inflammatory response facilitated by interleukin-6 and TNF α which are strong inducers of hepcidin production (Nemeth et al., 2003). Increased hepcidin expression results in reduced iron export through ferroportin and the consequent accumulation of iron in macrophages, hepatocytes and enterocytes (Nemeth et al., 2004).

Patients with CKD may suffer increased iron loss through uraemia-induced platelet dysfunction, occult bleeding and impaired dietary absorption (Peng & Uprichard, 2016). In addition, some blood loss can occur during the surgical procedure despite the use of haemostatic material to minimise losses. Vitamin D deficiency and a reduced erythrocyte life span may also further exacerbate ACD in CKD. (Nurko, 2006). The onset of anaemia following nephrectomy occurs as early as 3 weeks post-surgery and is maintained throughout duration of study (Smith et al., 2010).

Ferumoxytol treatment did not modify PCV in uraemic animals (Figure 3.4). In contrast to these results, previous studies have shown that administration of erythropoietin resulted in significantly increased haematocrit to levels comparable with controls (Smith, 2009). Erythropoietin stimulates red blood cell production and inhibits apoptosis of erythrocyte precursors, increasing the number of circulating erythrocytes (Fisher, 2003). The disparities between studies suggest that the dosing regimen or iron therapy alone may be insufficient to stimulate erythropoiesis in uraemia.

3.4.3 Conclusions

5/6 nephrectomy resulted in significant renal dysfunction by 12 weeks. This was characterised by uraemia, cardiac hypertrophy and anaemia, consistent with previous studies. The absence of cachexia and fluid accumulation on the lungs at this stage suggest cardiac hypertrophy was compensatory in nature. Administration of

ferumoxytol did not impact on the progression of renal dysfunction or ameliorate the associated anaemia. Collectively these data establish the present model as a valuable tool for investigating disease mechanisms and exploring potential therapeutic interventions.

4. *In Vivo* Cardiac Glucose

Metabolism

4.1 Introduction

Cardiac hypertrophy, a major risk factor for heart failure, is a common cardiac adaptation in CKD patients (Foley et al., 1995). Although initially beneficial, cardiac hypertrophy can become a maladaptive response which may lead to a progressive decline in cardiac function and ultimately failure (Drazner, 2011). The transition from hypertrophy to failure is characterised by a number of structural and metabolic changes (Shimizu & Minamino, 2016). One such adaptation is a switch in substrate preference from fatty acids to an enhanced reliance on glucose metabolism (Drazner, 2011). Although a number of experimental models have identified these alterations *ex vivo* in the uraemic heart (Aksentijevic, 2008 & Smith et al., 2010), cardiac glucose metabolism has yet to be studied in UCM *in vivo*. PET is a powerful nuclear imaging technique which provides a unique opportunity to investigate metabolic remodelling *in vivo* during disease progression.

4.1.1 Metabolic Remodelling

Experimental models of pressure (Akki et al., 2008) and volume-overload (el Alaoui-Talibi et al., 1992) cardiac hypertrophy have shown significant remodelling of cardiac metabolism, characterised by re-expression of the foetal phenotype and downregulation of the adult phenotype (Stanley et al., 2005). The foetal myocardium is dependent primarily on glucose and lactate for energy generation, switching to reliance on fatty acids within hours of birth (Lopaschuk et al., 1992). The shift in substrate preference in hypertrophied hearts is accompanied by altered expression

of transcription factors, including elements of the PPAR α -RXR-PGC-1 α transcriptional complex, leading to the downregulation of specific genes encoding fatty acid oxidation enzymes (Lehman & Kelly, 2002). Indeed, Barger et al. (2000) demonstrated that PPAR α expression is reduced during the progression of hypertrophy in rat neonatal cardiomyocytes, resulting in the diminished activities of enzymes such as carnitine palmitoyltransferase and MCAD. Similarly reduced enzyme activities have been associated with depressed fatty acid metabolism in human failing hearts (Sack et al., 1996) and rodent models of heart failure (Sack & Kelly, 1998). In addition, Garnier et al. (2003) observed a decrease in PGC-1 α expression in a rat model of aortic constriction-induced chronic heart failure. The down-regulation of PGC-1 α was associated with reduced mitochondrial enzyme activities, including citrate synthase and respiratory complex IV, and a reduced oxidative capacity.

Increased glucose oxidation may initially represent a beneficial response as ATP generated from glucose is more oxygen efficient than from fatty acids, potentially sustaining function during cardiac hypertrophy (Taegtmeyer, 1986). However, in the longer term, increased glucose metabolism may be insufficient to meet the energetic needs of the myocardium and ATP depletion gradually ensues, contributing to the transition from compensated hypertrophy to failure (Ingwall, 2009). As cardiac function further deteriorates in the failing heart, glucose utilisation diminishes and the capacity of the myocardium for substrate oxidation is exhausted (Neubauer, 2007).

4.1.2 Metabolic Remodelling in UCM

Cardiac hypertrophy is a frequent finding in experimental models of CKD and the clinical setting, hence it is likely metabolic remodelling also occurs in the uraemic heart. Indeed, experimental models of CKD have revealed a reduction in the myocardial phosphocreatine/ATP ratio, indicating that the uraemic myocardium is starved of its energy reserves (Raine et al., 1993). In addition, reduced fatty acid oxidation, carnitine palmitoyltransferase activity and mitochondrial oxygen consumption have all been reported in nephrectomised rats (Smogorzewski et al., 1988). Smith et al. (2010) used a similar model of uraemia and reported decreased palmitate oxidation at 12 weeks post-surgery associated with reduced expression of the fatty acid transporter CD36. Furthermore, 5/6 nephrectomy has also resulted in decreased myocardial expression of PPAR α (Mori et al., 2007). Collectively these *ex vivo* studies indicate that the uraemic heart undergoes significant remodelling of cardiac metabolism, however, the relevance of such studies has yet to be established *in vivo*.

4.1.3 ¹⁸F-FDG PET

PET is a unique *in vivo* imaging modality which can be used clinically and experimentally to evaluate metabolic substrate shifts in states of chronic stress, such as cardiac hypertrophy (Ghosh et al., 2010). The basis of PET is to quantify the activity concentration of radiotracers in tissues of interest such as the myocardium (Taegtmeyer, 2010). Positron emitting radiotracers, such as the glucose analogue ¹⁸F-

FDG, are biologically active molecules, similar to naturally occurring compounds, but with the incorporation of radioisotopes.

Immediately following uptake into the cell, glucose is rapidly phosphorylated by hexokinase into glucose-6-phosphate which is then further metabolised in pathways such as glycogenesis and glycolysis. The glucose analogue, 2-deoxy-D-glucose (2DG) has a hydroxyl group in place of a hydrogen group at the C2 position. Although 2DG can be phosphorylated by hexokinase into 2DG-6-phosphate, it cannot be further metabolised and thus becomes trapped within the cytosol (Slart et al., 2005). Tagging 2DG with a positron emitting ^{18}F atom produces ^{18}F -FDG and as both glucose and ^{18}F -FDG have similar structures they are phosphorylated by hexokinase at similar rates (Sheikine & Akram, 2010). Therefore the uptake and subsequent trapping of ^{18}F -FDG can give an indication of glucose metabolism in organs such as the myocardium (Taegtmeyer, 2010).

4.1.4 Principle of PET

PET image acquisition begins with a bolus intravenous injection of the radiotracer. During the subsequent uptake period, the radiotracer accumulates in metabolically active tissues (Pazhenkottil et al., 2011). As the radioactivity of the tracer decays, it emits a positron, which travels a short distance before colliding with an electron, causing the annihilation of both particles (Ghosh et al., 2010). The energy emitted is in the form of two 511 keV gamma photons travelling approximately 180° from each other, creating a line in space known as a line of response (Figure 4.1) (Le

Meunier et al., 2010). The photons are detected by scintillator detectors in the PET scanner, creating a burst of light which in turn is picked up by photomultiplier tubes (Ghosh et al., 2010). Photons that reach the detectors as temporal pairs are recorded by the PET scanner as a coincidence event. Each coincidence event is binned into a sinogram, based on the radial and angular offsets of each line of response, which is reconstructed to form a tomographic image (Shukla & Kumar, 2006).

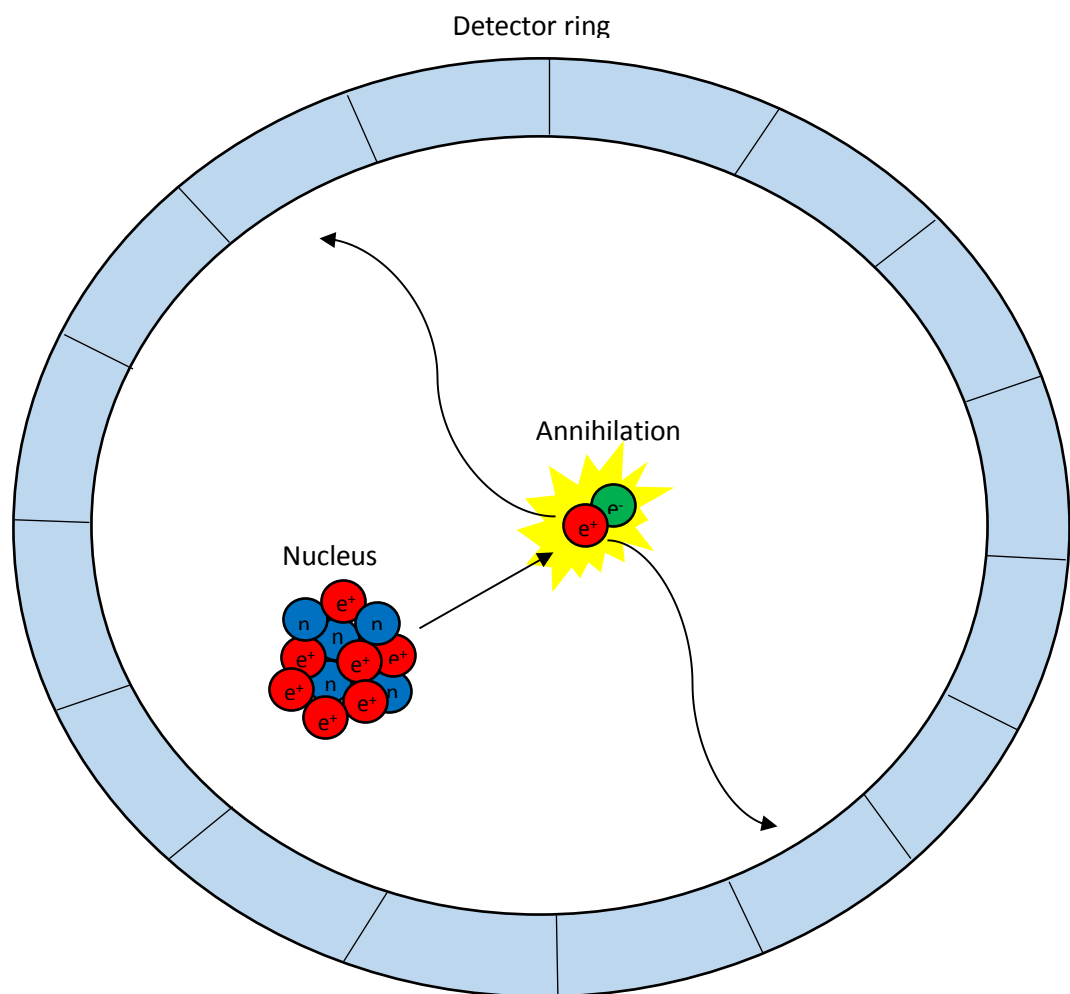


Figure 4.1. The principle of PET. A positron escapes the unstable nucleus during radioactive decay and travels a short distance before losing kinetic energy and decelerating. As the positron slows it collides with an electron, causing the annihilation of both particles. The energy emitted is in the form of two 511 keV gamma photons travelling approximately 180° from each other. Photons from the coincidence event that arrive as temporal pairs at the detectors are recorded by the PET scanner.

4.1.5 Objectives

Previous studies have highlighted evidence of metabolic remodelling in the uraemic heart, characterised by a shift in substrate preference from fatty acids to glucose oxidation. However, the relevance of such *ex vivo* studies has yet to be determined *in vivo* and during disease progression. Hence the aim of the work described in this chapter was to:

- Determine *in vivo* ^{18}F -FDG kinetics and standardised uptake values (SUVs) in the hearts of uraemic rats
- Investigate the rate and distribution of ^{18}F -FDG uptake in the heart over disease progression in a longitudinal study of UCM
- Develop an isolated rat heart perfusion system, compatible with a small animal PET scanner, for studies of radiotracer kinetics in the *ex vivo* myocardium

4.2 Methods

4.2.1 Experimental design

Sham surgery or sub-total nephrectomy was induced in 30 male Sprague-Dawley rats as described in section 2.1. This gave rise to the following experimental groups:

- Control (n=15)
- Uraemic (n=15)

Co-registered PET/CT scans were acquired at 5, 9 and 13 weeks post-surgery. Acquisitions deemed successful, confirmed by true injection of radiotracer, were used for subsequent analysis. Serum samples were collected immediately after each scan for metabolite analysis and animals were allowed to recover. Following a washout period of at least 2 days after the final set of scans at week 13, animals were sacrificed and hearts perfused as described below.

4.2.2 *In Vivo* Scanning Protocol

In vivo imaging was performed using a SuperArgus 2R preclinical PET/CT scanner (Sedecal, Spain), as described by Hernandez et al (2013) with modification. Animals were transferred to the imaging suite 24 hours prior to scanning and maintained under a 12:12 hour light:dark cycle. Animals were anaesthetised as described in section 2.1 and the tail vein cannulated. Rats were then placed in a small animal imaging bed (Minerve, Esternay, France) and positioned on a respiration pad

and temperature probe using a bite bar (Figure 4.2). ECG electrodes were attached to the front and left rear paws to monitor ECG throughout the experiment (Small Animal Monitoring and Gating System hardware, Model 1025T, SA Instruments Inc, New York, USA) (Figure 4.3). A CT scout view was used to centre the heart in the field of view (Figure 4.4) and approximately 40MBq ^{18}F -FDG (equivalent to less than a femtomolar of glucose) injected via the tail vein. Image acquisition was initiated at the time of injection and dynamic data acquired in list mode over 90 minutes. After the PET acquisition, a separate CT scan was acquired via 360 projections/8 shots with an x-ray tube operated at a voltage of 45kV and current of 140 μA .

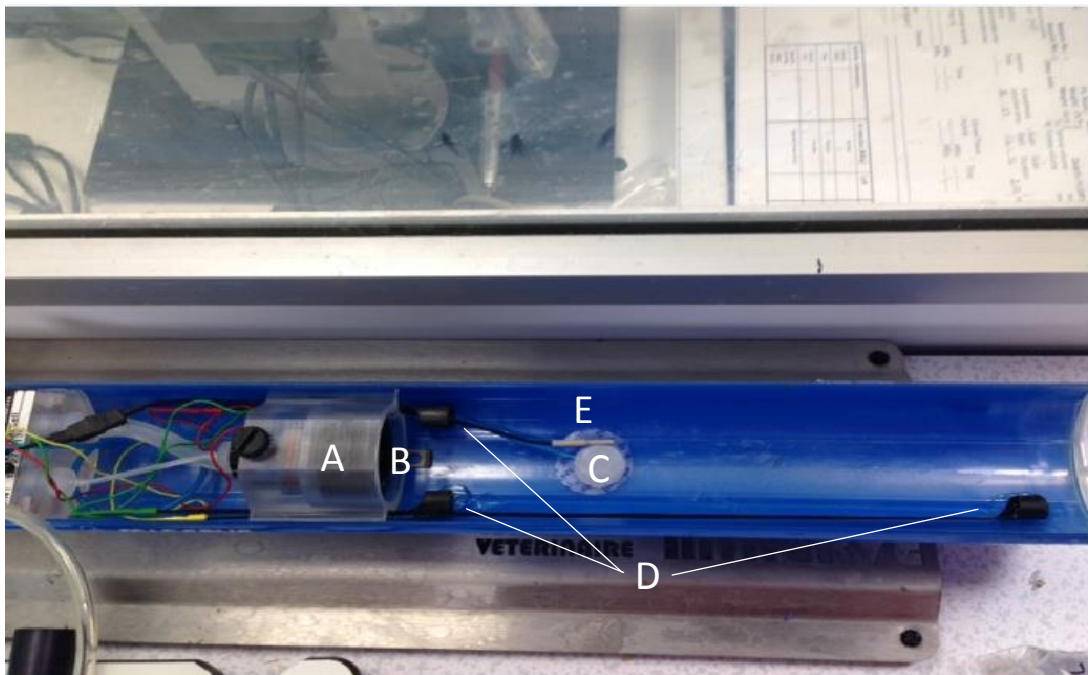


Figure 4.2. *In vivo* imaging bed setup. Isoflurane is continuously delivered via (A) the nose cone during imaging. The rat was placed in the animal bed and positioned on (B) the bite bar and (C) respiration pad. The front and left rear paws were attached to (D) ECG electrodes for physiological monitoring. (E) A temperature probe was placed under the animal to measure body temperature.

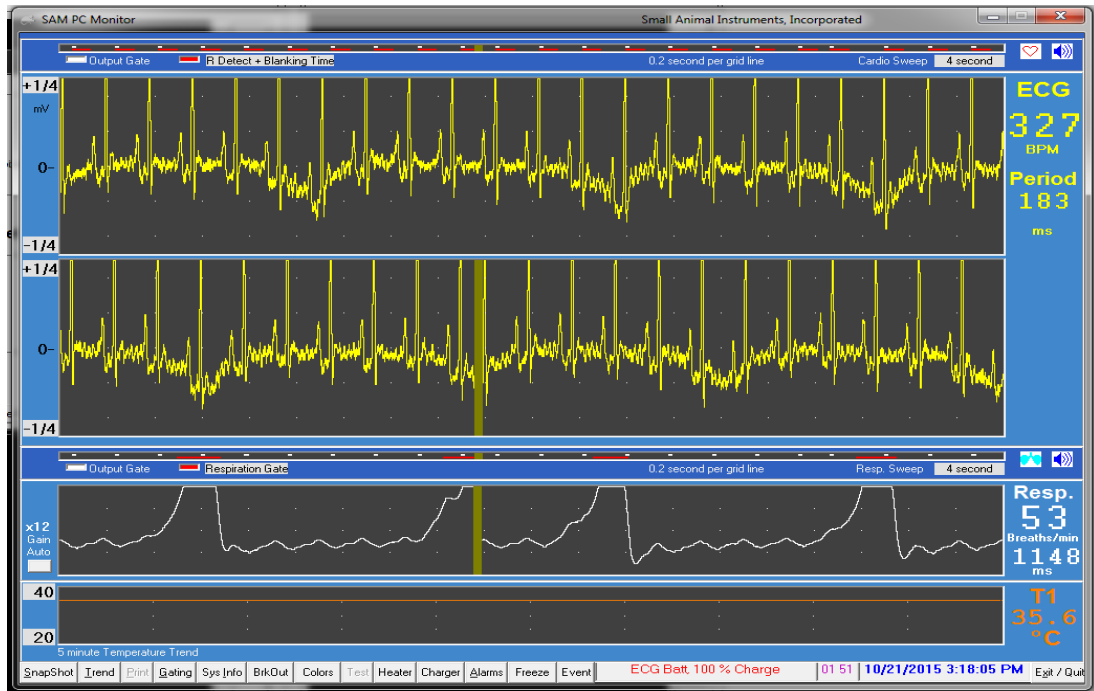


Figure 4.3. Example of continuous recording of ECG, respiration rate and body temperature throughout imaging.

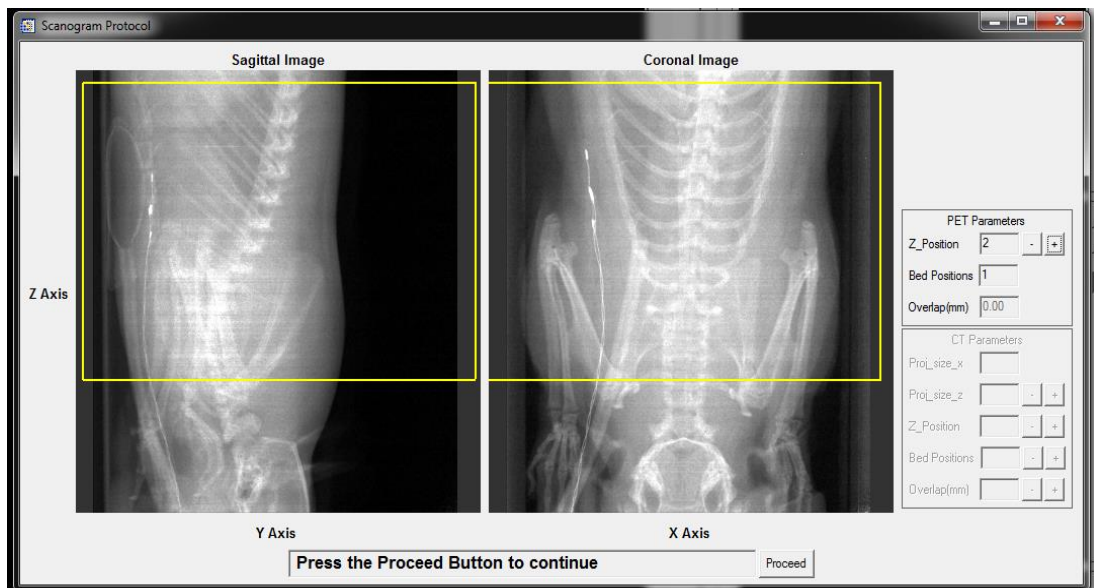


Figure 4.4. A CT scout view was used to centre the heart in the field of view.

4.2.3 Image Reconstruction

List mode PET data were reconstructed into 20 timeframes of 5 x 60s, 5 x 120s, 5 x 300s and 5 x 600s (using MMWKS software, Sedecal, Spain). The 3D ordered-subsets expectation maximization (3D OSEM) algorithm was used to reconstruct the data resulting in a matrix size of 175 x 175 x 61 with a corresponding voxel size of 0.3875 x 0.3875 x 0.775 mm. CT images were reconstructed using the Feldkamp reconstruction algorithm resulting in a matrix size of 516 x 516 x 372 and a voxel size of 0.121768 x 0.121768 x 0.121768 mm. Reconstructed PET data were subjected to random and scatter correction. Attenuation correction was achieved using the co-registered CT based attenuation map.

4.2.4 Image Analysis

4.2.4.1 Standardised Uptake Values

Time activity curves (TACs) and SUVs were calculated using Amide software (Version1.0.4; Loening & Gambhir, 2003) and equation 2 shown below (Zincirkeser et al., 2007). Regions of interest (ROI) were drawn around the left ventricle using the 3D isocontour drawing tool (Figure 4.5A). Left ventricular, aortic and vena cava derived blood SUVs were generated by manually drawing a small ROI (1-2 mm³) in the centre of each blood pool (Figure 4.5A, C & D). SUVs were calculated using the final 5 minute frame of the dataset.

$$SUV = \frac{C_{ROI}}{ID (MBq)/BW (kg)}$$

Equation 2. Standardised uptake value calculation where C_{ROI} is the concentration of activity in the region of interest, ID is the injected dose and BW is body weight. SUVs were calculated using the final 5 minute frame of the dataset.

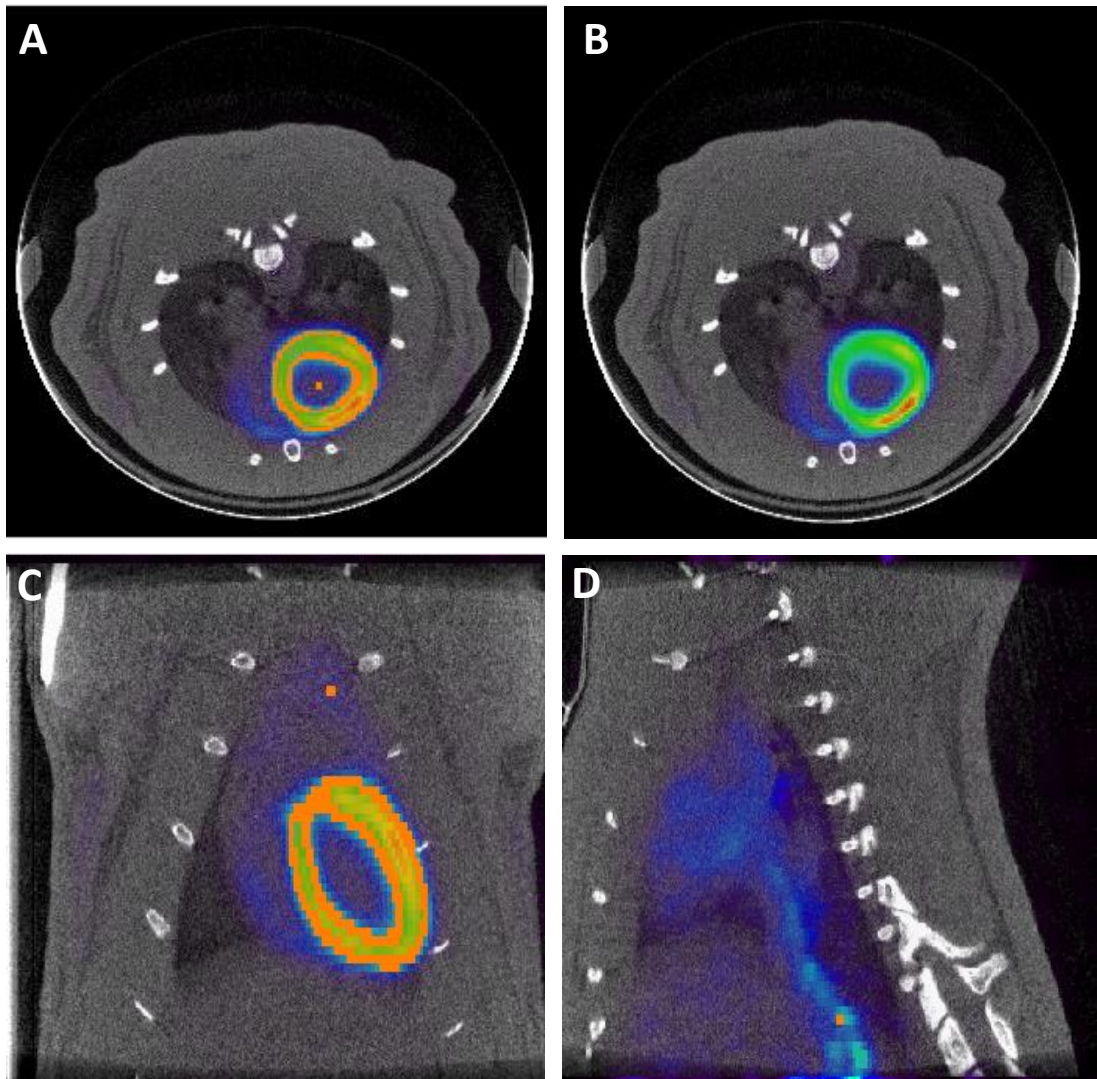


Figure 4.5. Co-registered PET/CT images highlighting analysed regions of interest (ROI). Transverse view of the myocardium (A) with and (B) without an ROI around the left ventricle and left ventricular blood pool. (C) Coronal and (D) sagittal views highlighting aortic and vena cava blood pool ROIs respectively.

4.2.4.2 Rate and Distribution of Cardiac ^{18}F -FDG Uptake

Myocardial influx rate constants for ^{18}F -FDG (K_i^{FDG}) were determined using Patlak multiple-time graphical analysis as described previously (Hernandez et al., 2013) using FlowQuant software (University of Ottawa Heart Institute, Ottawa, Canada). The myocardium was located using a summed image of the last 5 frames (Figure 4.6) and K_i^{FDG} calculated using the left ventricular blood pool as an image derived blood input function. Polar map analysis was used to determine regional differences in the rate of ^{18}F -FDG uptake by segmenting the myocardium into 9 distinct regions (4 proximal and 4 distal regions and the apex) (Klien et al., 2006) (Figure 4.7).

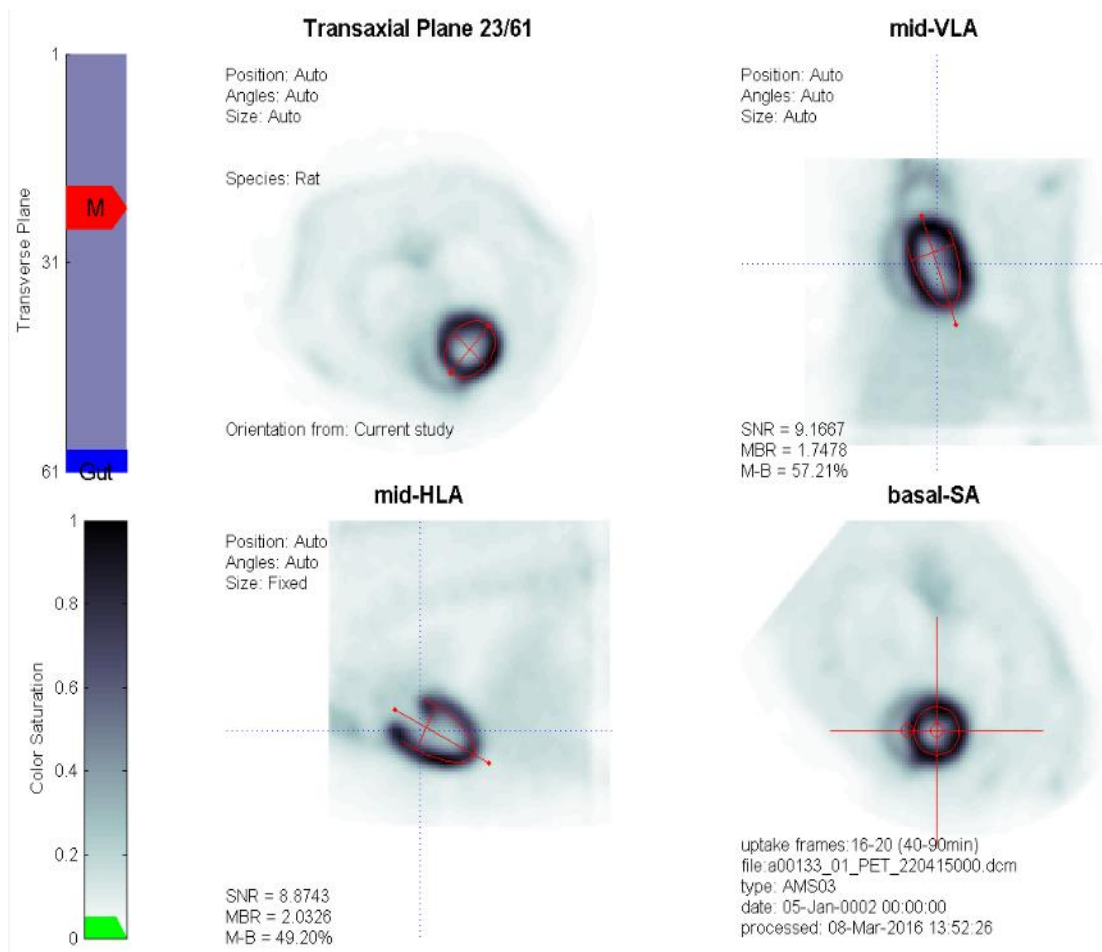


Figure 4.6. The myocardium was selected for subsequent analysis using a summed image of the final 5 frames of the data set.

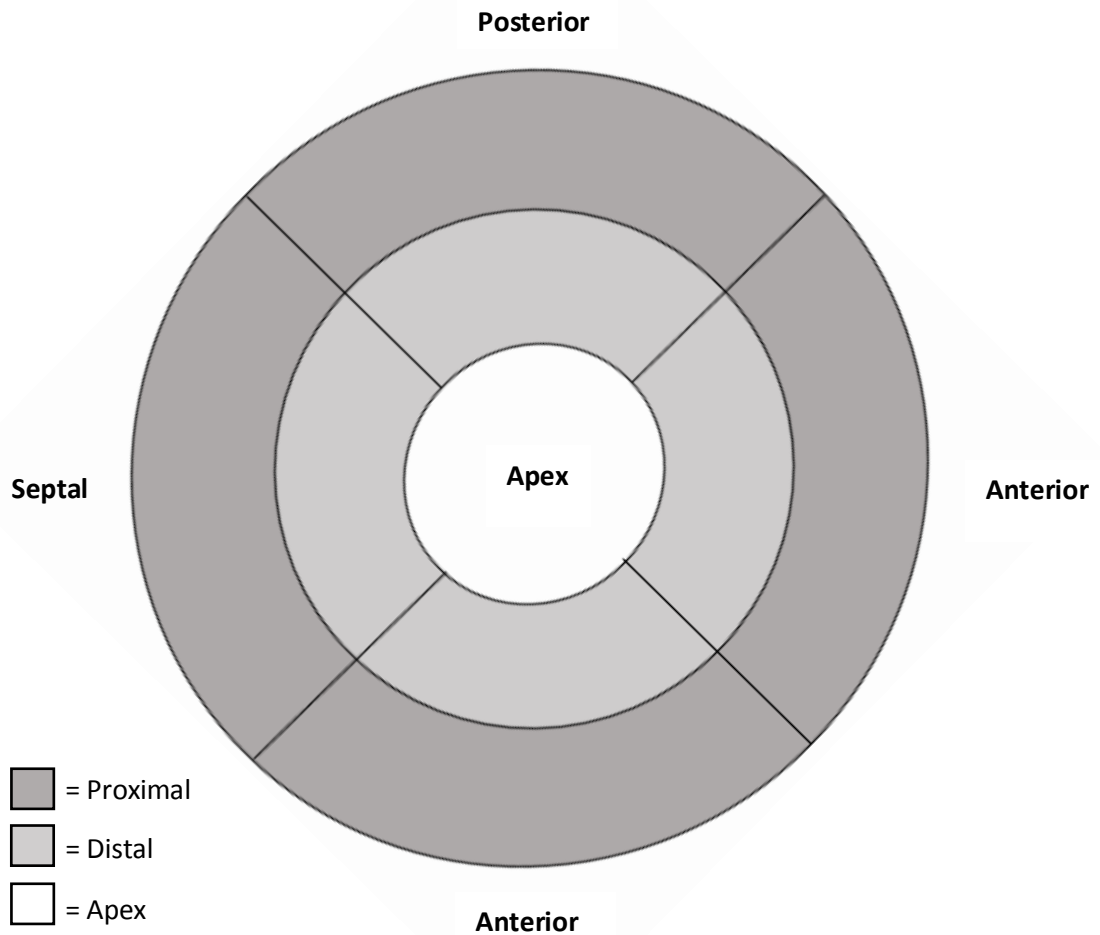


Figure 4.7. The heart was segmented into 9 distinct regions for polar map analysis.

4.2.5 Serum Metabolites

Blood glucose was measured immediately post-scan using an Accu-Chek digital blood glucose meter (Roche, Switzerland). 300µl whole blood was collected via the tail vein, centrifuged (3000g, 10 minutes, 4°C) and stored for subsequent metabolite analysis. Serum free fatty acid (kit: FA115) and lactate (kit: LC2389) concentrations were determined using an RX Monza clinical chemistry analyser (Randox Laboratories, County Antrim, UK). Serum insulin levels were measured using

a Rat Ultrasensitive Insulin ELISA Kit (kit: 10-1251-01, following the manufacturer's instructions, Mercodia, Uppsala, Sweden).

4.2.6 Ex Vivo Heart Perfusions

Isolated heart perfusions were carried out as described previously (Yamane et al., 2014) with modification. Animals were anaesthetised and hearts removed as described in section 2.3.1. Hearts were cannulated via the aorta on a Perspex platform which fitted a modified small animal imaging bed (Minerve, Esternay, France). Coronary flow was set to 10ml/min using a peristaltic pump (Watson Marlow, Falmouth, UK) and hearts perfused with oxygenated Krebs-Henseleit buffer (118mM NaCl, 25mM NaHCO₃, 4.8mM KCl, 1.2mM KH₂PO₄, 1.2mM MgSO₄, 1.25mM CaCl₂, 5mM glucose, 0.1mM sodium pyruvate, 1mM sodium lactate and 0.5mM glutamine, filtered using a 0.45µm Millipore filter) for 5 minutes to wash residual blood. The buffer was then switched to Krebs-Henseleit buffer containing 0.1MBq/ml ¹⁸F-FDG, and the heart perfused for a further 35 minutes at 37°C (Figure 4.8). Image acquisition was initiated at the time ¹⁸F-FDG was added to the buffer reservoir.

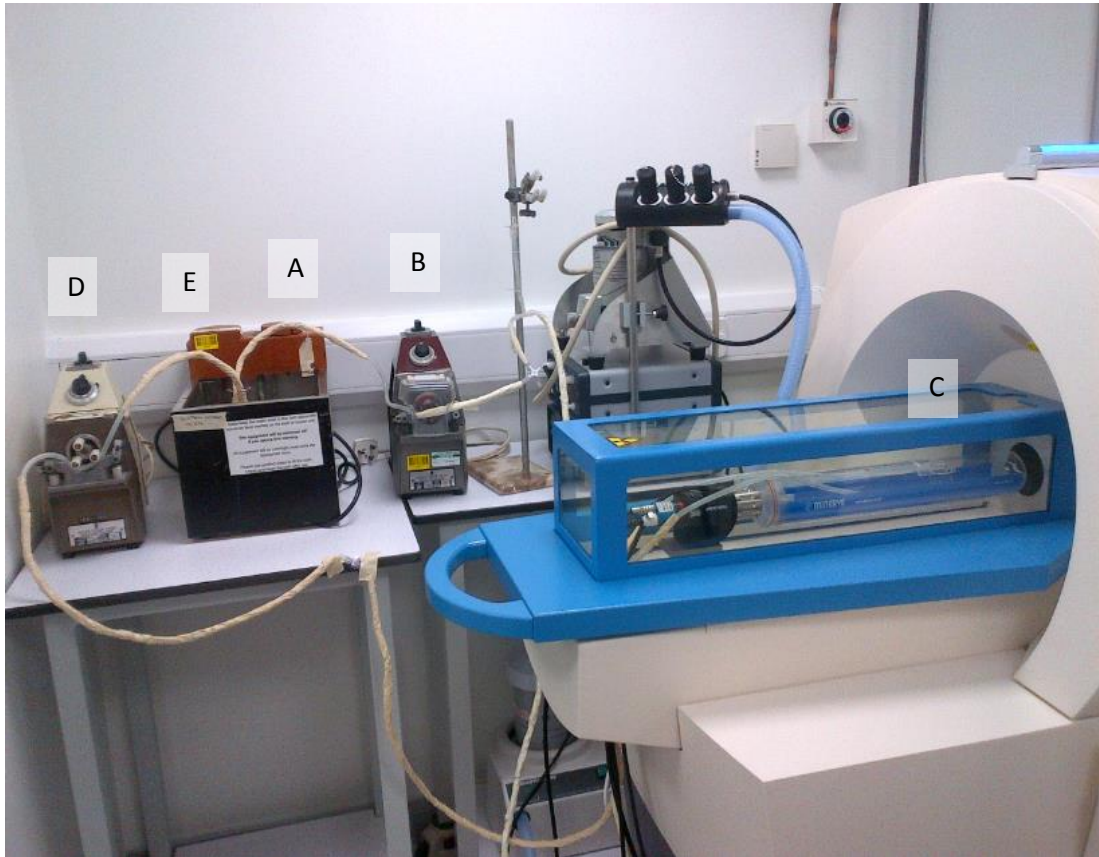


Figure 4.8. (A) KH buffer is drawn up via (B) a peristaltic pump and Tygon tubing. The perfusate travels through the tubing, (C) perfuses the heart and is (D) subsequently scavenged by a second peristaltic pump in to (E) a waste container.

4.2.7 Image Reconstruction and Analysis

PET data were reconstructed into 7 frames (7 x 300s) using the 3D OSEM algorithm as described in section 4.2.2 resulting in identical matrix and voxel sizes. Reconstructed data were subjected to attenuation, random and scatter correction as described in section 4.2.2. ROIs were drawn around the entire cardiac activity using the 3D isocontour drawing tool and the final 5 frames of the dataset used to generate a TAC. The slope of the curve was calculated by linear regression to determine the rate of ^{18}F -FDG uptake (Yamane et al., 2014).

4.3 Results

4.3.1 Standardised Uptake Values

SUV characteristics are listed in Table 4.1. TACs showed ^{18}F -FDG uptake increased linearly in the left ventricle of both control and uraemic animals before starting to plateau at approximately 60 minutes (Figure 4.9).

Table 4.1

SUV data

	Week	Control	Uraemic
Body weight (g)	5	418.5 ± 9.9 (n=7)	429.7 ± 8.2 (n=9)
	9	498.4 ± 10.4 (n=8)	503.4 ± 14.4 (n=7)
	13	546.8 ± 19.5 (n=6)	551.2 ± 12.7 (n=8)
Injected dose (MBq)	5	40.7 ± 4.3 (n=7)	38.9 ± 1.8 (n=9)
	9	38.2 ± 3.4 (n=8)	40 ± 2.5 (n=7)
	13	35.3 ± 1.7 (n=6)	35.5 ± 0.8 (n=8)

Data are presented as mean ± SEM.

Left Ventricle

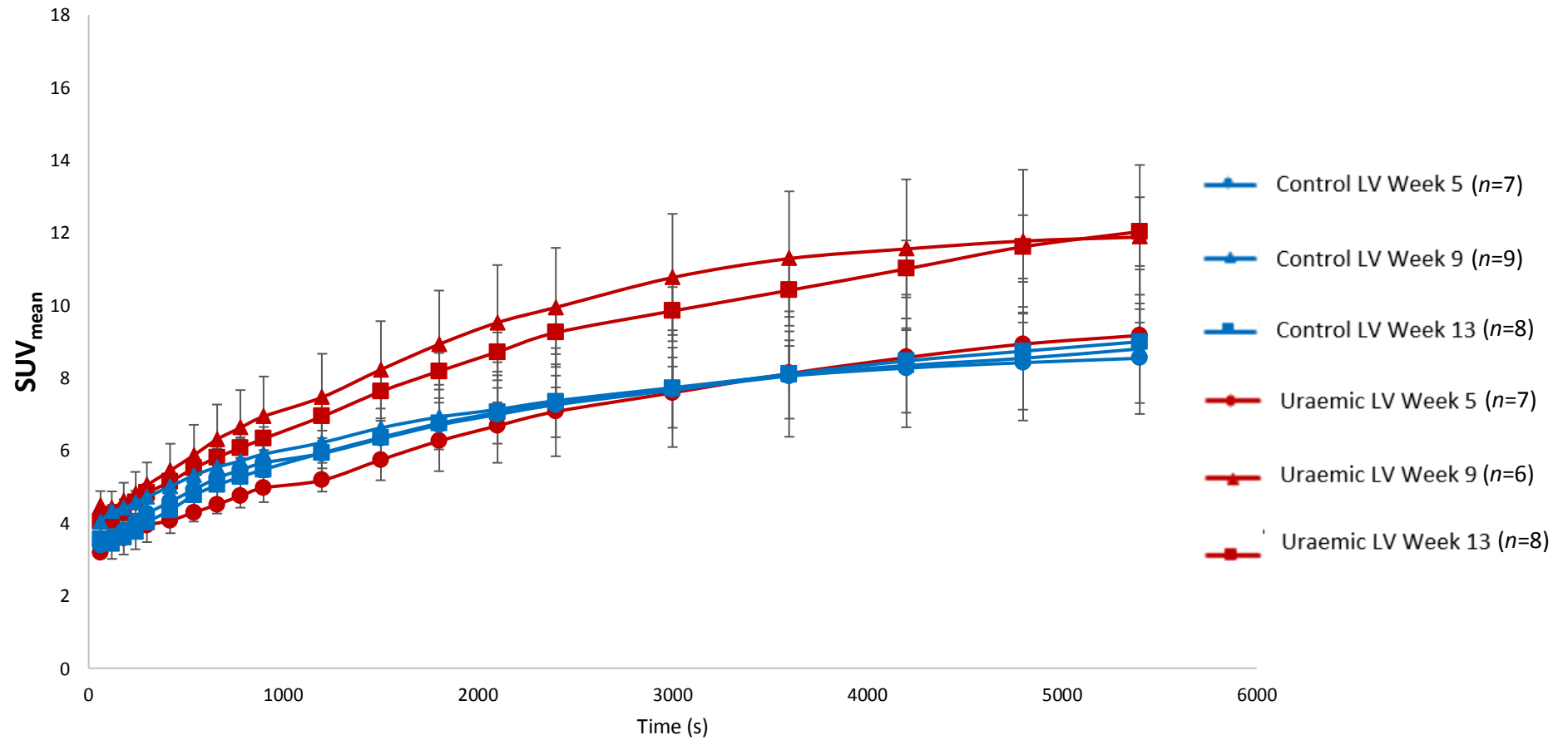


Figure 4.9. Mean time activity curves for the control and uraemic left ventricle (LV) at 5, 9 and 13 weeks post-surgery. Data are presented as mean \pm SEM.

Left ventricle SUVs were similar in both groups at week 5 (Figure 4.10A). By weeks 9 and 13, SUVs were higher in the uraemic groups compared to their respective controls, though this narrowly failed to reach significance (Figure 4.10B & Figure 4.10C).

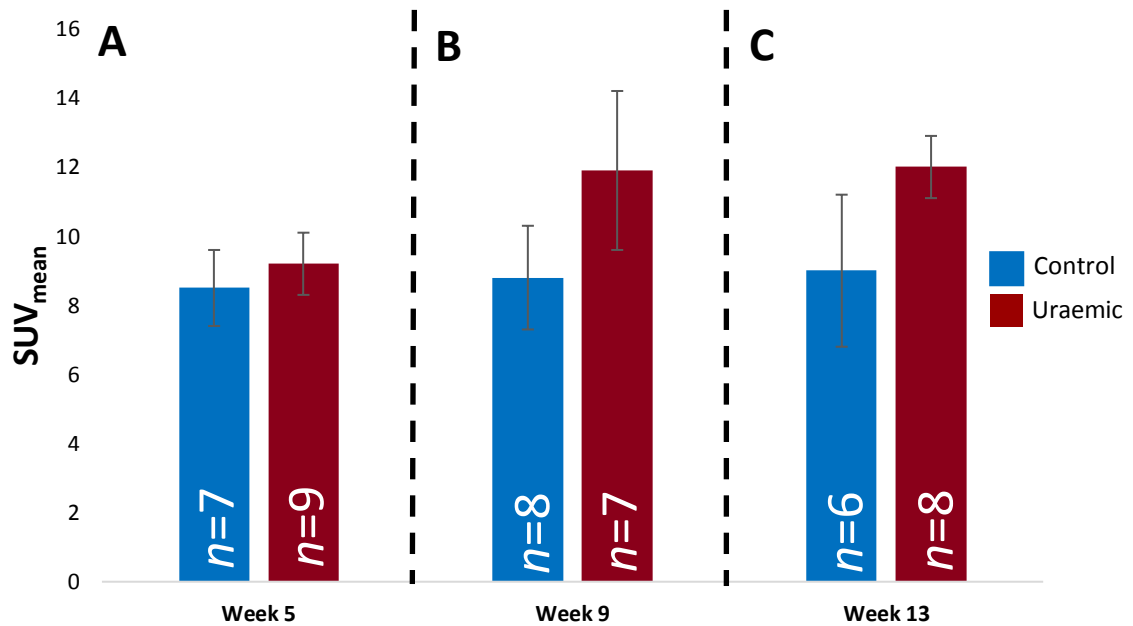


Figure 4.10. Standardised uptake values for the left ventricle (LV) at (A) 5, (B) 9 and (C) 13 weeks post-surgery. Data are presented as mean \pm SEM.

Left ventricular blood pool and vena cava TACs revealed a sharp spike in radioactivity at the beginning of the scan followed by subsequent plateau, indicative of injection of the radiotracer followed by rapid wash-out (Figure 4.11 & Figure 4.12). However, ^{18}F -FDG accumulated in a linear fashion in the aortic blood pool of both experimental groups over the course of the scan (Figure 4.13)

Left Ventricular Blood Pool

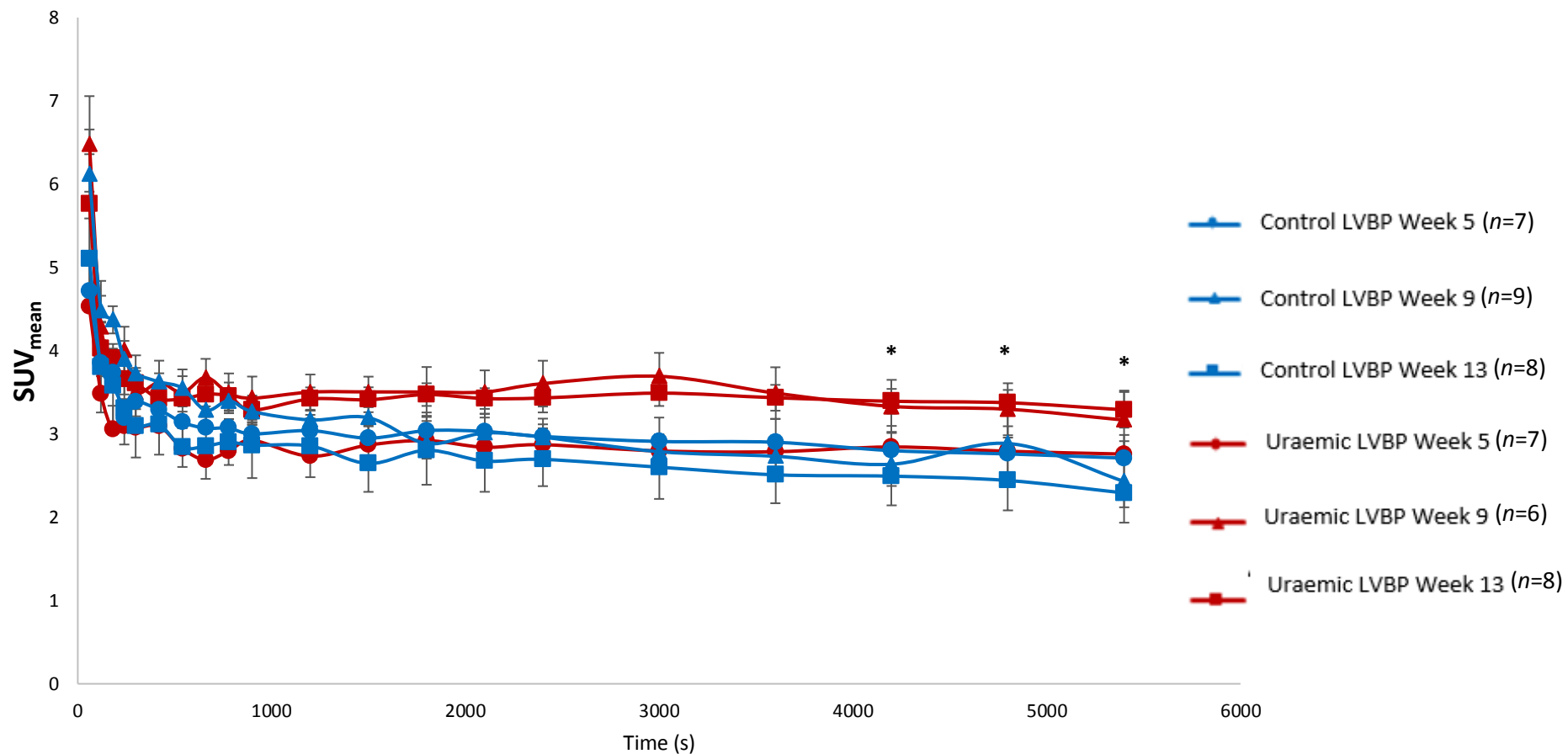


Figure 4.11. Mean time activity curves for the control and uraemic left ventricular blood pool (LVBP) at 5, 9 and 13 weeks post-surgery. Data are presented as mean \pm SEM. * = uraemic LVBP week 13 $p < 0.05$ vs control LVBP week 13 between 4200 – 5400s.

Vena Cava

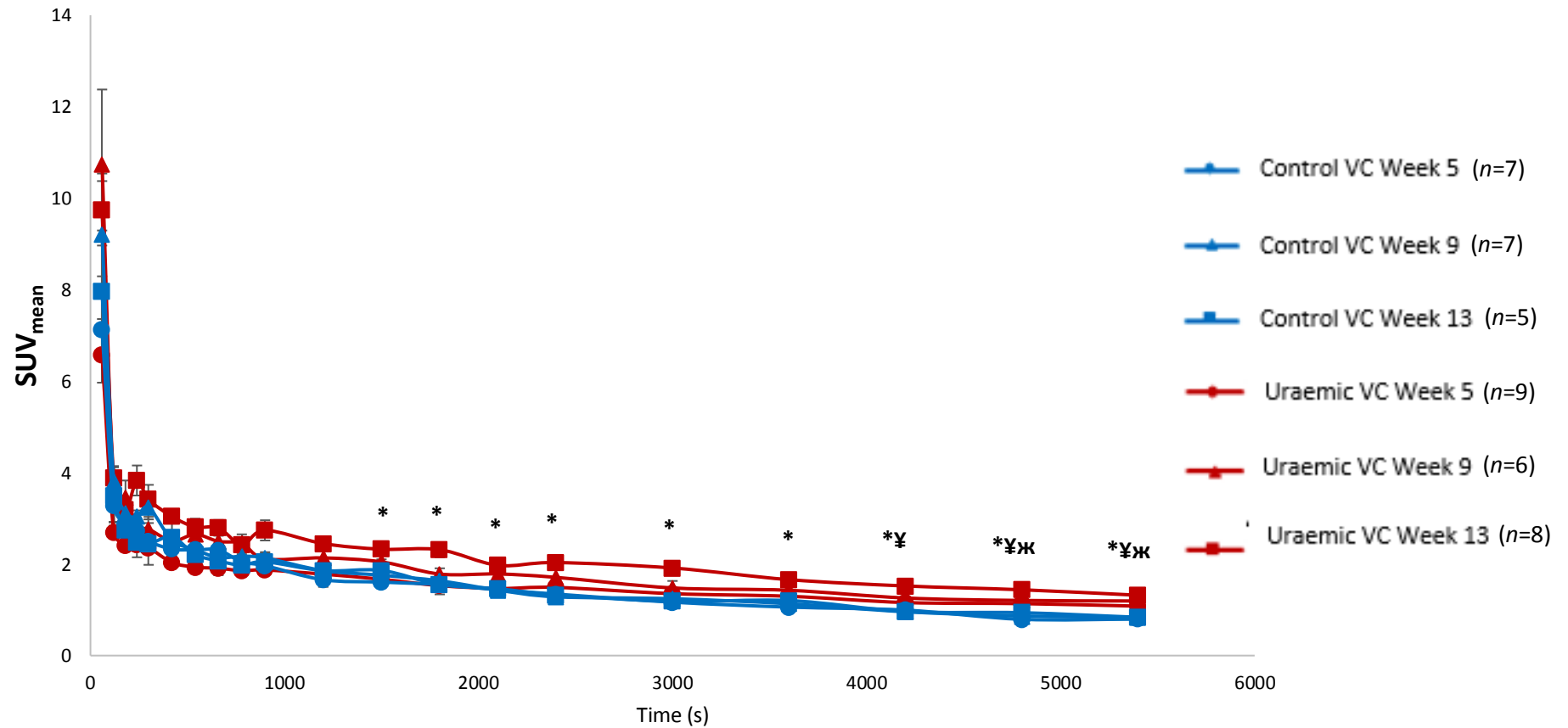


Figure 4.12. Mean time activity curves for the control and uraemic vena cava (VC) at 5, 9 and 13 weeks post-surgery. Data are presented as mean \pm SEM.

Ж = uraemic VC week 5 $p < 0.05$ vs control VC week 5 between 4800 – 5400s. ¥ = uraemic VC week 9 $p < 0.05$ vs control VC week 9 between 4200 – 5400s. * = uraemic VC week 13 $p < 0.05$ vs control VC week 13 between 1500 – 5400s.

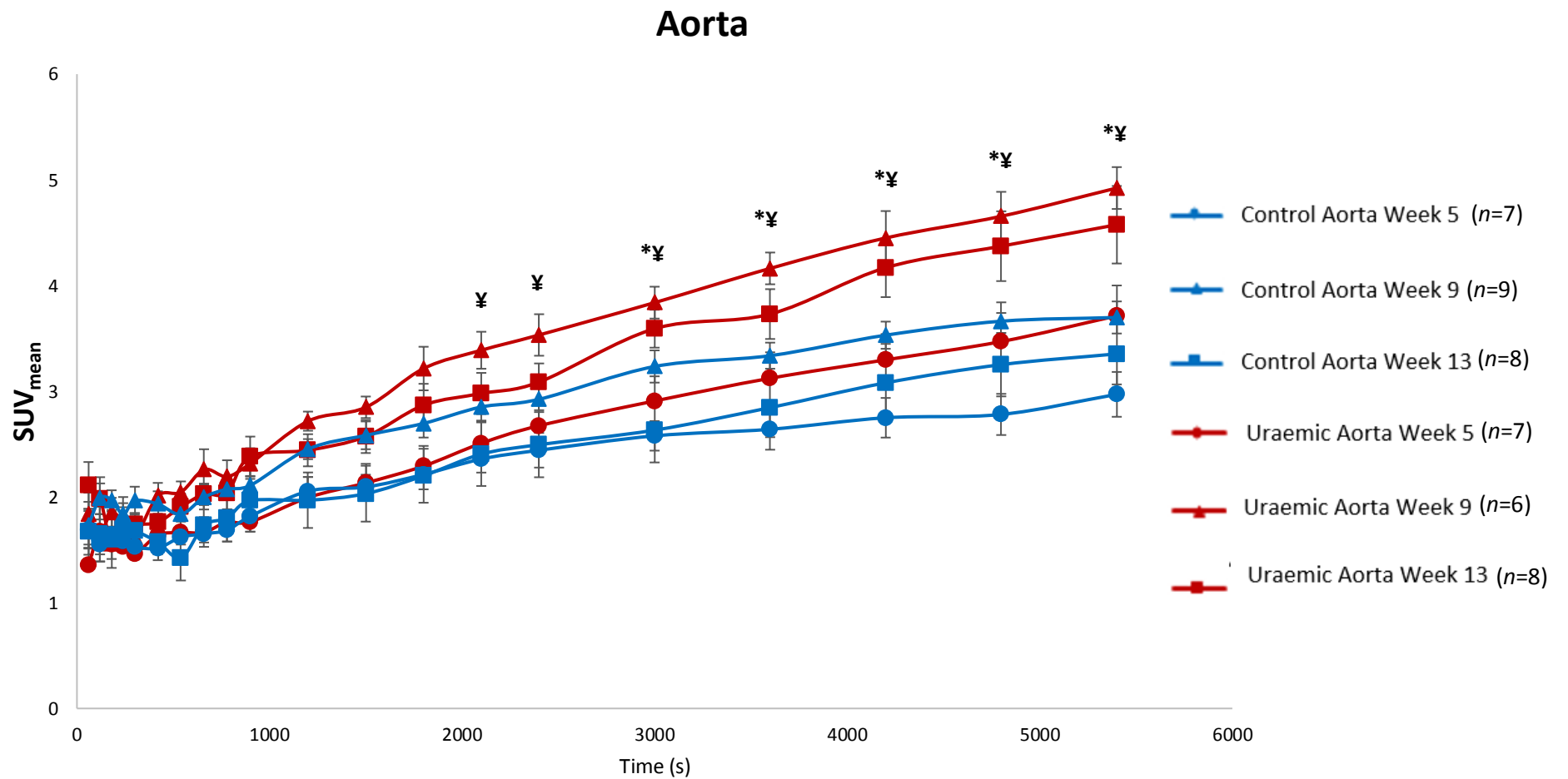


Figure 4.13. Mean time activity curves for the control and uraemic aorta at 5, 9 and 13 weeks post-surgery. Data are presented as mean \pm SEM.

¥ = uraemic aorta week 9 $p < 0.05$ vs control aorta week 9 between 2100 – 5400s. * = uraemic aorta week 13 $p < 0.05$ vs control aorta week 13 between 3000 – 5400s.

Left ventricular blood pool SUVs were similar in both the control and uraemic group at week 5 (Figure 4.14A). By week 9 of the study, SUVs were moderately increased in uraemic animals compared with their respective control group, though narrowly failing to reach significance (Figure 4.14B). However, by week 13 left ventricular blood pool SUVs were significantly increased compared with controls at the same time point (Figure 4.14C). Aorta and vena cava derived blood pool SUVs were significantly increased in uraemic animals throughout study duration (Figure 4.15 & Figure 4.16). Collectively, these data indicate a potential impaired renal clearance of ^{18}F -FDG.

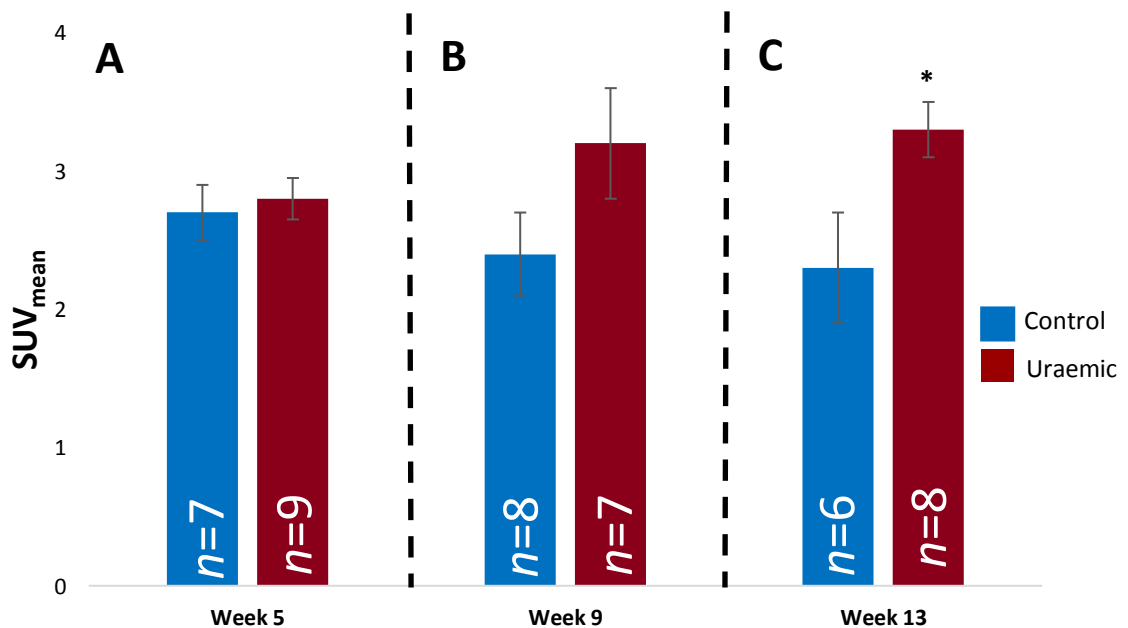


Figure 4.14. Standardised uptake values for the left ventricular blood pool (LVBP) at (A) 5, (B) 9 and (C) 13 weeks post-surgery. Data are presented as mean \pm SEM. * = uraemic LVBP week 13 $p < 0.05$ vs control LVBP week 13.

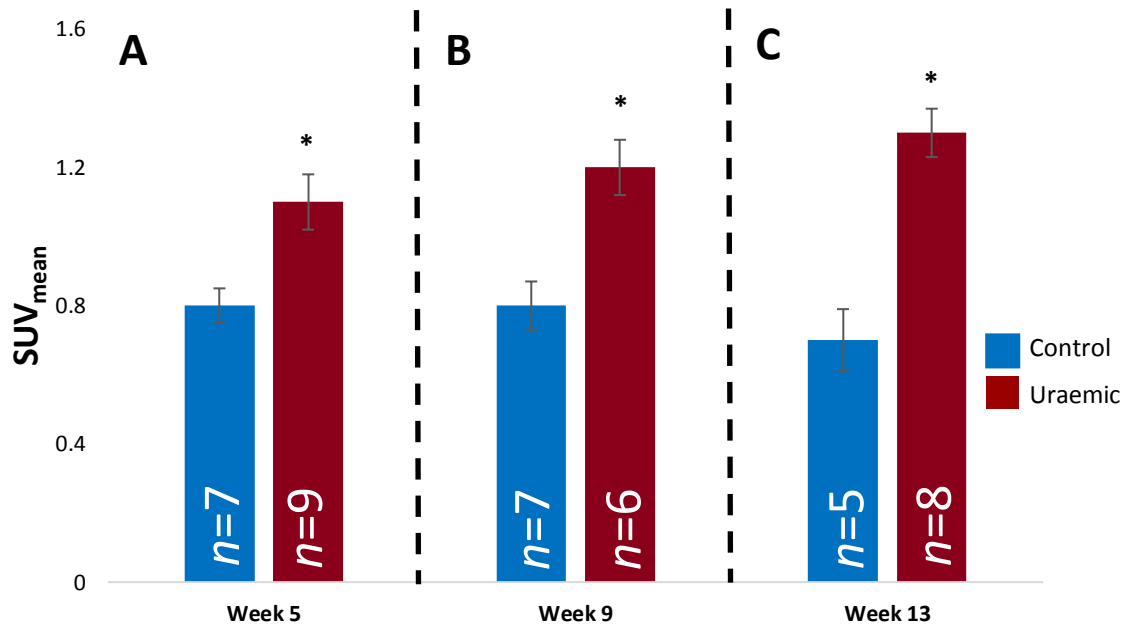


Figure 4.15. Standardised uptake values for the vena cava blood pool (VC) at (A) 5, (B) 9 and (C) 13 weeks post-surgery. Data are presented as mean \pm SEM. * = uraemic VC $p < 0.05$ vs controls at all time points.

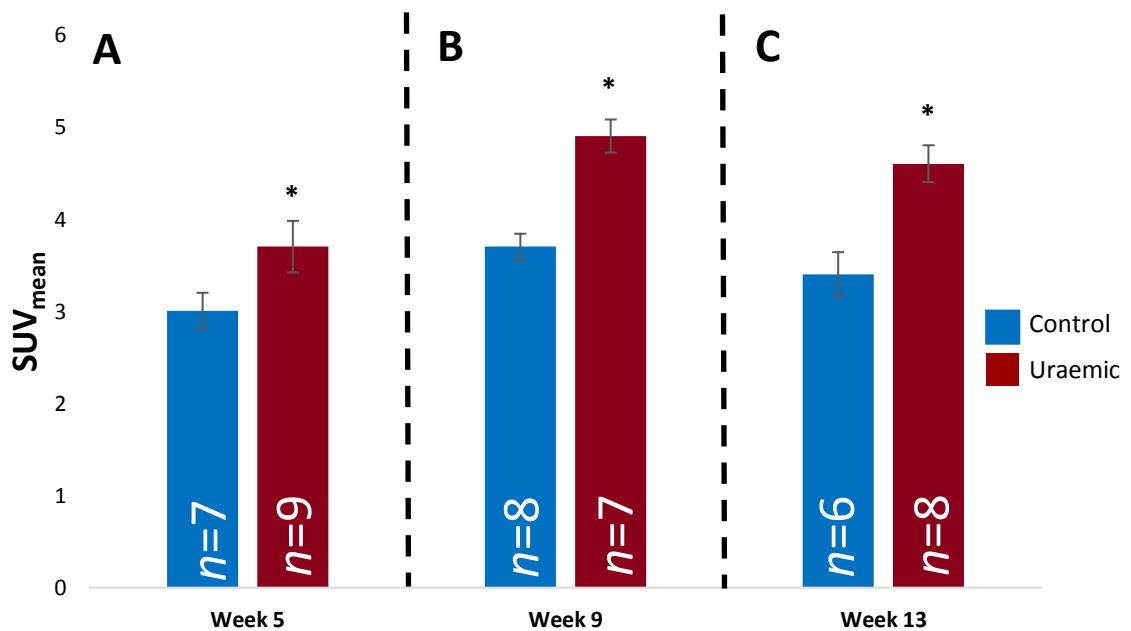


Figure 4.16. Standardised uptake values for the aortic blood pool at (A) 5, (B) 9 and (C) 13 weeks post-surgery. Data are presented as mean \pm SEM. * = uraemic aorta $p < 0.05$ vs all respective controls.

4.3.2 Rate and Distribution of Cardiac ^{18}F -FDG Uptake

Although Patlak analysis did not reveal any significant differences in the rate of ^{18}F -FDG uptake between groups at 5 (Figure 4.17A), 9 (Figure 4.17B) or 13 weeks (Figure 4.17C), there was a moderate 15-20% increase in ^{18}F -FDG uptake in the uraemic group at all time points.

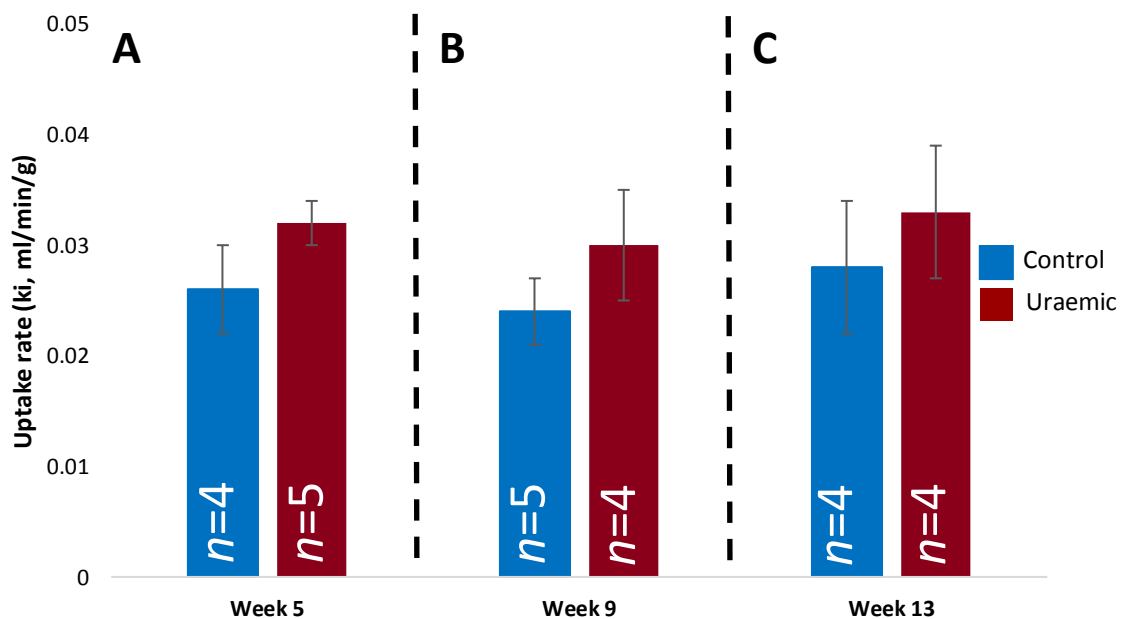


Figure 4.17. Myocardial ^{18}F -FDG uptake rates in control and uraemic hearts at 5, 9 and 13 weeks post-surgery. Data are presented as mean \pm SEM.

Polar map analysis revealed that induction of uraemia did not alter the distribution of cardiac ^{18}F -FDG uptake at 5 (Figure 4.18), 9 (Figure 4.19) or 13 weeks post-surgery (Figure 4.20).

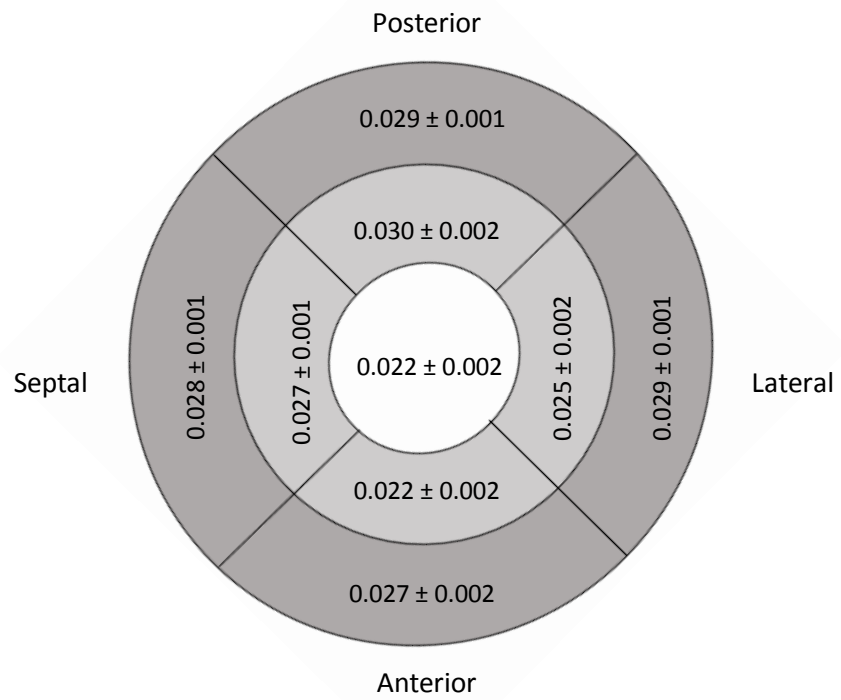
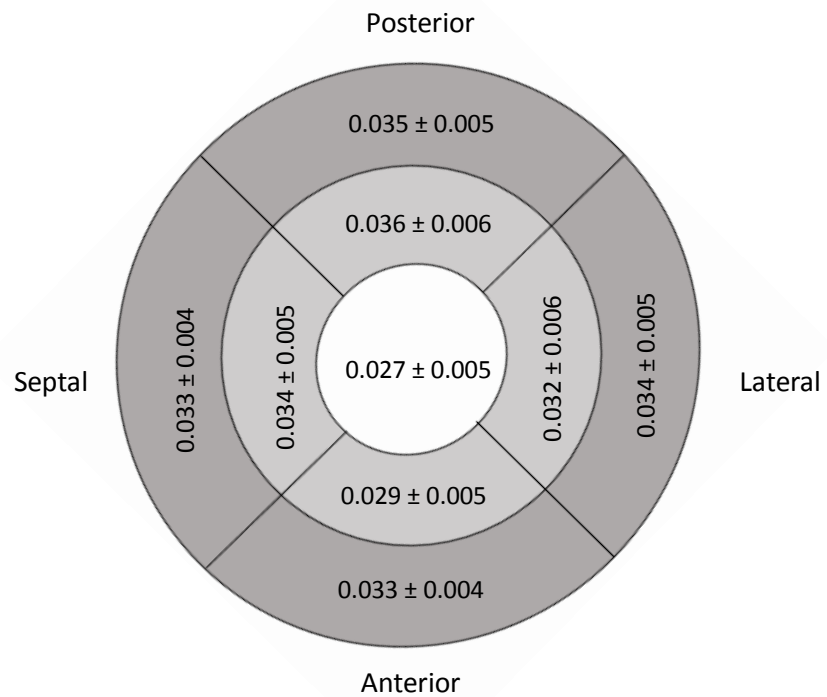
A**B**

Figure 4.18. Polar maps showing regional rates of uptake (K_i , ml/min/g) in (A) control ($n=4$) and (B) uraemic ($n=5$) hearts at 5 weeks post-surgery. Data are presented as mean \pm SEM.

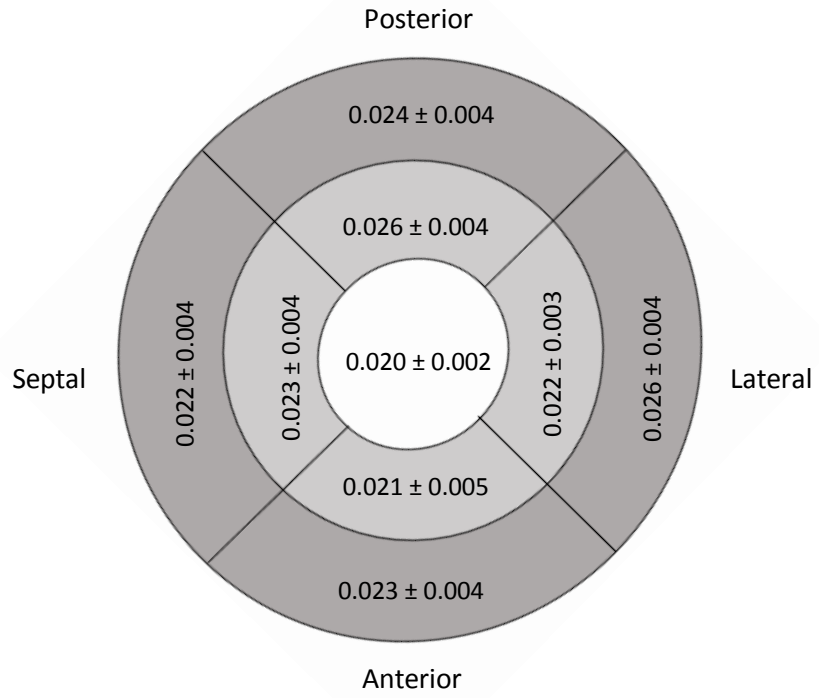
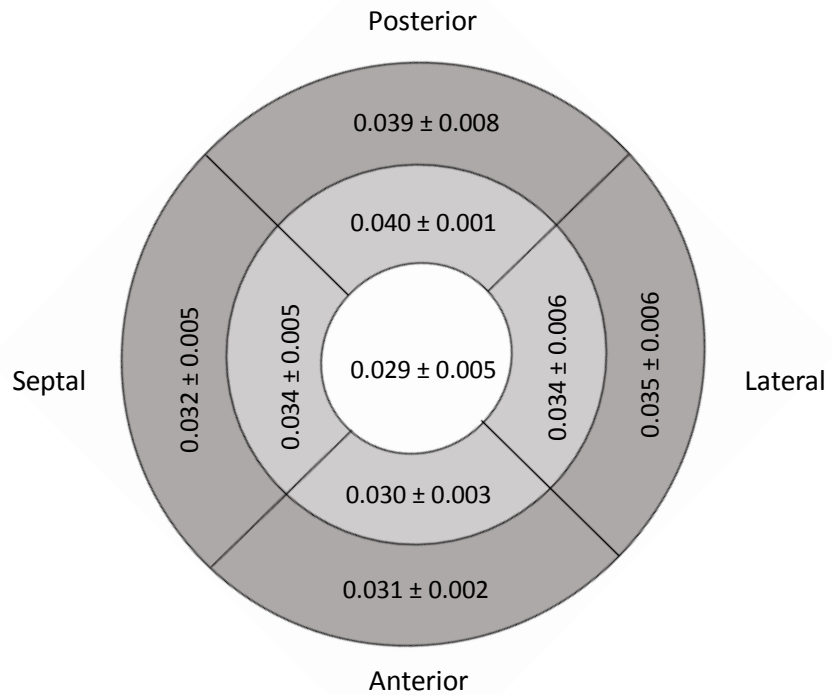
A**B**

Figure 4.19. Polar maps showing regional rates of uptake (K_i , ml/min/g) in (A) control ($n=5$) and (B) uraemic ($n=4$) hearts at 9 weeks post-surgery. Data are presented as mean \pm SEM.

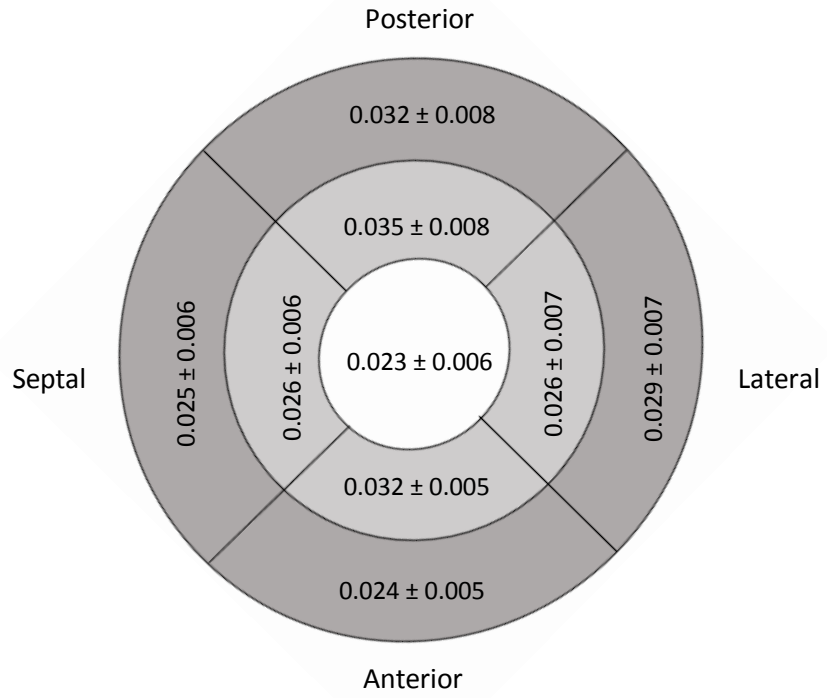
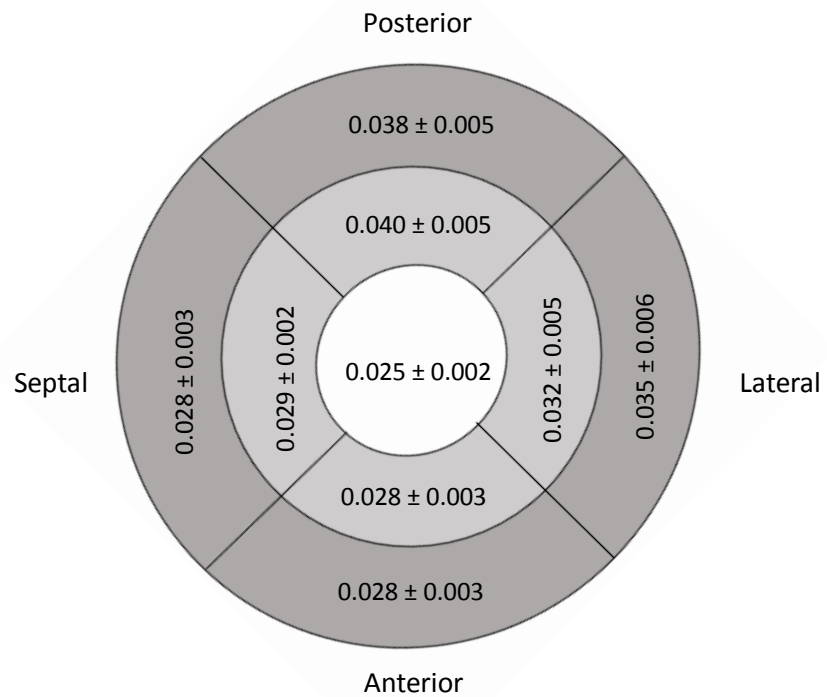
A**B**

Figure 4.20. Polar maps showing regional rates of uptake (K_i , ml/min/g) in (A) control ($n=4$) and (B) uraemic ($n=4$) hearts at 13 weeks post-surgery. Data are presented as mean \pm SEM.

4.3.3 Serum Metabolites

There were no differences in serum glucose, insulin, non-esterified fatty acid and lactate concentrations in control or uraemic animals at 5, 9 or 13 weeks post-surgery (Table 4.2).

Table 4.2

Serum metabolites

Metabolite	Week 5		Week 9		Week 13	
	Control	Uraemic	Control	Uraemic	Control	Uraemic
Glucose (mM)	13 ± 0.74 <i>n</i> =7	12.6 ± 0.61 <i>n</i> =9	12.3 ± 0.78 <i>n</i> =7	12.4 ± 1.06 <i>n</i> =6	12.2 ± 0.66 <i>n</i> =6	12.6 ± 0.60 <i>n</i> =8
Insulin (µg/L)	1.1 ± 0.02 <i>n</i> =3	1 ± 0.02 <i>n</i> =3	1.3 ± 0.03 <i>n</i> =5	1 ± 0.20 <i>n</i> =3	1.3 ± 0.08 <i>n</i> =4	1.4 ± 0.50 <i>n</i> =3
NEFA (mM)	0.79 ± 0.07 <i>n</i> =5	0.83 ± 0.07 <i>n</i> =5	0.8 ± 0.20 <i>n</i> =6	0.87 ± 0.13 <i>n</i> =3	0.83 ± 0.14 <i>n</i> =4	0.91 ± 0.18 <i>n</i> =3
Lactate (mM)	3.5 ± 0.52 <i>n</i> =3	3.1 ± 0.73 <i>n</i> =3	3.7 ± 0.38 <i>n</i> =8	3.6 ± 0.70 <i>n</i> =4	3.9 ± 0.30 <i>n</i> =4	3.5 ± 1.06 <i>n</i> =3

NEFA = non esterified fatty acids. Data are presented as mean ± SEM.

4.3.4 Development of Ex vivo Heart Perfusion System

Due to the narrow bore opening of the PET scanner it was necessary to modify a small animal imaging bed to facilitate the incorporation of the perfusion apparatus, the original schematic for these modifications is shown in Figure 4.21. A 7 x 4cm hole was cut out of the Perspex surround of a Minerve small animal imaging bed (Esternay, France). A Perspex platform of identical dimensions was then fabricated and a right-angled metal cannula attached (Figure 4.22). Two peristaltic pumps were also used, the first to perfuse the heart at a constant flow rate and the second to rapidly scavenge perfusate once it had been ejected from the heart.

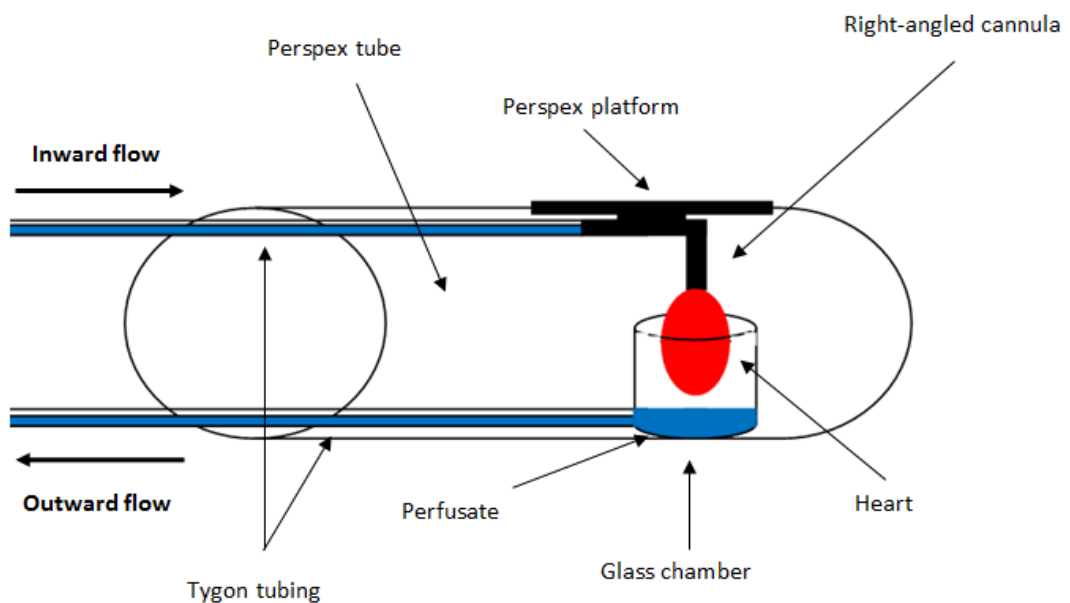


Figure 4.21. Original schematic of perfusion set up.

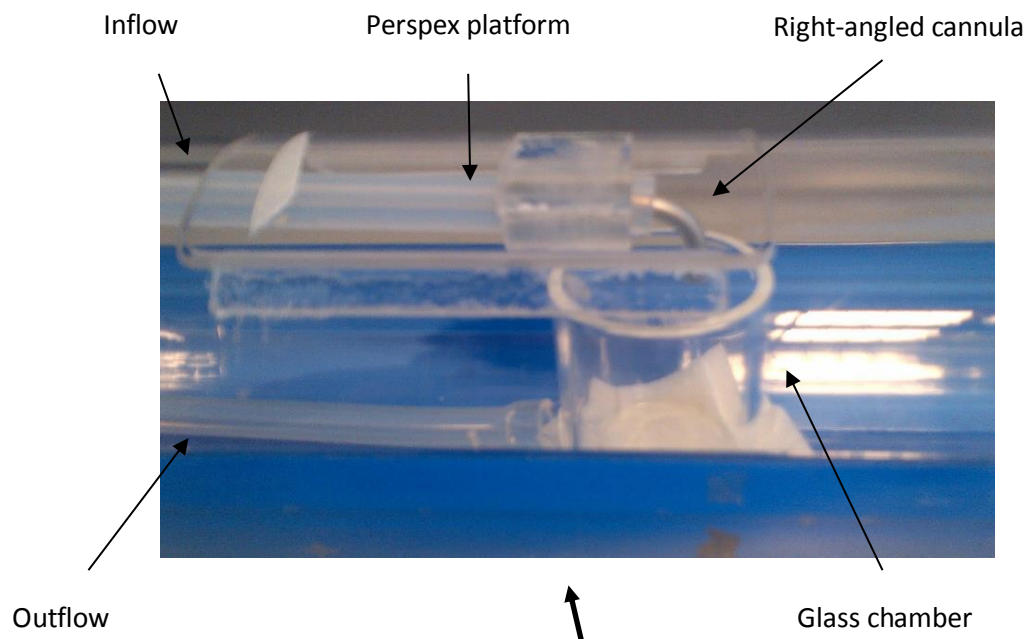


Figure 4.22. Modified Minerve small animal imaging bed

4.3.5 *Ex Vivo Heart Perfusions*

Under constant infusion, ^{18}F -FDG accumulated steadily in the isolated perfused heart demonstrating excellent linearity (Figure 4.23 & 4.24). However, no differences in ^{18}F -FDG uptake were observed between control and uraemic hearts (Figure 4.25).



Figure 4.23. Representative PET/CT image demonstrating accumulation of ^{18}F -FDG in the left ventricle.

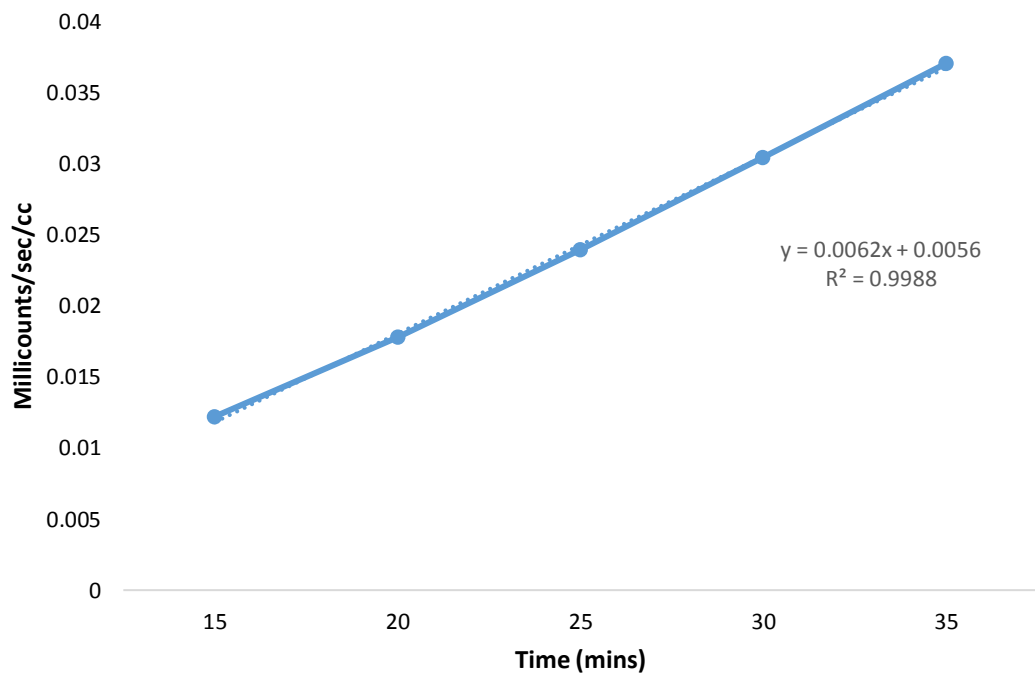


Figure 4.24. Representative time activity curve showing accumulation of ^{18}F -FDG in the isolated perfused rat heart under constant infusion of radiotracer.

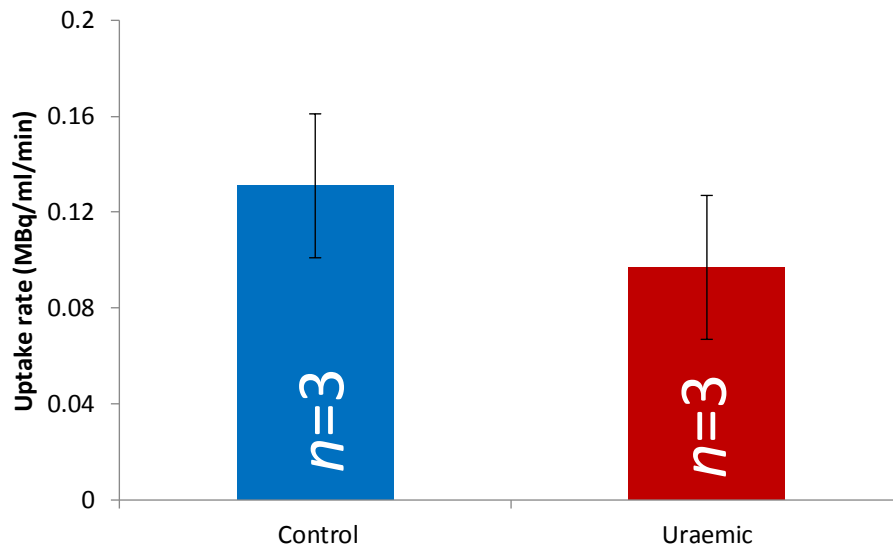


Figure 4.25. Uptake rate of ^{18}F -FDG in isolated perfused control and uraemic hearts. Data are presented as mean \pm SEM.

4.4 Discussion

SUVs were moderately increased in the left ventricle of uraemic animals at weeks 9 and 13 of the study, though this failed to reach statistical significance. Left ventricular, aortic and vena cava derived blood pool SUVs were significantly increased, suggesting impaired renal clearance of ^{18}F -FDG. Although Patlak and polar map analysis revealed no significant differences in the rate or distribution of ^{18}F -FDG uptake in the left ventricle, collectively there was a trend towards enhanced ^{18}F -FDG uptake in uraemic hearts in vivo.

4.4.1 *Standardised Uptake Values*

4.4.1.1 *Left Ventricle*

The pattern of ^{18}F -FDG uptake in the left ventricle was similar in control and uraemic animals over the 90 minute scan, increasing linearly from the time of injection and starting to plateau by approximately 60 minutes (Figure 4.9). SUVs for the left ventricle were comparable between groups at week 5 (4.10A) but moderately increased in the uraemic group at weeks 9 (Figure 4.10B) and 13 (Figure 4.10C).

An increased reliance on glucose metabolism is a hallmark of the hypertrophied heart and has been demonstrated in a number of models of cardiac hypertrophy and heart failure using ^{18}F -FDG PET. Handa et al. (2007) reported significantly greater SUVs in salt-sensitive Dahl rats in a model of pressure overload hypertrophy. Glucose uptake increased proportionally with the progression of cardiac hypertrophy, determined with echocardiography prior to the PET scan,

throughout study duration. In addition, progression from compensated hypertrophy to failure was accompanied by a significant reduction in ejection fraction and fractional shortening. Fink et al. (2010) conducted a study on stage II CKD patients undergoing dialysis treatment using ^{18}F -FDG PET and demonstrated increased myocardial glucose utilization significantly correlated with worsening kidney function. However, comparisons between that and the present study are difficult as only 15% of patients presented with cardiac hypertrophy.

Although *in vivo* data on glucose utilisation in UCM is scarce, several studies have used ^{13}C NMR to assess cardiac metabolism in the isolated perfused rat heart. Indeed, Reddy et al. (2007) identified a moderate increase in glucose utilisation and concurrent decrease in palmitate oxidation in uraemic hearts at 6 weeks using a physiological mixture of substrates. Aksentijevic (2008) observed a significant increase in the contributions of glucose and lactate to cardiac metabolism in the uraemic heart over the same timeframe. Similar findings were reported by Smith et al. (2010) when the model was extended to 12 weeks. They reported a significantly reduced contribution of palmitate to oxidative metabolism, with a corresponding increase in glucose utilisation, in uraemic hearts at 6 and 12 weeks.

4.4.1.2 Blood Pool Analysis

TACs for the Left ventricular blood pool and vena cava highlight a sharp spike in radioactivity at the beginning of the scan quickly followed by plateau, indicative of injection of the radiotracer followed by rapid wash-out (Figure 4.11 & Figure 4.12). However, ^{18}F -FDG accumulated in a linear fashion in the aorta of both control and

uraemic animals throughout scan duration (Figure 4.13). Aortic and vena cava derived blood pool SUVs were significantly higher in uraemic animals compared with respective controls at all time points investigated (Figure 4.15 & Figure 4.16). In addition, the uraemic left ventricular blood pool SUV was significantly higher than controls at week 13 (Figure 4.14). Collectively these data suggest that there is an impaired renal clearance of ^{18}F -FDG in uraemic animals.

Unlike glucose, which is completely reabsorbed in the kidney, ^{18}F -FDG is not filtered and is excreted in the urine (Moran et al., 1999). The difference in kinetics between the compounds is due to a reduced affinity of ^{18}F -FDG to sodium-coupled glucose transporters (SGLTs) in the proximal tubules of the kidney (Sala-Rabanal et al., 2016). Indeed, the addition of the ^{18}F moiety at the C2 position in place of the hydrogen atom results in an overall decreased hydrogen bonding ability of the radiotracer (Moran et al., 1999). Approximately 20% of the administered dose of ^{18}F -FDG is excreted two hours post-injection in individuals with normal renal function (Moran et al., 1999). However, it has been reported that impaired kidney function can limit excretion of ^{18}F -FDG, increasing radiotracer levels in the blood as observed here (Kinahan & Fletcher, 2010 & Huang, 2000).

The kinetics of ^{18}F -FDG in the aorta did not follow a similar pattern of uptake compared with the other blood pools. It is possible that this could be the result of radiotracer spillover from the left ventricle in to aortic blood pool. However, this would seem unlikely as the left ventricular blood pool is in closer proximity to the left ventricle and exhibits conventional blood pool kinetics. Other studies have observed enhanced ^{18}F -FDG uptake in the walls of large vessels such as the aorta

(Tatsumi et al., 2003 & Courtois et al., 2013). However these studies reported only SUVs rather than radiotracer kinetics, therefore it is difficult to make a direct comparison between the studies.

Impaired renal clearance of ^{18}F -FDG in uraemic animals may contribute to enhanced cardiac uptake of the radiotracer. Myocardial substrate uptake is largely dependent on blood glucose, insulin and free fatty acid levels (Scholtens et al., 2016). Elevated blood glucose and insulin coupled with a decreased level of circulating free fatty acids leads to a rise in glucose uptake and consumption. On the other hand, decreased glucose and insulin and elevated free fatty acid levels in the blood shift cardiac energy consumption away from carbohydrate metabolism and towards fatty acids (Scholtens et al., 2016). However, it was difficult to quantify how much of an impact elevated ^{18}F -FDG in the blood had on cardiac radiotracer uptake using SUVs alone, therefore Patlak analysis was used to account for tracer concentration in the plasma.

4.4.2 Rate and Distribution of ^{18}F -FDG Uptake in the Left Ventricle

Although Patlak analysis revealed a moderate 15-20% increase in the influx rate constant K_i^{FDG} in uraemic animals over the longitudinal study, there was no significant differences compared with controls at any of the time points investigated (Figure 4.17). In addition, induction of uraemia did not alter the distribution of ^{18}F -FDG uptake in the left ventricle (Figure 4.18 – Figure 4.20).

Patlak is a useful model-independent graphical analysis method which corrects cardiac ^{18}F -FDG uptake to myocardial blood pool activity (Patlak et al., 1983). Patlak analysis assumes all reversible compartments are in equilibrium with plasma, usually following the initial spike in activity of the blood pool TAC. Then only radiotracer trapping in the irreversible compartment is contributing to changes in the total myocardial tissue concentration (Patlak et al., 1983). In these circumstances the plot becomes linear and the slope of the graph represents the influx rate constant, K_i^{FDG} which can give an indication of the rate of myocardial glucose uptake. In the present study K_i^{FDG} was in the range of 0.025 – 0.035 ml/min/g, this is consistent with previous *in vivo* studies on the spontaneously hypertensive rat heart (Hernandez et al., 2013). This group reported substantial alterations in myocardial substrate preference as evidenced by significantly enhanced glucose uptake. Furthermore, there was an increase in end diastolic volume and reduced ejection fraction indicating mechanical dysfunction. However, in contrast to the present model, the Hernandez et al. (2013) study developed into an end-stage model of heart failure over a substantially longer timeframe. Indeed, the study lasted 20 months in total and only one spontaneously hypertensive rat survived to the final time point.

Although a useful indicator, care should be exercised when extrapolating k_i^{FDG} to the true rate of glucose uptake as k_i^{FDG} purely reflects ^{18}F -FDG. Furthermore, while k_i^{FDG} can be used together with the lumped constant and the plasma concentration of glucose to calculate the myocardial metabolic uptake rate of glucose, the lumped constant itself has been shown to be variable in states of disease and metabolic stress (Botker et al., 1999; Doenst & Taegtmeyer, 1998 & Ng et al., 1991). Therefore it is possible that true glucose uptake may have been changing in ways that ^{18}F -FDG was

not reporting on. Indeed, a change in the lumped constant may go some way to explaining the disparities observed between the present study and those reported previously on the uraemic heart using ^{13}C NMR (Aksentijevic, 2008 & Smith et al., 2010).

The lumped constant was originally calculated in dogs to account for differences in the affinity of glucose and ^{18}F -FDG to myocardial glucose transporters and hexokinase-mediated phosphorylation (Ratib, et al., 1983). The mechanisms underpinning lumped constant variability are largely attributed to altered hexokinase kinetics, specifically increased translocation of the enzyme to the mitochondria. Indeed, Southwell et al. (2007) employed immunogold labelling and electron microscopy to directly visualise hexokinase biodistribution in the heart. They reported significantly increased translocation of the enzyme to the mitochondria within 30 minutes of insulin stimulation or ischemic insult. It is considered that the hexokinase translocation is part of a cardioprotective mechanism which inhibits mPTP formation and apoptotic cell death, a process mediated by Akt. Indeed, the association of hexokinase with the mitochondria is promoted by Akt activation while inhibition of Akt leads to the rapid dissociation of hexokinase and subsequent apoptosis (Southwell, 2009).

In addition to the enhanced recruitment of hexokinase to mitochondria, increased translocation of GLUT4 to cardiac membranes has also been reported in response to insulin, hypoxia and ischemia, though this has not always been reflected by enhanced ^{18}F -FDG uptake (Southwell, 2009). Indeed, even under basal conditions in the cytosol, hexokinase preferentially phosphorylates glucose over its tracer

analogues such as ^{18}F -FDG. Furthermore, it has been estimated that this effect is compounded a further 8-9 fold in states of metabolic stress (Russell et al., 1992). Therefore changes in GLUT4 and hexokinase kinetics may impact on lumped constant variability and consequently measured radiotracer uptake.

While the disparities between the present study and those using ^{13}C NMR may be due to lumped constant variability, there are a number of other factors which could also have impacted on ^{18}F -FDG uptake such as blood glucose levels, core body temperature and mode of anaesthesia. As ^{18}F -FDG competes with glucose for intracellular transport and phosphorylation, elevated blood glucose can decrease ^{18}F -FDG uptake (Wahl et al., 1992). However, this seems unlikely as blood metabolites, including glucose, were largely unaltered in control and uraemic animals throughout the study (Table 4.2). Previous studies in mice have highlighted that ^{18}F -FDG uptake is significantly increased in brown fat and reduced in metabolically active tissues when core body temperature drops below 30°C (Fueger et al., 2006). However, again this seems unlikely as indices of body mass were similar in the control and uraemic groups (section 3.3.2.1) and animals were maintained between $35\text{-}37^{\circ}\text{C}$ on a specialised heated imaging bed during image acquisition.

Isoflurane, which was used to maintain anaesthesia during the scan, has been shown to substantially impact on glucose uptake in organs including the myocardium and brain. Indeed, Fueger et al. (2006) and Toyama et al. (2004) reported significantly increased myocardial ^{18}F -FDG uptake when isoflurane was used to maintain anaesthesia compared with unanaesthetised animals. Conversely, brain uptake of the radiotracer was significantly reduced when isoflurane was used

to maintain anaesthesia in both studies. The effects of isoflurane on ^{18}F -FDG uptake are thought to be due to an insulin suppressive effect exerted by the anaesthetic agent which would support the decreased pattern of ^{18}F -FDG uptake observed in the brain (Lee et al., 2005). However, the mechanism underlying enhanced myocardial ^{18}F -FDG uptake in the presence of isoflurane is poorly understood (Fueger et al., 2006). In addition, it is unclear if isoflurane had differential effects on ^{18}F -FDG uptake in control and uraemic animals as both groups had similar serum metabolite concentrations at the time of scanning (Table 4.2).

As with most PET studies, the gold standard for determining input functions for Patlak and kinetic modelling is blood sampling at multiple time-points during the scan (Fang & Muzic, 2008). However, this method has several limitations in a rodent including small blood vessel size, limited total blood volume and the invasive nature of the procedure. In addition, the overall blood loss in a small animal, such as the rat, may be physiologically relevant and impact on the experimental outcome. Therefore, in the present study an image derived blood input function, taken from the left ventricular cavity, was used in the Patlak analysis. Image derived blood input functions are TACs drawn over the major vascular structures, such as the ventricular cavity, aorta and large arteries (van der Weerd et al., 2001). Although this technique avoids the need for invasive blood sampling methods, the rat myocardium and vasculature are small compared with the spatial resolution of the scanner. Consequently, areas of low radiotracer uptake can seem more radioactive than they are when next to a structure with relatively high uptake and vice versa, these effects are termed spillover and partial volume respectively (Fang & Muzic, 2008). This can be particularly relevant in polar map analysis where the myocardium is sub-divided

in to distinct regions. Indeed, the rat left ventricle is approximately 2mm at its thickest point while the resolution of a small animal PET scanner is 1-2mm (Yagi et al., 2004). Consequently it is unlikely differences in cardiac tissue sub-structures, such as the epicardium and endocardium, can be accurately resolved with this technique and care must be exercised when interpreting such results.

While ^{18}F -FDG is a useful radiotracer for investigating cardiac glucose uptake, there are a number of limitations associated with the glucose analogue as discussed previously. An alternative PET-based method for investigating cardiac glucose metabolism *in vivo* could be ^{11}C -glucose PET (Herrero et al., 2002). Unlike ^{18}F -FDG, ^{11}C -glucose is a “true” radiotracer and is completely metabolised and not trapped inside the cell. However, the half-life of ^{11}C -glucose is only about 11 minutes and thus for routine measurements a ^{11}C producing cyclotron would be needed on site. Consequently only ^{18}F -FDG is currently used for imaging glucose metabolism in routine clinical practice (Herrero et al., 2002).

In addition to PET, there are two other techniques which can be used to image myocardial glucose uptake noninvasively; NMR and single photon emission computed tomography (SPECT). NMR has been used successfully in rodents *in vivo* and *ex vivo* in the isolated perfused heart, as previously discussed using ^{13}C (Aksentijevic 2008 & Smith et al 2010). Furthermore, this technique has a number of advantages over PET including the ability to investigate multiple metabolic pathways simultaneously and the lack of ionizing radiation. However, cardiac applications for NMR in humans are limited compared to rodents. This is largely due to the higher field strength in small bore systems and the use of radiofrequency coils which are in closer proximity to the entire heart in small animal imaging (Gropler, 2010). Indeed,

while measurements of the entire left ventricle are obtained in rodents, measurements in the human heart are limited to the anterior myocardium. Consequently the initial success of imaging cardiac glucose metabolism in animals using ^{13}C has not been translated into the clinical setting (Lewandowski, 2002).

The advantages of SPECT for studying cardiac metabolic processes are similar to those for PET and include high sensitivity and the ability to use ECG-gating while imaging. However, unlike PET, SPECT has a relatively poor spatial and temporal resolution and limited photon attenuation (Gropler, 2010). Therefore SPECT is unable to accurately quantify cellular metabolic processes, indeed, only ^{18}F -FDG has been used to assess glucose uptake using SPECT under specific conditions (He et al. 2003).

4.4.3 Ex Vivo Heart Perfusions

The isolated perfused heart model was used in this study as it removed the potential impact of anaesthesia on ^{18}F -FDG uptake in the uraemic heart and also allowed a more direct comparison to previous studies using ^{13}C NMR. ^{18}F -FDG accumulated steadily in the perfused rat heart under constant infusion of radiotracer (Figure 4.23 & Figure 4.24), consistent with previous studies using ^{18}F -FDG and gamma coincidence counters (Nguyen et al. 1990) and a dedicated small animal PET scanner (Yamane et al., 2014). However, no differences in ^{18}F -FDG uptake rates were observed between control and uraemic hearts (Figure 4.14). These findings differ from those reported by Smith et al. (2010) and Aksentijevic (2008) on the isolated uraemic heart. The disparities between studies may be due to differences in buffer composition, indeed, the Krebs-Henseleit buffer used by Smith et al. (2010) and

Aksentijevic (2008) contained additional physiological components such as insulin and albumin which would affect ^{18}F -FDG uptake. Furthermore, excising the heart from the body causes a decrease in wall tension as the structural support of the pericardium and connective tissue are lost (Lekven, 1981). Consequently the myocardium can lose shape and ROIs can be difficult to draw around the left ventricle alone as with the *in vivo* analyses. Therefore myocardial ROIs were drawn around the whole cardiac activity, including left ventricular blood pool, which could have increased variability in the analysis.

In addition, while normal coronary flow in the rat is approximately 1.5ml/min *in vivo*, poor oxygen solubility and low oncotic pressure mean that significantly higher flow rates are required in the isolated perfused heart *ex vivo* (Suckow et al., 2005). The 10ml/min flow rate selected here was based on the method by Yamane et al. (2014), however coronary flow rates of upto 18ml/min have been used in other studies (Suckow et al., 2005). Furthermore, due to logistical limitations, the Langendorff preparation used in the present study was relatively simple and did not include an intraventricular balloon or cardiac pacing. Both the balloon and pacing are important factors in maintaining ventricular wall tension and contractility, which are intrinsically linked to myocardial oxygen consumption (Hoffman & Buckberg, 2014). Therefore it is possible that a sub-optimal coronary flow rate combined with the absence of an intraventricular balloon and cardiac pacing resulted in the hearts becoming ischemic, in which case myocardial glucose utilisation would have been significantly increased regardless of surgical intervention. The present study therefore would have benefited from the inclusion of certain controls such as an ischemic heart and/or a heart perfused with Krebs

buffer containing insulin, both of these interventions would have increased ^{18}F -FDG uptake and served as a useful validation tool.

The development of a perfused heart system which can be incorporated into a PET scanner is a valuable technique for investigating radiotracer kinetics in the uraemic heart *in vitro*. Parameters such as uptake rate and washout can be probed without radiotracer recirculation and hormonal and neuronal interference. In addition, PET scanners can provide tomographic images highlighting regional uptake which is not possible with ^{13}C NMR and traditional gamma coincidence counters (Yamane et al., 2014). As previous studies on the uraemic heart have highlighted an impaired functional recovery to ischemia reperfusion and the presence of fibrosis (Semple et al., 2012 & Smith, 2009), this technique may be useful in localising infarcts and scar tissue in the uraemic myocardium.

4.4.4 Conclusions

Myocardial ^{18}F -FDG uptake was determined at 5, 9 and 13 weeks post-surgery. SUVs were moderately increased in the left ventricle of uraemic animals at weeks 9 and 13 of the study, though this failed to reach statistical significance at this stage. A similar pattern of ^{18}F -FDG uptake was observed using Patlak and polar map analysis at all timepoints investigated. Though limitations in the study may have masked more profound changes, collectively there was a trend towards enhanced ^{18}F -FDG uptake in uraemic hearts *in vivo*.

5. Impact of Iron Therapy on Mitochondrial Function

5.1 Introduction

Mitochondria are often referred to as the powerhouses of the cell due to their role in energy production (Abel & Doenst, 2011). In addition, mitochondria also play a key role in calcium signalling, iron homeostasis and regulating apoptotic cell death, thus determining the life and death of the cell (Kasahara & Scorrano, 2014). Previous studies have shown that treating anaemic heart failure patients with IV iron therapy can improve exercise capacity and oxygen utilisation, a mechanism potentially involving mitochondria (Finch et al., 1976). However, little is known about the impact of iron therapy on mitochondrial function in CKD.

5.1.1 *The Electron Transport Chain*

Mitochondrial ATP synthesis occurs via the transport of electrons across a series of enzyme complexes on the intricately folded IMM. Acetyl-CoA produced from fatty acid and glucose oxidation enters the TCA cycle generating reducing equivalents (NADH/FADH₂) (Kuzmicic et al., 2011). Initially these intermediates donate electrons to complex I and complex II respectively. Electrons are then transferred to complex III via the mobile electron transporter coenzyme Q (ubiquinone) and finally complex IV via cytochrome c. At complex IV, 2 electrons reduce the terminal electron acceptor, molecular oxygen, forming water (Figure 5.1) (Kuzmicic et al., 2011).

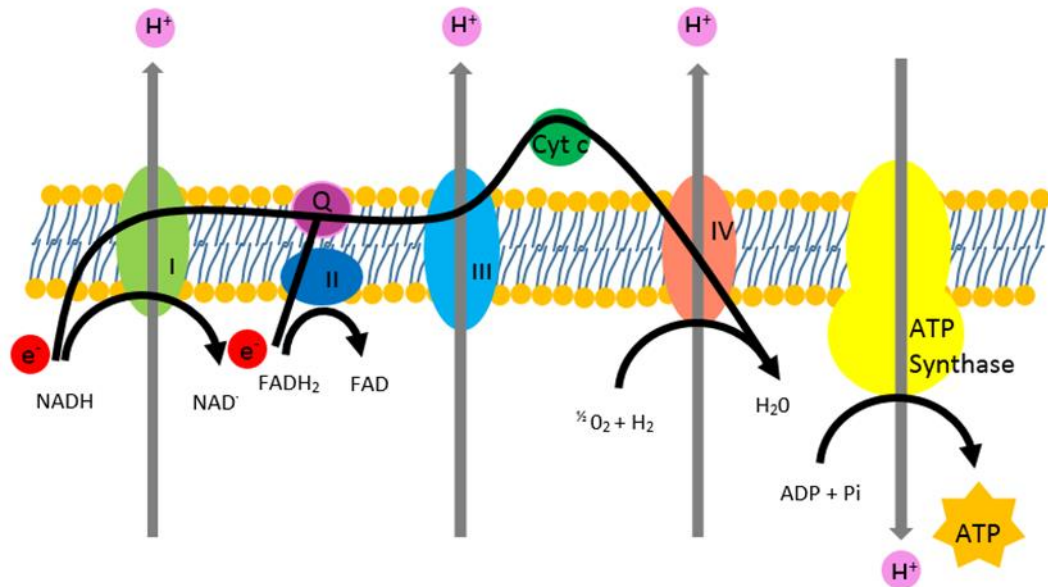


Figure 5.1. The mitochondrial electron transport chain. Adapted from Kuzmicic et al. (2011). Electrons from the reducing intermediates NADH and FADH₂ enter the electron transport chain at complexes I (I) and II (II) respectively. Electrons are then passed to complex IV (IV), via complex III (III), coenzyme Q (Q) and cytochrome c (Cyt c), where the electrons reduce molecular oxygen into water. The transfer of electrons is coupled to the translocation of protons from the matrix side of the inner membrane to the intermembrane space by complexes I, III and IV. This creates an electrochemical gradient which drives ATP synthase to generate ATP from ADP and inorganic phosphate (Pi).

Complexes I, III and IV of the electron transport chain also act as proton translocators, moving H⁺ from the matrix side of the IMM to the intermembrane space (Figure 5.1). This creates an electrochemical gradient, known as the protonmotive force (Δp), which provides energy for ATP synthase to generate ATP (Equation 3). ATP synthesis resulting from the coupling of electron transfer to proton translocation within the mitochondria is termed coupled respiration or oxidative phosphorylation (Kuzmicic et al., 2011).

$$\Delta p \text{ (mV)} = \Delta\psi_m - 60\Delta pH_m$$

Equation 3. Protonmotive force (Perry et al., 2011)

5.1.2 Reactive Oxygen Species

Although molecular oxygen can undergo complete reduction to water during oxidative phosphorylation, it can also be partially reduced to the more reactive superoxide anion ($O_2^{\cdot-}$) (Turrens, 2003). $O_2^{\cdot-}$ is the major ROS produced, predominantly from electron leakage at complex I and III of the electron transport chain. In addition, $O_2^{\cdot-}$ is also the precursor of other ROS such as hydrogen peroxide (H_2O_2) and the highly reactive hydroxyl radical (OH^{\cdot}) (Muller et al., 2004). Although under normal physiological conditions, approximately 0-2% of oxygen consumption forms $O_2^{\cdot-}$, ROS toxicity is prevented by scavenging enzymes such as superoxide dismutase, catalase and glutathione peroxidase (Kudin et al., 2004). However, mitochondrial dysfunction, which can include uncoupling of oxidative phosphorylation, can significantly increase ROS production and overcome the antioxidant capacity of these protective enzymes (Sam et al., 2005). Enhanced ROS production can damage mitochondrial DNA which encodes subunits of electron transport chain enzymes, leading to worsening mitochondrial function and further ROS generation. This creates a catastrophic cycle of ROS production, damage and gradual ATP depletion, potentially leading to mPTP opening and cell death.

5.1.3 Mitochondrial Dysfunction in the Failing Heart

Mitochondrial dysfunction is a hallmark of the failing heart, giving rise to altered myocardial bioenergetics and a decreased rate of ATP production (Rimbaud et al., 2009). Reduced ATP synthesis may be a consequence of defects in the mitochondrial energy generation machinery, manifesting as decreased ADP stimulated (state 3) respiratory rates and/or reduced respiratory complex activities. Indeed, Rosca et al. (2008) & Doenst et al. (2010) have reported significantly reduced state 3 respiratory rates in mitochondria isolated from heart failure dogs and rats respectively. In addition, Moe et al. (2004), Ide et al. (1999) and Marin-Garcia et al. (2001) have all observed reduced activities of electron transport chain enzymes in both experimental models and human heart failure patients. Furthermore, these defects are often associated with enhanced mitochondrial ROS production, including the generation of $O_2^{\cdot -}$ (Ide et al., 1999).

The rate of ATP synthesis may also be reduced by changes in the expression of key enzymes and proteins which modulate substrate oxidation. PPAR α regulates gene transcription of fatty acid oxidising enzymes as part of a transcriptional complex which also includes RXR and PGC-1 α (Lehman & Kelly, 2002). In addition, PGC-1 α is the master regulator of mitochondrial biogenesis and can be activated by ligands for PPAR α (Lehman & Kelly, 2002). Thus, down regulation of individual or multiple components of this complex in the failing heart may lead to decreased fatty acid oxidation and impaired mitochondrial biogenesis. Indeed, reduced mitochondrial density has been reported in a number of models of heart failure (Quigley et al., 2000 & Melenovsky et al., 2016).

There is a close relationship between intra-cellular calcium handling and mitochondrial energy generation. Indeed, the SR calcium transporter SERCA is one of the most energy consuming proteins in the myocyte (Luo & Anderson, 2013). In addition, calcium influx into the mitochondria can activate 3 key mitochondrial enzymes; PDH, isocitrate dehydrogenase and oxoglutarate dehydrogenase, and stimulate ATP synthase activity (Denton & McCormack, 1980). Furthermore, mitochondria can play an important role as a buffer to high cytoplasmic calcium concentrations, facilitated by the mitochondrial calcium uniporter and the organelles close proximity to the SR (Csordas et al., 2006).

However, the mitochondria's large capacity for calcium storage can become potentially lethal to the myocyte in states of stress, such as ischemia reperfusion, in which there is an abnormally high intracellular calcium concentration. Excess calcium is transported to the matrix via the mitochondrial calcium uniporter and reverse action of the mitochondrial sodium-calcium exchanger (Montero et al., 2001 & Williams et al., 2015). This increase in matrix calcium is sufficient to trigger mPTP opening, which in turn causes dissipation of the mitochondrial membrane potential and cessation of ATP production (see section 1.13). Opening of the mPTP also results in the release of pro-apoptotic proteins such as cytochrome c ultimately initiating cell death (Zorov et al., 2000).

5.1.4 Mitochondria and Iron

In addition to their role in energy generation, mitochondria are also the site of haem and iron-sulphur cluster synthesis, cofactors required for the activities of

respiratory chain enzymes (Levi & Rovina, 2009). Mitochondria therefore play a key role in cellular iron homeostasis and mitochondrial dysfunction may potentially impact on iron availability (Schueck et al., 2001). Furthermore, iron availability itself may play a key role in regulating mitochondrial fate as proteins involved iron homeostasis and mitochondrial biogenesis are highly coordinated. (Rensvold et al., 2013). Indeed, depletion of cellular iron results in a dose-dependent decrease in mitochondrial number, protein content and oxidative capacity (Rensvold et al., 2013).

5.1.5 Mitochondrial Iron Transport

TfR1 regulates iron transport into the cell via endocytosis, a process also involving the iron carrier protein, transferrin (West et al., 2000). Upon entering the cell, the imported iron can undergo one of several fates: (I) immediate use in the cytosol in its Fe^{2+} form (II) storage in the cytosol as part of ferritin or (III) transport to the mitochondria (Horowitz & Greenamyre, 2010). Although the manner in which iron is transported into the mitochondria from the cytosol is poorly understood, three mechanisms have been proposed (Levi & Rovida, 2009). The first mechanism suggests that iron is taken up by the mitochondria in its Fe^{2+} form and transported across the IMM energetically using the membrane potential (Lange et al, 1999). The second mechanism proposes that iron is transported to the mitochondria in a non-reactive form as part of a complex with chaperone-like moieties to avoid detrimental interactions in the cytosol (Shvartsman et al., 2007). Finally, Fe^{2+} may be directly transferred from endosomes to mitochondria via the transient contact of their membranes (Sheftel et al., 2007).

Metabolites can easily cross the OMM via the voltage dependent anion channel (VDAC), however, the IMM is highly impermeable and uses specialized carriers to transport elements to the mitochondria. These belong to the mitochondrial carrier family (MCF), including Mrs3 and Mrs4, both of which are thought to be involved in mitochondrial iron transport in yeast (Foury & Roganti, 2002 & Nury et al. 2006). Furthermore, human homologues of Mrs3/4 have been identified which restore growth in yeast Mrs3/4 knockout mutations suggesting the proteins are highly conserved, however, the role of Mrs3/4 in mammalian mitochondrial iron transport has yet to be elucidated (Li et al., 2001). Another member of the MCF is mitoferrin-1 (mfrn), a mammalian homologue of the frs protein, first identified in zebrafish by Ransom et al. (1996). Knockout of frs in zebrafish resulted in hypochromic anaemia, due to defects in mitochondrial iron uptake, which could be corrected via transfection with murine mfrn suggesting a potential role in mammalian mitochondrial iron import (Shaw et al., 2006).

5.1.6 Mitochondrial Iron Handling

Mitochondrial Fe^{2+} can react with H_2O_2 , via the Fenton reaction, to produce $\text{OH}\cdot$, a highly reactive ROS which can stimulate mPTP opening (Assaly et al., 2012) (Figure 5.2). Therefore it is critical that cellular iron is carefully handled and stored in a bio-available and safe form (Levi & Rovida, 2009). Although iron processing within the mitochondria is incompletely understood, several proteins are thought to play key roles in mitochondrial iron homeostasis. The protein frataxin has been linked to iron related functions within the mitochondria, including acting as a chaperone for

Fe^{2+} and as an iron storage protein (Park et al., 2002). Frataxin has also been found to associate with, and regulate, other proteins involved in haem and iron-sulphur cluster synthesis (Gonzalez-Cabo et al., 2005, Muhlenhoff et al., 2002 & Zhang et al., 2006).

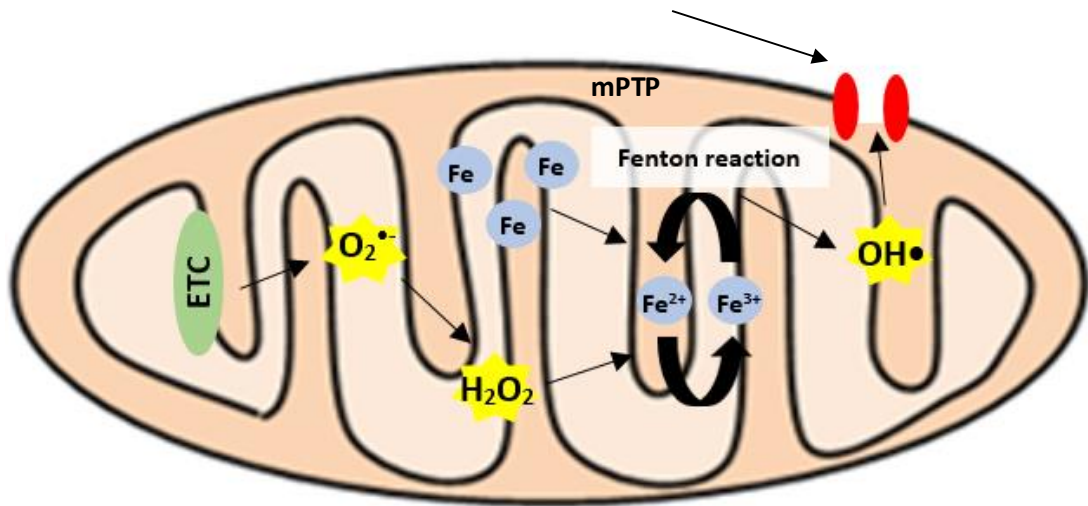


Figure 5.2. The Fenton reaction. Superoxide ($\text{O}_2^{\cdot-}$) produced from the electron transport chain (ETC) can react with free iron and hydrogen peroxide (H_2O_2) within the mitochondria to form the highly reactive hydroxyl radical ($\text{OH}\cdot$), via the Fenton reaction, which can trigger mitochondrial permeability transition pore (mPTP) opening.

Another protein linked to mitochondrial iron processing is mitochondrial ferritin (MtFt) which is exclusively found in metabolically active cells such as cardiomyocytes (Santambrogio et al., 2007). Similar to cytosolic ferritin, the primary role of MtFt is iron storage and detoxification, however, MtFt is not ubiquitously expressed and likely acts as a reserve in times of metabolic demand (Levi & Rovida, 2009). Indeed, previous studies have demonstrated that MtFt expression can modulate the activities of electron transport chain enzymes such as respiratory complex II (Campanella et al., 2009). Furthermore, iron alone is sufficient to enhance expression of MtFt (Campanella et al., 2009).

5.1.7 Objectives

Evidence suggests that changes in cellular iron homeostasis may modulate mitochondrial function. However, iron excess can also have deleterious consequences for the cell as Fe^{2+} is the precursor for ROS generation, via the Fenton reaction, which can stimulate mPTP opening. Hence the aim of the work described in this chapter was to:

- Investigate the effect of ferumoxytol administration on mitochondrial respiratory rates and enzyme activities
- Assess the impact of iron therapy on calcium induced mitochondrial swelling

5.2 Methods

5.2.1 *Experimental design*

Sham surgery or sub-total nephrectomy was induced in 60 male Sprague-Dawley rats as described in section 2.1. This gave rise to the following experimental groups:

- Control (n=15)
- Uraemic (n=15)
- Control + ferumoxytol treatment (n=15)
- Uraemic + ferumoxytol treatment (n=15)

Six weeks post surgery, the iron complex, ferumoxytol (Rienso, Takeda, Japan), was administered as a single IV bolus injection (10mg/kg), via the tail vein. Saline was administered as a control. Animals were sacrificed 6 weeks later, at 12 weeks post-surgery. Immediately following sacrifice, Cardiac mitochondria were isolated and mitochondrial function was assessed as described below.

5.2.2 *Isolation of Cardiac Mitochondria*

Animals were anaesthetised and hearts removed as described in section 2.3.1. Cardiac mitochondria were then isolated as described in section 2.3.1.

5.2.3 Mitochondrial Respiratory Rates

Mitochondrial oxygen consumption was measured in isolated mitochondria using a Clark-type oxygen electrode as described in section 2.3.2. Mitochondrial state 3 and state 4 respiratory rates were measured in the presence of the following substrates:

- 5mM glutamate & 1mM malate – These substrates provide carbon sources for dehydrogenase reactions in the TCA cycle that generate NADH, which is subsequently oxidized by complex I.
- 5mM succinate & 1 μ M rotenone – Rotenone induces a redox shift that effectively inhibits all of the NADH-linked dehydrogenases in the TCA cycle. Thus, in the presence of rotenone, succinate selectively stimulates electron flow through complex II.
- 40 μ M palmitoyl carnitine & 5mM malate – ATP production as a result of fatty acid β -oxidation can be assessed using these substrates, which provide electron flow through electron-transferring flavoprotein.

Therefore, the use of these individual substrate combinations facilitated the investigation of potential dysfunction in the mitochondria's ability to synthesize ATP via electron transfer through complexes I, II and fatty acid β -oxidation.

5.2.4 Mitochondrial Enzyme Activities

Activities of mitochondrial respiratory complexes I, II, II+III and IV were assayed in isolated freeze/thawed mitochondria as described in sections 2.3.3.1 – 2.3.3.4. Citrate synthase activities were evaluated in isolated mitochondria as described in 2.3.3.5.

5.2.5 Calcium induced mitochondrial swelling

Initial rates of mitochondrial swelling were determined in isolated mitochondria in the presence of either 0, 40, 60 or 80 μ M calcium as described in 2.3.4.

5.3 Results

5.3.1 Mitochondrial Respiratory Rates

ADP stimulated state 3 respiratory rates were similar in control and uraemic cardiac mitochondria, irrespective of the substrates used (Figure 5.3). However, state 4 respiratory rates were significantly increased in uraemic mitochondria in the presence of glutamate & malate and succinate & rotenone, indicative of decreased mitochondrial efficiency (Figure 5.4). As state 3 rates were unaltered in uraemia and state 4 rates elevated, the respiratory control ratio (RCR) was significantly reduced when glutamate & malate were used as substrates (Figure 5.5). State 3 and state 4 respiratory rates were similar in ferumoxytol treated and untreated groups suggesting iron therapy had little impact on mitochondrial respiration (Figures 5.3 – 5.5).

State 3 Respiration

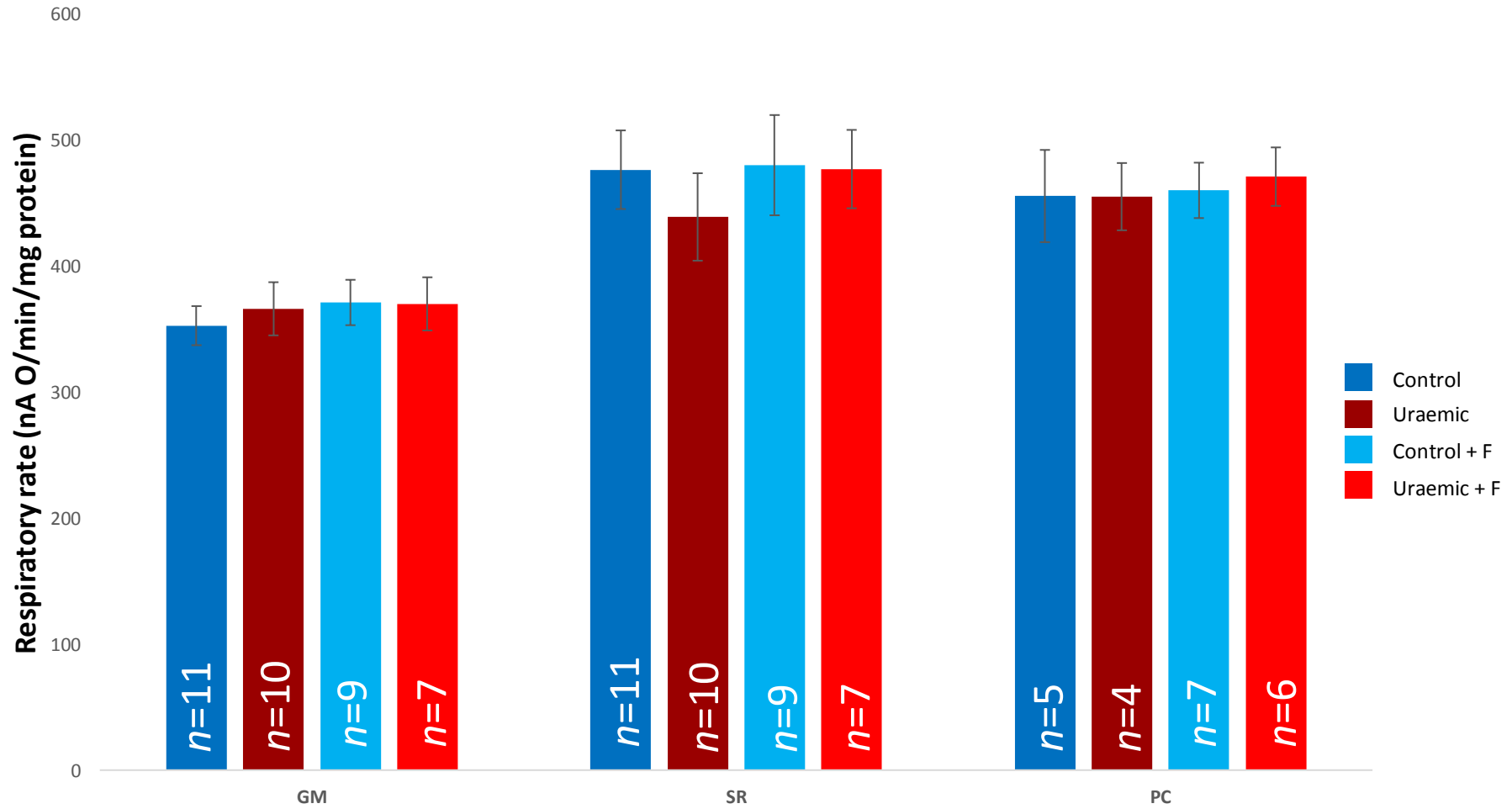


Figure 5.3. Mitochondrial state 3 respiratory rates. Data are presented as mean \pm SEM. GM = 5mM glutamate & 1mM malate, SR = 5mM Succinate & 1µM rotenone, PC = 40µM Palmitate carnitine & 1mM malate. F = ferumoxytol

State 4 Respiration

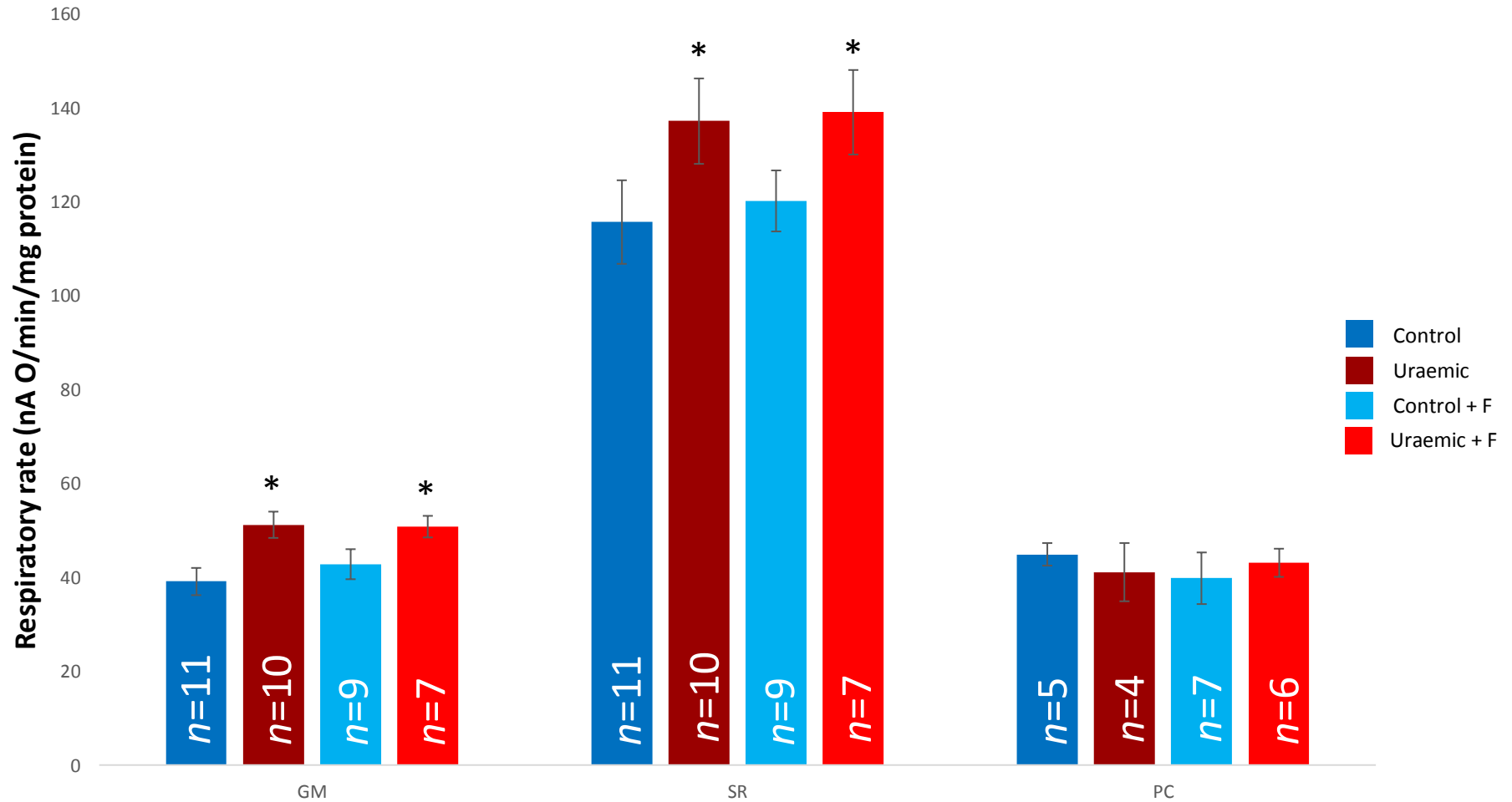


Figure 5.4. Mitochondrial state 4 respiratory rates. Data are presented as mean \pm SEM. GM = 5mM glutamate & 1mM malate, SR = 5mM Succinate & 1 μ M rotenone, PC = 40 μ M Palmitate carnitine & 1mM malate. * = $p < 0.05$ vs control. F = ferumoxytol

Respiratory Control Ratio

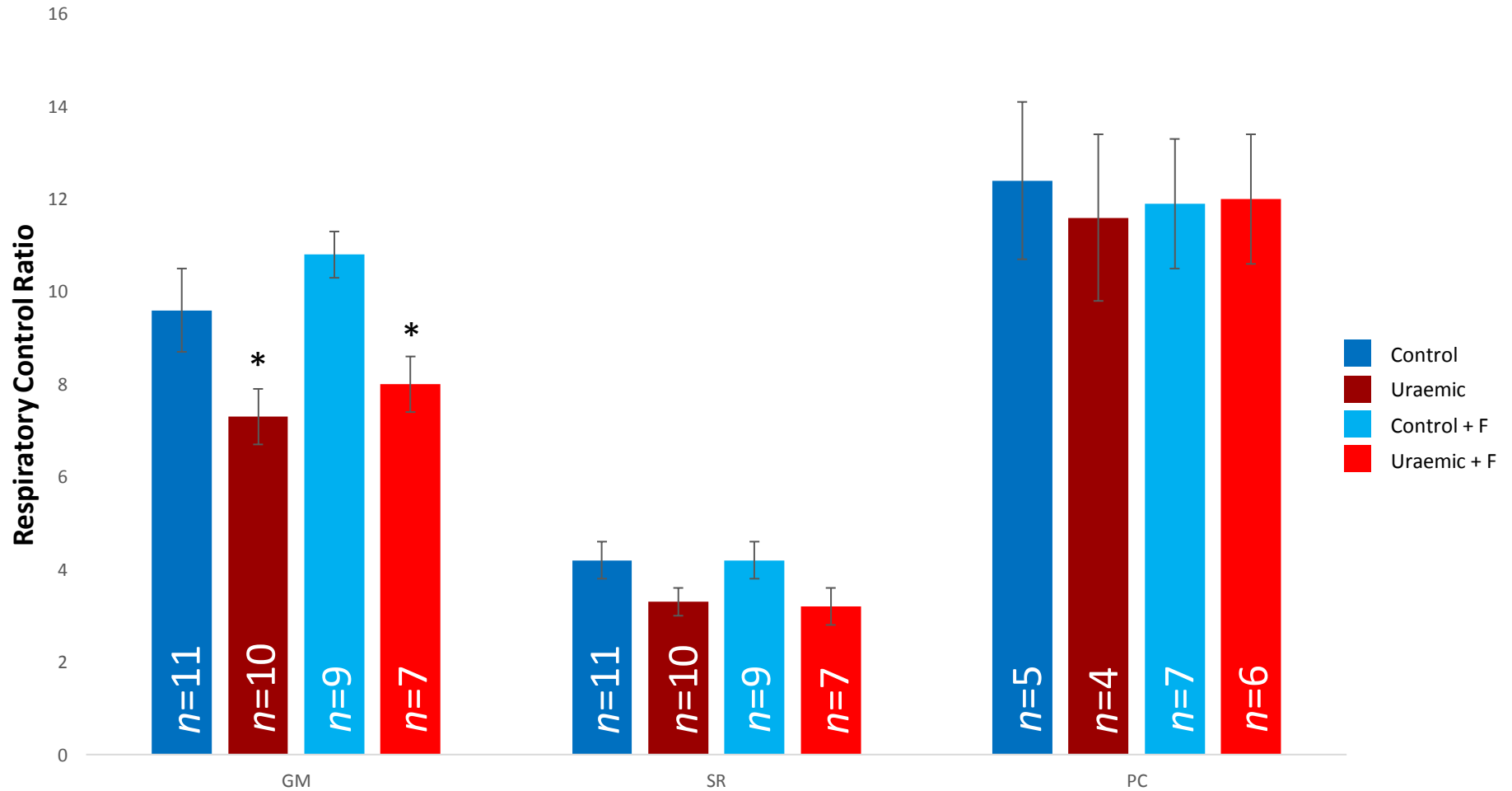


Figure 5.5. Mitochondrial respiratory control ratio. Data are presented as mean \pm SEM. GM = 5mM glutamate & 1mM malate, SR = 5mM Succinate & 1 μ M rotenone, PC = 40 μ M Palmitate carnitine & 1mM malate. * = p < 0.05 vs control. F = ferumoxytol

5.3.2 Mitochondrial Enzyme Activities

5.3.2.1 Citrate Synthase Activities

Protein concentrations and citrate synthase activities were similar in mitochondrial pellets isolated from hearts of all experimental groups, highlighting comparable degrees of mitochondrial density (Table 5.1)

Table 5.1

Protein concentration and citrate synthase activity of mitochondrial pellets

	Untreated		Ferumoxytol	
	Control	Uraemic	Control	Uraemic
Protein concentration (mg/ml)	26 ± 1.6 (n=13)	27.6 ± 1.8 (n=11)	28.2 ± 3.4 (n=9)	27.6 ± 1.7 (n=7)
Citrate synthase activity (µmol/min/mg protein)	229.2 ± 13.7 (n=13)	211.5 ± 14.3 (n=11)	212.2 ± 12.7 (n=9)	222.2 ± 10 (n=7)

Data are presented as mean ± SEM.

5.3.2.2 Respiratory Complex Activities

Mitochondrial respiratory complex activities were similar in the control and uraemic groups at baseline and following iron therapy (Table 5.2).

Table 5.2*Mitochondrial enzyme activities*

	Untreated		Ferumoxytol	
	Control	Uraemic	Control	Uraemic
Complex I (mmol/min/mg protein)	1.75 ± 0.1 (n=13)	1.62 ± 0.09 (n=11)	1.67 ± 0.08 (n=9)	1.7 ± 0.1 (n=7)
Complex II (mmol/min/mg protein)	0.71 ± 0.02 (n=13)	0.67 ± 0.03 (n=11)	0.73 ± 0.03 (n=9)	0.69 ± 0.03 (n=7)
Complex II + III (mmol/min/mg protein)	1.05 ± 0.05 (n=12)	1 ± 0.06 (n=11)	1.09 ± 0.05 (n=9)	1.12 ± 0.05 (n=6)
Complex IV (k/min/mg protein)	820.3 ± 13 (n=13)	802.4 ± 14.1 (n=11)	811 ± 9 (n=9)	824.1 ± 13.7 (n=7)

Data are presented as mean ± SEM.

5.3.3 Calcium Induced Mitochondrial Swelling

Representative time courses from which initial rates of mitochondrial swelling were calculated are shown in Figure 5.6 & Figure 5.7. Control and uraemic mitochondria isolated from ferumoxytol treated and untreated animals exhibited similar rates of swelling in the absence of calcium (Figure 5.8). However, the addition of 40µM calcium resulted in a rapid increase in mitochondrial swelling in all experimental groups which was significantly reduced by treatment with CsA (Figure 5.9). A similar pattern in mitochondrial swelling was observed upon treatment with 60µM & 80µM calcium (Figure 5.10 & Figure 5.11). Overall no differences in swelling rates were observed between control or uraemic mitochondria isolated from either ferumoxytol treated or untreated animals.

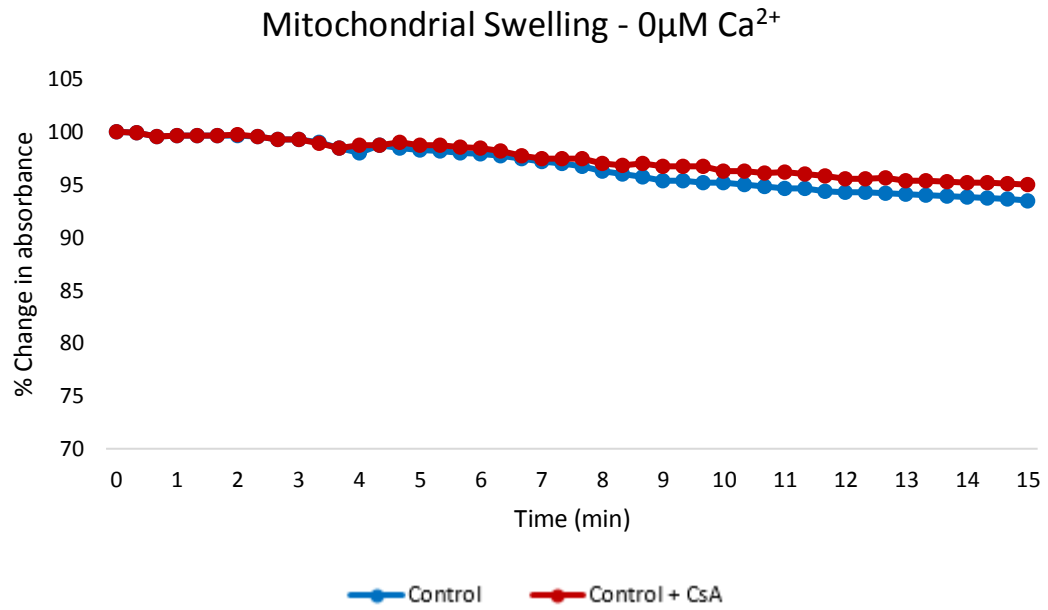


Figure 5.6. Representative time course of mitochondrial swelling determined as a decrease in light absorption at 560nm in the presence of 0 μ M calcium. Absorbance changes expressed as percentages relative to initial absorbance. CsA = cyclosporine A

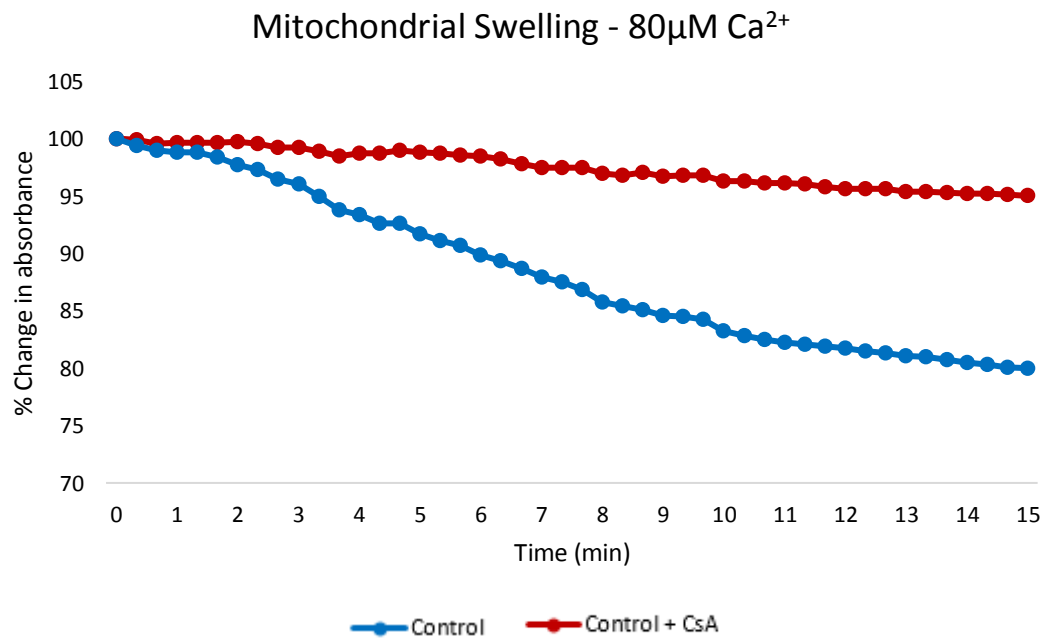


Figure 5.7. Representative time course of mitochondrial swelling determined as a decrease in light absorption at 560nm in the presence of 80 μ M calcium. Absorbance changes expressed as percentages relative to initial absorbance. CsA = cyclosporine A

Initial Rate of Swelling - Basal

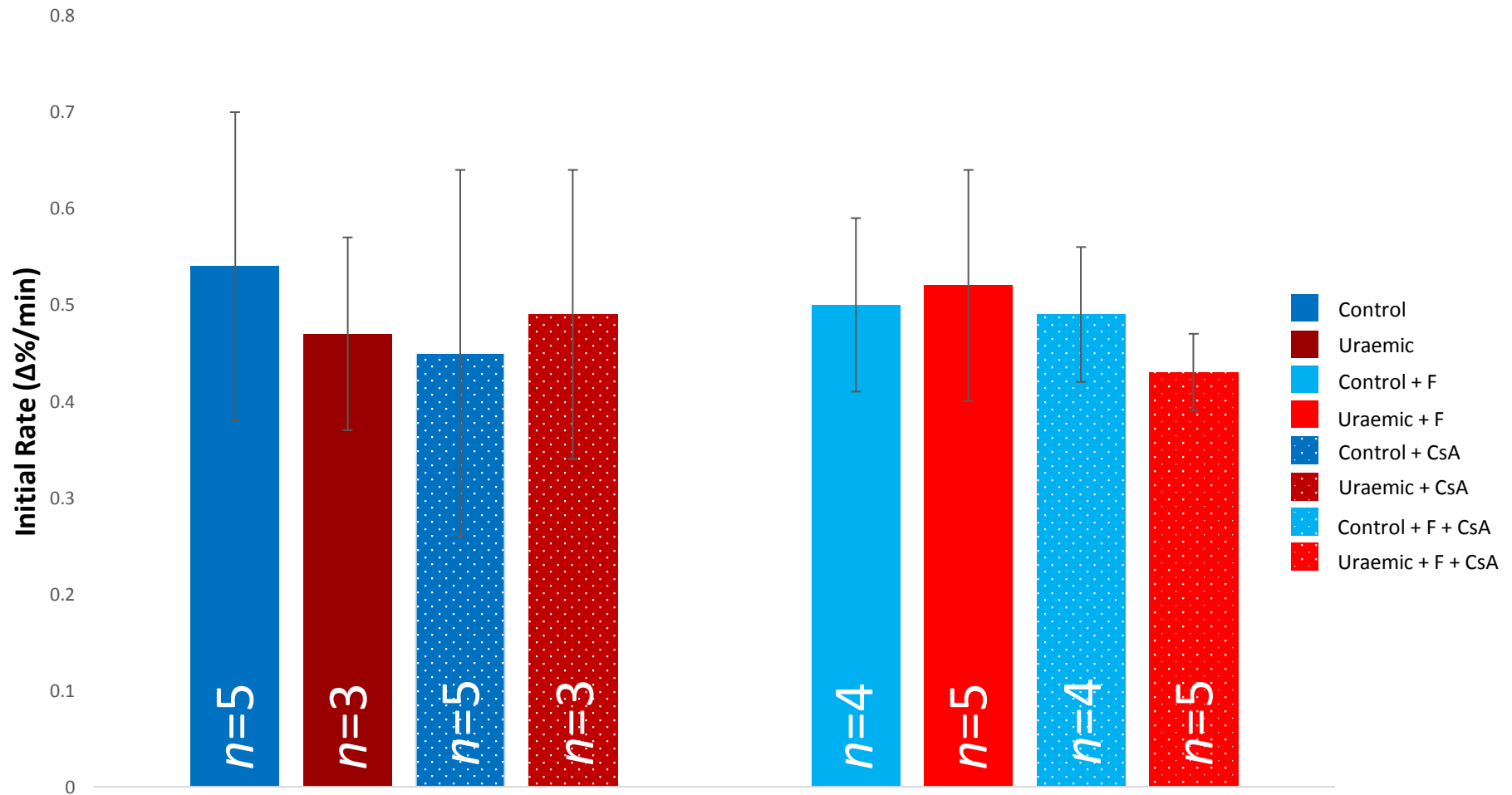


Figure 5.8. Initial rate of mitochondrial swelling in the absence of calcium. Data are presented as mean \pm SEM. F = ferumoxytol, CsA = cyclosporine A

Initial Rate of Swelling - 40 μ M Ca²⁺

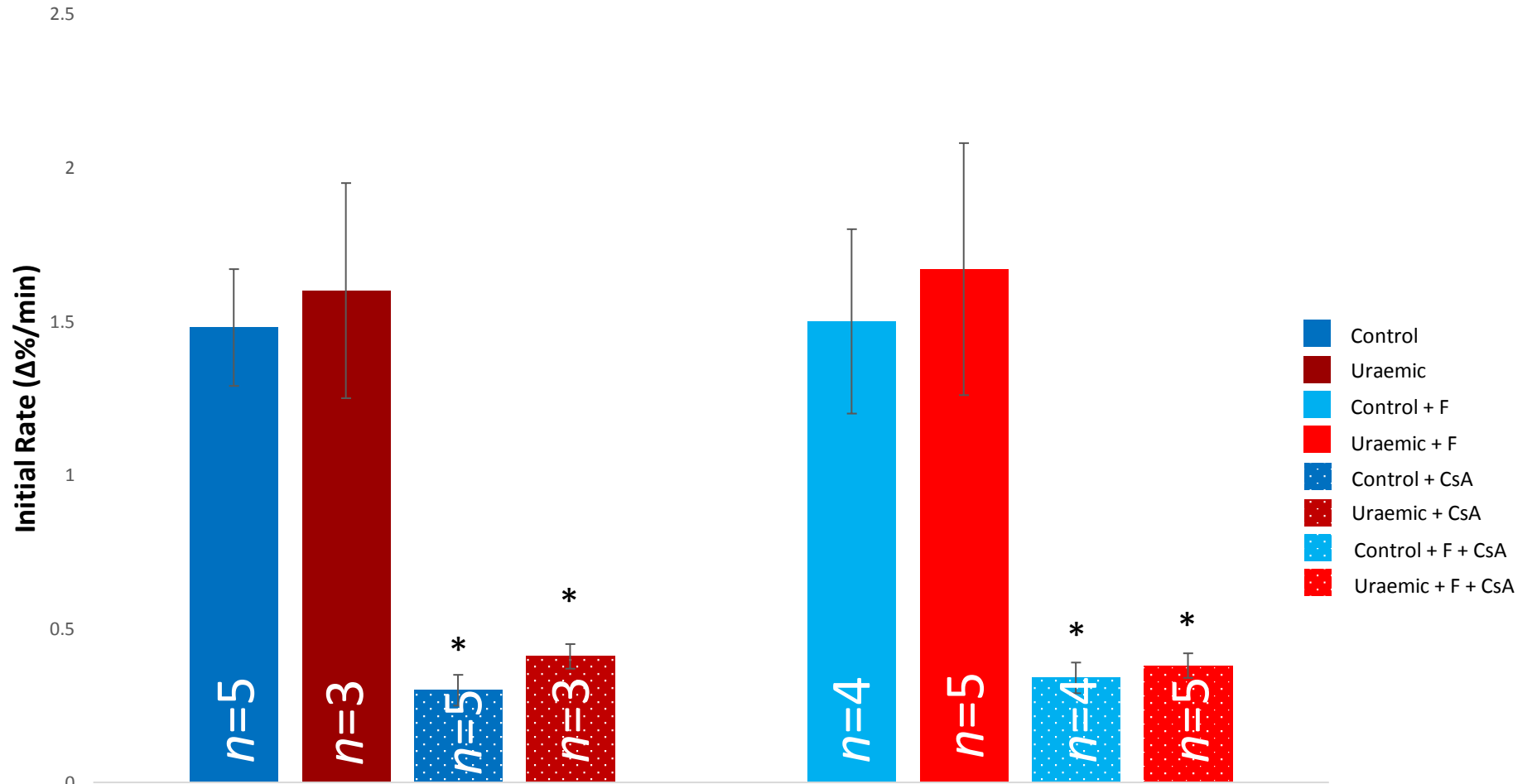


Figure 5.9. Initial rate of mitochondrial swelling in the presence of 40 μ M calcium. Data are presented as mean \pm SEM. F = ferumoxytol, CsA = cyclosporine A. * = $p < 0.05$ vs non-cyclosporine A treated group.

Initial Rate of Swelling - 60 μ M Ca²⁺

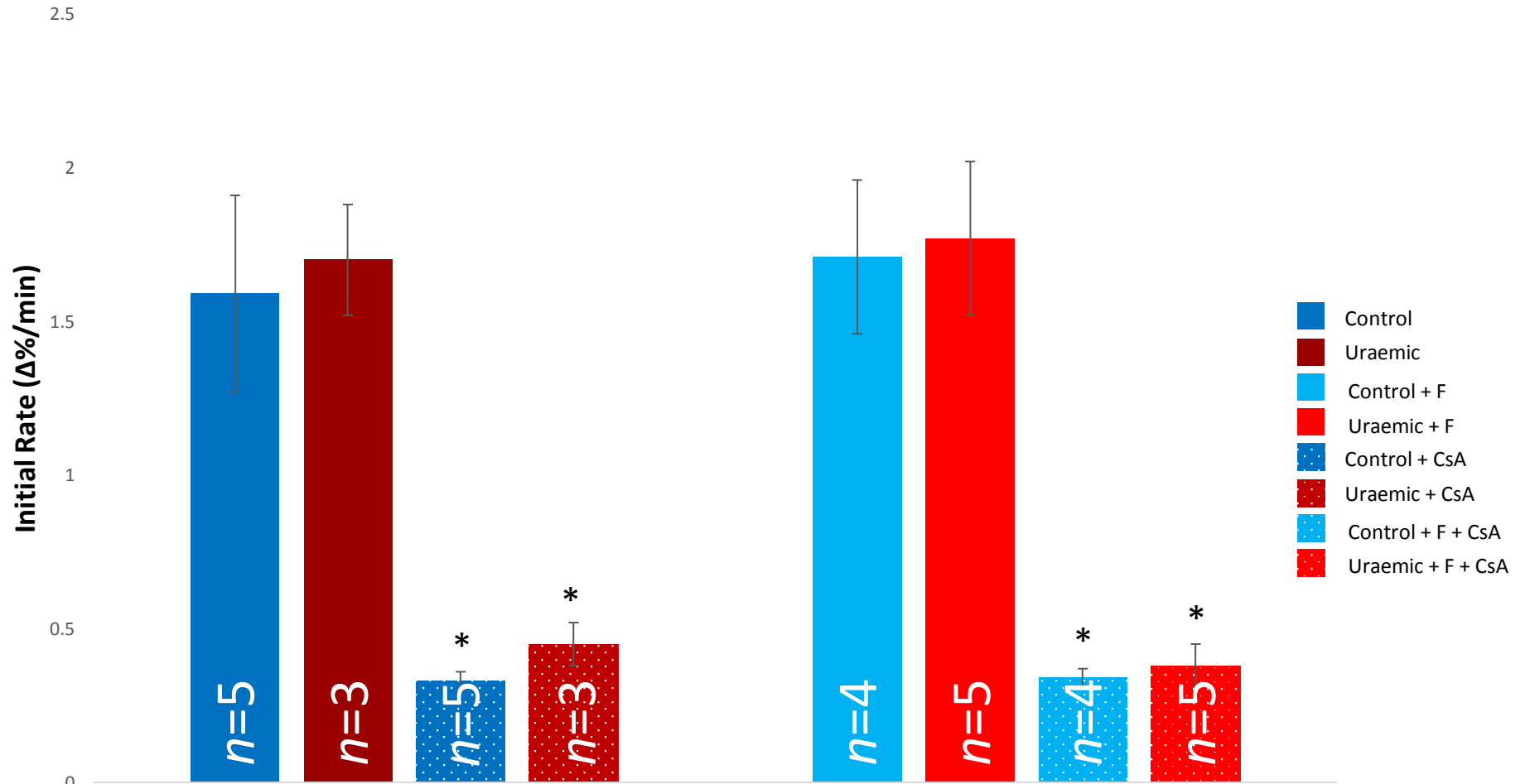


Figure 5.10. Initial rate of mitochondrial swelling in the presence of 60 μ M calcium. Data are presented as mean \pm SEM. F = ferumoxytol, CsA = cyclosporine A. * = $p < 0.05$ vs non-cyclosporine A treated group.

Initial Rate of Swelling - 80 μ M Ca²⁺

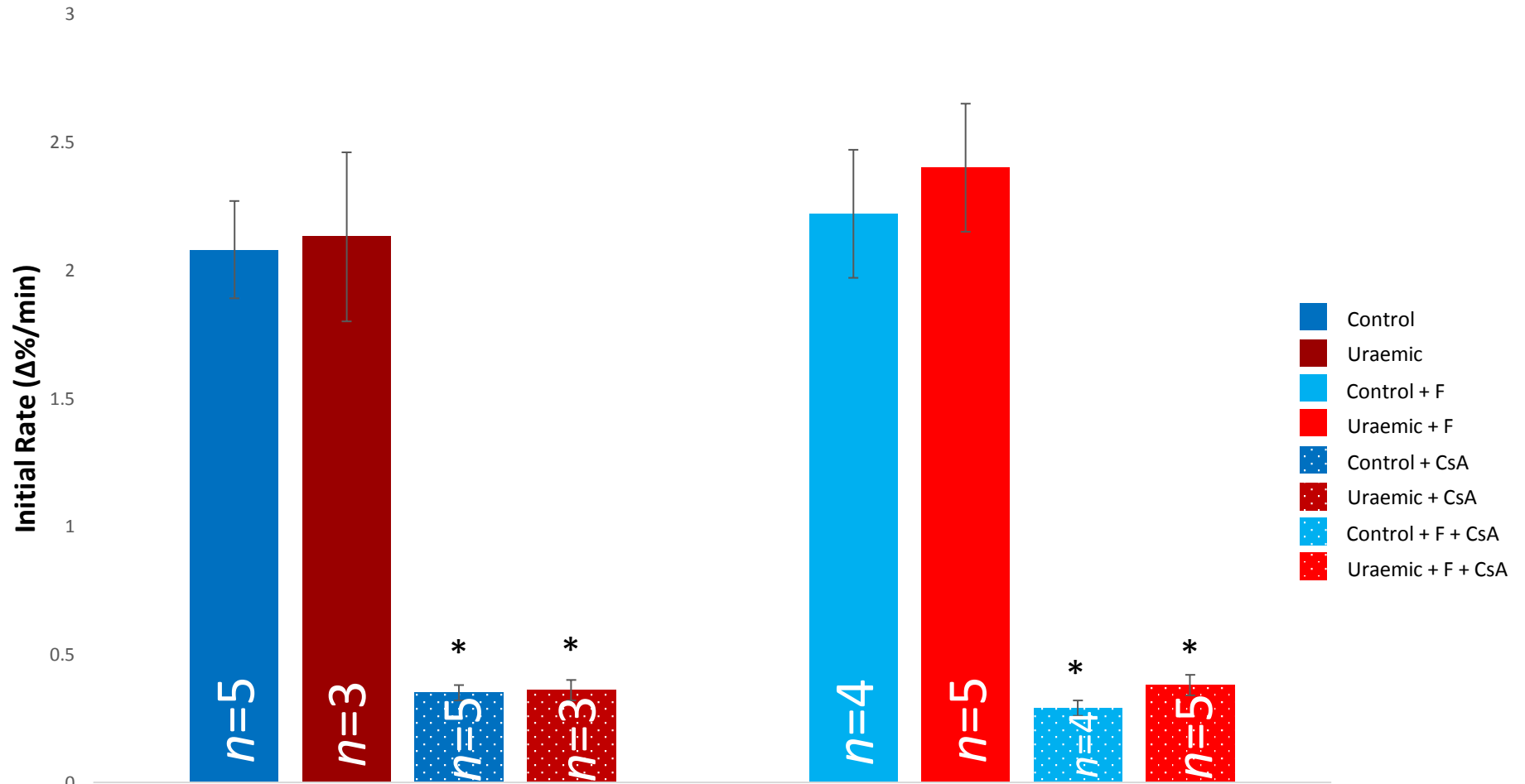


Figure 5.11. Initial rate of mitochondrial swelling in the presence of 80 μ M calcium. Data are presented as mean \pm SEM. F = ferumoxytol, CsA = cyclosporine A. * = $p < 0.05$ vs non-cyclosporine A treated group.

5.4 Discussion

This study has shown that 12 weeks uraemia resulted in altered mitochondrial bioenergetics characterised by increased state 4 respiratory rates. As state 3 respiration remained unaltered, the RCR (state 3/state 4) was consequently reduced, indicative of decreased mitochondrial efficiency. No changes in cardiac mitochondrial enzyme activities or mitochondrial swelling parameters were observed in uraemia. Ferumoxytol administration had little impact on any markers of mitochondrial function that were assessed.

5.4.1 Mitochondrial Respiratory Rates

5.4.1.1 State 3 Respiration

State 3 respiratory rates were comparable in cardiac mitochondria isolated from control and uraemic animals with all substrates used (Figure 5.3). State 3 respiration is controlled by ADP availability, ATP turnover (ATP synthase and ANT) and substrate availability, and inhibition of any of these processes could result in impaired respiration (Brand & Nicholls, 2011). As state 3 rates were similar between experiment groups, it is likely this stage of uraemia did not impact on these processes *in vitro*.

Many studies have observed impaired state 3 respiratory rates in a number of different models of heart failure. Rosca et al. (2008) reported a 50% reduction in ADP stimulated respiration in cardiac mitochondria isolated from dogs exposed to coronary microembolization-induced heart failure. Although individual respiratory

complex activities were conserved, there was a defect in the electron transport chain supercomplex (complex I, complex III & complex IV) possibly due to impaired assembly. Doenst et al. (2010) observed a 70% decrease in state 3 respiratory rates in cardiac mitochondria isolated from rats following 20 weeks of aortic constriction. Bugger et al. (2010) reported similar findings in another pressure-overload rat model of heart failure over the same time frame. In addition, the reduced state 3 respiratory rates were associated with a 50% decrease in electron transport chain protein in failing hearts. This may have contributed to the impaired respiratory function of cardiac mitochondria in the model. Indeed, a decrease of approximately 30% in mitochondrial protein content has been reported as being functionally relevant (Johnson et al., 2007).

Little data exist on mitochondrial function in the compensatory phase of cardiac hypertrophy. However, the study by Doenst et al. (2010) reported mitochondrial respiratory rates at 10 weeks, during the compensatory phase of hypertrophy, in addition to the 20 week data. They observed similar rates of state 3 respiration in cardiac mitochondria isolated from control and aortic constricted animals, similar to the control and uraemic groups in the present study. This would suggest that mitochondrial state 3 respiration is conserved at this stage of compensated cardiac hypertrophy in the uraemic model.

Ferumoxytol treatment did not modify mitochondrial state 3 respiration in control or uraemic mitochondria (Figure 5.4). Oxele et al. (1999) conducted a study to investigate the impact of iron perturbations on oxidative phosphorylation and mitochondrial enzyme activities in the K-562 human cell line. They observed

enhanced activities of several mitochondrial enzymes including aconitase and isocitrate dehydrogenase upon supplementation with FeCl₂. Although the study did not investigate the impact of iron supplementation on mitochondrial respiration, cellular ATP content was significantly increased suggesting enhanced oxidative phosphorylation. In addition, this study also revealed that the addition of the iron chelator, desferrioxamine, significantly reduced mitochondrial respiration. Collectively these data indicate that cellular iron content played a key role in modulating mitochondrial energy generation. However, a number of methodological differences exist between that and the present study making a direct comparison difficult. For example, no state 4 respiration or RCR data were reported and it was unclear if desferrioxamine treatment impacted on other iron dependent functions in the cell which may have contributed to the decline in mitochondrial respiration. In addition, serum ferritin was not increased in either the control or uraemic group in the present study despite ferumoxytol treatment (see section 3.3.2.2). This suggested that the dosing regimen or iron therapy alone was insufficient to stimulate iron uptake into the tissues, possibly underpinning the blunted mitochondrial response to iron therapy observed here.

5.4.1.2 State 4 Respiration

Mitochondrial state 4 respiratory rates were significantly increased in uraemic mitochondria when glutamate & malate and succinate & rotenone were used as substrates (Figure 5.4). However, no significant changes in respiration were observed when palmitoyl carnitine & malate were used. These findings are consistent

with previous studies on this model (Taylor et al., 2015). Ferumoxytol administration had little impact on state 4 respiration in both groups suggesting iron therapy did not modify mitochondrial efficiency (Figure 5.4). Collectively these data indicate an uncoupled mitochondrial phenotype at this stage of cardiac hypertrophy in uraemia.

Enhanced state 4 rates are somewhat rare in models of heart failure as the majority of studies report decreased state 3 respiration through reduced mitochondrial number or function rather than evidence of uncoupling. However, Heather et al. (2010) reported significantly increased uncoupled respiration associated with conserved state 3 rates in the hyperthyroid rat heart. They hypothesised that upregulation of uncoupling protein (UCP) 2/3 may have underpinned such changes. UCPs have been proposed to protect the heart against ROS mediated damage in increased states of stress by catalysing the dissipation of the mitochondrial membrane potential and increasing permeability of the IMM (Laskowski & Russell, 2008). However, the exact role of UCPs is still unclear as increased uncoupling is energetically unfavourable (Boehm et al., 2001). In addition, UCP2 and 3 expression are unaltered in uraemia suggesting an alternative means of uncoupling (Taylor, 2014).

5.4.1.3 Respiratory Control Ratio

Given the change in state 4 respiration, the RCR was markedly decreased in uraemic mitochondria in the presence of glutamate & malate and succinate & rotenone as substrates, although the latter narrowly failed to reach statistical significance (Figure 5.5). Studies of heart failure have demonstrated more

pronounced changes in RCRs resulting from markedly reduced state 3 rates as discussed previously (Doenst et al., 2010; Bugger et al., 2010 & Rosca et al., 2008). A high RCR indicates that the mitochondria have a high oxidative capacity and are well coupled (Brand & Nicholls, 2011). On the other hand, a low RCR could demonstrate that the mitochondria either have a low capacity for substrate oxidation and/or are uncoupled as observed here, which may contribute to energy deficiency in the uraemic heart (Raine et al., 1993).

5.4.2 Mitochondrial Enzyme Activities

5.4.2.1 Citrate Synthase

Citrate synthase activities were similar in mitochondrial pellets isolated from both control and uraemic animals irrespective of ferumoxytol treatment (Table 5.1). Citrate synthase is considered an important marker of mitochondrial content and oxidative capacity and has been shown to be reduced in both heart failure patients and experimental models of heart failure. Indeed, Quigley et al. (2000) observed significantly reduced citrate synthase activities in patients suffering from idiopathic dilated cardiomyopathy. Garnier et al. (2003) reported similar findings in aortic constricted heart failure rats. However, experimental models of pressure-overload induced cardiac hypertrophy have demonstrated citrate synthase activities remain unaltered (Nishio et al., 1995 & Iemitsu et al., 2003). This is consistent with the present study and suggests that mitochondrial density matches the energetic requirements of the heart during the compensated phase of cardiac hypertrophy.

5.4.2.2 Mitochondrial Respiratory Complex Activities

At 12 weeks post-induction of uraemia, mitochondrial respiratory complex activities were unchanged (Table 5.2). In addition, ferumoxylol treatment did not alter respiratory complex activities in control or uraemic mitochondria (Table 5.2). These findings are consistent with data on mitochondrial respiration (see section 5.3.1). In tandem with altered state 3 respiration, studies of heart failure have revealed depressed respiratory complex activities contributing to impaired bioenergetics. Jarreta et al. (2000) found significantly reduced complex III activities in patients diagnosed with idiopathic dilated cardiomyopathy. Furthermore, Marin-Garcia et al. (1995) reported a range of individual and multiple complex defects in patients with the same condition. Of these, complex I was the most common single deficiency and complexes III and IV the most frequent combined defect. Depressed complex II and complex III activities were reported by Lashin et al. (2006) in rats with diabetic cardiomyopathy, a model which shares some common features, such as altered substrate metabolism and calcium handling, with the uraemic heart. Defects in the electron transport chain can have deleterious consequences and lead to increased generation of ROS, resulting in damage to the mitochondria and ultimately cell death (see section 5.1.2).

Iron deficiency has been shown to lead to mitochondrial dysfunction (Schueck et al., 2001). Reduced iron availability and uptake into the mitochondria can result in impaired iron-sulphur cluster incorporation into redox enzymes in the respiratory chain. Interestingly, this in turn can actually lead to iron accumulation as enhanced ROS production can catalyse the oxidation of Fe^{2+} into an insoluble form of

Fe³⁺, which then becomes trapped in the mitochondrial matrix (Lichtenstein et al., 2016). Although anaemia is a feature of the present model it is unclear if it leads to mitochondrial iron deficiency. Indeed, studies have demonstrated conserved mitochondrial respiratory chain activities despite the presence of anaemia, suggesting myocardial iron deficiency and systemic anaemia may be differentially regulated (Melenovsky et al., 2016). Although the mechanisms are poorly understood, this would go some way to explaining the results observed in the present study.

5.4.3 Calcium Induced Mitochondrial Swelling

Initial rates of mitochondrial swelling in the absence of calcium were similar in control and uraemic mitochondria isolated from ferumoxytol treated and untreated animals (Figure 5.8). Incremental increases in calcium concentration were associated with a decrease in light absorption at 540nm, indicative of increased mitochondrial swelling (Figure 5.9 – Figure 5.11). However, the presence of CsA inhibited swelling to similar degrees, regardless of calcium concentration. CsA is a potent inhibitor of mPTP formation in isolated mitochondria and acts by binding, and thereby inhibiting, CyP-D, the key regulator of pore opening (Crompton et al., 1988). Indeed, both ROS and calcium overload are sufficient to trigger mPTP formation (Elrod & Molkenin, 2013). Furthermore, increased cellular iron can catalyse ROS formation via the Fenton reaction, however, the results observed here suggest that ferumoxytol treatment did not contribute to enhanced mPTP opening in isolated mitochondria.

While ferumoxytol did not improve haematocrit or mitochondrial function in this study, it is unclear if using an alternative iron preparation would have proved more successful. Indeed, while both oral iron and other IV compounds have corrected anaemia in several different animal models, none of these studies investigated mitochondrial function (Egeli & Framstad, 1998; Tait & Dureski, 1979 & Reece et al., 1985). Furthermore, all IV iron compounds have a very similar mode of action (see section 3.1.3.2) and ferumoxytol has been shown to ameliorate anaemia in rats, though the effective dose was not reported (European Medicines Agency, 2012). This suggests that the dosing regimen or iron therapy alone was insufficient and not ferumoxytol itself.

5.5 Conclusions

Induction of uraemia resulted in significantly increased state 4 respiratory rates in cardiac mitochondria, indicative of uncoupling. While ADP stimulated respiratory rates were unchanged, the increase in uncoupled respiration resulted in a significantly reduced RCR suggesting inefficiency. This may be of importance when the uraemic heart is exposed to stress and merits further investigation. Individual respiratory complex activities were conserved in uraemia as were initial rates of calcium induced mitochondrial swelling. Administration of ferumoxytol had no effect on any markers of mitochondrial function that were assessed.

6. Mitochondrial Morphology

6.1 Introduction

6.1.1 *Mitochondrial Dynamics*

Mitochondria are highly dynamic organelles, maintaining a large integrated network by constantly undergoing fusion and fission (Chen & Chan, 2010). These events determine the intracellular distribution, number and individual morphology of mitochondria within the cardiomyocyte (Marin-Garcia & Akhmedov, 2013). Maintaining the delicate balance between these processes is of particular importance in energy demanding organs such as the myocardium. A shift towards fusion will result in an overall reduced number of mitochondria that are large in size, whereas a shift towards fission will result in numerous small fragmented mitochondria (Marin-Garcia & Akhmedov, 2013) (Figure 6.1).

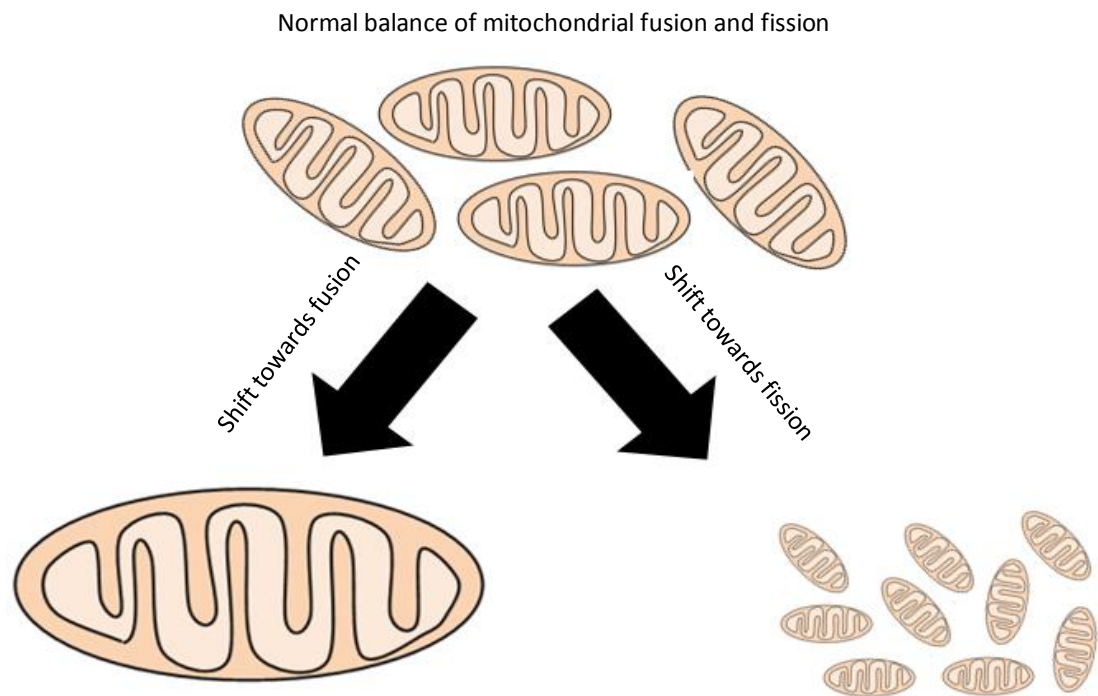


Figure 6.1. The balance of mitochondrial dynamics. Under normal physiological conditions mitochondria maintain a delicate balance of fusion and fission. However, pathological stress can result in a shift towards fusion resulting in giant mitochondria, or fission resulting in numerous small fragmented mitochondria.

6.1.2 Mitochondrial Fusion

Fusion facilitates the transfer of genetic material, proteins, ATP and other soluble components from one mitochondrion to another (Margineantu et al., 2002). This enables the restoration of function to damaged/dysfunctional mitochondria via functional complementation (Ong & Hausenloy, 2010). However, complete fusion of the inner and outer membranes is a complex sequence of events and must occur fully to allow adequate exchange of matrix components (Chen et al., 2005). Therefore a number of key proteins are involved in maintaining mitochondrial shape and integrity.

Mitofusin (MFN) 1 and 2 are transmembrane proteins localised to the OMM and regulate outer membrane fusion. (Dorn II, 2013). The mitofusins, discovered in 2001, are mammalian homologues of fuzzy onions protein (Fzo1p), first identified in drosophila development by Hales and Fuller (1997). MFN1 and 2 are structurally similar, consisting of a GTPase domain at the amino terminal, a heptad repeat, two closely related transmembrane domains and a second heptad repeat at the carboxyl terminal (Figure 6.2) (Koshiba et al., 2004).

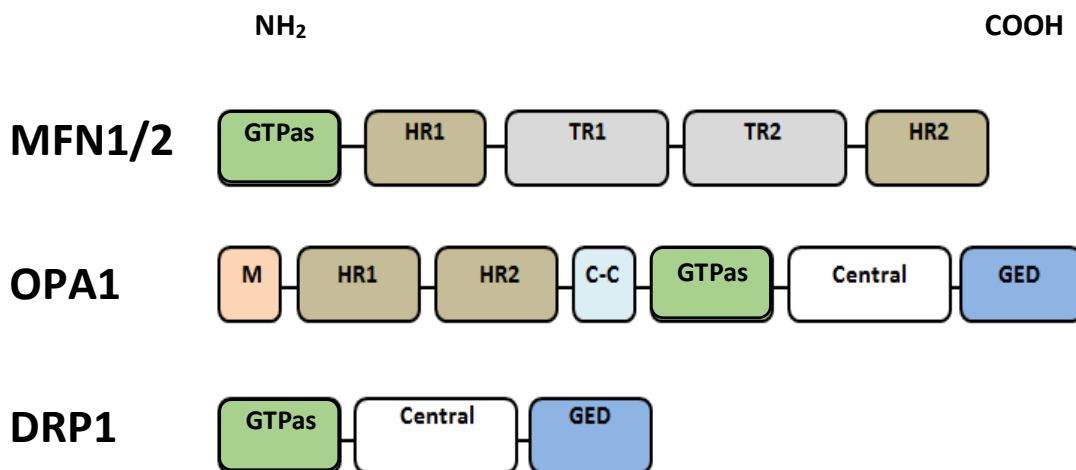


Figure 6.2. Schematic representation of the structure of key mitochondrial fusion and fission proteins. Mitofusin (MFN) 1 and 2 are involved in outer mitochondrial membrane fusion and consist of a GTPase domain at the amino terminal, a heptad repeat (HR1), two transmembrane domains (TR1/2) and a second heptad repeat (HR2). Fusion of the inner mitochondrial membrane is mediated by the inner membrane protein optic atrophy 1 (OPA1) which consists of a mitochondrial import sequence (M), two heptad repeats, a coiled coil domain (C-C), a GTPase domain, a central domain and a GTPase effector domain (GED). Dynamin related protein 1 (DRP1) orchestrates mitochondrial fission and is structurally made up of a GTPase domain, a central domain and a GTPase effector domain.

The transmembrane domains anchor the protein in the OMM while the amino and carboxyl terminals project in to the cytosol (Ong & Hausenloy, 2010). Both proteins are largely conserved in most tissues and mediate mitochondrial fusion in a GTP dependent manner (Koshiba et al. 2004). The heptad repeat at the carboxyl

terminal tethers the identical region of a neighbouring mitochondria resulting in either homotypic or heterotypic dimers, which then fuse resulting in a common intermembrane space with distinct matrices (Dorn II, 2013) (Figure 6.3).

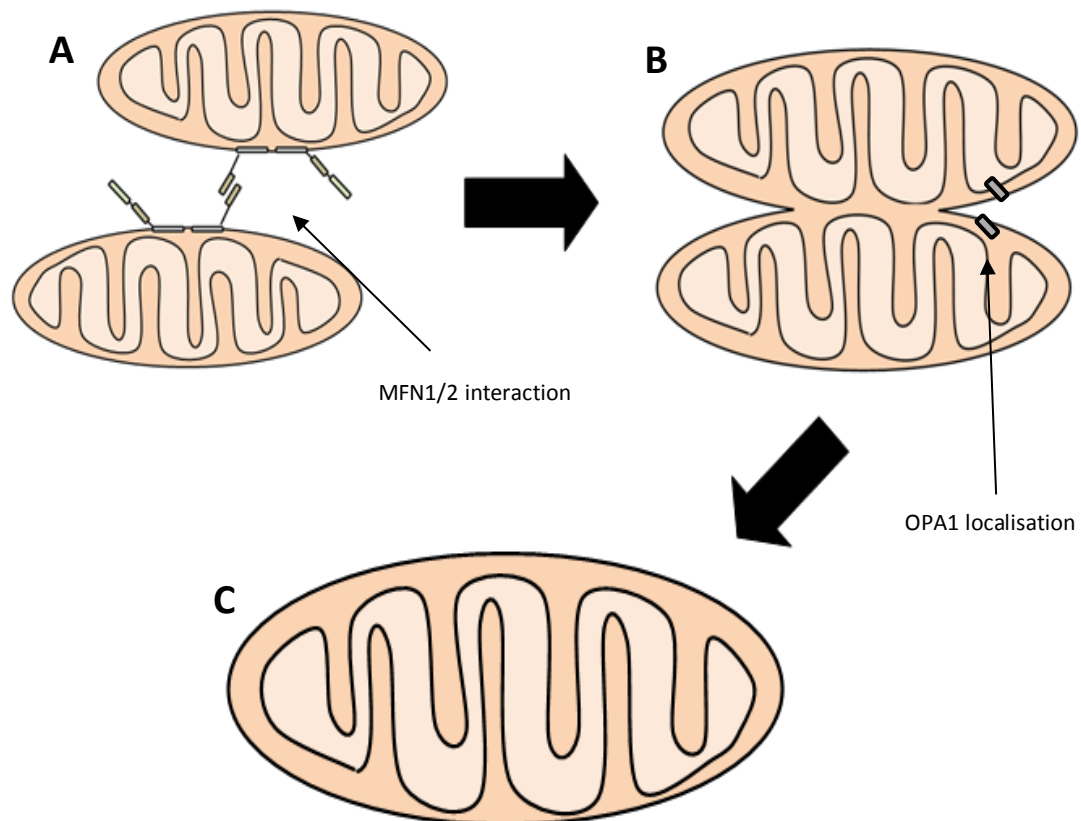


Figure 6.3. The mechanics of mitochondrial fusion. (A) Neighbouring mitochondria tether via their respective heptad repeat domains of MFN1 or 2. (B) Subsequent outer membrane fusion results in a common inter membrane space and two distinct matrices. (C) Complete fusion is a consequence of both inner and outer membrane fusion facilitated by OPA1.

The possible formation of heterotypic dimers suggests an overlap in function between the mitofusins. Indeed, reduction of either MFN1 or 2 in mouse embryonic stem cells can be partially compensated by the other isoform (Chen et al., 2005). Nevertheless, functional differences do exist between the two proteins. MFN1 has been shown to possess a higher GTPase activity compared with MFN2 in HeLa cells resulting in an enhanced tethering ability (Koshiba et al., 2004). Furthermore, it has

been suggested that MFN2 may also play a stabilizing role in homotypic MFN1 dimer formation, albeit through an unknown mechanism (Ishihara et al., 2004).

As well as their role in mitochondrial fusion, the mitofusins have been reported to exert other pleiotropic actions. MFN1 has been identified in correct placental formation during embryonic development (Chen et al., 2003), in addition to inhibition of pro-apoptotic proteins such as endonuclease G and caspase activation (Ong & Hausenloy, 2010). On the other hand, MFN2 is also present on the SR and can mediate mitochondrial-SR tethering which is required for calcium-induced apoptotic signalling (de Brito & Scorrano, 2008). It has also been suggested that MFN2 may form complexes with the pro-apoptotic proteins BAX and DRP1 at scission sites to initiate apoptosis (Karbowski et al., 2002). Furthermore, Chen et al., (2004) demonstrated that MFN2 can act as a hyperplasia suppresser gene, inhibiting vascular smooth muscle cell proliferation in spontaneously hypertensive rat vasculature.

As fusion of the OMM and IMM occur independently, an additional protein is involved in inner membrane fusion. Optic atrophy 1 (OPA1) is the mammalian homologue of the yeast mitochondrial-shaping protein Mgm1, and was identified by Delettre et al. (2000) as fulfilling this role. OPA1 consists of a mitochondrial import sequence at the amino terminal, two hydrophobic heptad repeats, a coiled coil domain, a GTPase domain, a central domain and a GTPase effector domain (GED) at the carboxyl terminal (Ong & Hausenloy, 2010) (Figure 6.2). The mitochondrial import sequence is involved in mitochondrial targeting and the GED domain controls GTPase activity (Smirnova et al., 2001). The hydrophobic heptad repeat is considered

an anchor for OPA1 when fusing inner membranes of neighbouring matrix compartments (Ong & Hausenloy, 2010). Unlike outer membrane fusion which requires little GTP activity, inner membrane fusion requires high GTP hydrolysis and an intact membrane potential. Although fusion of the inner and outer membranes occur independently, it is likely other regulatory proteins are involved in synchronizing the processes. Ugo1 has been identified as fulfilling this role in yeast however, as yet, no such candidate has been discovered in mammals (van der Bliek et al, 2013).

As with the mitofusins, OPA1 has been reported to exert effects outside of its role in fusion. These include preventing apoptotic cell death by inhibition of cytochrome c release from cristae junctions and tagging depolarised mitochondria for removal by the autophagosome during mitophagy (Frezza et al., 2006; Twig et al., 2008).

6.1.3 Mitochondrial Fission

Fission is an essential part of normal cellular homeostasis. Damaged/dysfunctional mitochondria can be segregated from the mitochondrial network by fission and preferentially selected for degradation via mitophagy (Song et al., 2015). In addition, fission results in the release of pro-cell death proteins, such as cytochrome c, endonuclease G and apoptosis inducing factor, which are normally membrane bound within the mitochondria (Arnoult et al., 2005), triggering apoptosis and cell death (Marin-Garcia & Akhmedov, 2013). Such mechanisms limit the production of ROS, providing the cell with a form of quality control (Twig et al., 2008).

Mitochondrial fission in mammals is largely orchestrated by a large GTPase containing protein, dynamin related protein 1 (DRP1), first identified in 1997 by Shin et al. Consisting of a GTPase domain, a central domain and a GED (Figure 6.2), DRP1 is mainly localised to the cytosol and recruited to the OMM where it binds the docking molecule fission protein 1 (Fis1) (Dorn II, 2013). Fis1 is a small protein of 17kDa which contains a tetratricopeptide repeat motif that acts as a scaffold to promote protein–protein interactions. Fis1 circumscribes the outer membrane forming scission sites, the binding and oligomerization of DRP1 causes constriction which subsequently results in fission (Smirnova et al., 2001) (Figure 5.4).

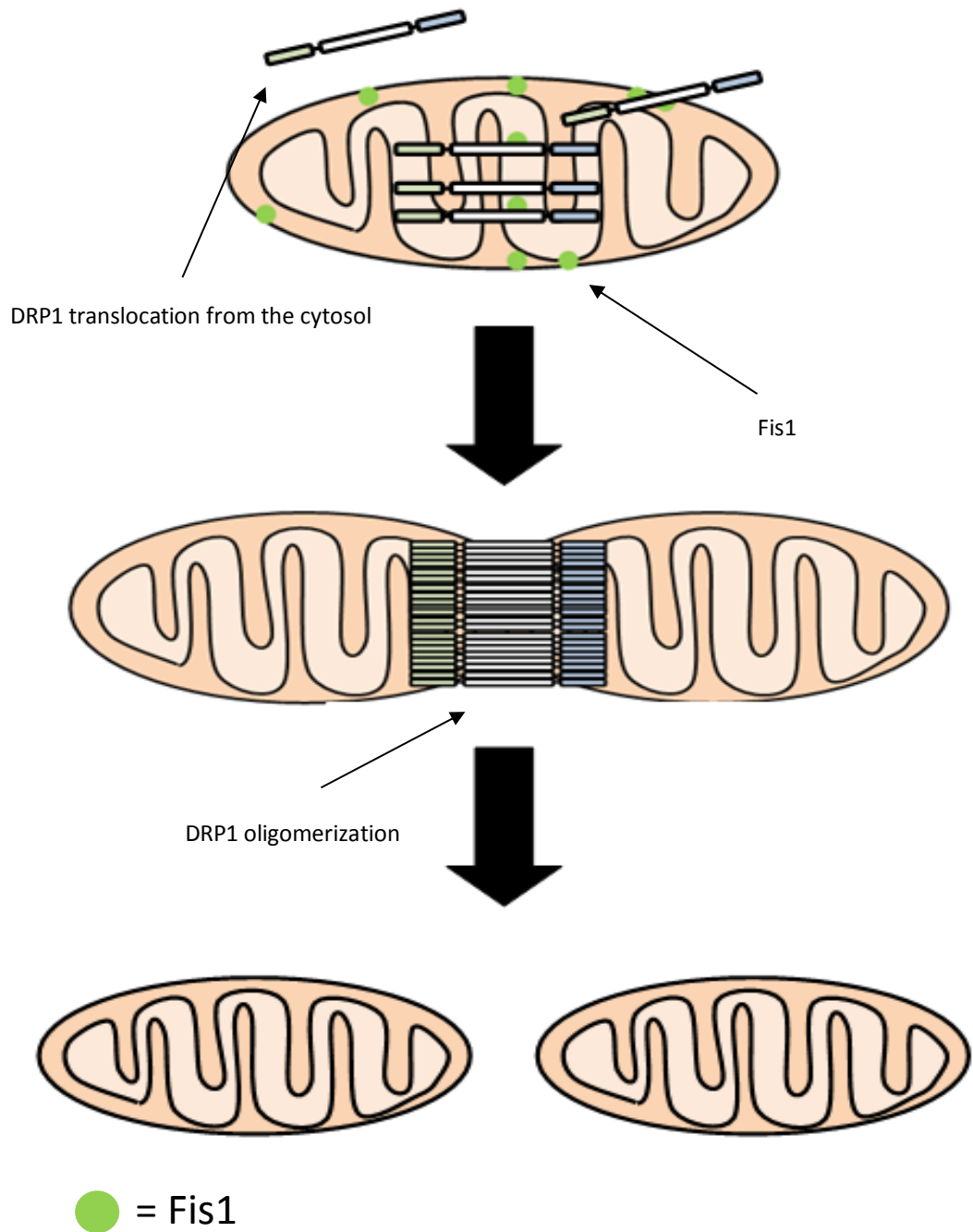


Figure 6.4. The process of mitochondrial fission. (A) Dynamin related protein 1 (DRP1) is recruited to the mitochondrial outer membrane where it binds the scaffold molecule fission protein 1 (Fis1). (B) The oligomerization of DRP1 and subsequent constriction causes (C) fission.

The regulation of DRP1 translocation to the OMM is incompletely understood, however, a variety of post translational modifications and adapter

proteins have been hypothesised to be involved (Ong et al., 2010). These include phosphorylation of serine residues within the GED (Bossy et al., 2010) and enhancing GTPase activity by S-nitrosylation (Cho et al., 2009). Another interesting candidate is mitochondrial fission factor (MFF), a small transmembrane protein present on the OMM. Otera et al. (2010) reported MFF down regulation resulted in inhibition of DRP1 recruitment to the OMM and subsequent mitochondrial elongation. Furthermore, recruitment of DRP1 is reduced in cells using RNA interference of MFF (Marin-Garcia & Akhmedov, 2013).

6.1.4 Mitochondrial Dynamics in Heart Failure

The delicate balance of fusion and fission is essential for normal mitochondrial function and disruption may have profound effects on mitochondrial energy generation, potentially leading to dysfunction and subsequent cell death (Westermann, 2010). Furthermore, as mitochondrial fission can be an initiating factor in cell death mechanisms, perturbations in mitochondrial dynamics have become a major focus of cardiac research in recent years (Ong et al., 2010; Disatnik et al., 2013 & Gao et al., 2013).

Double knockout of MFN1 and MFN2 in mice resulted in death approximately two weeks after birth due to severe dilated cardiomyopathy (Papanicolaou et al., 2012). TEM analysis of cardiac tissue revealed a multitude of small, spherical mitochondria exhibiting disorganised cristae structure. Functional consequences included a three-fold increase in the left ventricular end diastolic volume and a

significantly reduced heart rate and ventricular wall thickness. However, single knockout of either MFN1 or MFN2 resulted in distinct phenotypes. MFN1 deletion produced multiple small fragmented mitochondria paralleled with an increase in apoptosis (Li et al., 2010). On the other hand, MFN2 deficiency did not impair mitochondrial fusion in the heart (Chen & Dorn II. 2013). However, these mitochondria were dysfunctional and exhibited elevated ROS production and a dissipated membrane potential.

Several phenotypes arising from OPA1 knockout have been reported, including abnormally large mitochondria containing multiple unfused matrices, a consequence of partial fusion (Zong et al., 2009). In contrast, Frezza et al. (2006) observed mitochondrial fragmentation and reduced cristae density in mouse embryonic fibroblasts. These structural changes caused a decreased membrane potential and diminished respiratory capacity. In another study in heterozygous OPA1 mice, electron microscopy revealed large mitochondria with an altered cristae structure grouped in clusters (Piquereau et al., 2012). These animals exhibited abnormal ventricular contractility, calcium handling and an increased susceptibility to IRI.

Although it is accepted that deficiency of DRP1 leads to enlarged mitochondria, the consequences of DRP1 deletion are somewhat controversial. Ikeda et al (2015) concluded that as DRP1 was a key component of quality control in the cell via mitophagy, ablation of the protein resulted in the accumulation of damaged/dysfunctional mitochondria. This in turn led to increased ROS production, damaged mtDNA and ultimately cardiac dysfunction. However, this is in contrast to

other studies which have used increased fusion/inhibited fission as a means of cardioprotection (Zhang et al., 2013; Disatnik et al., 2013). Indeed, Ong et al. (2010) overexpressed MFN1 and 2 in HL-1 cells, shifting the balance in favour of fusion and reducing fission in a model of IRI. They found that elongated mitochondria conferred protection against IRI mediated opening of the mPTP and consequent necrosis.

Another approach which can be used for cardioprotection is direct inhibition of fission using pharmacological inhibitors. Mitochondrial division inhibitor 1 (Mdivi-1) is a selective inhibitor of DRP1 and has been shown to protect against IRI in both the heart and cerebrum (Ong et al., 2012 & Zhang et al., 2013). Although this mechanism remains incompletely understood, it is considered Mdivi-1 inhibits DRP-1 self-assembly. Another DRP1 inhibitor, Dynasore, prevented mitochondrial fission and maintained cardiac function in the isolated rat heart following exposure to IRI (Gao et al., 2013). Furthermore, Disatnik et al. (2013) showed P110, a specific inhibitor of the Fis1 and DRP1 interaction, reduced infarct size and increased mitochondrial respiration in *ex vivo* and *in vivo* myocardial infarction models.

Previous studies on the isolated uraemic rodent heart have highlighted impaired contractile function characterised by a decreased cardiac output and a reduced phosphocreatine to ATP ratio in normoxia and low-flow ischemia (Raine et al., 1993). In addition, UCM mitochondria exhibited an increased susceptibility to oxidant induced damage (Taylor et al., 2015) and impaired bioenergetics (see Chapter 5). As mitochondrial morphology and energy generation are closely linked, it is feasible that the enhanced vulnerability to cardiovascular complications in UCM may be underpinned by altered mitochondrial fusion and fission.

6.1.5 Objectives

Disruption of the balance between fusion and fission may render cardiac mitochondria in UCM more susceptible to injury. Hence the aim of the work described in this chapter was to:

- Probe possible changes in expression of key mitochondrial fusion and fission proteins in cardiac tissue and isolated mitochondria
- Investigate mitochondrial morphology in left ventricular tissue and isolated mitochondria

6.2 Methods

6.2.1 *Experimental design*

Sham surgery or sub-total nephrectomy was induced in 20 male Sprague-Dawley rats as described in section 2.1. This gave rise to the following experimental groups:

- Control (n=10)
- Uraemic (n=10)

Animals were sacrificed 12 weeks post-surgery and hearts rapidly excised. Approximately 200mg left ventricular tissue was removed and snap frozen in liquid nitrogen for Western blotting. A further 50mg of left ventricular tissue was also removed and used for TEM analysis. The remainder of the heart was homogenised and mitochondria isolated as described in section 2.3.1.

6.2.2 *Expression of Mitochondrial Fusion and Fission Proteins*

Freeze ground left ventricular tissue and isolated mitochondrial protein extracts were separated using SDS-PAGE on a 10% running gel and transferred to a nitrocellulose membrane as described in section 2.4. Membranes were probed for MFN1, MFN2, OPA1 and DRP1 via western blotting as described in section 2.4 using actin as a loading control for whole tissue extracts and VDAC for mitochondria. Optimum antibody dilutions and incubation conditions are given in Table 2.1. Protein

bands were visualised using enhanced chemiluminescence as described in section 2.4.

6.2.3 Mitochondrial Morphology

Left ventricular tissue was harvested as described in section 2.3.1 and immediately fixed in glutaraldehyde solution. Mitochondrial size and structure was investigated using TEM as described in section 2.3.5.1.

6.2.4 Citrate Synthase Activity

Citrate synthase activity was determined in freeze ground left ventricular tissue as described in section 2.3.3.5.2.

6.2.5 Isolated Mitochondrial Size

6.2.5.1 Flow Cytometry

Mitochondrial size was assessed in isolated cardiac mitochondria by flow cytometry as described in section 2.3.5.2.

6.2.5.2 *Dynamic Light Scattering*

Mitochondrial size was assessed in isolated cardiac mitochondria by DLS as described in section 2.3.5.3.

6.3 Results

6.3.1 Expression of Mitochondrial Fusion and Fission Proteins

Expression levels of mitochondrial fusion and fission proteins MFN1, MFN2, OPA1 and DRP1 were unchanged in cardiac tissue despite induction of uraemia (Figure 6.5 – Figure 6.8). Similar findings were observed in isolated cardiac mitochondrial extracts (Figure 6.9 – Figure 6.11).

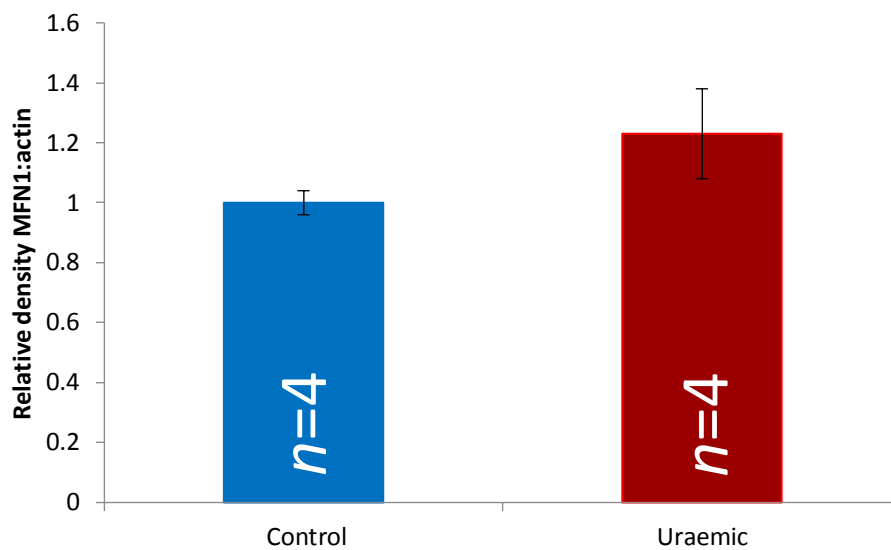
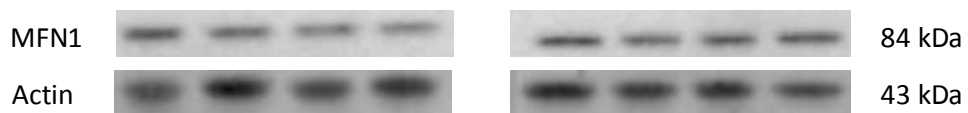


Figure 6.5. Relative expression of MFN1 in cardiac tissue at 12 weeks uraemia. Data are presented as mean \pm SEM

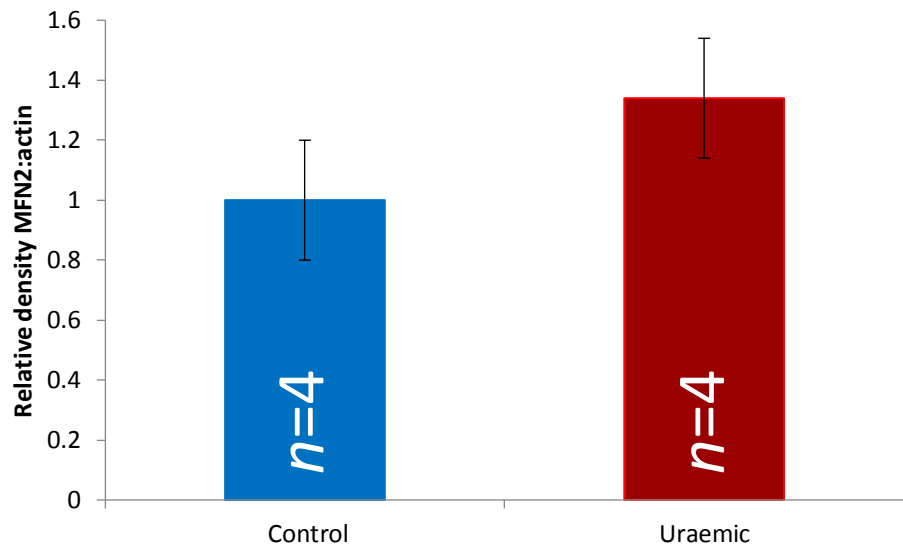


Figure 6.6. Relative expression of MFN2 in cardiac tissue at 12 weeks uraemia. Data are presented as mean \pm SEM

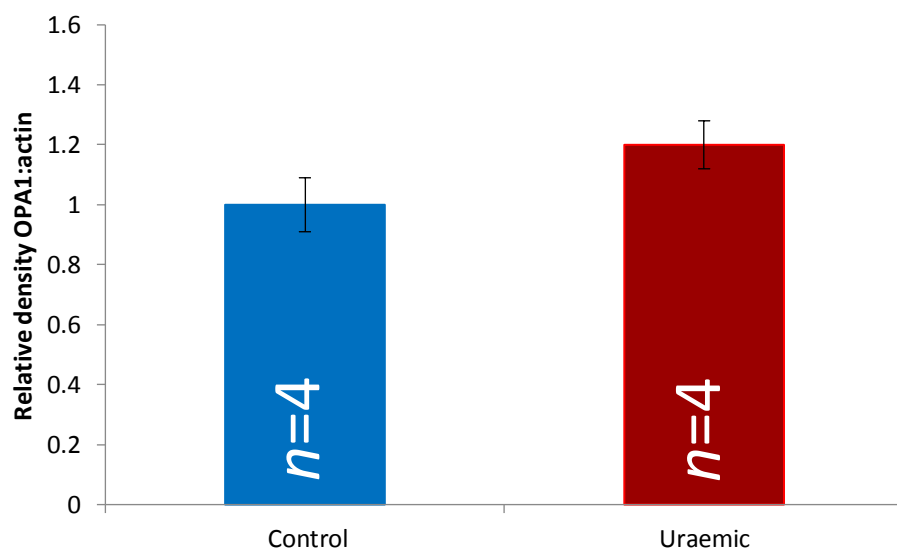
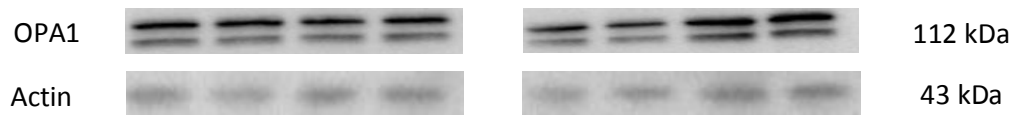


Figure 6.7. Relative expression of OPA1 in cardiac tissue at 12 weeks uraemia. Data are presented as mean \pm SEM

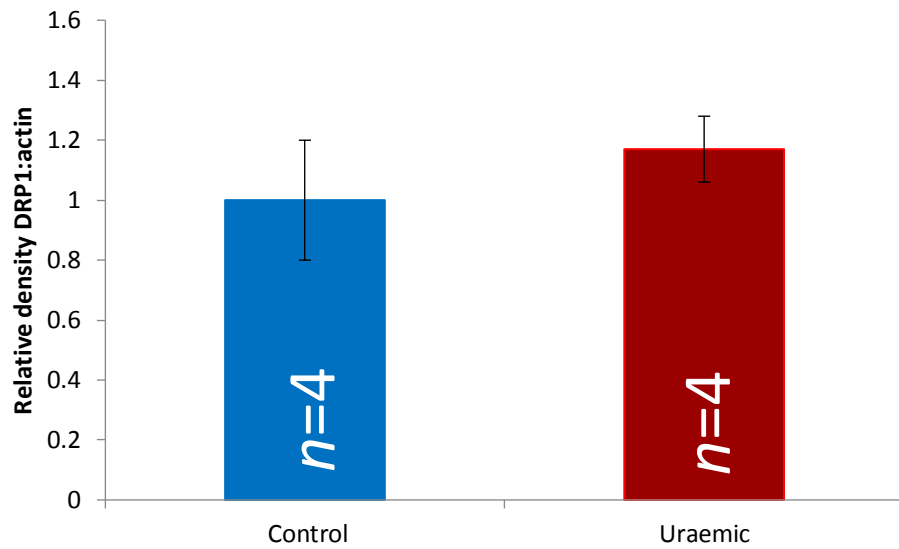
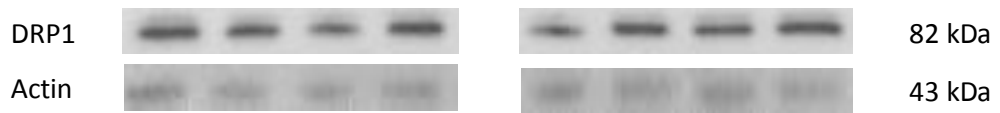


Figure 6.8. Relative expression of DRP1 in cardiac tissue at 12 weeks uraemia. Data are presented as mean ± SEM

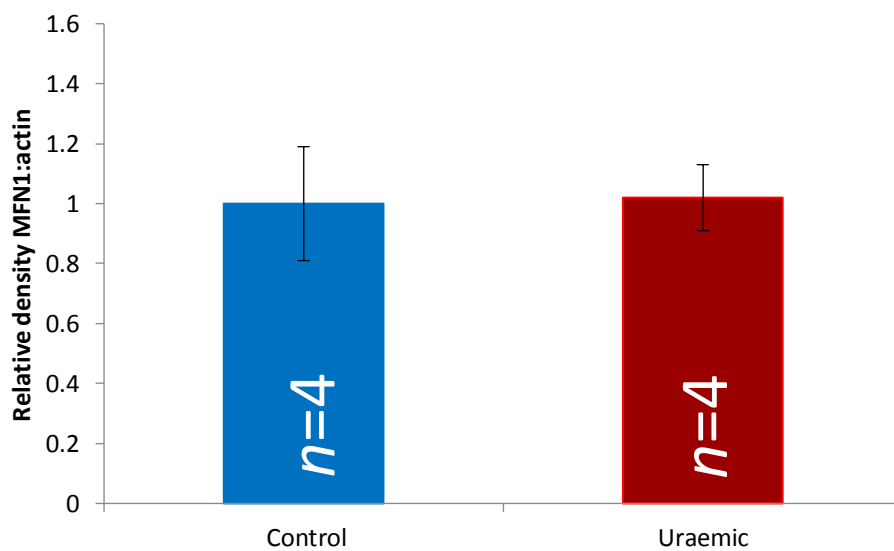
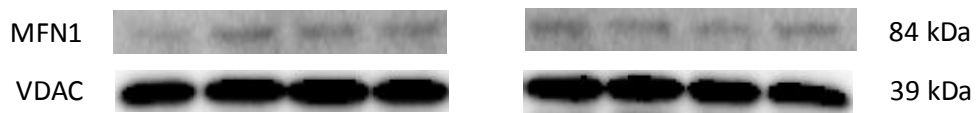


Figure 6.9. Relative expression of MFN1 in isolated cardiac mitochondria at 12 weeks uraemia. Data are presented as mean ± SEM

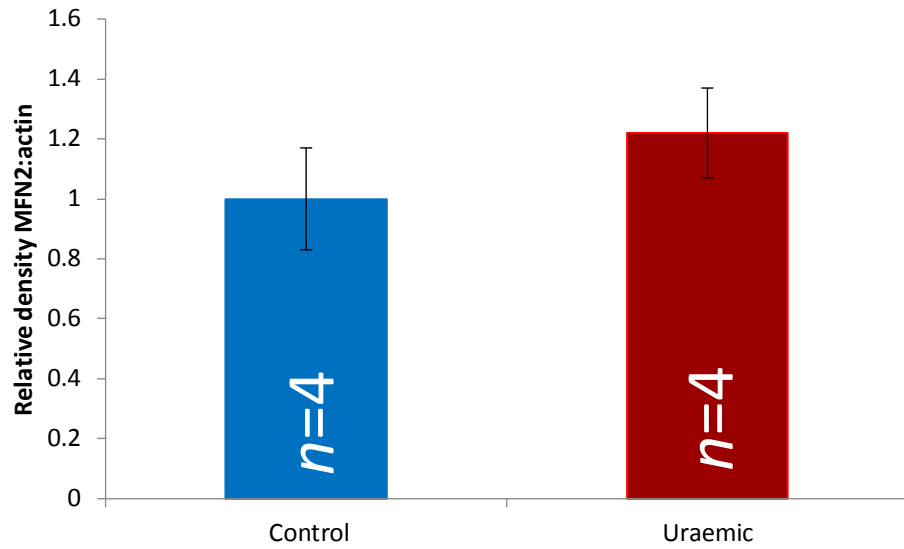
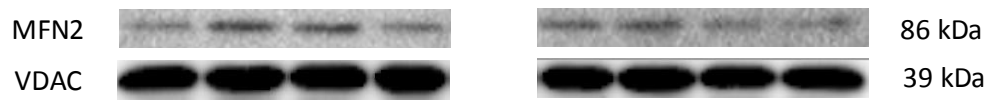


Figure 6.10. Relative expression of MFN2 in isolated cardiac mitochondria at 12 weeks uraemia. Data are presented as mean \pm SEM

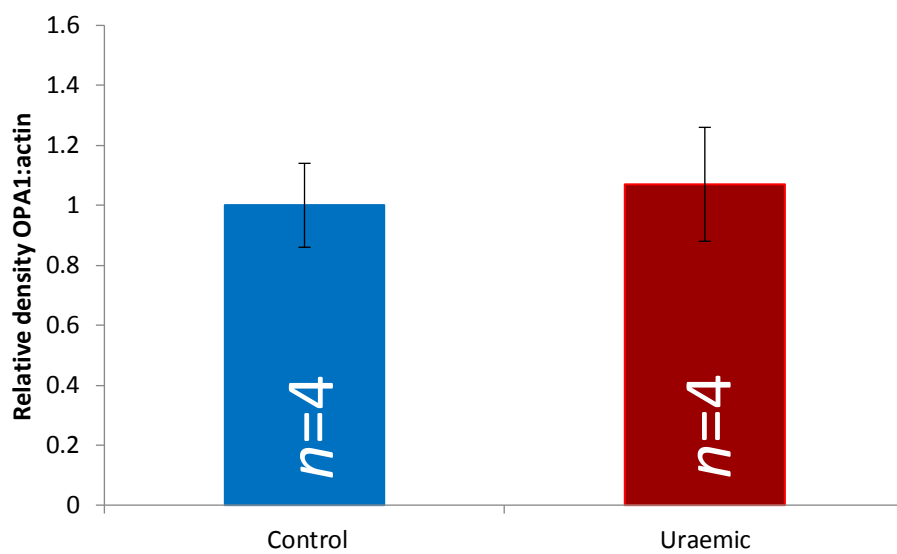


Figure 6.11. Relative expression of OPA1 in isolated cardiac mitochondria at 12 weeks uraemia. Data are presented as mean \pm SEM

6.3.2 Citrate Synthase Activity

Citrate synthase activities were similar in control and uraemic cardiac tissue indicating that induction of uraemia did not affect mitochondrial density (Figure 6.12).

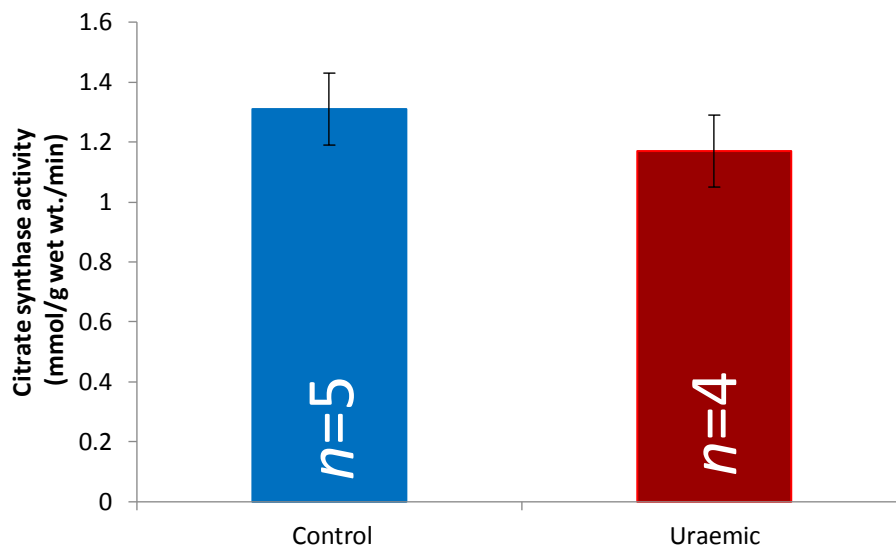


Figure 6.12. Citrate synthase activity. Data are presented as mean \pm SEM

6.3.3 Mitochondrial Morphology

TEM revealed individual mitochondrial length, width and aspect ratios were similar in control and uraemic mitochondria (Table 6.1 & Figure 6.13 – Figure 6.14). Although no overall changes in gross mitochondrial size and shape were observed, uraemic mitochondria displayed distinct ultrastructural remodelling characterised by a more sparsely packed cristae (Figure 6.15).

Table 6.1.

Mitochondrial dimensions

Dimension	Control	Uraemic
Length (µm)	1.09 ± 0.02 (n=383)	1.12 ± 0.03 (n=308)
Width (µm)	0.53 ± 0.01 (n=383)	0.54 ± 0.01 (n=308)
Aspect ratio	2.08 ± 0.04 (n=383)	2.10 ± 0.06 (n=308)

Data are presented as mean ± SEM

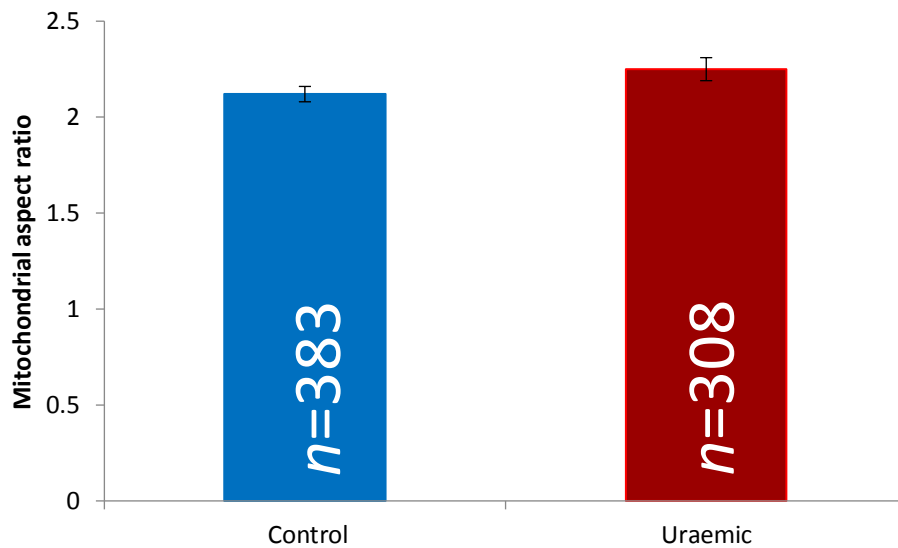
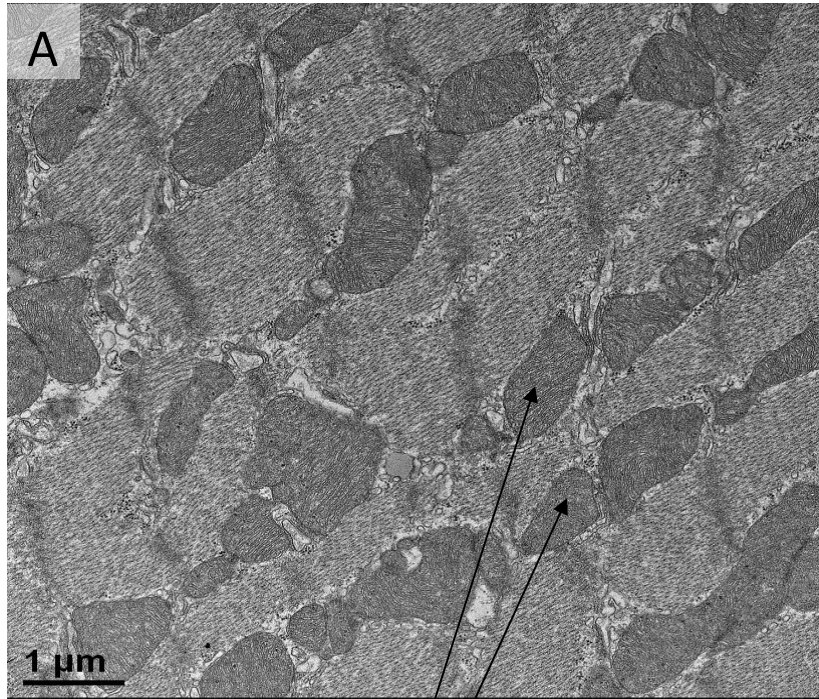
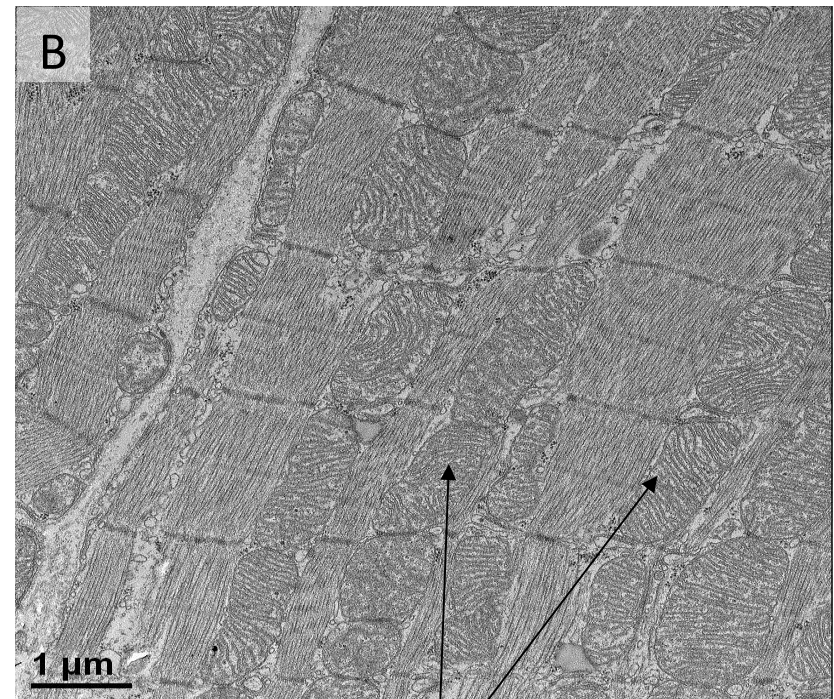


Figure 6.13. Mitochondrial aspect ratios. Data are presented as mean ± SEM



Mitochondria



Mitochondria

Figure 6.14. Transmission electron micrograph (6000x magnification) showing (A) control and (B) uraemic mitochondria of similar size in a longitudinal arrangement along the sarcomere.

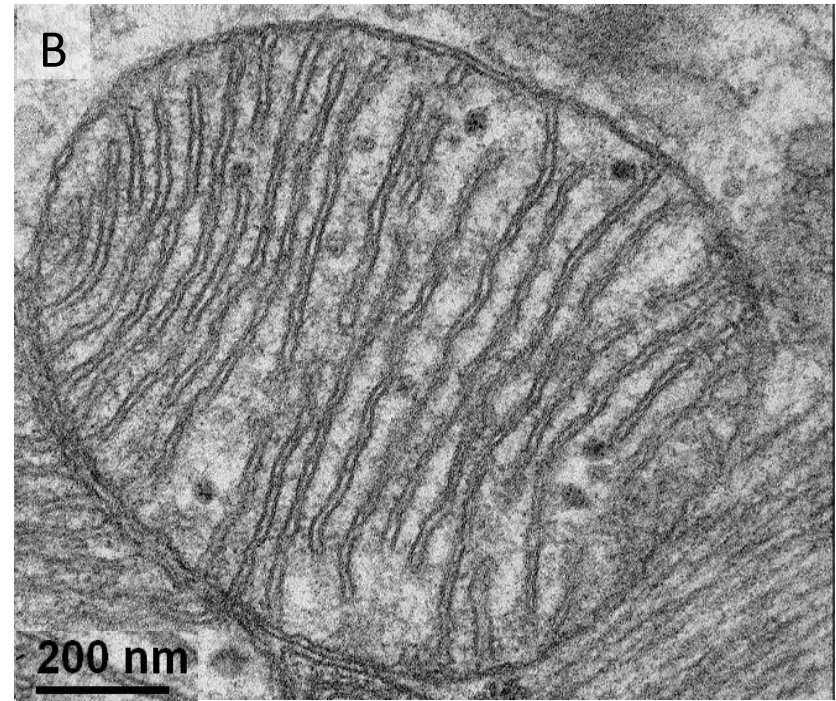
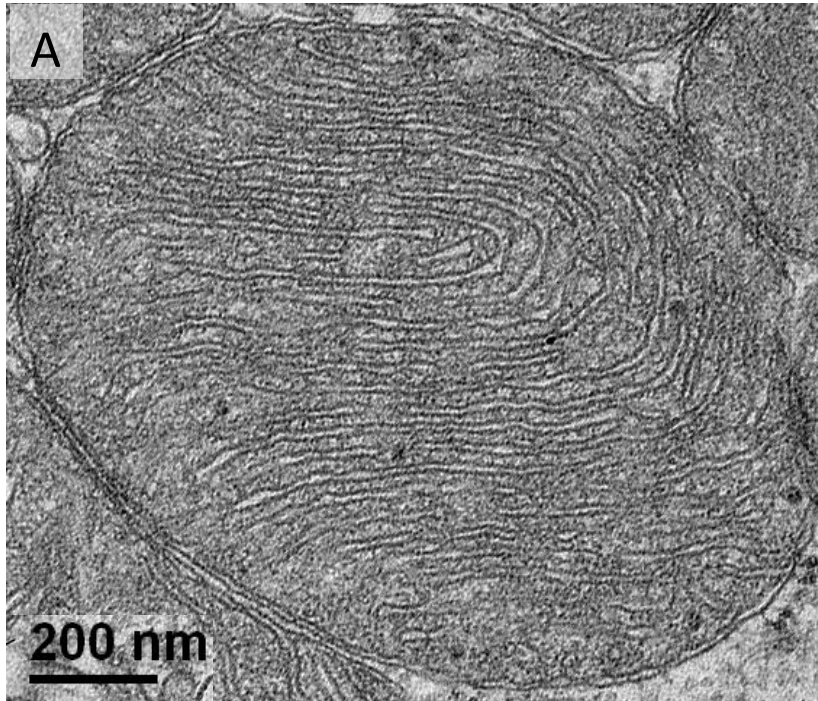


Figure 6.15. Enlarged transmission electron micrograph (30000x magnification) showing differences in cristae structure between (A) control and (B) uraemic mitochondria.

6.3.4 Isolated Mitochondrial Size

Flow cytometric analysis revealed little difference between control and uraemic mitochondrial size (Figure 6.16 & Figure 6.17). In addition, both experimental groups had similar hydrodynamic diameters (Figure 6.18) suggesting uraemic mitochondria retain the same overall structure as their control counterparts during the isolation process.

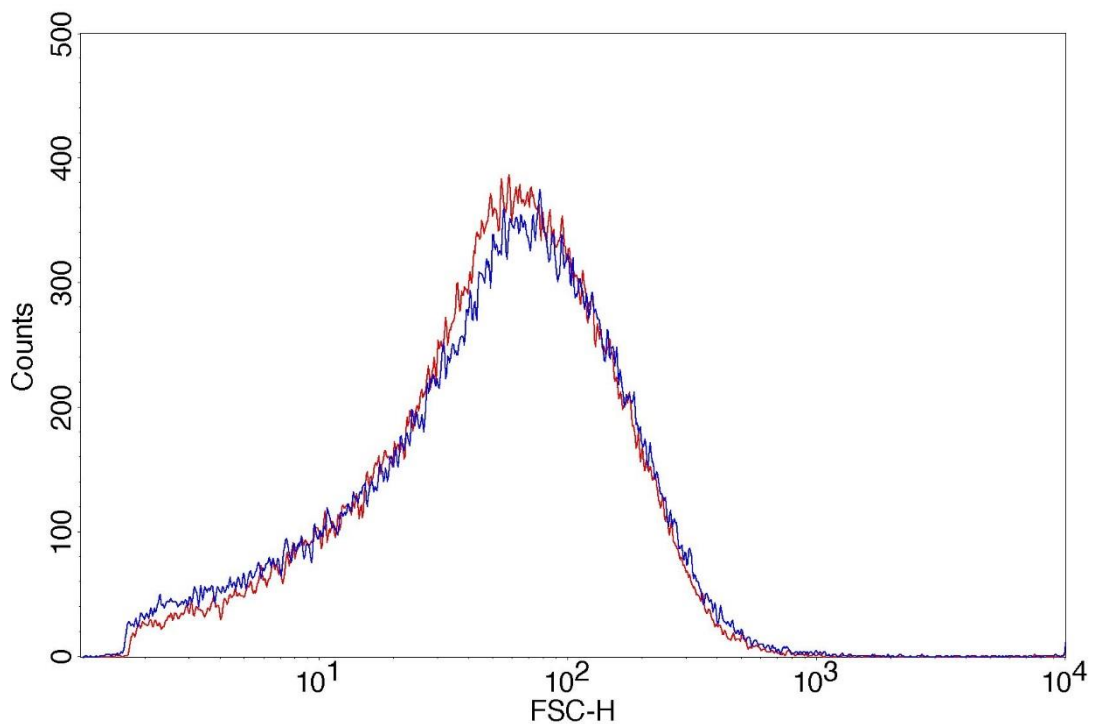


Figure 6.16. Representative histogram showing control (blue) and uraemic (red) mitochondrial populations.

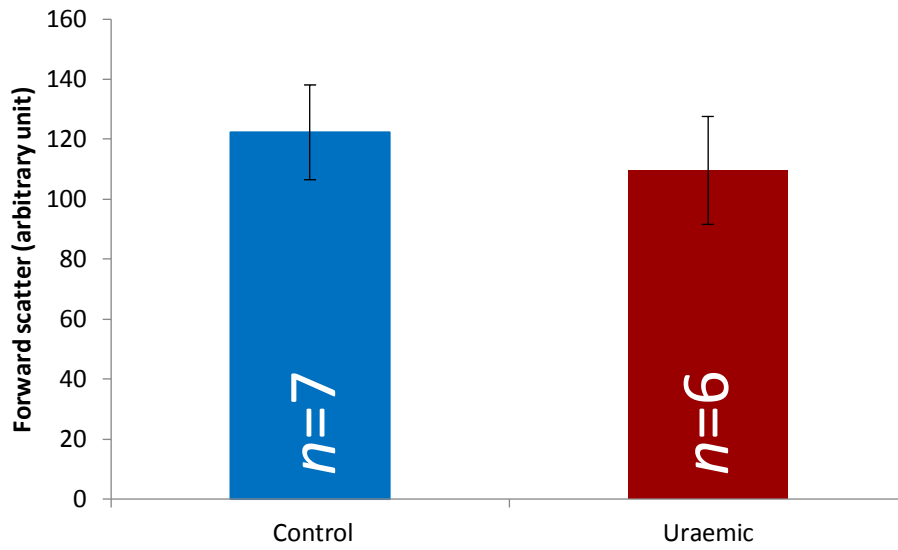


Figure 6.17. Relative forward scatter as a measure of isolated mitochondrial size. Data are presented as mean \pm SEM

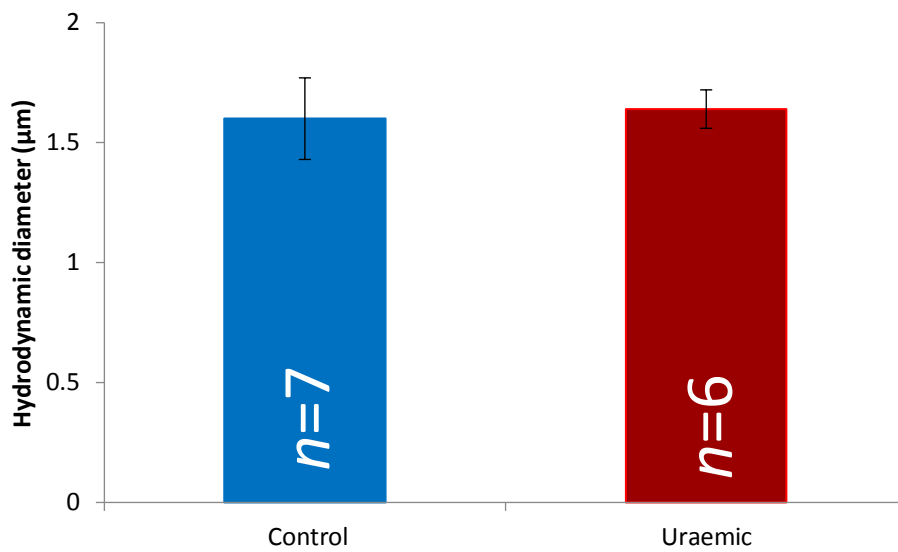


Figure 6.18. Hydrodynamic diameter of isolated mitochondria. Data are presented as mean \pm SEM

6.4 Discussion

This study has shown that following 12 weeks uraemia, expression of cardiac mitochondrial fusion and fission proteins was unaltered in whole tissue and isolated mitochondria. In addition, gross mitochondrial size and structure were conserved and there was a comparable degree of mitochondrial density in both control and uraemic hearts. However, uraemic mitochondria exhibited distinct cristae remodelling characterised by a more sparsely packed cristae.

6.4.1 *Myocardial Protein Expression*

Expression of key mitochondrial fusion and fission proteins, MFN1, MFN2, OPA1 and DRP1, in the heart was unaffected by the induction of uraemia (Figure 6.5 – Figure 6.8). A similar profile of protein expression was observed in isolated cardiac mitochondria (Figure 6.9 – Figure 6.11). These findings suggest that the fusion and fission machinery is conserved at this stage of UCM and the balance of mitochondrial dynamics may still be co-ordinated under basal conditions.

Mitochondrial fission is an initiating factor in programmed cell death, and apoptosis itself plays a significant role in the transition from compensated cardiac hypertrophy to heart failure (Diwan et al., 2008). Therefore it is conceivable that a shift towards fission is a feature specific to the failing heart rather than the compensated phase of cardiac hypertrophy as observed at this stage of uraemia. This notion is supported by Chen et al. (2011) who observed double knockout of MFN1 and MFN2 did not result in contractile dysfunction or induce mitochondrial fission

until the development of heart failure. Furthermore, small fragmented mitochondria, indicative of fission, are a common finding in a number of models of heart failure including diabetic cardiomyopathy (Yu et al., 2008), systolic heart failure (Chen et al., 2009) and dilated cardiomyopathy (Schaper et al., 1991).

A number of studies have highlighted that mitochondria may undergo fusion in states of acute stress. An early response to pressure-overload is an increased accumulation of mitochondria in the cardiomyocyte (Albin et al., 1973). This is associated with a shift towards fusion and an overall increase in mitochondrial size as early as 48 hours post-aortic constriction (Zak et al., 1980). Similar observations were reported by Sun et al. (1969) who identified that acute cardiac injury caused by brief hypoxia resulted in mitochondrial elongation, consistent with an increase in fusion. This mechanism was transient however, and the mitochondrial network soon returned to a balanced state (Albin et al., 1973). This has led to the hypothesis that mitochondria undergo fusion in states of acute stress to confer protection against further hypoxic/ischemic insult (Ong & Hausenloy, 2010).

Although evidence supports a role for both mitochondrial fusion and fission in different states of cardiac stress, little is known about mitochondrial dynamics in the compensated phase of cardiac hypertrophy. Fang et al. (2007) investigated changes in MFN2 in a variety of *in vivo* and *in vitro* models of cardiac hypertrophy. They observed reduced MFN2 expression in neonatal rat ventricular myocytes in response to phenylephrine. Although similar findings were reported in spontaneously hypertensive rats and aortic constricted mice as early as 1 week post-surgery, MFN2 levels were similar to controls by 15 weeks. This suggested that the

balance between mitochondrial fusion and fission in cardiac hypertrophy may be dependent on the time-course of hypertrophy progression, possibly due to changes in substrate availability and cellular energy requirements. However, direct comparisons between these models of hypertrophy and the current model must be limited as only a single time point was used in this study.

In addition, only DRP1 content in left ventricular tissue was assessed in the present study. As discussed previously, DRP1 is a cytosolic protein which is recruited to the OMM to facilitate fission (Dorn II, 2013). Therefore it is possible that while total tissue content of DRP1 may not have altered, the dynamics of the protein could have changed resulting in either increased or decreased translocation from the cytosol to the OMM. One approach to have mitigated this could have been to have used the subcellular fractionation technique of Smirnova et al. (2001). The group isolated mitochondria from bovine brain using a method comparable to the present study with the exception of using cycles of ultra-high speed centrifugation. This resulted in significantly improved separation of mitochondria and cytosol and allowed the group to probe expression of DRP1 in both fractions. Though this technique may have been useful in characterising DRP1 localisation in the present model, significant changes in DRP1 translocation could have been expected to have led to either mitochondrial fragmentation (increased translocation) or elongation (decreased translocation). However, this was not the case as gross mitochondrial size and structure were conserved at this stage of uraemia (see Sections 6.4.2 & 6.4.3), suggesting that the balance of DRP1 dynamics was also maintained.

6.4.2 Mitochondrial Morphology

Mitochondrial length, width and aspect ratios were similar in control and uraemic mitochondria (Table 6.1 & Figure 6.13), in line with the expression of key fusion and fission proteins (see Section 6.4.1). Citrate synthase activities were similar in control and uraemic cardiac tissue suggesting a comparable degree of mitochondrial density (Figure 6.12). However, uraemic mitochondria displayed distinct ultrastructural remodelling characterised by a more sparsely packed cristae (Figure 6.14 – Figure 6.15).

Several studies investigating mitochondrial morphology in heart disease have revealed altered cristae structure using electron microscopy. Papanicolaou et al. (2012) observed small fragmented mitochondria with a complete loss of cristae organization two weeks after birth in a double knockout model of MFN1 and MFN2. Piquereau et al. (2012) also reported disorganised cristae in OPA heterozygous mice subjected to transverse aortic constriction. Furthermore, Chen et al. (2009) observed small spherical mitochondria with a sparsely packed cristae in both human heart failure patients and rats subjected to coronary ligation.

The cristae are the site of the respiratory chain, therefore it is conceivable that ultrastructural changes are closely linked to mitochondrial bioenergetics. Indeed, recent studies on the present model have highlighted an increased susceptibility to calcium and oxidant-induced cell death arising from altered mitochondrial function (Taylor et al., 2015). In addition, UCM mitochondria exhibit significantly increased state 4 respiratory rates with no change in state 3 respiration (see Chapter 5), indicative of a decreased mitochondrial efficiency. However, elevated state 4

respiration rates in UCM mitochondria are not associated with a concurrent increase in UCP expression suggesting an alternative aetiology of uncoupling (Taylor, 2014). It is possible that the remodelling of cristae observed here may contribute to the mitochondrial inefficiency associated with UCM. Furthermore, unpublished data in our laboratory has highlighted significant changes in mitochondrial membrane constituents, such as cardiolipin, in uraemic mitochondria (Nuhu, 2017).

Cardiolipin accounts for approximately 20% of the total lipid composition of the inner mitochondrial membrane and is directly involved in maintaining mitochondrial cristae organisation and morphology (Acehan et al., 2011). In addition, cardiolipin has a role in mitochondrial energy generation by stabilising individual enzyme complexes of the respiratory chain (Houltkooper & Vaz, 2008). Indeed, studies have shown that components of the electron transport chain, such as complexes I and III, need cardiolipin to function correctly (Fry & Green, 1981). Furthermore, the unique dimeric structure of cardiolipin has been suggested to play a part in the phospholipid preventing the leak of protons from the IMM during oxidative phosphorylation (Haines & Dencher, 2002). Thus, significant remodelling of membrane cardiolipin would go some way to explaining the uncoupled phenotype in uraemic mitochondria.

As OPA1 plays a large part in governing mitochondrial structure and integrity given its role in inner membrane fusion, it is perhaps surprising that expression levels of this protein are unaltered. Indeed, small fragmented mitochondria with a decreased matrix density have been associated with reduced OPA1 expression (Marin-Garcia & Akhmedov, 2013). A possible explanation for the disparity may be

that the majority of studies to date have focused on genetic models of OPA1 knockout rather than investigating the pathological effects of heart disease and failure on the protein itself (Piquereau et al., 2012 & Zong et al., 2009).

Another alternative explanation may lie with the pleotropic actions of the protein. OPA1 overexpression has been shown to directly inhibit the release of cytochrome c from cristae junctions in mouse embryonic stem cells by maintaining inner membrane structure (Frezza et al., 2006). In addition, a potential role for OPA1 in tagging depolarised mitochondria for degradation via mitophagy has also been identified (Twigg et al., 2008). Therefore it is possible that OPA1 levels are conserved at this stage of uraemia due to actions independent of its role in fusion, however, it is unclear what functional implications this may have.

6.4.3 *Isolated Mitochondrial Size*

Electron microscopy is largely considered the gold standard for investigating organelle morphology (Yancey et al., 2015). However, TEM is labour intensive and interpretation of results is usually based on scoring randomly selected images which may be complemented with other techniques (Song et al., 2015 & Disatnik et al., 2013). Therefore flow cytometry and DLS were also used to assess gross mitochondrial size as they offered the ability to rapidly analyse large populations of mitochondria. Isolated control and uraemic mitochondria were of a comparable size when measured with flow cytometry and DLS (Figure 6.16 – Figure 6.18). This is consistent with the morphological data already discussed and also suggests that

uraemic mitochondria retain the same structural integrity as their control counterparts during the isolation process.

Flow cytometric analysis of mitochondrial morphology is based on forward scatter which is directly proportional to organelle size (Chen et al., 2011). Although typically used for whole cells, recent studies have used flow cytometry to assess morphological changes in isolated cardiac mitochondria. Chen et al. (2011) identified an increase in mitochondrial fission highlighted by a 40% reduction in forward scatter in MFN1 and MFN2 deficient mice. As double knockout of both proteins can be embryonically lethal, the group used transgenic mice expressing *MFN1* and *MFN2* genes flanked by a tamoxifen-inducible modified estrogen receptor (MER) cardiac-specific MYH6-Cre transgene. Tamoxifen administration catalyzed recombination of the MER-CRE-MER protein and ablation of the *MFN1* and *MFN2* genes. Disatnik et al. (2013) observed a similar decrease in forward scatter in mitochondria isolated from perfused rat hearts subjected to ischemia reperfusion.

The mitochondrial hydrodynamic diameter can be measured by DLS as scattered light intensity is proportional to mass (Buchanan & Walker, 1996). Although hydrodynamic diameter is calculated assuming a spherical sample, the ellipsoidal shape of mitochondria results in only negligible error in estimated size (Kristal & Dubinsky, 1997). However, DLS is conventionally used to measure the size of nanoparticles in solution and thus data on mitochondrial size measurements are relatively scarce. Kandaurova et al. (1999) observed that acute treatment of isolated mitochondria with oligomycin and the calcium uniporter inhibitor ruthenium red resulted in 40% and 17% increases in hydrodynamic diameter respectively. Wagner

et al. (2003) used DLS to characterise mitochondrial interactions with neurofilaments. The mitochondria–neurofilament complex resulted in a greater hydrodynamic diameter than mitochondria alone.

6.4.4 Conclusions

Uraemic cardiac mitochondria displayed ultrastructural changes characterised by distinct remodelling of the cristae. This was paralleled with an elevated state 4 respiration rate highlighting decreased mitochondrial efficiency, consistent with previous observations. However, these adaptations were independent of altered fusion and fission protein expression and overall mitochondrial size was conserved. In addition, mitochondrial content was comparable between experimental groups. Collectively, these data would indicate that mitochondrial ultrastructural remodelling precedes gross morphological changes at this stage of UCM and may potentially contribute to an enhanced susceptibility to cell injury and death during disease progression.

7. Discussion and Future Work

This study has shown that surgical induction of uraemia resulted in substantial renal dysfunction by 12 weeks, as evidenced by significant cardiac hypertrophy, elevated serum creatinine and urea and the presence of anaemia. The development of cardiac hypertrophy was associated with moderately increased ¹⁸F-FDG uptake in the uraemic heart at 5, 9 and 13 weeks. This was paralleled at the cellular level by mitochondrial ultrastructural remodelling and uncoupled respiration, indicative of reduced mitochondrial efficiency. Administration of the iron complex, ferumoxytol, did not ameliorate anaemia or impact mitochondrial function at this stage of uraemia. Collectively these data suggest there may be enhanced glucose utilisation in the uraemic heart *in vivo* and these changes are associated with altered mitochondrial structure and bioenergetics.

7.1 Discussion

Subtotal nephrectomy resulted in substantial kidney dysfunction as evidenced by elevated serum creatinine, urea and anaemia. Although serum creatinine can also be affected by muscle mass, the urine analysis employed in this study provided a more comprehensive evaluation of kidney function. The combination of serum and urine markers allowed for the determination of creatinine clearance, a marker of GFR. Creatinine clearance was reduced by 60% in uraemic animals, this roughly equates to stage IIIB CKD in humans and represents moderately reduced kidney function (National Kidney foundation, 2013). This degree of renal insufficiency allowed the study of cardiac alterations in uraemia prior to the onset of heart failure. LVH was prominent in uraemic animals and is also a consistent finding

in stage III CKD patients (Levin et al., 1996). LVH is a strong independent indicator of mortality in CKD, indeed, patients with substantial LVH are more likely to die from cardiovascular events than progress to end stage renal disease (ESRD) (Schiffrin et al., 2007). However, there was no evidence of fluid on the lungs in this study and the survival rate of approximately 90% from induction of uraemia to the time of sacrifice would indicate the cardiac hypertrophy observed was compensatory in nature.

Future work should include increasing the severity of the present model by either extending study duration or increasing the amount of tissue excised from the upper and lower kidney poles during nephrectomy. Alternatively, infarcting the kidney via chronic ligation of the renal vasculature can also result in ESRD as the degree of ischemia is proportional to the rate of renal failure (Liu et al., 2003). The enhanced kidney damage would be more consistent with ESRD and facilitate the investigation of cardiac metabolism during transition from compensated cardiac hypertrophy to failure in uraemia.

In parallel with the development of cardiac hypertrophy in this study was a moderate increase in ^{18}F -FDG uptake in uraemic hearts at 5, 9 and 13 weeks, though this failed to reach significance at this stage. In contrast to these data, previous studies on the isolated perfused rat heart using ^{13}C NMR have highlighted more profound differences in radiotracer uptake (Smith et al., 2010 & Aksentijevic, 2008). A major assumption of ^{18}F -FDG PET is that ^{18}F -FDG uptake and trapping in the cytosol accurately reflects glycolytic flux. However, care must be exercised when extrapolating the results from ^{18}F -FDG studies to the true rate of glucose uptake and metabolism. Indeed, it is well established that ^{18}F -FDG and glucose have different

affinities for GLUT1/4 facilitated intracellular transport and hexokinase mediated phosphorylation (Southwell, 2009). Although the lumped constant has been used to correct for these differences, the lumped constant itself has been shown to be variable in states of metabolic stress and disease (Botker et al., 1999 & Doenst & Taegtmeyer, 1998). Therefore, while PET has promise as a technique for applications such as myocardial imaging, ^{18}F -FDG may not be a suitable radiotracer for such applications.

An alternative radiotracer for imaging myocardial glucose metabolism could be ^{11}C -glucose. This compound is considered a “true” radiotracer as, unlike ^{18}F -FDG, ^{11}C -glucose is chemically identical to unlabelled glucose and is thus metabolised in the same way (Gropler, 2010). However, as with ^{18}F -FDG there are limitations with using this radiotracer, primarily the half-life of ^{11}C which is only around 11 minutes. The short half-life limits studies using ^{11}C -glucose to the few sites which have ^{11}C producing cyclotrons, making the use of this radiotracer impractical for most studies.

The moderate increase in ^{18}F -FDG uptake in the uraemic heart was accompanied by altered mitochondrial structure and bioenergetics. Indeed, while overall gross structure was conserved, uraemic mitochondria displayed distinct ultrastructural remodelling characterised by a more sparsely packed cristae. This was paralleled by an increase in state 4 respiration, indicative of reduced mitochondrial efficiency. Although altered mitochondrial morphology and function have been reported in heart failure (Piquereau et al., 2012 & Frezza et al., 2006), little is known about mitochondrial dynamics in UCM. These results have demonstrated for the first time that mitochondrial morphology is altered at this stage of uraemia and that

ultrastructural remodelling precedes gross morphological changes. Furthermore, such changes may alter the delicate balance of mitochondrial dynamics, potentially leading to more profound structural and functional changes during disease progression.

Though a range of different techniques were used to characterise mitochondrial morphology, a limitation of this study was that it represented only a single time point. Given that mitochondria are highly dynamic organelles, constantly undergoing events of fusion and fission to maintain the overall integrity of the mitochondrial network (Chen & Chan, 2010), further investigation of the rates of turnover might be of importance using imaging techniques, such as far-field fluorescence microscopy in real-time. This approach relies on the uptake of fluorescent dyes and/or probes which are specifically targeted to the mitochondria and taken up in a membrane potential dependent manner (Jakobs et al., 2011). In addition, another limitation of this study was the absence of a more severe animal disease model as a control/comparator. The incorporation of such a model would have allowed a more direct comparison to mitochondrial morphology in this study, in particular the TEM work where freeze/thawed mitochondria could not be used as a control.

Altered mitochondrial morphology can precede apoptosis and autophagy, while mPTP opening may underpin enhanced susceptibility to cell injury and death following IRI (Twig et al., 2008 & Ong et al., 2010). Indeed, previous studies on nephrectomised rats have revealed increased myocardial fibrosis and caspase 3 activation, indicative of necrosis and apoptosis respectively (Smith 2009 & Harwood

et al., 2003). However, direct investigation of cell death in UCM has yet to be carried out and thus remains poorly understood. Approaches that could be employed include using the terminal deoxynucleotidyl transferase dUPT nick end labelling (TUNEL) assay, a key method for detecting DNA fragmentation during apoptosis (Zeng et al., 2008). This method has successfully been used to identify increased apoptotic cell death in both heart failure patients (Sato et al., 2007) and experimental models of heart failure (Jiang et al., 2003). In addition, during autophagy, a cytosolic form of the protein microtubule-associated proteins 1A/1B light chain 3B LC3 (LC3-I) binds to phosphatidylethanolamine forming LC3-phosphatidylethanolamine conjugate (LC3-II) (Tanida et al., 2005). LC3-II is recruited to autophagosomal membranes and subsequently degraded by lysosomal hydrolases after the fusion of the autophagosome with a lysosome. Therefore measuring lysosomal turnover of LC3-II can reflect autophagic activity in tissues of interest such as the myocardium (Tanida et al., 2005).

It was hypothesised in this study that administration of the iron complex, ferumoxytol, would ameliorate the anaemia associated with CKD and enhance mitochondrial function. However, neither correction of anaemia or improved mitochondrial function were observed as part of this work. Ferumoxytol is structurally and pharmacologically similar to other IV iron compounds which have been shown improve haematocrit in several different animal models (Egeli & Framstad, 1998; Tait & Dureski, 1979 & Reece et al., 1985). Therefore it is likely the ineffectiveness of the drug observed here was due to an inadequate dosing regime and not ferumoxytol itself. A significant limitation of this work was that no pilot

dosing studies were conducted to identify the effective dose of ferumoxytol for treating anaemia in rats. Indeed, the dose chosen for this study was based on the effective clinical dose needed to ameliorate anaemia in CKD patients, as no effective dose in rats has been reported in the literature. While mammalian iron metabolism is highly conserved, there are subtle differences in iron homeostasis in humans and rodents including increased mucosal membrane shedding and a reduced erythrocyte lifespan in mice (Ganz & Nemeth, 2012). Collectively this may result in increased iron requirements in rodents and explain the lack of effectiveness in this study.

Given the disruption of iron metabolism in CKD, an important area for future investigation would be to characterise the role of hepcidin in the present model. Indeed, it has been suggested that hepcidin over-expression plays a key role in anaemia in cardio-renal syndrome (van der Putton et al., 2007). Hepcidin is a key regulator of iron metabolism and acts by binding to, and subsequently degrading, ferroportin, the principal exporter of intracellular iron. This leads to the accumulation of iron within the reticuloendothelial system, reducing iron availability for haemoglobin synthesis, and thus leading to anaemia (Nemeth et al., 2004). Increased expression of hepcidin has been reported in anaemic heart failure patients and CKD patients undergoing haemodialysis (Divakaran et al., 2011 & van der Putton et al., 2007). Interestingly, a recent study by Garrido et al. (2015) revealed no changes in hepcidin expression in nephrectomised rats. However, these measurements were in renal and hepatic tissue only and serum hepcidin is considered a more sensitive and reliable marker of the protein (Delaby et al., 2014).

7.2 Conclusion

Overall this study has shown that there may be enhanced glucose utilisation in the uraemic heart *in vivo* and these adaptations are associated with altered mitochondrial structure and bioenergetics. These changes may underpin the enhanced susceptibility to cell injury and death reported in previous experimental studies and also contribute to the increased number of adverse cardiovascular effects observed in CKD patients.

8. Appendix

8.1 Development of Cannulation Method

To enable optimal cannulation, animals were warmed on a heated pad following induction of anaesthesia and the tail immersed in warm water to induce vasodilation of the lateral vein. The vein was then cannulated and the needle taped in place prior to placing the animal in the imaging bed. Initially the catheter system was developed using a standard 25G butterfly needle, Tygon tubing (0.5mm inner diameter, 1.5mm outer diameter, Cole Palmer, UK) and a 23G needle connected to a syringe for injection (Figure 8.1). However, a limitation of this system was the difficulty confirming if the vein had been fully cannulated or if the needle was paravenous.

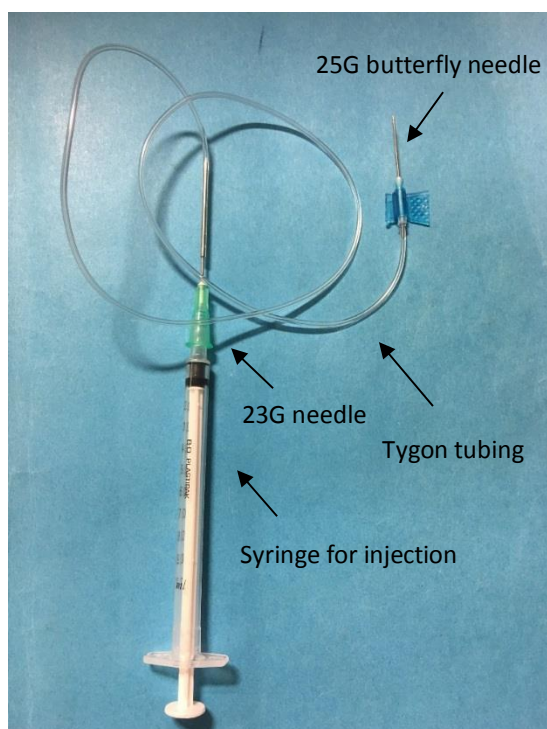


Figure 8.1. Initial cannulation system used for PET studies.

Due to the cannulation difficulties, a different catheter system was developed. The new system employed a 24G IV cannula which was housed in a PTFE membrane (Troge Medical, Hamburg, Germany). During the cannulation process the needle could be partially withdrawn leaving the membrane in the blood vessel (Figure 8.2). If the vein was fully cannulated the membrane would rapidly fill with blood whereas a poor cannulation would result in no/very little blood filling the membrane. If the blood vessel was not fully cannulated the needle could be withdrawn and the vein re-cannulated until successful.

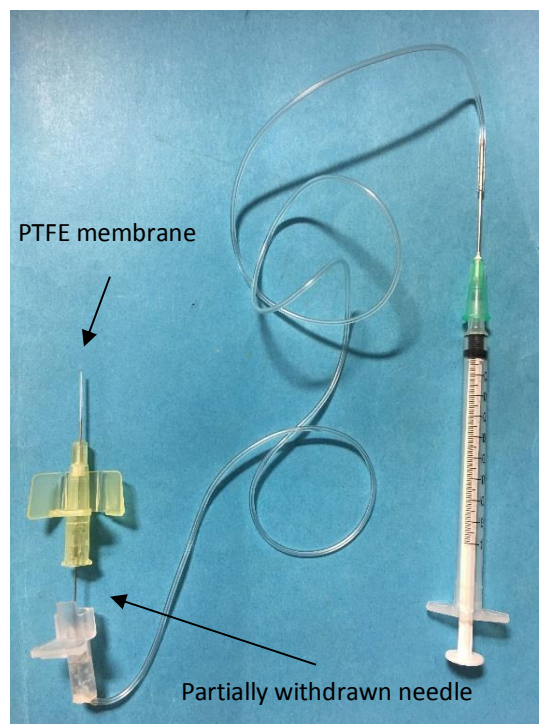


Figure 8.2. Modified cannulation system. The original 25G butterfly needle was replaced by a 24G IV cannula. When the needle was partially withdrawn the PTFE membrane remained in the blood vessel and filled with blood if the vein was fully cannulated.

A successful cannulation could be confirmed at 3 points during the scan and subsequent analysis. Firstly, during injection of radiotracer there should have been no back pressure, the first sign of a para-venous cannulation was resistance during radiotracer administration. Secondly, the acquisition monitor had a live fly through feature which showed the number of annihilation events in the field of view. If the injection was successful, the number of events increased significantly 5-10s post injection whereas a poor injection resulted in a very slow and steady increase in counts as the radiotracer diffused into the vein from the tail. Finally, once the data were reconstructed a successful injection was characterised by a sharp spike in the plasma TAC quickly followed by plateau (see Section 4.3). If the injection was poor the spike in the TAC was absent or significantly flatter.

8.2 Optimisation of Western Blotting Conditions

Preliminary Western blots were performed to identify positive controls for the mitochondrial fusion and fission proteins MFN1, OPA1, MFN2 and DRP1. An example blot is shown in Figure 8.3.

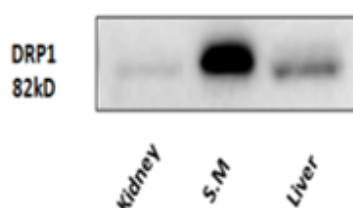


Figure 8.3. Western blot analysis of various tissues to find a positive control for DRP1. All lanes contained 50 μ g of protein. S.M = skeletal muscle.

A range of protein concentrations were also run (in duplicate) to optimise Western blotting conditions for the fusion and fission proteins. An example blot is shown in Figure 8.4.

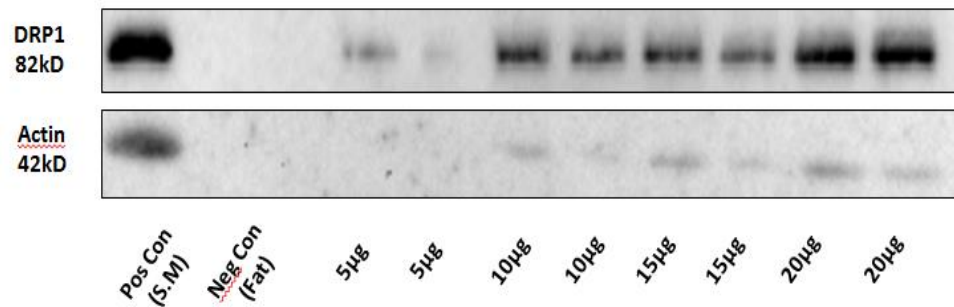


Figure 8.4. Western blot analysis of various protein concentrations to optimise conditions for probing of DRP1. Pos con = positive control, neg con = negative control and S.M = skeletal muscle.

8.3 Validation of Mitochondrial Size Using Flow Cytometry

Flow cytometry was used to assess mitochondrial size by measuring forward scatter in freshly prepared and freeze/thawed isolated mitochondria. Freeze thawed mitochondria were significantly smaller than freshly prepared mitochondria indicating this technique was sensitive enough to assess changes in mitochondrial size (Figure 8.5).

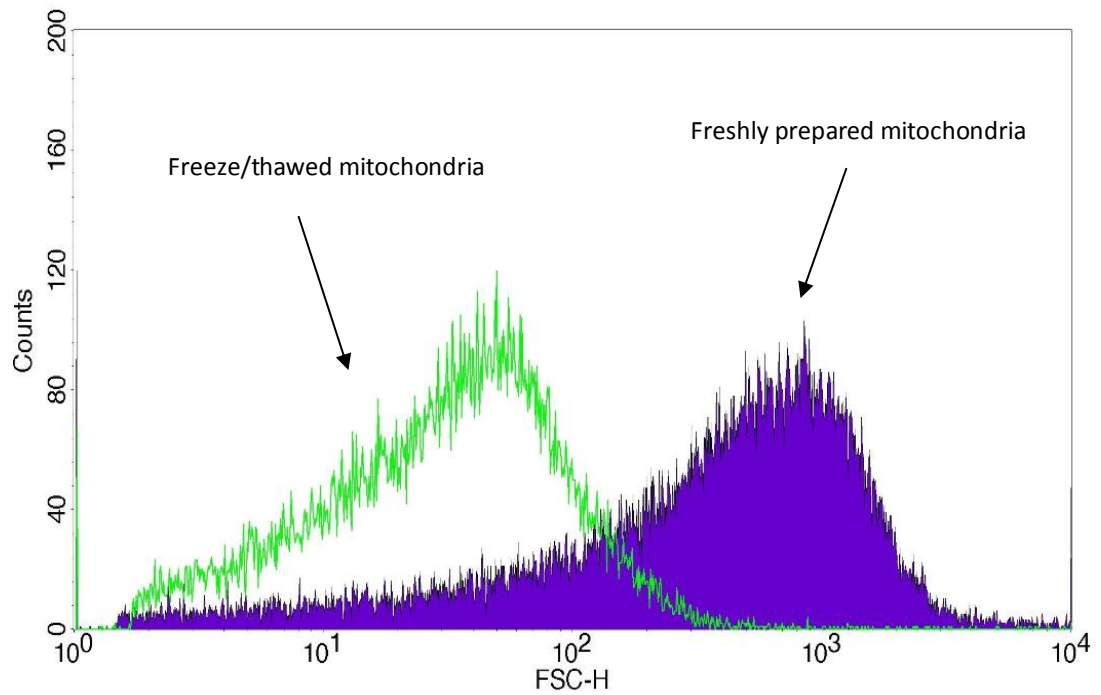


Figure 8.5. Flow cytometric analysis of mitochondrial size in freshly prepared and freeze/thawed mitochondria. The green population represents mitochondria which were subjected to three rounds of freeze thawing, resulting in substantial fragmentation. The purple population represents freshly prepared mitochondria which were significantly larger than their freeze/thawed counterparts.

Publications

Papers

Atkinson, R., Nuhu, F., Cawthorne, C., Bhandari, S., Archibald, S. & Seymour, AML. (2017) Imaging myocardial glucose metabolism in experimental uraemia *in vivo* using ¹⁸F-FDG PET. (In preparation).

Atkinson, R., Nuhu, F., Bhandari, S. & Seymour, AML. (2017). Altered mitochondrial morphology and function in uraemic cardiomyopathy. (In preparation).

Abstracts

Atkinson, R., Bhandari, S. & Seymour, AML. (2014). Mitochondrial dynamics in experimental uraemic cardiomyopathy. *Heart*, **100**(4). Abstract – Poster presentation at BSCR Autumn meeting, Reading

Atkinson, R., Ruest, T., Cawthorne, C., Bhandari, S & Seymour, AML. (2015). Imaging myocardial glucose metabolism in an experimental model of uraemic cardiomyopathy using ¹⁸F-FDG PET. *Journal of Molecular and Cellular Cardiology*, (Poster presentation at European section of ISHR, Bordeaux).

Atkinson, R., Cawthorne, C., Bhandari, S., Archibald, S. & Seymour, AML. (2015). Probing myocardial metabolism in ureamic cardiomyopathy *in vivo*. Oral Presentation at annual Post-Graduate Medical Conference, Prague.

References

- Abel, ED. & Doenst, T. (2011). Mitochondrial adaptations to physiological vs. pathological cardiac hypertrophy. *Cardiovascular Research*, **90**(2):234-242.
- Acehan, D., Malhotra, A., Xu, Y., Ren, M., Stokes, DL. & Schlame, M. (2011). Cardiolipin Affects the Supramolecular Organization of ATP Synthase in Mitochondria. *Biophysical Journal*, **9**(4):2184–2192.
- Agarwal, R. (2006). Proinflammatory effects of iron sucrose in chronic kidney disease. *Kidney International*, **69**(7):1259-63.
- Akki, A. & Seymour, AML. (2009). Western diet impairs metabolic remodeling and contractile efficiency in cardiac hypertrophy. *Cardiovascular Research*, **81**:610-617.
- Akki, A., Smith, K. & Seymour, AML. (2008). Compensated cardiac hypertrophy is characterized by a decline in palmitate oxidation. *Molecular and Cellular Biochemistry*, **311**:215-224.
- Aksentijevic, D. (2008). Myocardial insulin resistance in experimental uraemia. PhD thesis, University of Hull.
- Aksentijevic, D., Bhandari, S. & Seymour, AML. (2009). Insulin resistance and altered glucose transporter 4 expression in experimental uraemia. *Kidney International*, **75**:711-718.
- Albin, R., Dowell, RT., Zak, R. & Rabinowitz, M. (1973). Synthesis and degradation of mitochondrial components in hypertrophied rat heart. *Biochemical Journal*, **136**(3):629-637.

Alcala, S., Klee, M., Fernandez J., Fleischer, A. & Pimentel-Muinos, FX. (2008). A highthroughput screening for mammalian cell death effectors identifies the mitochondrial phosphate carrier as a regulator of cytochrome c release. *Oncogene*, **27**:44–54.

Anker, SD., Colet, JC., Filippatos, G., Willenheimer, R., Dickstein, K., Drexler, H., Lüscher, TF., Bart, B., Banasiak, W., Niegowska, J., Kirwan, BA., Mori, C., von Eisenhart Rothe, B., Pocock, j., Poole-Wilson, PA. & Ponikowski, P. (2009). Ferric carboxymaltose in patients with heart failure and iron deficiency. *The New England Journal of Medicine*, **361**:2436-2448.

Arany, Z., He, H., Lin, J., Hoyer, K., Handschin, C., Toka, O. & Ahmad, F. (2005). Transcriptional coactivator PGC-1 alpha controls the energy state and contractile function of cardiac muscle. *Cell Metabolism*, **1**:259–271.

Arany, I. & Safirstein, RL. (2003). Cisplatin Nephrotoxicity. *Seminars in Nephrology*, **23**(5): 460-464.

Arnoult, D., Grodet, A. & Lee, YJ. (2005). Release of OPA1 during apoptosis participates in the rapid and complete release of cytochrome c and subsequent mitochondrial fragmentation. *The Journal of Biological Chemistry*, **280**:35742-35750.

Arora, NP. & Ghali, JK. (2013). Iron deficiency anaemia in heart failure. *Heart Failure Reviews*, **18**:485-501.

Assaly, R., d'Anglemont De Tassigny, A., Paradis, S., Jacquin, S., Berdeaux, A. & Morin, D. (2012). Oxidative stress, mitochondrial permeability transition pore opening and cell death during hypoxia-reoxygenation in adult cardiomyocytes. *European Journal of Pharmacology*, **675**(1-3):6-14.

Bart, B., Banasiak, W., Niegowska, J., Kirwan, BA., Mori, C., von Eisenhart Rothe, B., Pocock, J., Poole-Wilson, PA. & Ponikowski, P. (2009). Ferric carboxymaltose in patients with heart failure and iron deficiency. *The New England Journal of Medicine*, **361**:2436-2448.

Barger, PM., Brandt, JM., Leone, TC., Weinheimer, CJ. & Kelly, DP. (2000). Deactivation of peroxisome proliferator-activated receptor- α during cardiac hypertrophic growth. *Journal of Clinical Investigation*, **105**:1723-1730.

Basso, E., Fante, L., Fowlkes, J., Petronilli, V., Forte, MA. & Bernardi P. (2005) Properties of the permeability transition pore in mitochondria devoid of cyclophilin D. *The Journal of Biological Chemistry*, **280**:18558–18561.

Beadle, RM. & Frenneaux, M. (2010). Modification of myocardial substrate utilisation: a new therapeutic paradigm in cardiovascular disease. *Heart*, **96**:824-830.

Beer, M., Seyfarth, T., Sandstede, J., Landschultz, W., Lipke, C., Kostler, H., Von Kienlin, M., Harre, K., Hahn, D. & Neubauer, S. (2002). Absolute concentrations of high-energy phosphate metabolites in normal, hypertrophied and failing human myocardium measured noninvasively with $(^{31}\text{P})\text{-SLOOP}$ magnetic resonance spectroscopy. *Journal of American College of Cardiology*, **40**:1267-74.

Ben-Haim, S., Sopov, V., Stein, A., Moskovitz, B., Front, A., Mecz, Y., Las, L., Kastin, A., Nativ, O. & Groshar, D. (2000). Kidney function after radical nephrectomy: assessment by quantitative SPECT of $^{99\text{mTc}}$ -DMSA uptake by the kidneys. *Journal of Nuclear Medicine*, **41**:1025-1029.

Bergström, J. & Lindholm, B. (1998). Malnutrition, cardiac disease, and mortality: an integrated point of view. *American Journal of Kidney Disease*, **32**(5):834-41.

- Bers, DM. (2002). Cardiac excitation-contraction coupling. *Nature*, **415**:198-205.
- Boehm, EA., Jones, BE., Radda, GK., Veech, RL. & Clarke, K. (2001). Increased uncoupling proteins and decreased efficiency in palmitate-perfused hyperthyroid rat heart. *American Journal of Physiology*, **280**:977-983.
- Bolger, AP., Bartlett, FR., Pentson, H., O'Leary, J., Pollock, N., Kaprielian, R. & Chapman, CM. (2006). Intravenous iron therapy alone for treatment of anaemia in patients with chronic heart failure. *Journal of the American College of Cardiology*, **48**:1225-1227.
- Bossy, B., Petrilli, A., Klinglmayr, E., Chen, J., Lutz-Meindl, U. & Knott, AB. (2010). S-Nitrosylation of DRP1 does not effect enzymatic activity and is not specific to Alzheimer's disease. *Journal of Alzheimer's Disease*, **20**:513-526.
- Botker, HE., Goodwin, GW., Holden, JE., Doenst, T., Gjedde, A. & Taegtmeyer, H. (1999). Myocardial glucose uptake measured fluorodeoxyglucose: a proposed method to account for variable lumped constants. *The Journal of Nuclear Medicine*, **7**:1186-1196.
- Bowker-Kinley, MM., Davis, WI., Wu, P., Harris, RA. & Popov, KM. (1998) Evidence for existence of tissue-specific regulation of the mammalian pyruvate dehydrogenase complex. *Biochemical Journal*, **329**:191-196.
- Brand, MD. & Nichols, DG. (2011). Assessing mitochondrial dysfunction in cells. *Biochemical Journal*, **435**:297-312.
- Braunlich, H., Marx, F., Fleck, C. & Stein, G. (1997). Kidney function in rats after 5/6 nephrectomy (5/6NX): effort of treatment with vitamin E. *Experimental and Toxicological Pathology*, **49**:135-139.

- Buchanan, SK. & Walker, JE. (1996). Large-scale chromatographic purification of F1Fo-ATPase and complex I from bovine heart mitochondria. *Biochemical Journal*, **318**:343-349.
- Buerkert, J., Martin, D., Prasad, J., Chambless, S. & Klahr, S. (1979). Response of deep nephrons and the terminal collecting ducts to a reduction in mass. *American Journal of Physiology*, **236**:454-464.
- Bugger, H., Schwarzer, M., Chen, D., Schrepper, A., Amorim, PA., Schoepe, M., Nguyen, TD., Mohr, FW., Khalimonchuk, O., Weimer, BC. & Doenst, T. (2010). Proteomic remodelling of mitochondrial oxidative pathways in pressure overload-induced heart failure. *Cardiovascular Research*, **85**:376-384.
- Cagalinec, M., Safiulina, D., Liiv, M., Liiv, J., Choubey, V., Wareski, P., Veksler, V. & Kaasik, A. (2013). Principles of the mitochondrial fusion and fission cycle in neurons. *Journal of Cell Science*, **126**:2187-2197.
- Campanella, A., Rovelli, E., Santambrogio, P., Cozzi, A., Taroni, F. & Levi, S. (2009). Mitochondrial ferritin limits oxidative damage regulating mitochondrial iron availability: hypothesis for a protective role in Friedreich ataxia. *Human Molecular Genetics*, **18**(1): 1–11.
- Cancado, RD. & Munoz, M. (2011). Intravenous iron therapy: how far have we come? *Revista Brasileira de Hematologia e Hemoterapia*, **33**(6):461-469.
- Carabello, BA. (2002) Evolution of the study of left ventricular function: everything old is new again, *Circulation*, **105**:2701-2703.
- Chamberlain, RM. & Shirley, DG. (2007). Time course of the renal response to partial nephrectomy: measurements in conscious rats. *Experimental Physiology*, **92**:251-262.

- Chen, L., Gong, Q., Stice, JP. & Knowlton, AA. (2009). Mitochondrial OPA1, apoptosis and heart failure. *Cardiovascular Research*, **84**:91-99.
- Chen, Y. & Chan, DC. (2010). Physiological functions of mitochondrial fusion. *Annals of the New York Academy of Sciences*, **1201**:21–25.
- Chen, Y., Chomyn, A. & Chan, DC. (2005). Disruption of fusion results in mitochondrial heterogeneity and dysfunction. *Journal of Biological Chemistry*, **280**(28):26185–92.
- Chen, Y., Detmer, SA., Ewald, AJ., Griffin, EE., Fraser, SE. & Chan DC. (2003). Mitofusins Mfn1 and Mfn2 coordinately regulate mitochondrial fusion and are essential for embryonic development. *Journal of Cell Biology*, **160**(2):189-200.
- Chen, Y. & Dorn II, G. (2013). PINK1-phosphorylated mitofusin 2 is a Parkin receptor for culling damaged mitochondria. *Science*, **340**(6131):471-5.
- Chen, Y., Guo, X., Ma, D., Guo, Y., Li, Q., Yang D. (2004). Dysregulation of HSG triggers vascular proliferative disorders. *Nature Cell Biology*, **6**:872–883.
- Chen, Y., Liu Y. Dorn II, G. (2011). Mitochondrial fusion is essential for organelle function and cardiac homeostasis. *Circulation Research*, **109**(12):1327-31.
- Chevalier, RL. (2006). Obstructive nephropathy: towards biomarker discovery and gene therapy. *Nature Clinical Practice Nephrology*, **2**:157–168.
- Chiong, M., Wang, ZV., Pedrozo, Z., Cao, DJ., Troncoso, R., Ibacache, M., Criollo, A., Nemchenko, A., Hill, AJ. & Lavandero, S. (2011). Cardiomyocyte death: mechanisms and translational implications. *Cell Death and Disease*, **2**(12):e244.

Cho, DH., Nakamura, T., Fang., J., Cieplak, P., Godzik, A. & Gu, Z. (2009). S-Nitrosylation of DRP1 mediates beta-amyloid-related mitochondrial fission and neural injury. *Science*, **324**:102-105.

Chow, KM, Liu, ZC. & Chang, TMS. (2003). Animal remnant kidney model of chronic renal failure revisited. *Hong Kong Journal of Nephrology*, **5**:57-64.

Courtois, A., Nusgens, BV., Hustin, R., Namur, G., Gomez, P., Somja, J., Defraigne, JO., Delvenne, P., Michel, JB., Colige, AC. & Sakalihasan, N. (2013). 18F-FDG Uptake Assessed by PET/CT in Abdominal Aortic Aneurysms Is Associated with Cellular and Molecular Alterations Prefacing Wall Deterioration and Rupture. *Journal of Nuclear Medicine*, **54**(10):1740-1747.

Coresh, J., Selvin, E., Stevens, LA., Manzi, J., Kusek, JW., Eggers, P., Van Lente, F. & Levey AS. Prevalence of chronic kidney disease in the United States. (2007). *JAMA*, **298**(17):2038–47.

Crichton, RR., Danielson, BG. & Geisser, P. (2008). Iron Therapy with Special Emphasis on Intravenous Administration, 4th ed.; UNI-MED Verlag AG, Bremen, Germany.

Crow, MT., Mani, K., Nam, YI. & Kitsis, RN. (2004). The mitochondrial death pathway and cardiac myocyte apoptosis. *Circulation research*, **95**: 957-970.

Crompton, M., Costi, A. & Hayat. (1987). Evidence for the presence of a reversible Ca²⁺-dependent pore activated by oxidative stress in heart mitochondria. *The Biochemical Journal*, **245**:915-918.

Crompton, M., Ellinger, H. & Costi, A. (1988). Inhibition by cyclosporin A of a Ca²⁺-dependent pore in heart mitochondria activated by inorganic phosphate and oxidative stress. *The Biochemical Journal*, **255**(1):357-360.

Csordás, G., Renken, C., Várnai, P., Walter, L., Weaver, D., Buttle, KF., Balla, T., Mannella, CA. & Hajnóczky, G. (2006). Structural and functional features and significance of the physical linkage between ER and mitochondria. *Journal of Cell Biology*, **174**(7): 915–921.

Dai, DF., Hsieh, EJ., Liu, Y., Chen, T., Beyer, RP., Chin, MT. (2012). Mitochondrial proteome remodeling in pressure overload-induced heart failure: the role of mitochondrial oxidative stress. *Cardiovascular research*, **93**(1):79–88.

Danielson, J. (2004). Structure, chemistry, and pharmacokinetics of intravenous iron agents. *American Society of Nephrology*, **15**:S93-S98.

de Brito, OM. & Scorrano, L. (2008) Mitofusin 2 tethers endoplasmic reticulum to mitochondria. *Nature*, **456**:605–610.

de Silva, R., Rigby, AS., Witte, KK., Nikitin, NP., Tin, L., Goode, K., Bhandari, S., Clark, AL. & Cleland, JG. (2006) Anemia, renal dysfunction, and their interaction in patients with chronic heart failure. *American Journal of Cardiology*, **98**(3):391–398.

Delabya, C., Vialareta, j., Brosa, P., Gabellea, A., Lefebvred, T., Puyd, H., Hirtza, C. & Lehmann, S. (2014). Clinical measurement of Hepcidin-25 in human serum: Is quantitative mass spectrometry up to the job? *Open Proteomics*, **3**:60-67.

Delettre, C., Lenaers, G., Griffoin¹, JM., Gigarel, N., Lorenzo, C., Belenguer, P., Pelloquin, L., Grosgeorge, J., Turc-Carel, C., Perret, E., Astarie-Dequeker, C., Lasquellec, L., Arnaud, B., Ducommun, B., Kaplan, J. & Hamel, CP. (2000). Nuclear gene OPA1, encoding a mitochondrial dynamin-related protein, is mutated in dominant optic atrophy. *Nature Genetics*, **26**:207–210.

Després, JP., Lamarche, B., Mauriège, P., Cantin, B., Dagenais, GR., Moorjani, S. & Lupien, PJ. (1996). Hyperinsulinemia as an independent risk factor for ischemic heart disease. *The New England Journal of Medicine*, **334**(15):952-957.

Dikow, R., Kihm, LP., Zeier, M., Kapitza, J., Toring, J., Amann, K., Tiefenbacher, C. & Ritz, E. Increased infarct size in uraemic rats: reduced ischemia tolerance? *Journal of the American Society of Nephrology*, **15**:1530-1536.

Disatnik, MH., Ferreira, JCB., Cruz, JC., Gomes, KS., Dourado, PMM., Qi, X. & Mochly-Rosen, D. (2013). Acute inhibition of mitochondrial fission after myocardial infarction prevents long-term cardiac dysfunction. *Journal of the American Heart Association*, **2**:1-14.

Divakaran, I., Mehta, S., Yao, D., Hassan, S., Simpson, S., Wiegerinck, E., Swinkels, DW., Mann, DL. & Afshar-Kharghan V. (2011). Heparin in anemia of chronic heart failure. *American Journal of Haematology*, **86**(1):107-9.

Diwan, A., Wansapura, J., Syed, FM., Matkovich, SJ., Lorenz, JN. & Dorn II, G. (2008). Nix-mediated Apoptosis Links Myocardial Fibrosis, Cardiac Remodeling, and Hypertrophy Decompensation. *Circulation*, **117**(3): 396–404.

Doenst, T., Pytel, G., Schreppe, A., Amorim, P., Farber, G., Shingu, Y., Mohr, FW. & Schwarzer, M. (2010). Decreased rates of substrate oxidation ex vivo predict the onset of heart failure and contractile dysfunction in rats with pressure overload. *Cardiovascular Research*, **86**:461-470.

Doenst, T. & Taegtmeyer, H (1998). Complexities underlying the quantitative determination of myocardial glucose uptake with 2-deoxyglucose. *Journal of Molecular and Cellular Cardiology*, **30**:1595-1604.

Dorn II, GW. (2013). Mitochondrial dynamics in heart failure. *Biochimica et Biophysica Acta*, **1883**:233-241.

Drazner, M. (2011). The progression of hypertensive heart disease. *Circulation*, **123**:327-334.

Dorn II, GW. (2013). Mitochondrial dynamics in heart failure. *Biochimica et Biophysica Acta*, **1883**:233-241.

Dubrelle, MP., Terzi, F., Gubler, MC., Kleinknecht, C. & Schaefferbeke. (1992). Changes in thickness and anionic sites of the glomerular basement membrane after subtotal nephrectomy in the rat. *American Journal of Pathology*, **141**:1481-1489.

Efstratiadis, G., Konstantinou, D., Chytas, I. & Vergoulas, G. (2008). Cardio-renal anaemia syndrome. *Hippokratia*, **12**:6-11.

Egeli, AK. & Framstad, T. (1998). Evaluation of the efficacy of perorally administered glutamic acid-chelated iron and iron-dextran injected subcutaneously in Duroc and Norwegian Landrace piglets. *Zentralbl Veterinarmed A*, **45**(1):53-61.

Eisner, DA., Caldwell, JL., Kistamas, K. & Trafford, AW. (2017). Calcium and Excitation-Contraction Coupling in the Heart. *Circulation Research*, **121**:181-195.

el Alaouti-Talibi, Z., Landormy, S., Loireau, A. & Moravec, J. (1992). Fatty acid oxidation and mechanical performance of volume-overloaded rat hearts. *American Journal of Physiology*, **262**:1068-1074.

Elrod, JW. & Molkenin, JD. (2013). Physiologic Functions of Cyclophilin D and the Mitochondrial Permeability Transition Pore. *Journal of the Japanese Circulation Society*, **77**(5):1111-22.

Ertl, G. & Frantz, S. (2005). Healing after myocardial infarction. *Cardiovascular Research*, **66**:22-32.

Eschbach, JW. (2005). Iron requirements in erythropoietin therapy. *Best Practice & Research in Clinical Haematology*, **18**(2):347-361.

Eskelinen, EL. & Saftig, P. (2009). Autophagy: a lysosomal degradation pathway with a central role in health and disease. *Biochimica et Biophysica Acta*, **1793**(4):664-73.

European Medicines Agency. (2010). Committee for Medicinal Products for Human Use (CHMP): Ferumoxytol. Retrieved 18th October 2017 from: http://www.ema.europa.eu/docs/en_GB/document_library/EPAR_Public_assessment_report/human/002215/WC500129751.pdf

Fabiato, A. & Fabiato, F. (1979). Calcium and cardiac excitation-contraction coupling. *Annual Review of Physiology*, **41**:473-484.

Fang, JHD. & Muzic, RF. (2008). Spillover and Partial-Volume Correction for Image-Derived Input Functions for Small-Animal ¹⁸F-FDG PET Studies. *The Journal of Nuclear Medicine*, **49**(4):606-614.

Fang, L., Moore, XL., Gao, XM., Dart, AM., Lim, YL. & Du, XJ. (2007). Down-regulation of mitofusin-2 expression in cardiac hypertrophy in vitro and in vivo. *Life Sciences*, **80**:2154–2160.

Feldman, AM., Weinberg, EO., Ray, PE. & Lorell, BH. (1993). Selective changes in cardiac gene expression during compensated hypertrophy and the transition to cardiac decompensation in rats with chronic aortic banding. *Circulation Research*, **73**:184-192.

Field, ML., Clark, JF., Henderson, C., Seymour, AML. & Radda, GK. (1994). Alterations in the myocardial creatine kinase system during chronic anaemic hypoxia. *Cardiovascular Research*, **28**(1):86-91.

Finch, CA., Miller, LR., Inamdar, AR., Person, R., Seiler, K. & Mackler, B. (1976). Iron deficiency in the rat. Physiological and biochemical studies of muscle dysfunction. *Journal of Clinical Investigation*, **58**:447-453.

Finck, BN. & Kelly, DP. (2002). Peroxisome Proliferator-activated Receptor α (PPAR α) Signalling in the Gene Regulatory Control of Energy Metabolism in the Normal and Diseased Heart. *Journal of Molecular Cellular Cardiology*, **34**:1249-1257.

Finck, BN. & Kelly, DP. (2006). PGC-1 coactivators: inducible regulators of energy metabolism in health and disease. *The Journal of Clinical Investigation*, **116**(3):615-22.

Fink, JC., Lodge, MA., Smith, MF., Hinduja, A., Brown, J., Dinits-Pensy, MY. & Dilsizian, V. (2010). Pre-clinical myocardial metabolic alterations in chronic kidney disease. *Cardiology*, **116**(3):160-7.

Fishbane, S., Frei, GL. & Maesaka, J. (1995). Reduction in recombinant human erythropoietin doses by the use of chronic intravenous iron supplementation. *American Journal of Kidney Disease*, **26**(1):41-6.

Fishbane, S. & Kowalski, EA. (2000). The comparative safety of intravenous iron dextran, iron saccharate, and sodium ferric gluconate. *Seminars in Dialysis*, **13**(6):381-384.

Fisher, JW. (2003). Erythropoietin: physiology and pharmacology update. *Experimental Biology and Medicine*, **228**:1-14.

Fisher, SA., Langille, BL. & Srivastava, D. (2000). Apoptosis during cardiovascular development, *Circulation Research*, **87**:856-864.

Foley, RN., Parfrey, PS., Harnett, JD., Kent, GM., Martin, CJ., Murray, DC., Barre, PE. (1995). Clinical and echocardiographic disease in patients starting end-stage renal disease therapy. *Kidney International*, **47**:186-192.

Foley, RN., Parfrey, PS. & Sarnak, MJ. (1998). Clinical epidemiology of cardiovascular disease in chronic renal disease. *American Journal of Kidney Disease*, **32**:112-119.

Fouque, D., Kalantar-Zadeh, K., Kopple, J., Cano, N., Chauveau, P., Cuppari, L., Franch, H., Guarnieri, G., Ikizler, TA., Kaysen, G., Lindholm, B., Massy, Z., Mitch, W., Pineda, E., Stenvinkel, P., Trevino-Becerra, A. & Wanner, C. (2008). A proposed nomenclature and diagnostic criteria for protein wasting in acute chronic kidney disease. *Kidney International*, **73**:391-398.

Foury, F. & Roganti, T. (2002). Deletion of the mitochondrial carrier genes MRS3 and MRS4 suppresses mitochondrial iron accumulation in a yeast frataxin-deficient strain. *The Journal of Biological Chemistry*, **277**:24475-24483.

Fragasso, G. (2016). Deranged cardiac metabolism and the pathogenesis of heart failure. *Cardiac Failure Review*, 2016:**2**(1):8–13.

Frey, N., Katus, HA., Olson, EN. & Hill, JA. (2004). Hypertrophy of the heart: a new therapeutic target? *Circulation*, **109**:1580-1589.

Frezza, C., Cipolat, S., Martins de Brito, O., Micaroni, M., Beznoussenko, GV., Rudka, T., Bartoli, D., Polishuck, RS., Danial, NN., De Strooper, B. & Scorrano, L. (2006). OPA1 controls apoptotic cristae remodelling independently from mitochondrial fusion. *Cell*, **126**(1):177-89.

Fry, M. and Green, DE. (1981). Cardiolipin requirement for electron transfer in complex I and III of the mitochondrial respiratory chain. *Journal of Biological Chemistry*, **256**:1874–1880.

Fueger, BJ., Czernin, J., Hildebrandt, I., Tran, C., Halpern, BS., Stout, D., Phelps, ME. & Weber, WA. (2006). Impact of animal handling on the results of ¹⁸F-FDG PET studies in mice. *Journal of Nuclear Medicine*, **47**(6):999-1006.

Gao, S., Long, CL., Wang, RH. & Wang, H. (2009). KATP activation prevents progression of cardiac hypertrophy to failure induced by pressure overload via protecting endothelial function. *Cardiovascular Research*, **83**(3):444-456.

Gao, J., Schatton, D., Martinelli, P., Hansen, H., Pla-Martin D., Barth E., Becker C., Altmueller, J., Frommolt P., Sardiello M. & Rugarli, E. (2014). CLUH regulates mitochondrial biogenesis by binding mRNAs of nuclear-encoded mitochondrial proteins. *The Journal of Cell Biology*, **207**(2):213-23.

Gao, D., Zhang, L., Dhillon, R., Hong, TT., Shaw, RM. & Zhu, J. (2013). Dynasore protects mitochondria and improves cardiac lusitropy in Langendorff perfused mouse heart. *PLoS ONE*, **8**:e60967

Ganz, T. & Nemeth, E. (2012). Hepcidin and iron homeostasis. *Biochim Biophys Acta*, **1823**(9): 1434–1443.

Garnier, A., Fortin, D., Delomenie, C., Momken, I., Veksler, V. & Ventura-Capular, R. (2003). Depressed mitochondrial transcription factors and oxidative capacity in failing rat cardiac and skeletal muscles. *Journal of Physiology*, **551**:491-501.

Garrido, P., Ribeiro, S., Fernandes, J., Vala, H., Bronze-da-Rocha, E., Rocha-Pereira, P., Belo, L., Costa, E., Santos-Silva, A. & Reis, F. (2015). Iron-Hepcidin Dysmetabolism, Anemia and

Renal Hypoxia, Inflammation and Fibrosis in the Remnant Kidney Rat Model. *PLoS One*, **10(4)**:1-24.

Geisser, P. & Burckhardt, S. (2011). The Pharmacokinetics and Pharmacodynamics of Iron Preparations. *Pharmaceutics*, **3**:12-33.

Gharagouzloo, CA., Timms, L., Qiao, J., Fang, Z., Nneji, J., Pandya, A., Kulkarni, P., van de Ven, AL., Ferris, C. & Sridhar, S. (2017). Quantitative vascular neuroimaging of the rat brain using superparamagnetic nanoparticles: New insights on vascular organization and brain function. *Journal of Neuroimaging*, **163**:24-33.

Ghosh, N., Rimoldi, OE., Beanlands, RSB. & Camici, PG. (2010). Assessment of myocardial ischemia and viability: role of positron emission tomography. *European Heart Journal*, **31**:2984-2995.

Gill, VM. & Ferreira, JS. (2013). Anaemia and iron deficiency in heart failure. *Portuguese Journal of Cardiology*, **1**:39-44.

Go, AS., Chertow, GM., Fan, D., McCulloch, CE. & Hsu, C. (2004). Chronic Kidney Disease and the Risks of Death, Cardiovascular Events, and Hospitalization. *The New England Journal of Medicine*, **351**:1296-1305.

Goldblatt, HJL., Hanzal, RF. & Summerville, WW. (1934). Studies on experimental hypertension: I. The production of persistent elevation of systolic blood pressure by means of renal ischemia. *The Journal of Experimental Medicine*, **59**:347-379.

Gonzalez-Cabo, P., Vazquez-Manrique, RP., Garcia-Gimeno, MA., Sanz, P., Palau, F. (2005). Frataxin interacts functionally with mitochondrial electron transport chain proteins. *Human Molecular Genetics*, **14**:2091–2098.

Gottlieb, RA., Burlison, KO., Kloner, RA., Babior, BM. & Engler, RL. (1994). Reperfusion injury induces apoptosis in rabbit cardiomyocytes. *Journal of Clinical Investigation*, **94**:1621-1628.

Gorski, PA., Ceholski, DK. & Hajjar, RJ. (2015). Altered myocardial calcium cycling and energetics in heart failure - a rational approach for disease treatment. *Cell Metabolism*, **21**(2): 183-194.

Griffiths, ER., Friehs, I., Scherr, E., Poutias, D., McGowan, FX. & Del Nido, PJ. (2010). Electron transport chain dysfunction in neonatal pressure-overload hypertrophy precedes cardiomyocyte apoptosis independent of oxidative stress. *The Journal of thoracic and cardiovascular surgery*, **139**(6):1609–1617.

Gropler, RJ. (2010). Radionuclide imaging of Myocardial Metabolism. *Circulation: Cardiovascular Imaging*, **3**(2):211-222.

Grossman, W. (1980). Cardiac hypertrophy: Useful adaption or pathologic process? *American Journal of Medicine*, **69**:576-584.

Guimbal, C. & Kilimann, MWA. (1993). A Na(+) dependent creatine transporter in rabbit brain, muscle, heart and kidney: Cdna cloning and functional expression. *The Journal of Biological Chemistry*, **268**:8418-8421.

Haden, RL. (1938). Historical aspects of iron therapy in anemia. *The Journal of the American Medical Association*, **111**:1059-1061.

Haines, TH. & Dencher, NA. (2002). Cardiolipin: a proton trap for oxidative phosphorylation. *FEBS Letters*, **528**:35–39.

Hales, KG. & Fuller, MT. (1997). Developmentally regulated mitochondrial fusion mediated by a conserved, novel, predicted GTPase. *Cell*, **90**(1):121-9.

Halestrap, AP., Clarke, SJ. & Javadov, SA. (2004). Mitochondrial permeability transition pore opening during myocardial reperfusion – a target for cardioprotection. *Cardiovascular Research*, **61**:372-385.

Halestrap, AP. & Pasdois. (2009). The role of the mitochondrial permeability transition pore in heart disease. *Biochimica et Biophysica Acta*, **1787**:1402-1415.

Handa, N., Magata, Y., Mukai, T., Nishina, T., Konishi, J. & Komeda, M. (2007). Quantitative FDG-uptake by positron emission tomography in progressive hypertrophy of rat hearts in vivo. *Annals of Nuclear Medicine*, **21**:569–576.

Handelman, GJ. & Levin, NW. (2008). Iron and anemia in human biology: a review of mechanisms. *Heart Failure Reviews*, **13**:393-414.

Hanley, & Welsh, C. (2004). Current diagnosis and treatment in pulmonary disease. McGraw-Hill, New York.

Harwood, SM., Allen, DA., Chesser, AM., New, DI., Raferty, MJ. & Yaqoob, MM. (2003). Calpain is activated in experimental uraemia: is calpain a mediator or uraemia-induced myocardial injury? *Kidney international*, **63**:866-877.

Hasenfuss, G. (1998). Alterations of calcium-regulatory proteins in heart failure. *Cardiovascular Research*, **37**:279-289.

He, ZX., Shi, RF., Wu, YJ., Tian, YQ., Liu, XJ., Wang, SW., Shen, R., Qin, XW., Gao, RL., Narula, J. & Jain, D. (2003). Direct imaging of exercise-induced myocardial ischemia with fluorine-18-labeled deoxyglucose and Tc-99m-sestamibi in coronary artery disease. *Circulation*, **108**:1208–1213.

Headley & Wall. (2007). Flash pulmonary edema in patients with chronic kidney disease and end stage renal disease. *Nephrology Nursing Journal*, **34**(1):15-26.

Heather, LC., Cole, MA., Atherton, HI., Coumans, WA., Evans, RD., Tyler, DJ., Glatz, JF., Luiken, JJ. & Clarke, K. (2010). Adenosine Monophosphate-activated protein kinase activation, substrate transporter translocation, and metabolism in the contracting hyperthyroid rat heart. *Endocrinology*, **151**:422-431.

Heidemann, HT., Hoffman, K. & Inselmann, G. (1990). Long-term effects of acetazoleamide and sodium chloride loading on cisplatin nephrotoxicity in the rat. *European Journal of Clinical Investigation*, **20**:214-218.

Heinrich, HC., Gabbe, EE. & Whang, DH. (1969). Dose relationship of intestinal iron absorption in men with normal iron stores and persons with prelatent/latent iron deficiency. *Z. Naturforschg*, **24**:1301-1310.

Hentze, MW., Muckenthaler, MU. & Andrews, NC. (2004). Balancing Acts: Molecular control of mammalian iron metabolism. *Cell*, **117**:285-297.

Hernandez, AM., Huber, JS., Murphy, ST., Janabi, M., Zeng, GL., Brennan, KM., O'Neil, JP., Seo, Y. & Gullberg, GT. (2013). Longitudinal Evaluation of Left Ventricular Substrate Metabolism, Perfusion, and Dysfunction in the Spontaneously Hypertensive Rat Model of Hypertrophy Using Small-Animal PET/CT Imaging. *Journal Nuclear Medicine*, **54**(11):1938–1945.

Herrero, P., Weinheimer, CJ., Dence, C., Oellerich, WF. & Gropler, RJ. (2002). Quantification of myocardial glucose utilization by PET and 1-carbon-11-glucose. *The Journal of Nuclear Medicine*, **9**(1):5-14.

Hill, NR., Fatoba, ST., Oke, JL., Hirst, JA., O'Callaghan, CA., Lasserson, DS. & Hobbs, FDR. (2016). Global Prevalence of Chronic Kidney Disease – A Systematic Review and Meta-Analysis. *PLoS One*, **11**(7):1-18.

Hoffman, JIE. & Buckberg, GD. (2014). The Myocardial Oxygen Supply: Demand Index Revisited. *Journal of the American Heart Association*, **3**(1):1-10.

Home Office. (2014). Retrieved 18th August 2015 from:

<https://www.gov.uk/government/publications/operation-of-aspa>

Hood, DA., Joseph, AM. (2004). Mitochondrial assembly: protein import. *Proceedings of the Nutrition Society*, **63**:293–300.

Horowitz, MP. & Greenamyre, JT. (2010). Mitochondrial iron metabolism and its role in neurodegeneration. *Journal of Alzheimer's Disease*, **20**(2):S551-68.

Hotstetter, TH., Olson, JL., Rennke, HG., Venkatachalam, MA. & Brenner, BM. (1981). Hyperfiltration in remnant nephrons: a potentially adverse response to renal ablation. *American Journal of Physiology: Renal Physiology*, **241**:85-93.

Houtkooper, RH. & Vaz, FM. (2008). Cardiolipin, the heart of mitochondrial metabolism. *Cell and Molecular Life Sciences*, **65**:2493–2506.

Hsueh, CH., Chen, NX., Lin, SF., Chen, PS., Gattone, VH., Allen, MR., Fishbein, MC. & Moe SM. (2014). Pathogenesis of Arrhythmias in a Model of CKD. *Journal of the American Society of Nephrology*, **25**(12): 2812–2821.

Huss, JM. & Kelly, DP. (2004). Nuclear receptor signalling and cardiac energetics. *Circulation Research*, **95**, 568–578.

Huang, SC. (2000). Anatomy of SUV. Standardized uptake value. *Nuclear Medicine and Biology*, **27**(7):643-6.

Icardi, A., Paoletti, E., De Nicola, L., Mazzaferro, S., Russo, R. & Cozzolino, M. (2013). Renal anaemia and EPO hyporesponsiveness associated with vitamin D deficiency: the potential role of inflammation. *Nephrology Dialysis Transplantation*, **28**:1672-1679.

Ide, T., Tsutui, H., Kingugawa, S., Kang, D., Egashira, K. & Takeshita, A. (1999). Mitochondrial electron transport complex I is a potential source of oxygen free radicals in the failing myocardium. *Circulation Research*, **85**:357-363.

Iemitsu, M., Miyauchi, T., Maeda, S., Sakai, S., Fujii, N. & Miyazaki, H. (2008). Cardiac hypertrophy by hypertension and exercise training exhibits different gene expression of enzymes in energy metabolism. *Hypertension Research*, **26**(10):829–837.

Iglewski, M., Hill, JA., Lavandero, S. & Rothermel, BA. (2010). Mitochondrial Fission and Autophagy in the Normal and Diseased Heart. *Current Hypertension Reports*, **12**(6):418-425.

Ikeda, Y., Shirakabe, A., Maejima, Y., Zhai, P., Sciarretta, S., Toli, J., Nomura, M., Mihara, K., Egashira, K., Ohishi, M., Abdellatif, M. & Sadoshima J. (2015). Endogenous Drp1 mediates mitochondrial autophagy and protects the heart against energy stress. *Circulation Research*, **116**(2):264-78.

Ingwall, JS. (2009). Energy metabolism in heart failure and remodelling. *Cardiovascular Research*, **81**:412-419.

Ishihara, I., Nomura, M., Jofuku, A., Kato, H., Suzuki, SO., Masuda, K., Otera, H., Nakanishi, Y., Nonaka, I., Goto, Y., Taguchi, N., Morinaga, H., Maeda, H., Takayanagi, R., Yokota, S. & Mihara,

K. (2009). Mitochondrial fission factor Drp1 is essential for embryonic development and synapse formation in mice. *Nature Cell Biology*, **11**:958-966.

Izem-Meziane, M., Djerdjouri, B., Rimbaud, S., Caffin, F., Fortin, D., Fortin, D., Garnier, A., Veksler, V., Joubert, F. & Ventura-Clapier, R. Catecholamine-induced cardiac mitochondrial dysfunction and mPTP opening: protective effect of curcumin. *American Journal of Physiology: Heart and Circulatory Physiology*, **302**:665-674.

Jianga, L., Huanga, Y., Hunyora, S. & dos Remediosb CG. (2003). Cardiomyocyte apoptosis is associated with increased wall stress in chronic failing left ventricle. *European Heart Journal*, **24**:742–751.

Jakobs, S., Stoldt, S. & Neumann, D. (2011). Light microscopic analysis of mitochondrial heterogeneity in cell populations and within single cells. *Advances in Biochemical Engineering/Biotechnology*, **124**:1-19.

Jankowska, JA., von Haehling, S., Anker, SD. (2013). Iron deficiency and heart failure: diagnostic dilemmas and therapeutic perspectives. *European Heart Journal*, **34**:816-826.

Jarreta, D., Orus, J., Barrientos, A. Miro, O., Roig, E., Heras, M., Moraes, CT., Cardellach, F. & Casademont, J. (2000). Mitochondrial function in heart muscle from patients with idiopathic dilated cardiomyopathy. *Cardiovascular Research*, **45**:860-865.

Jaswal, JS., Keung, W., Wang, W., Ussher, JR. & Lopascuk. (2011). Targeting fatty acid and carbohydrate oxidation – A novel therapeutic intervention in the ischemic and failing heart. *Biochimica et Biophysica Acta*. **1813**(7):1333-1350.

Jelkmann, W. (1998). Proinflammatory cytokines lowering erythropoietin production. *Journal of Interferon and Cytokine Research*, **18**:555–559.

Johnson, DT., Harris, RA., French, S., Blair, PV., You, J., Bemis, KG., Wang, M. & Balaban, RS. (2007). Tissue heterogeneity of the mammalian mitochondrial proteome. *American Journal of Physiology: Cell Physiology*, **292**:689–697.

Kandaurova, NV., Chunikhin, O, Babich, LG., Shlykov, SG. & Kosterin, SO. (1999). Modulators of transmembrane calcium exchange in myometrium mitochondria change their hydrodynamic diameter. *Ukrainian Biochemistry*, **318**:343-9.

Karbowski, M., Lee, YJ., Gaume, B., Jeong, SY., Frank, S. & Nechushtan, A. (2002) Spatial and temporal association of Bax with mitochondrial fission sites, Drp1, and Mfn2 during apoptosis. *Journal of Cellular Biology*, **159**:931–938.

Kasahara, A. & Scorrano, L. (2014). Mitochondria: from cell death executioners to regulators of cell differentiation. *Trends in Cell Biology*, **24**(12):761-770.

Kaukonen, J., Juselius, JK., Tiranti, V., Kyttälä, A., Zeviani, M., Comi, GP., Keränen, S., Peltonen, L. & Suomalainen, A. (2000). Role of adenine nucleotide translocator 1 in mtDNA maintenance. *Science*, **289**(5480):782-5.

KDIGO. (2013). Chapter 1: Definition and classification of CKD. *Kidney International Supplements*, **3**:19–62.

Kelly, DP., Scarpulla, RC. (2004). Transcriptional regulatory circuits controlling mitochondrial biogenesis and function. *Genes & Development*, **18**:357–368.

Kennedy, D., Omran, E., Periyasamy, SM., Nadoor, J., Priyadarshi, A., Willey, JC., Malhotra, D. Xie, Z. & Shapiro, JI. (2003). Effect of chronic renal failure on cardiac contractile function, calcium cycling, and gene expression of proteins important for calcium homeostasis in the rat. *Journal of the American Society of Nephrology*, **14**:90-97.

- Kim, NH. & Kang, PM. (2010). Apoptosis in cardiovascular diseases: mechanism and clinical implications. *Korean Circulation Journal*, **40**(7):299-305.
- Kinahan, PE. & Fletcher, JW. (2010). Positron emission tomography-computed tomography standardized uptake values in clinical practice and assessing response to therapy. *Seminars in Ultrasound, CT and MR*, **31**(6):496-505.
- Kintaka, T., Tanaka, T., Imai, M., Adachi, I., Narabayashi, I. & Kitaura, Y. (2002). CD36 genotype and long chain fatty acid uptake in the heart. *Circulation Journal*, **66**: 819–825.
- Klein, R., Lortie, M., Adler, A., Beanlands, RS. & deKemp, R. (2006). Fully Automated Software for Polar-Map Registration and Sampling from PET Images. *IEEE Nuclear Science Symposium Conference Record*, **M14-246**:3185-3188.
- Kong, W., Duan, X., Shi, Z. & Chang, Y. (2008). Iron metabolism in the mononuclear phagocyte system. *Progress in Natural Science*, **18**:1197-1202.
- Konstantinidis, K., Whelan, RS. & Kitsis, RN. (2012). Mechanisms of cell death in heart disease. *Artherosclerosis, Thrombosis and Vascular Biology*, **32**(7):1552-1562.
- Koshiha, T., Detmer, SA., Kaiser, JT., Chen, H., McCaffery, JM. & Chan, DC. (2004). Structural basis of mitochondrial tethering by mitofusin complexes. *Science*, **6**:858-862.
- Kristal, BS. & Dubinsky, JM. (1997). Mitochondrial Permeability Transition in the Central Nervous System: Induction by Calcium Cycling-Dependent and -Independent Pathways. *Journal of Neurochemistry*, **69**(2):524-538.
- Kudin, AP., Bimpong-Buta, NY., Vielhaber, S., Elger, CE. & Kunz, WS. (2004). Characterisation of superoxide-producing sites in isolated brain mitochondria, *Journal of Biological Chemistry*, **279**:4127-4135.

Kuzmicic, J., Del Campo, A., Lopez-Cristosto, C., Morales, PE., Pennanenn, C., Bravo-Sagua, R., Hechenleitner, J., Zepeda, R., Castro, PF., Verdejo, HE., Parra, V., Chiong, M. & Levandero, S. (2011). Mitochondrial dynamics: a potential new therapeutic target for heart failure. *Revista Espanola de Cardiologia*, **64**:916-923.

Kwong, JQ., Davis, J., Baines, CP., Sargent, MA., Karch, J., Wang, X., Huang, T. & Molkenin, JD. (2014). Genetic deletion of the mitochondrial phosphate carrier desensitizes the mitochondrial permeability transition pore and causes cardiomyopathy. *Cell Death and Differentiation*, **21**(8):1209-1217.

Lange, H., Kispal, G. & Lill, R. (1999). Mechanism of iron transport to the site of heme synthesis inside yeast mitochondria, *Journal of Biological Chemistry*, **274**:18989–18996.

Laskowski, KR. & Russell, RR. (2008). Uncoupling proteins in heart failure. *Current Heart Failure reports*, **5**:75-79.

Lashin, OM., Szweda, PA., Szweda, LI. & Romani, AMP. (2006). Decreased complex II respiration and HNE-modified SDH subunit in diabetic heart. *Free Radical Biology and Medicine*, **40**:886 – 896.

Latunde-Dada, GO. (2009). Iron metabolism: microbes, mouse, and man. *Bioessays*, **31**(12):1309-1317.

Le Meunier, L., Slomka, PJ., Dey, D., Ramesh, A., Thomson, LEJ., Hayes, SW., Friendman, JD., Cheng, V., Germano, G. & Berman, DS. (2010). Enhanced definition PET for cardiac imaging. *Journal of Nuclear Cardiology*, **17**(3):414-426.

Lee, VW. & Harris, DC. (2011). Adriamycin nephropathy: a model of focal segmental glomerulosclerosis. *Nephrology (Carlton)*, **16**(1):30-8.

- Lee, KH., Ko, BH. & Paik, JY. (2005). Effects of anesthetic agents and fasting duration on 18F-FDG biodistribution and insulin levels in tumor-bearing mice. *Journal of Nuclear Medicine*, **46**:1531–1536.
- Leenen, FH. & De Jong, W. (1971). A solid silver clip for induction of predictable levels of renal hypertension in the rat. *Journal of Applied Physiology*, **31**:142-144.
- Lehman, JJ. & Kelly DP. (2002). Gene regulatory mechanisms governing energy metabolism during cardiac hypertrophic growth. *Heart failure reviews*, **7**:175-185.
- Lehman, JJ., Boudina, S., Banke, NH., Sambandam, N., Han, X., Young, DM. (2008). Leone, TC. The transcriptional coactivator PGC-1 alpha is essential for maximal and efficient cardiac mitochondrial fatty acid oxidation and lipid homeostasis. *The American Journal of Physiology: Heart and Circulatory Physiology*, **295**:185–196.
- Lekven, J. (1981). Unchanged myocardial tissue perfusion following pericardiotomy in acutely loaded cat hearts. *Cardiovascular Research*, **15**:14-19.
- Leone, TC., Lehman, JJ., Finck, BN., Schaeffer, PJ., Wende, AR., Boudina, S. & Courtois, M. (2005). PGC-1alpha deficiency causes multi-system energy metabolic derangements: muscle dysfunction, abnormal weight control and hepatic steatosis. *PLoS One*, **3**:e101.
- Levi, S. & Rovida, E. (2009). The role of iron in mitochondrial function. *Biochimica et Biophysica Acta*, **1790**: 629–636.
- Levin, A. (2002). Anaemia and left ventricular hypertrophy in chronic kidney disease populations: a review of the current state of knowledge. *Kidney international supplements*, 35-38.

Levin, A., Singer, J., Thompson, CR., Ross, H. & Lewis, M. (1996). Prevalent left ventricular hypertrophy in the predialysis population: identifying opportunities for intervention. *American Journal of Kidney Disease*, **27**:347-354.

Lewandowski, ED. (2002). Cardiac carbon 13 magnetic resonance spectroscopy: on the horizon or over the rainbow? *The Journal of Nuclear Medicine*, **9**:419-428.

Li, FY., Leibiger, B., Leibiger, I. & Larsson, C. (2002). Characterization of a putative murine mitochondrial transporter homology of hMRS3/4. *Mammalian Genome*, **13**:20-23.

Li, J., Zhou, J., Li, Y., Qin, D. & Li P. (2010). Mitochondrial fission controls DNA fragmentation by regulating endonuclease G. *Free Radical Biology and Medicine*, **49**(4):622-31.

Lichtenstein, DA., Crispin, AW., Sendamarai, AK., Campagna, DR., Schmitz-Abe, K., Sousa, CM., Kafina, MD., Schmidt, PJ., Niemeyer, CM., Porter, J., May, A., Patnaik, MM., Heeney, MM., Kimmelman, A., Bottomley, SS., Paw, BH., Markianos, K. & Fleming, MD. (2016). A recurring mutation in the respiratory complex 1 protein NDUFB11 is responsible for a novel form of X-linked sideroblastic anemia. (2016). *Blood*, **128**(15):1913-1917.

Lip, GY., Gammage, MD. & Beevers, DG. (1994). Hypertension and the heart. *British Medical Bulletin*, **50**:299-321.

Lim, VS., Fangman, J., Flanigan, MJ., Degowin, RL. & Abels, RT. (1990). Effect of recombinant human erythropoietin on renal function in humans. *Kidney International*, **37**: 131-136.

Loening, AM. & Gambhir, SS. (2003). AMIDE: a free software tool for multimodality medical image analysis. *Molecular Imaging*, **2**(3):131-7.

Lopaschuk, GD., Collins-Nakai, RL. & Itoi, T. (1992). Developmental changes in energy substrate use by the heart. *Cardiovascular Research*, **26**:1172-1180.

London, GM. & Parfrey, PS. (1997). Cardiac disease in chronic uraemia: pathogenesis. *Advances in Renal Replacement Therapy*, **4**:194-211.

Long, J., Ma, J., Luo, C., Mo, X., Sun, L., Zang, W, Liu, J. (2009). Comparison of two methods for assaying complex I activity in mitochondria isolated from rat liver, brain and heart. *Life Sciences*, **85**:276-280.

Luo, M. & Anderson, ME. (2013). Ca²⁺ Cycling in Heart Failure. *Circulation Research*, **113**(6): 690–708.

Ma, LJ., Nakamura, S., Aldigier, JC., Rossini, M., Yang, H., Liang, X., Nakamura, I., Marcantoni, C. & Fogo, AB. Regression of glomerulosclerosis with high-dose angiotensin inhibition is linked to decreased plasminogen activator inhibitor-1. *Journal of American Society of Nephrology*, **16**(4):966-76.

MacDougall, IC., Canaud, B., De Francisco, ALM., Filippatos, G., Ponikowski, P., Silverberg, D., Van Veldhuisen, DJ. & Anker, SD. (2012). Beyond the cardiorenal anaemia syndrome: recognising the role of iron deficiency. *European Journal of Heart Failure*, **14**:882-886.

Magnoni, R., Palmfeldt, J., Christensen, JH., Sand, M., Maltecca, F., Corydon, TJ., West, M., Casari, G. & Bross P. (2013). Late onset motoneuron disorder caused by mitochondrial Hsp60 chaperone deficiency in mice. *Neurobiology of Disease*, **54**:12-23.

Mancini, C., Roncaglia, P., Brussino, A., , G., Lo Buono, N., Krmac, H., Maltecca, F., Gazzano, E., Bartoletti Stella, A., Calvaruso, MA., Iommarini, L., Cagnoli, C., Forlani, S., Le Ber, I., Durr, A., Brice, A., Ghigo, D., Casari, G., Porcelli, AM., Funaro, A., Gasparre, G., Gustincich, S. & Brusco, A. (2013). Genome-wide expression profiling and functional characterization of SCA28

lymphoblastoid cell lines reveal impairment in cell growth and activation of apoptotic pathways. *BMC Medical Genomics*, **6**:1-11.

Mar, T. (1981). Measurement of mitochondrial volume independent of refractive index by light scattering. *Journal of Biochemical and Biophysical Methods*, **4**(3-4):177-84.

Marchant, DJ., Boyd, JH., Lin, DC., Granville, DJ., Garmaroudi, FS. & McManus, BM. (2012). Inflammation in Myocardial Diseases. *Circulation Research*, **110**:126-144.

Margineantu, DM., Gregory Cox, W., Sundell, L., Sherwood, SW., Beechem, JM. & Capaldi, RA. (2002). Cell cycle dependent morphology changes and associated mitochondrial DNA redistribution in mitochondria of human cell lines. *Mitochondrion*, **1**:425-435.

Marin-Garcia, J. & Akhmedov, AT. (2013). Mitochondria in heart failure: the emerging role of mitochondrial dynamics. *Heart Failure Reviews*, **18**:439-456.

Marin-Garcia, J., Goldenthal, MJ. & Moe, GW. (2001). Abnormal cardiac and skeletal muscle mitochondrial function in pacing induced cardiac function. *Cardiovascular research*, **52**:103-110.

Marin-Garcia, J., Goldenthal, MJ., Pierpont, ME. & Ananthakrishnan, R. (1995). Impaired mitochondrial function in idiopathic dilated cardiomyopathy: biochemical and molecular analysis. *Journal of Cardiac Failure*, **1**(4):285-91.

McAlister, FA., Ezekowitz, J., Tonelli, M. & Armstrong, PW. (2004). Renal insufficiency and heart failure: prognostic and therapeutic implications from a prospective cohort study. *Circulation*, **109**:1004-1009.

McCormack, JG. & Denton, RM. (1980). Role of calcium ions in the regulation of intramitochondrial metabolism. Properties of the Ca²⁺-sensitive dehydrogenases within

intact uncoupled mitochondria from the white and brown adipose tissue of the rat. *The Biochemical Journal*, **190**(1):95-105.

McKie, AT., Barrow, D. & Latunde-Dada, GO. (2001). An iron regulated ferric reductase associated with the absorption of dietary iron. *Science*, **291**:1755-1759.

McMahon, AC., Greenwald, SE., Dodd., SM., Hurst, MJ. & Raine, AE. (2002). Prolonged calcium transients and myocyte remodelling in early experimental uraemia. *Nephrology Dialysis Transplantation*, **17**:759-764.

Meerson, FZ. (1971). Mechanism of hypertrophy of the heart and experimental prevention of acute cardiac insufficiency. *British Heart Journal*, **33**:100-108.

Melenovsky, V., Petrak, J., Mracek, T., Benes, J., Borlaug, BA., Nuskova, H., Pluhacek, T., Spatenka, J., Kovalcikova, J., Drahota, Z., Kautzner, J., Pirk, J., Housstek, J. (2016). Myocardial iron content and mitochondrial function in human heart failure: a direct tissue analysis. *European Journal of Heart Failure*, **19**(4):522-530.

Moe, GW., Marin-Garcia, J., Konig, A., Goldenthal, M., Lu, X. & Feng, Q. (2004). In vivo TNF- α inhibition ameliorates cardiac mitochondrial dysfunction, oxidative stress and apoptosis in experimental heart failure. *American Journal of Physiology*, **287**:1813-1829.

Montero, M., Alonso, MT., Albillos, A., Garcia-Sancho, J. & Alvarez, J. (2001). Mitochondrial Ca²⁺-induced release mediated by the Ca²⁺ uniporter. *Molecular Biology of the Cell*, **12**:63-71.

Montessuit, C. & Lerch, R. (2013). Regulation and dysregulation of glucose transport in cardiomyocytes. *Biochimica et Biophysica Acta*, **1833**(4):848-856.

Moran, JK., Lee, HB. & Blaufox, MD. (1999). Optimization of Urinary FDG Excretion During

PET Imaging. *Journal Nuclear Medicine*, **40**:1352-1357.

Morgan-Hughes, JA., Darveniza, P., Kahn, SN., Landan, DN., Sherratt, RM., Land, JM. & Clark, JB. (1977). A mitochondrial myopathy characterized by a deficiency in reducible cytochrome b. *Brain*, **100**:617-640.

Mori, Y., Hirano, T., Nagashima, M., Shiraishi, Y., Fukui, T. & Adachi, M. (2007). Decreased peroxisome proliferator-activated receptor gene expression is associated with dyslipidemia in a rat model of chronic renal failure. *Metabolism*, **56**:1714-1718.

Muhlenhoff, U., Richhardt, N., Ristow, M., Kispal, G. & Lill, R. (2002). The yeast frataxin homolog Yfh1p plays a specific role in the maturation of cellular Fe/S proteins. *Human Molecular Genetics*, **11**: 2025–2036.

Muller, FL., Liu, Y. & Van Remmem, H. (2004). Complex III releases superoxide to both sides of the inner mitochondrial membrane. *Journal of Biological Chemistry*, **279**:49064-49073.

Naito, Y., Tsujino, T., Matsumoto, M., Sakoda, T., Ohyanagi, M. & Masuyama, T. (2009). Adaptive response of the heart to long-term anaemia induced by iron deficiency. *American Journal of Physiology: Heart and Circulatory Physiology*, **296**:585-593.

Nakai, A., Yamaguchi, O., Takeda, T., Higuchi, Y., Hikoso S. & Taniike M. (2007). The role of autophagy in cardiomyocytes in the basal state and in response to hemodynamic stress. *Nature Medicine*, **13**:619–624.

National Kidney Foundation (2013). Retrieved 16th January from: <http://www.renal.org/information-resources/the-uk-eckd-guide/ckd-stages#sthash.FgrCXjSY.6iPrwoFh.dpbs>

Nemeth, E., Tuttle, MS., Powelson, J., Vaughn, MB., Donovan, A., Ward, DM., Ganz, T. & Kaplan, J. (2004). Hepcidin regulates cellular iron efflux by binding to ferroportin and inducing its internalization. *Science*, **306**(5704):2090-3.

Neubauer, S. (2007). The failing heart – an engine out of fuel. *New England Journal of Medicine*, **356**:1140-1151.

Ng, CK., Holden, JE., DeGrado, TR., Raffel, DM., Kornguth, ML. & Gatley, SJ. (1991). Sensitivity of myocardial fluorodeoxyglucose lumped constant to glucose and insulin. *American Journal of Physiology*, **260**:593-603.

Nguyen, VTB., Mossberg, KA., Tewson, TJ., Wong, WH., Rowe, RW., Coleman, GM. & Taegtmeyer, H. (1990). Temporal analysis on myocardial glucose metabolism by 2-(¹⁸F)Fluoro-2-deoxy-D-glucose. *The American Physiological Society*, **90**:1022-1031.

Nishida, K., Kyoi, S., Yamaguchi, O., Sadoshima, J. & Otsu, K. (2009). The role of autophagy in the heart. *Cell Death and Differentiation*, **16**:31-38.

Nishino, T. (1994). The conversion of xanthine dehydrogenase to xanthine oxidase and the role of the enzyme in reperfusion injury. *Journal of Biochemistry*, **116**(1):1-6.

Nishio, ML., Ornatsky, OI., Craig, EE. & Hood, DA. (1995). Mitochondrial biogenesis during pressure overload induced cardiac hypertrophy in adult rats. *Canadian journal of physiology and pharmacology*, **73**(5):630–637.

Nociari, M., Ocheretina, O., Schoggins JW. & Falck-Pedersen, E. (2007). Sensing infection by adenovirus: Toll-like receptor-independent viral DNA recognition signals activation of the interferon regulatory factor 3 master regulator. *Journal of Virology*, **81**:4145-4157.

Novalija, E., Kevin, LG., Eells, TJ., Henry, MM. & Stowe, DF. (2003). Anaesthetic preconditioning improves adenosine triphosphate synthesis and reduces reactive oxygen species formation in mitochondria after ischemia by a redox dependent mechanism.

Anaesthesiology, **98**:1155-1163.

Nurko, S. (2006) Anaemia in chronic disease: causes, diagnosis, treatment. *Cleveland Clinic Journal of Medicine*, **73**:289-297.

Nury, H., Dahout-Gonzalez, C., Trezeguet, V., Lauquin, GJ., Brandolin, G. & Pebay-Peyroula, E. (2006). Relations between structure and function of the mitochondrial ADP/ATP carrier.

Annual Reviews in Biochemistry, **75**:713–741.

Oexle, H., Gnaiger, E. & Weiss, G. (1999). Iron-dependent changes in cellular energy metabolism: influence on citric acid cycle and oxidative phosphorylation. *Biochimica et*

Biophysica Acta, **1413**:99-107.

Okonko, DO., Grzeslo, AB., Witkowski, TB., Mandal, AKJ., Slater, RM., Roughton, M., Foldes, G., Thum, T., Majda, J., Banasiak, W., Missouriis, CG., Poole-Wilson, PA., Anker, SD. & Ponikowski, P. (2009). Effect of intravenous iron sucrose on exercise tolerance in anemic and nonanemic patients with symptomatic chronic heart failure and iron deficiency. FERRIC-HF: a randomized, controlled, observer-blinded trial. *The Journal of American Cardiology*, **51**:103-112.

Okuda, S., Tsuruda, H., Onoyama, K., Fujimi, S. & Fujishima, M. (1986). Adriamycin-induced nephropathy as a model of chronic progressive glomerular disease. *Kidney International*, **29**:502-510.

Olivetti, G., Quaini, F., Sala, R., Lagrasta, C., Corradi, D., Bonacina, E., Gambert, SR., Cigola, E. & Anversa, P. (1996). Acute myocardial infarction in humans is associated with activation of programmed myocyte cell death in the surviving portion of the heart. *Journal of Molecular and Cellular Cardiology*, **28**(9):2005-2016.

Olivetti, G., Abbi, R., Quaini, F., Kajstura, J., Cheng, W., Nitahara, JA., Quaini, E., Di Loreto, C., Beltrami, CA., Krajewski, S., Reed, JC. & Anversa, P. (1997). Apoptosis in the failing human heart. *The New England Journal of Medicine*, **336**(16): 1133-1141.

Ong, SB. & Hausenloy, DJ. (2010). Mitochondrial morphology and cardiovascular disease. *Cardiovascular Research*, **88**:16-29.

Ong, SB., Subrayan, S., Lim, SY., Yellon, DM., Davidson, SM. & Hausenloy, DJ. (2010). Inhibiting mitochondrial fission protects the heart against ischemia/reperfusion injury. *Circulation*, **121**(18):2012–22.

Otera, H., Wang, C., Cleland, MM., Setoguchi, K., Yokota, S., Youle, RJ. & Mihara, K. (2010). Mff is an essential factor for mitochondrial recruitment of Drp1 during mitochondrial fission in mammalian cells. *The Journal of Cell Biology*, **191**:1141-1158.

Pai, AB. & Garba, AO. (2012). Ferumoxytol: a silver lining in the treatment of anemia of chronic kidney disease or another dark cloud? *Journal of Blood Medicine*, **3**:77–85

Paiva, MA., Gonçalves, LM., Providência, LA., Davidson, SM., Yellon, DM. & Mocanu, MM. (2010). Transitory activation of AMPK at reperfusion protects the ischaemic-reperfused rat myocardium against infarction. *Cardiovascular Drugs and Therapy*, **24**:25-32.

Palermo, V., Rinalducci, S., Sanchez, M., Grillini, F., Sommers, JA., Brosh, RM., Zolla, L. Franchitto, A. & Pichierri, P. (2016). CDK1 phosphorylates WRN at collapsed replication forks. *Nature Communications*, **7**:12880.

Papanicolaou, KN., Kikuchi, R., Ngoh, GA., Coughlan, KA., Dominguez, I., Stanley, WC. & Walsh, K. (2012). Mitofusins 1 and 2 are Essential for Postnatal Metabolic Remodeling in Heart. *Circulation Research*, **111**(8): 1012–1026.

Parfrey, PS., Foley, RN., Harnett, JD., Kent, GM., Murray, D. & Barre, PE. (1996). Outcome and risk factors of ischemic heart disease in chronic uraemia. *Kidney International*, **49**:1428-1434.

Park, S., Gakh, O., Mooney, SM., Isaya, G. (2002). The ferroxidase activity of yeast frataxin. *The Journal of Biological Chemistry*, **277**:38589–38595.

Patlak, CS., Blasberg, RG. & Fenstermacher, JD. (1983). Graphical evaluation of blood-to-brain transfer constants from multiple-time uptake data. *Journal of Cerebral Blood Flow and Metabolism*, **3**(1):1-7.

Pazhenkottil, AP., Buechel, RR., Nkoulou, R., Ghadri, JR., Herzog, BA., Husmann, L., Wolfrum, M., Kuest, SM., Fiechter, M., Gaemperli, O. & Kaufmann, PA. (2011). Left ventricular assessment by phase analysis from gated PET-FDG scans. *Journal of Nuclear Cardiology*, **18**(5):920-925.

Peng, YY. & Uprichard, J. (2016). Ferritin and iron studies in anaemia and chronic disease. *Annals of Clinical Biochemistry*, **54**(1):43-48.

Perry, SW., Norman, JP., Barbieri, J., Brown, EB. & Gelbard, HA. (2011). Mitochondrial membrane potential probes and the proton gradient: a practical usage guide, *BioTechniques*, **50**:98-115.

Pfeffer, MA., Burdmann, EA., Chen, CY., Cooper, M.E., Zeeuw, DD., Eckardt, KE., Feyzi, JM., Ivanovich, P., Kewalramani, R., Levey, AS., Lewis, EF., McGill, JB., McMurray, JIV., Parfrey, P., Parving, HH., Remuzzi, G., Singh, AK., Solomon, SD., & Toto, S. (2009). A trial of darbepoetin alfa in type 2 diabetes and chronic kidney disease. *The New England Journal of Medicine*, **361**:2019-2032.

Piquereau, J., Caffin, F., Novotova, M., Prola, A., Garnier, A. & Mateo, P. (2012). Down-regulation of OPA1 alters mouse mitochondrial morphology, PTP function, and cardiac adaptation to pressure overload. *Cardiovascular Research*, **94**, 408–417.

Pon, LA., & Schon, EA. (2007). *Mitochondria 2nd Edition*. Academic Press, San Diego.

Ponikowski, P., Anker, SD., Szachniewicz, J., Okonko, D., Ledwidge, M., Zymlinski, R., Ryan, E., Wasserman, SM., Baker, N., Rosser, D., Rosen, SD., Poole-Wilson, PA., Banasiak, W., Coats, AJS. & McDonald, K. (2007). Effect of darbepoetin alfa on exercise tolerance in anemic patients with symptomatic chronic heart failure. a randomized, double-blind, placebo-controlled trial. *Journal of the American College of Physiology*, **47**:753-762.

Popat, R. (2011). Chronic kidney disease: clinical features and renal replacement therapies. *Clinical Pharmacist*, **3**:15-19.

Price, SR., Gooch, JL., Donaldson, SK. & Roberts-Wilson, TK. (2010). Muscle atrophy in chronic kidney disease results from abnormalities in insulin signaling. *Journal of Renal Nutrition*, **20**:24-28.

Public Health England. (2014). Retrieved 15th March 2017 from: www.yhpho.org.uk/resource/view.aspx?RID=204692

- Quigley, AF., Kapsa, RMI., Esmore, D., Hale, G. & Byrne, E. (2000). Mitochondrial Respiratory Chain Activity in Idiopathic Dilated Cardiomyopathy. *Journal of Cardiac Failure*, **6**(1):47-55.
- Raine, AE., Margreiter, R., Brunner, FP., Ehrich, JH., Geerlings, W., Landis, P., Loirat, C., Mallick, NP., Selwood, NH., Tufveson, G. (1992). Report on management of renal failure in Europe XXII, 1991. *Nephrology, Dialysis and Transplantation*, **7**(2):7-35.
- Raine, AE., Seymour, AML, Roberts, AF., Radda, GK. & Ledingham. (1993). Impairment of cardiac function and energetics in experimental renal failure. *Journal of Clinical Investigations*, **92**:2934-2940.
- Randle, PJ., Garland, PB., Hales, CN. & Newsholme, EA. (1963). The glucose fatty-acid cycle. Its role in insulin sensitivity and the metabolic disturbances of diabetes mellitus. *Lancet*, **1**(7285): 785–789.
- Randle, PJ. (1986). Fuel selection in animals. *Biochemical Society Transactions*, **14**:799–806.
- Ransom, DG., Haffter, P., Odenthal, J., Brownlie, A., Vogelsang, E., Kelsh, RN., Brand, M., van Eeden, FJ., Furutani-Seiki, M., Granato, M., Hammerschmidt, M., Heisenberg, CP., Jiang, YJ., Kane, DA., Mullins, MC. & Nüsslein-Volhard, C. (1996). Characterization of zebrafish mutants with defects in embryonic hematopoiesis. *Development*, **123**:311-9.
- Ratib, O., Phelps, M., Huang, S., Henze, E., Selin, C. & Schelbert, H. (1982). Positron tomography with deoxyglucose for estimating local myocardial glucose metabolism. *Journal of Nuclear Medicine*, **23**:577-586.
- Razeghi, P., Young, ME., Alcorn, JL., Moravec, CS., Frazier, OH. & Taegtmeier, H. (2001). Metabolic gene expression in foetal and failing human and heart. *Circulation*, **104**:2923-2931.

Reddy, V., Bhandari, S. & Seymour, AML. (2007). Myocardial function, energy provision, and carnitine deficiency in experimental uraemia. *Journal of the American Society of Nephrology*, **18**:84-92.

Reece, WO., Brackelsberg, PO. & Hotchkiss, DK. (1985). Erythrocyte changes, serum iron concentration and performance following iron injection in neonatal beef calves. *Journal of Animal Science*, **61**(6):1387-1394.

Rensvold, JW., Ong, S., Jeevananthan, A., Carr, SA., Mootha, VK. & Pagliarini, DJ. (2013). Complementary RNA and Protein Profiling Identifies Iron as a Key Regulator of Mitochondrial Biogenesis. *Cell Reports*, **3**(1):237-245.

Rigatto, C. & Parfrey, PS. (2001). Uraemic cardiomyopathy: an overload cardiomyopathy. *Journal of Clinical and Basic Cardiology*, **4**(2):93-95.

Rimbaud, S., Garnier, A. & Ventura-Clapier, R. (2009). Mitochondrial biogenesis in cardiac pathophysiology. *Pharmacological Reports*, **61**(1):131-138.

Robards, AW. & Wilson, AJ. (1993). *Procedures in Electron Microscopy*. Wiley, England.

Ronco, C., House, AA. & Haapio, M. (2008). Cardiorenal syndrome: refining the definition of a complex symbiosis gone wrong. *Intensive Care Medicine*, **34**:957-962.

Rosca, MG., Vazquez, EJ., Kerner, J., Parland, W., Chandler, MP., Stanley, WC., Sabbah, HN. & Hoppel, CL. (2008). Cardiac mitochondria in heart failure: decrease in respirasomes and oxidative phosphorylation. *Cardiovascular Research*, **80**:30-39.

Russell, RR., Mrus, JM., Mommessin, JI. & Taegtmeier, H. (1992). Compartmentation of hexokinase in rat heart. A critical factor for tracer kinetic analysis of myocardial glucose metabolism. *Journal of Clinical Investigation*, **90**:1972-1977.

Sack, MN. & Kelly, DP. (1998). The energy substrate switch during development of heart failure: gene regulatory mechanisms (Review). *International Journal of Molecular Medicine*, **1**(1):17-24.

Sack, MN., Rader, TA., Park, S., Bastin, J., McCune, SA. & Kelly, DP. (1996). Fatty acid oxidation enzyme gene expression is downregulated in the failing heart. *Circulation*, **94**(11):2837-42.

Sala-Rabanal, S., Hirayama, BA., Ghezzi, C., Liu, J., Huang, SC., Kepe, V., Koepsell, H., Yu, A., Powell, DR., Thorens, B., Wright, EM. & Barrio, JR. (2016). Revisiting the physiological roles of SGLTs and GLUTs using positron emission tomography in mice. *The Journal of Physiology*, **594**: 4425–4438.

Sam, F., Kerstetter, DL., Pimental, DR., Mulukutla, S., Tabaee, A., Bristow, MR. & Sawyer, DB. (2005). Increased reactive oxygen species production and functional alterations in antioxidant enzymes in human failing myocardium. *Journal of Cardiac Failure*, **11**:473-480.

Sanchis, D., Llovera, M., Ballester, M. & Comella, JX. (2008). An alternative view of apoptosis in heart development and disease. *Cardiovascular Research*, **77**(3):448-451.

Santalucía, T., Camps, M., Castelló, A., Muñoz, P., Nuel, A., Testar, X., Palacin, M. & Zorzano, A. (1992). Developmental regulation of GLUT-1 (erythroid/Hep G2) and GLUT-4 (muscle/fat) glucose transporter expression in rat heart, skeletal muscle, and brown adipose tissue. *Endocrinology*, **130**(2):837-46.

Santambrogio, P., Biasiotto, G., Sanvito, F., Olivieri, S., Arosio, P. & Levi, S. (2007). Mitochondrial ferritin expression in adult mouse tissues. *Journal of Histochemistry & Cytochemistry*, **55**:1129–1137.

Santos, LS., Chin, EW., Ioshii, SO. & Yamaura. (2006). Surgical reduction of the renal mass in rats: morphologic and functional analysis on the remnant kidney. *Acta Cirurgica Brasileira*, **21**:252-257.

Sato, H., Shiraishi, I., Takamatsu, T. & Hamaoka, K. (2007). Detection of TUNEL-positive cardiomyocytes and c-kit-positive progenitor cells in children with congenital heart disease. *Journal of Cellular and Molecular Cardiology*, **43**(3):254-61.

Schaper, J., Froede, R., Hein, S., Buck, A., Hashizume, H. & Speiser, B. (1991). Impairment of the myocardial ultrastructure and changes of the cytoskeleton in dilated cardiomyopathy. *Circulation*, **83**:504-514.

Schiffrin, EL., Lipman, ML. & Mann, JF. (2007). Chronic kidney disease: effects on the cardiovascular system. *Circulation*, **116**:85-97.

Schmitt, JP., Kamisago, M., Asahi, M., Li, GH., Ahmad, F., Mende, U., Kranias, EG., MacLennan, DH., Seidman, JG. & Seidman, CE. (2003). Dilated cardiomyopathy and heart failure caused by a mutation in phospholamban. *Science*, **299**(5611):1410-3.

Scholtens, AM., Verberne, HJ., Budde, RPJ. & Lam, MGEH. (2016). Additional Heparin Preadministration Improves Cardiac Glucose Metabolism Suppression over Low Carbohydrate Diet Alone in 18F-FDG PET Imaging. *Journal of Nuclear Medicine*, **57**(4):568-573.

Schueck, ND., Woontner, M. & Koeller, DM. (2001). The role of the mitochondrion in cellular iron homeostasis. *Mitochondrion*, **1**:51-60.

Segura, AM., Frazier, OH. & Buja, LM. (2014). Fibrosis and heart failure. *Heart Failure Reviews*, **19**(2):173-185.

Semple, D., Bhandari, S. & Seymour, AML. (2012). Uraemic cardiomyopathy is characterised by loss of the cardioprotective effects of insulin. *American Journal of Renal Physiology*, **22**:207-215.

Shaw, GC., Cope, JJ., Li, L., Corson, K., Hersey, C., Ackermann, GE., Gwynn, B., Lambert, AJ., Wingert, RA., Traver, D., Trede, NS., Barut, BA., Zhou, Y., Minet, E., Donovan, A., Brownlie, A., Balzan, R., Weiss, MJ., Peters, LL., Kaplan, J., Zon, LI & Paw, BH. (2006). Mitoferrin is essential for erythroid iron assimilation. *Nature*, **440**(7080):96-100.

Sheftel, AD., Zhang, AS., Brown, C., Shirihai, OS. & Ponka, P. (2007). Direct interorganellar transfer of iron from endosome to mitochondrion. *Blood*, **110**:125–132.

Sheikine, Y. & Akram, K. (2010). FDG-PET imaging of atherosclerosis: Do we know what we see? *Atherosclerosis*, **211**:371-380.

Shimizu, I. & Minamino, T. (2016). Physiological and pathological cardiac hypertrophy. *Journal of Molecular and Cellular Cardiology*, **97**:245-262.

Shimomura, H., Terasaki, F., Hayashi, T., Kitaura, Y., Isomura, T. & Suma H. (2001). Autophagic degeneration as a possible mechanism of myocardial cell death in dilated cardiomyopathy. *Japanese Circulation Society*, **65**: 965–968.

Shin, HW., Shinotsuka, C., Torii, S., Murakami, K. & Nakayama, S. (1997). Identification and subcellular localization of a novel mammalian dynamin-related protein homologous to yeast Vps1p and Dnm1p. *Journal of Biochemistry*, **122**:525–530.

Shlipak, MG. (2003). Pharmacotherapy for heart failure in patients with renal insufficiency. *Annals of International Medicine*, **138**:917-924.

Shukla, AK. & Kumar, U. (2006). Positron emission tomography: *An overview. Journal of medical Physics*, **31**(1):13-21.

Shvartsman, M., Kikkeri, R., Shanzer, A., Cabantchik, ZI. (2007). Non-transferrin-bound iron reaches mitochondria by a chelator-inaccessible mechanism: biological and clinical implications. *American Journal of Physiology: Cellular Physiology*, **293**:1383–1394.

Siah, CW., Ombiga, J., Adams, LA., Trinder, D. & Olynyk, JK. (2006). Normal Iron Metabolism and the Pathophysiology of Iron Overload Disorders. *The Clinical Biochemist Reviews*, **27**:5-16.

Siamopoulos, KC. & Kalaitzidis, RG. (2008). Inhibition of the renal-angiotensin system and chronic kidney disease. *International Urology and Nephrology*, **40**:1015-1025.

Siedlecki, AM., Jin, X. & Muslin, AJ. (2009). Uraemic cardiac hypertrophy is reversed by rapamycin but not by lowering of blood pressure. *Kidney International*, **75**:800-808.

Slart, RHJA., Bax, JJ., van der Wall, EE., van Veldhuisen, DJ., Jager, PL. & Dierckx, RA. (2005). Nuclear cardiac imaging for the assessment of myocardial viability. *Netherlands Heart Journal*, **13**(11):408-415.

Smirnova, E., Griparic, L., Shurland, DL. & van der Bliek, AM. (2001). Dynamin-related protein Drp1 is required for mitochondrial division in mammalian cells. *Molecular Biology of the cell*, **12**:2245–2256.

Smith, K. (2009). The impact of erythropoietin on uraemic cardiomyopathy. PhD thesis, University of Hull.

Smith, K., Semple, D., Aksentijevic, D., Bhandari, S. & Seymour, AM. (2010). Functional and metabolic adaptation in uraemic cardiomyopathy. *Frontiers in Bioscience*, **2**:1492-1501.

Smorgorzewski, M., Perna, AF., Borum, PR. & Massry, SG. (1988). Fatty acid oxidation in the myocardium: effects of parathyroid hormone and CRF. *Kidney International*, **34**:797-803.

Song, M., Mihara, K., Chen, Y., Scorrano, L. & Dorn II. (2015). Mitochondrial fission and fusion factors reciprocally orchestrate mitophagic culling in mouse hearts and cultured fibroblasts. *Cell Metabolism*, **21**(2): 273–285.

Southwell, R. (2009). Hexokinase-mitochondrial interaction in cardiac tissue: implications for cardiac glucose uptake, the 18FDG lumped constant... *Journal of Bioenergetics*, **41**:187-193.

Southwell, R., Davey, KA., Warley, A. & Garlick, PB. (2007). A reevaluation of the roles of hexokinase I and II in the heart. *American Journal of Physiology, Heart and Circulatory Physiology*, **292**:378-386.

Stanley, WC., Recchia, FA. & Lopaschuk, GD. (2005). Myocardial substrate metabolism in the normal and failing heart. *Physiological Reviews*, **85**:1093-1129.

Suckow, MA., Weisbroth, SH. & Franklin, CL. (2005). *The laboratory rat*. Academic Press, Massachusetts, USA.

Sun, CN., Dhalla, NS. & Olson, RE. (1969). Formation of gigantic mitochondria in hypoxic isolated perfused rat hearts. *Experientia*, **25**:763-764.

Swedberg, K., Young, JB., Anand, IS., Cheng, S., Desai, AS., Diaz, R., Maggioni, AP., McMurray, JJV., O'Connor, C., Pfeffer, MA., Solomon, SD., Sun, Y., Tendera, M., & van Veldhuisen, DJ. (2013). Treatment of anemia with darbepoetin alfa in Systolic Heart Failure. *The New England Journal of Medicine*, **368**:1210-1219.

Swaminathan, R., Major, P., Snieder, H. & Spector, T. (2000). Serum creatinine and fat-free mass (lean body mass). *Clinical Chemistry*, **46**:1695-1696.

Taddei, S., Nami, R., Bruno, RM., Quatrini, I. & Nuti, R. (2011). Hypertension, left ventricular hypertrophy and chronic kidney disease. *Heart Failure Reviews*, **16**(6):615-620.

Taegtmeyer, H. (1986). Myocardial metabolism. In: Phelps, MMJ. & Shelbert, H. Positron emission tomography and autoradiography: principles and applications for the brain and heart. New York Press.

Taegtmeyer, H. (2010). Tracing Cardiac Metabolism In Vivo: One Substrate at a Time. *The Journal of Nuclear Medicine*, **51**:80-87.

Tait, RM. & Dureski, PL. (1979). Response of new born lambs to iron dextran injection. *Canadian Journal of Animal Science*, **59**(4): 809-811.

Takemura, G., Ohno, M., Hayakawa, Y., Misao, J., Kanoh, M., Ohno, A., Uno, Y., Minatoguchi, S., Fujiwara, T. & Fujiwara, H. (1998). Role of apoptosis in the disappearance of infiltrated and proliferated interstitial cells after myocardial infarction. *Circulation Research*, **82**(11):1130-1138.

Tanida, I., Minematsu-Ikeguchi, N., Ueno, T. & Kominami, E. (2005). Lysosomal turnover, but not a cellular level, of endogenous LC3 is a marker for autophagy. *Autophagy*, **1**:84-91.

Tatsumi, M., Cohade, C., Nakamoto, Y. & Wahl, RL. (2003). Fluorodeoxyglucose Uptake in the Aortic Wall at PET/CT: Possible Finding for Active Atherosclerosis. *Radiology*, **229**(3):831-837.

Taylor, D. (2012). Mitochondrial function in Uraemic Cardiomyopathy. PhD Thesis. University of Hull.

Taylor, D., Bhandair, S. & Seymour, AML. (2015). Mitochondrial dysfunction in uraemic cardiomyopathy. *American Journal of Physiology; Renal Physiology*, **308**: 579–587.

Terman, A. & Brunk, UT. (2005). Autophagy in cardiac myocyte homeostasis, aging, and pathology. *Cardiovascular Research*, **68**(3):355-365.

Thomas, R., Kanso, A. & Sedor, JR. (2008). Chronic Kidney Disease and Its Complications. *Primary Care*, **35**(2):329-334.

Toblli, JE., Lombrana, A., Duarte, P. & Di Gennero, F. (2007). Intravenous iron reduces NT-pro-brain natriuretic peptide in anemic patients with chronic heart failure and renal insufficiency. *Journal of the American College of Cardiology*, **50**:1657-1655.

Toyama, H., Ichise, M., Liow, JS., Vines, DC., Seneca, NM., Modell, KJ., Seidel, J., Green, MV. & Innis, RB. (2004). Evaluation of anesthesia effects on [18F]FDG uptake in mouse brain and heart using small animal PET. *Nuclear Medicine and Biology*, **31**(2):251-6.

Turrens, JF. (2003). Mitochondrial formation of reactive oxygen species, *The Journal of Physiology*, **552**:335-344.

Twig, G., Elorza, A., Molina, AJA., Mohamad, H., Wikstrom, JD. & Walzer, G. (2008). Fission and selective fusion govern mitochondrial segregation and elimination by autophagy. *EMBO journal*, **27**:433-446.

van der Blik, AM., Shen, Q. & Kawajiri, S. (2013). Mechanisms of Mitochondrial Fission and Fusion. *Cold Spring Harbour Perspectives in Biology*, **5**(6)1-15.

van der Putten, K., Braam, B., Jie, KE. & Gaillard, CA. (2008). Mechanisms of Disease: erythropoietin resistance in patients with both heart and kidney failure. *National Clinical Practice Nephrology*, **4**(1):47-57.

van der Weerdt, AP., Klein, LJ., Boellaard, R., Visser, CA., Visser, FC. & Lammertsma, AA. (2001). Image-derived input functions for determination of MRGlu in cardiac 18FFDG PET scans. *The Journal of Nuclear Medicine*, **42**:1622–1629.

Van der Vusse, GJ., van Bilsen, M. & Glatz, JF. (2000). Cardiac fatty acid uptake and transport in health and disease. *Cardiovascular Research* **45**: 279–293.

Van Empel, VP., Bertrand, AT., Hofstra, L., Crijns, HJ., Doevendans, PA. & De Windt, LJ. (2005). Myocyte apoptosis in heart failure. *Cardiovascular Research*, **67**:21-29.

Velasquez, MT., Kimmel, PL., Michaelis, OE., Carswell, N., Abraham, A. & Bosch, JP. (1989). Effect of carbohydrate intake on kidney function and structure in SHR/N-cp rats: a new model of NIDDM. *Diabetes*, **38**:679-685.

Vulpe, CD., Kuo, YM. & Murphy, TL. (1999) Hephaestin, a ceruloplasmin homologue implicated in intestinal iron transport, is defective in the sla mouse. *Nature Genetics*, **21**:195-9.

Wagner, Ol., Lifshitz, J., Janmey, PA., Linden, M., McIntosh, TK. & Leterrier, JF. (2003). Mechanisms of mitochondria-neurofilament interactions. *Journal of Neuroscience*, **23**(27):9046-9058.

Wahl, RL., Henry, CA. & Ethier, SP. (1992). Serum glucose: effects on tumor and normal tissue accumulation of 2-[F-18]-fluoro-2-deoxy-D-glucose in rodents with mammary carcinoma. *Radiology*, **183**(3):643-647.

Wanders, RJ., Ruiter, JP., IJLst, L., Waterham, HR. & Houten, SM. (2010). The enzymology of mitochondrial fatty acid beta-oxidation and its application to follow-up analysis of positive neonatal screening results. *Journal of Inherited Metabolic Disease*, **33**(5):479-494.

Wang, W., Zhang, F., Li, L., Tang F., Siedlak, SL., Fujioka, H., Liu, Y., Su, B., Pi Y. & Wang X. (2015). MFN2 couples glutamate excitotoxicity and mitochondrial dysfunction in motor neurons. *The Journal of Biological Chemistry*, **290**(1):168-182.

West, AP., Bennett, MJ., Sellers, VM., Andrews, NC., Enns, CA. & Bjorkman, PJ. (2000). Comparison of the interactions of transferrin receptor and transferrin receptor 2 with transferrin and the hereditary hemochromatosis protein HFE. *The Journal of Biological Chemistry*, **275**(49):38135–8.

Westermann, B. (2010). Mitochondrial fusion and fission in cell life and death. *Nature Reviews*, **11**:872-884.

Whelan, RS., Kaplinskiy, V. & Kitsis, RN. (2010). Cell death in the pathogenesis of heart disease: mechanisms and significance. *Annual Review of Physiology*, **72**:19-44.

Williams, GS., Boyman, L. & Lederer. (2015). Mitochondrial calcium and the regulation of metabolism in the heart. *Journal of Molecular and Cellular Cardiology*, **78**:35-45.

Wu, P., Peters, JM. & Harris, RA. (2001). Adaptive increase in pyruvate dehydrogenase kinase 4 during starvation is mediated by peroxisome proliferator-activated receptor alpha. *Biochemical and Biophysical Research Communications*, **287**:391–396,

Wu, J. & Yan, LJ. (2015). Streptozotocin-induced type 1 diabetes in rodents as a model for studying mitochondrial mechanisms of diabetic β cell glucotoxicity. *Diabetes, metabolic syndrome and obesity*, **8**:181–188.

Yagi, N., Shimizu, J., Mohri, S., Araki, J., Nakamura, K., Okuyama, H., Toyota, H., Morimoto, T., Kurusu, Y., Morizane, M., Miura, T., Hashimoto, K., Tsujioka, K. & Kajiya, F. (2004). X-ray Diffraction from a Left Ventricular Wall of Rat Heart. *Biophysical Journal*, **86**(4): 2286–2294.

Yamada, M., Ikeda, Y., Yano, M., Yoshimura, K., Nishino, S., Aoyama, H., Wang, L., Aokil, H. & Matsuzaki, M. (2006). Inhibition of protein phosphatase 1 by inhibitor-2 gene delivery ameliorates heart failure progression in genetic cardiomyopathy. *Federation of American Societies for Experimental Biology Journal*, **20**:1197–1199.

Yamane, T., Park, MJ., Richter, D., Nekolla, SG., Javadi, MS., Lapa, C., Samnick, S., Buck, AK., Herrmann, K. & Higuchi T. Small-animal PET imaging of isolated perfused rat heart. *Journal of Nuclear Medicine*, **55**(3):495-9.

Yan, L., Vatner, DE., Kim, SJ., Ge, H., Masurekar, M. & Massover, WH. (2005). Autophagy in chronically ischemic myocardium. *Proceedings of the National Academy of Sciences*, **102**: 13807–13812.

Yancey, DM., Guichard, JL., Ahmed, MI., Zhou, L., Murphy, MP., Johnson, MS., Benavides, GA., Collawn, J., Darley-Usmarm, V. & Dell'Italia LJ. (2015). Cardiomyocyte mitochondrial oxidative stress and cytoskeletal breakdown in the heart with a primary volume overload. *American Journal of Physiology: Heart and Circulatory Physiology*, **308**(6):651-63.

Yang, HC., Yiqin, Z. & Fogo, AB. (2010). Models of chronic kidney disease. *Drug Discovery Today Disease Models*, **7**(1-2):13-19.

Yin, FC., Spurgeon, HA., Rakusan, K., Weisfeldt, MT. & Lakatta, EG. (1982). Use of tibial length to quantify cardiac hypertrophy. *American Journal of Physiology Heart & Circulatory Physiology*, **243**:941-947.

Yu, T., Sheu, SS., Robotham, J. & Yoon, Y. (2008). Mitochondrial fission mediates high glucose-induced cell death through elevated production of reactive oxygen species. *Cardiovascular Research*, **79**:341-351.

- Zak, R., Rabinowitz, M., Rajamanickam, C., Merton, S. & Kwiatkowska-Patzer, B. (1980). Mitochondrial proliferation in cardiac hypertrophy. *Basic Research in Cardiology*, **75**:171-178.
- Zeng, Y., Cheng, H., Jiang, X., Han, X. (2008). Endosomes and lysosomes play distinct roles in sulfatide-induced neuroblastoma apoptosis: potential mechanisms contributing to abnormal sulfatide metabolism in related neuronal diseases. *Biochemical Journal*, **410**:81-92.
- Zhang, Y., Lyver, ER., Knight, SA., Pain, D., Lesuisse, E. & Dancis, A. (2006). Mrs3p, Mrs4p, and frataxin provide iron for Fe-S cluster synthesis in mitochondria. *The Journal of Biological Chemistry*, **281**:22493–22502.
- Zhang, N., Wang, S., Li, Y., Che, L. & Zhao, Q. (2013). A selective inhibitor of Drp1, mdivi - 1, acts against cerebral ischemia/reperfusion injury via an anti - apoptotic pathway in rats. *Neuroscience Letters*, **535**:104-109.
- Zincirkeser, S., Şahin, E., Halac, M. & Sager, S. (2007). Standardized uptake values of normal organs on 18F-fluorodeoxyglucose positron emission tomography and computed tomography imaging. *Journal of International Medical Research*, **35(2)**: 231–236.
- Zitvogel, L., Kepp, O. & Kroemer, G. (2010). Decoding Cell Death Signals in Inflammation and Immunity. *Cell*, **140(6)**:798-804.
- Zong, Z., Ghochani, M., McCaffery, JM., Frey, TG. & Chan, DC. (2009). Mitofusins and OPA1 mediate sequential steps in mitochondrial membrane fusion. *Molecular Biology of the Cell*, **20**:3525–3532.
- Zorov, DB., Filburn, CR., Klotz, LO., Zweier, JL. & Sollott, SJ. (2000). Reactive oxygen species (ROS)-induced ROS release: a new phenomenon accompanying induction of the

mitochondrial permeability transition in cardiac myocytes. *Journal of Experimental Medicine*,
192:1001-1014.